RHODES UNIVERSITY
Where leaders learn

Evolution of Fe-Ti-V oxides from the Main Magnetite Layer, Upper Zone, Bushveld Complex, South Africa: a comparison across the Western, Northern and Eastern Lobes

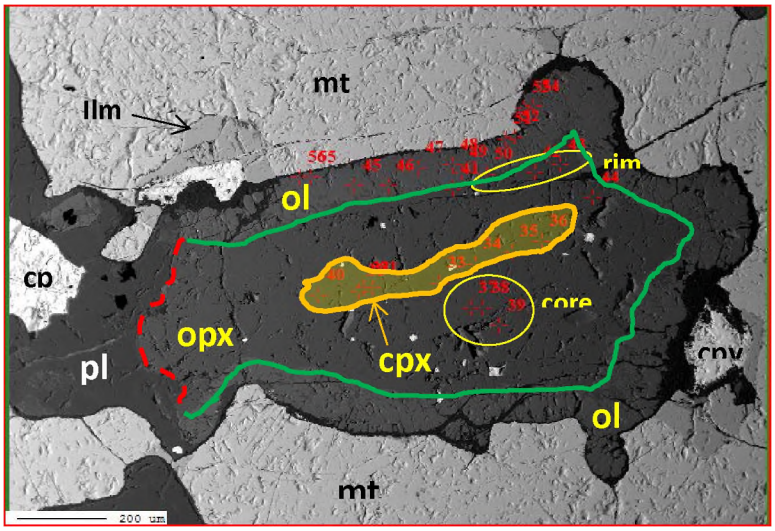

A thesis submitted in fulfilment of the requirements for the degree of

MASTER OF SCIENCE

of

RHODES UNIVERSITY

by

Adina Iorga-Pavel

Supervisor: Prof. Stephen Prevec

- March 2017 –

PLAGIARISM DECLARATION

1. I have read and understood the university plagiarism policy, and consequently understand what plagiarism is, and appreciate that it is wrong and if detected may result in penalties.
2. I know that plagiarism means taking and using ideas, writings, words or inventions of another person as if they were my own. I know that plagiarism not only includes verbatim copying, but also the extensive use of another person's ideas without proper acknowledgement (which includes proper use of quotation marks). I know that plagiarism covers this sort of use of material found in text sources and from the Internet.
3. I acknowledge and understand that plagiarism is wrong.
4. I understand that my research must be accurately referenced. I have followed the rules and conventions on referencing, citation and use of quotations as set out in the departmental guide.
5. This assignment is my own work, or my group's own unique group assignment. I acknowledge that copying someone else's assignment, or part of it, is wrong, and that submitting identical work to others constitutes a form of plagiarism.
6. I have not allowed anyone to copy my work, or part of it, in this assignment with the intention of passing it off as their own work.

Signed: 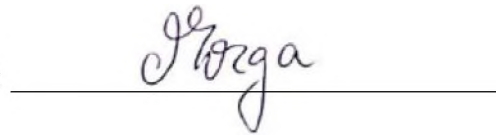 Date: 24.11.2016

Table of Contents

Acknowledgements

First and foremost, I want to thank Gabi (Dr Gelu Costin), my partner and husband, for all his moral, financial and professional support. He kindly helped with payment for the tuition fees, polished thin section preparation and microprobe analyses and he was there for me whenever I needed, to encourage and support me during field or laboratory work, all along during my MSc thesis, in and out of the University. I learned from our long geological discussions, home or in front of the microscope, about the Bushveld Complex and its challenging questions. I learned from him how to operate an electron microscope and EDS analysis, how to operate a modern Jeol electron microprobe at Rhodes University, how to use and interpret MELTS algorithms and other software. Without your support, this thesis would have not been possible. Thank you from the bottom of my heart!

Special and deep thanks to Prof. Steve Prevec, my supervisor, who gave me the opportunity to study in South Africa and to start an MSc thesis under his supervision. Thanks for welcoming me in the Department and support me over all these years, with high competence and kind heart. Thanks for this amazing subject on the Upper Zone of the Bushveld Complex. Thanks, Steve!

I am extremely grateful to Prof. Morris Viljoen from Bushveld Minerals, and his brother Richard, for allowing my access to the Bushveld Minerals cores, and for financial support during the last year of my MSc. Thank you for helping me in a difficult moment!

I kindly thank Dr. Liana Spies from Bushveld Minerals Ltd. who kindly assisted with access to borehole cores of MML from the Northern Lobe of the Bushveld Complex.

I want to express my gratitude to Pieter-Jan Gräbe of Glencore, for allowing us access to materials from the Western Limb of the Bushveld Complex for my thesis.

I want to warmly thank John Hepple for all his help during the execution of the thin sections in the preparation lab at Rhodes University. Thank you for your professionalism, calmness, politeness and kindness you showed to me, for teaching me how to make myself useful in the preparation lab. You had a lot of patience with me and you made me understand all the steps behind the preparation of a thin section. I really enjoyed spending time in the lab with you.

Thanks to Mr. Thulani Royi and Mr. Andile (Chris) Pikoli for the great help in the execution of polished thin sections. I am sorry that maybe I was too exigent in evaluating the quality of the polishing and I might have given you hard times. I thank you and appreciate your effort.

Thanks to Prof. Yong Yao for taking me on board to join him and his students on the field trip on Northern and Eastern Lobes of the Bushveld Complex.

Thanks to Mauritz Van der Merwe for helping me with important information related to the Northern Lobe of the Bushveld Complex, and for making me better understand the geological

relationships. I keep him in my heart as a friend and as the oldest geologist who knows the Bushveld Complex like he knows his own life. Thanks, Mauritz!

Thanks to Dr Roger Scoon for helping me in the process of understanding the Bushveld Complex. Thank you for your amazing discussions and sharing knowledge regarding the field relationship and textures at different levels of the Bushveld Complex. Thank you for providing significant references for the Upper Zone, and for critical and useful observations on my work.

Kind and warm thanks, for everybody in the Department of Geology at Rhodes University. You made me feel like home, you made me feel among friends. Thank you, Steve, Steffen, Goonie, Roger Jacob, Hari, Yong, Ashley, Vuyo, Rosie, and Andrea. Thanks to the NRF and Rhodes interns from the EPMA laboratory, Maggie, Lethabo and Thapelo for the time spent together at the microprobe but also outside of the University. Thanks to my colleagues, the graduate students who helped me accommodate to student life at Rhodes University and with teaching tutorials: Brenton, Briony, Bantu, Marcia, Darryn, Dave, X and others. Thanks to you all! It was great to be a Rhodent together with you! You guys rock! ☺

Lastly, I want to express my deep gratitude and to thank from all my heart to my mother, for always encouraging me in difficult times, for her concerns and her advices. Thank you, mama! I love you!

List of abbreviations

An	Anorthite
Cpy	Chalcopyrite
CRF	Crocodile River fault
EDS	Energy Dispersive Spectrometry
Ep	Epidote
ilm	Ilmenite
MML	Main Magnetite Layer
MAG	Magnetite
Ol	Olivine
Opx	Orthopyroxene
Pig	Pigeonite
Pl	Plagioclase
PM	Pyroxenite marker
Pntl	Pentlandite
Py	Pyrite
Qz	Quartz
Ru	Rutile
SF	Steelpoort faul
Sp	Spinel
Sympl	Symplectite
TML	Thabazimbi–Murchison lineament
UCZ	Upper Critical Zone
UMZ	Upper main Zone
uvsp	Ulvöspinel
UZ	Upper Zone
UZ	Upper Zone
WDS	Wavelength Dispersive Spectrometry
WF	Wonderkop fault

List of figures

Figure 13: Wavelength Dispersive Spectroscopy (WDS) element map distribution for "X" mixture (Cu and S not shown). Notice heterogeneous and discrete distribution of Al, Fe, Si, vs. Ca, Ti, V.

Figure 14: Depth 105.05: A) Pseudomorph of rutile and calcite included in Ti-magnetite (transmitted light, crossed polars); B) Rutile with calcite near chloritized biotite in pseudomorph-like inclusion in Ti-magnetite (BSE image); C) Rutile and chlorite in Ti-magnetite (transmitted light, crossed polars); D) Chlorite (Chamosite) replacing a mafic mineral, probably a pyroxene; notice the fine exsolutions in host Ti-magnetite. See List of abbreviations.

Figure 15: WDS element map distribution for rutile and calcite in Ti-magnetite (corresponding BSE image in Figure 13B).

Figure 16: Depth 125.08 m. Thin anorthosite layer. A) Coarse grain plagioclase with interstitial clinopyroxene and amphibole reaction corona in between magnetite and plagioclase (transmitted light, crossed polars); B) Coarse grain plagioclase with deformation twins.The opaque mineral (Ti-magnetite) seems to be engulf the plagioclase (transmitted light, crossed polars); C) (Chloritized) amphibole reaction corona developed in between magnetite and plagioclase (BSE image). D) The amphibole reaction corona also developed in between ilmenite and plagioclase (BSE image)

Figure 17: Depth 127.28 m. A) Kinked biotite aggregate within a clinopyroxene-plagioclase symplectite (transmitted light, crossed polars). B) Biotite aggregate in clinopyroxene – plagioclase symplectite. The plagioclase grain to the left is almost completely chloritized (BSE image).

Figure 18: Depth 129.83 m. A) Olivine reaction corona between magnetite and orthopyroxene. Notice the clinopyroxene inclusions in orthopyroxene (transmitted light, crossed polars); B) Olivine reaction corona between magnetite and orthopyroxene (BSE image). C) and D) Olivine corona does not develop in between magnetite and plagioclase (transmitted light, crossed polars); E) Kinked plagioclase with deformation twins included in magnetite (transmitted light, crossed polars); F) Fine cpx-pl symplectite growing towards plagioclase and originating in the fine mineral aggregate with olivine near the magnetite (transmitted light, crossed polars).

Figure 19: Depth 129.97m. WDS element map distribution in olivine reaction corona developed in between magnetite and orthopyroxene. The correspondent BSE image is in Figure 16B.

Figure 20: Symplectite of clinopyroxene and plagioclase developed from the olivine formed near the Ti-magnetite towards the igneous plagioclase.

Figure 21: A) Zones devoid of exsolution lamellae in Ti-magnetite (BSE image); B) "Patchy" healing of exsolution lamellae in Ti-magnetite

Figure 22: Depth 133.78 m. A) Secondary chlorite and small sulphides developed on the grain boundaries of igneous oxides and silicates (transmitted light, parallel polars); B) Same as A), in cross polars. C) Same as A and B, showing the opaque phases are magnetite and associated chalcopyrite (reflected light, crossed polars); D) Same as A, B and C in BSE image. E) Rare biotite as part of the secondary phase developed on the grain boundaries (transmitted light, parallel polars); F) Magnetite including and "cementing" plagioclase grains (BSE image).

Figure 23: Depth 135.44 m. Thin anorthosite inside the MML. A) Interstitial clinopyroxene with exsolution lamellae, magnetite and pyrite included in plagioclase (BSE image); B) Interstitial clinopyroxene with exsolution lamelae, magnetite, pyrite and coarse grains of plagioclase (BSE image); Depth 136. Anorthosite. C) Coarse grains of plagioclase and interstitial clinopyroxene with

exsolution lamellae of orthopyroxene (transmitted light, parallel polars); D) Small rounded magnetite grain in plagioclase (transmitted light, parallel polars);

Figure 24: Depth 135.44. WDS element distribution map of ilmenite.

Figure 25: Outcrop sketch at Magnet Heights. 1. Magnetitite; 2. Thin anorthosite separating two main layers of magnetitite; 3. White mica, limonite and disseminated pyrite at the floor contact; 4. Plane with limonite and disseminated sulphides (pyrite). MH1-MH10: sample location in the outcrop.

Figure 26: Sample MH1B (base of MML). A) Massive magnetite with frequent mafic inclusions transformed into epidote and chlorite (transmitted light, crossed polars); B) Massive magnetite showing polygranular texture of magnetite, with chlorite developed along grain boundaries (transmitted light, crossed nicols); C) and D) Ti-magnetite grains with exsolution lamellae and interstitial mafic minerals altered to epidote and chlorite (BSE image).

Figure 27: A) Sample MH2: Completely chloritized silicates associated with Ti-magnetite and ilmenite; B) Sample MH3: vein with chlorite and epidote in Ti-magnetite: C) Sample MH4. Ilmenite grains with fine sulphide and altered mafic minerals inclusions, surrounded by Ti-magnetite (BSE image); D) Sample MH4: Ilmenite grain nest with inclusions of chloritized mafic minerals; notice the very fine exsolution "droplets" of spinel as very fine black spots. The silicate inclusions are small and completely transformed into chlorite ± epidote. (BSE images).

Figure 28: A) Sample MH5: Spinel exsolution lamellae in Ti-magnetite (BSE image); B) Sample MH5: Chloritized mafic inclusion in Ti-magnetite; notice the Ti-magnetite surrounding the inclusion showing patches depleted in spinel exsolution lamellae; C) Sample MH9: igneous silicates totally transformed to chlorite in MML; D) Sample MH10, top of MML: fine spinel exsolutions in Ti-magnetite and igneous primary silicate totally transformed to chlorite (dark gray) and epidote (light gray). BSE images.

Figure 29: Sample MH12A: magnetite-anorthosite, above MML and four other magnetite layers. A) Interstitial magnetite and coarse grained plagioclase (Transmitted light, crossed polars); B) Ti-magnetite and ilmenite inter-locked with subhedral grains of plagioclase (BSE image).

Figure 30: The sampled outcrop of MML at Rhovan mone. Notice the non-planar anorthosite floor and the variable thickness at the outcrop scale.

Figure 31: Sample 10-30: A) Chloritized mafic minerals as oriented inclusions in Ti-magnetite. Notice the spinel exsolutions in Ti-magnetite (black droplets) (BSE image); B) Ilmenite developed on the grain boundaries (BSE); Sample 50-60B: C) Chloritized orthopyroxene and ilmenite included in Ti-magnetite. Notice areas of Ti-magnetite rich in spinel exsolution "droplets" (BSE image); D) Chloritized pyroxene and ilmenite grains in Ti-magnetite (BSE image).

Figure 32: Sample 70-80: A) Laths of plagioclase included in massive Ti-magnetite; elongated ilmenite developed along magnetite grain boundary (BSE image); B) Ilmenite along Ti-magnetite grain boundary, cross-cut by chlorite deposited on a fracture and at the intersection of fractures (BSE image).

Figure 33: Chemical variation in Ti-magnetite in MML (Northern limb). A) Negative correlations between TiO_2 and $FeO+Fe_2O_3$; B) No correlations between V_2O_3 and TiO_2 (notice V_2O_3 variation from 1.2 to 2 wt % for a range of TiO_2 of 10-15 wt%); C) Positive correlation between MnO and

TiO_2; D) Negative correlation between Cr_2O_3+MgO and FeO+Fe_2O_3+TiO_2 (see text for explanations).

Figure 34: Variation of Cr_2O_3, Fe_2O_3, MgO, TiO_2 and V_2O_3 with stratigraphic height (MML, borehole VK5).

Figure 35: Composition of plagioclase in MML, borehole VK5.

Figure 36: Reversals of An in plagioclase in MML from borehole VK5.

Figure 37: Composition of orthopyroxene and clinopyroxene from MML, Northern limb; Notice the pigeonite-rich core of some orthopyroxene and the diopside-augite range of the clinopyroxene.

Figure 38: Core to rim variation of Mg# in orthopyroxene included in Ti-magnetite, towards olivine corona. Notice the Mg# increase of Opx towards the olivine.

Figure 39: Olivine develops towards the opx, on the opx space, only. Numbers represent electron microprobe analyses in Ti-magnetite. (BSE image).

Figure 40: Mg vs $2Fe^{2+}$ (apfu) in olivine reaction band from core to rim towards the magnetite

Figure 41: Compositional variation in Ti-magnetite from the MML of the Eastern limb at Magnet Heights. A) MnO vs. TiO_2; B) Distinct Cr_2O_3 and V_2O_3 in three samples; C) Negative trend Cr_2O_3+MgO vs. FeO + TiO_2; d) distinct groupings of Cr_2O_3 + MgO vs Al_2O_3. See text for explanations.

Figure 42: Compositional profiles (Cr, Mg, Ti, V) with depth (in centimetres) for MML at Magnet Heights.

Figure 43: Compositional variation in Ti-magnetite of MML, Western limb. A) Discrete Cr_2O_3 wt% in two different samples; B) Negative correlation between TiO_2 vs. FeO+ Fe_2O_3; C) No correlation between TiO_2 vs. MnO; D) Strong negative correlation between V_2O_3+ TiO_2 and FeO+ Fe_2O_3 (see text for details)

Figure 44: Phase proportions during isobaric crystallization at P=2 kbar calculated parental magma of the Upper Zone from Tegner et al. (2006). Oxygen buffer Hematite-Magnetite (HM).

Figure 45: Phase proportions during isobaric crystallization at P=2 kbar calculated parental magma of the Upper Zone from Tegner et al. (2006). Oxygen buffer Fayalite-Magnetite-Quartz plus 2 log units (FMQ+2).

Figure 46: A) No correlation between Cr_2O_3 and TiO_2 in the three lobes. Cr_2O_3 varies across MML samples in the same lobe (e.g. E and W lobes) but it is homogenously distributed in the N limb; B) Highest V_2O_3 in the N limb MML; negative trend of V_2O_3 vs. TiO_2 in E and W limb, but no trend in the N limb; C) No correlation is observed between V_2O_3 and Cr_2O_3 in MML of the three lobes.

Figure 47: Model of oxides crystallization in the MML (Upper Zone, Bushveld Complex). The horizontal scale is exaggerated, in order to accommodate processes happening near but also far away from the magma feeder. See text for explanations.

List of tables

Abstract

The Main Magnetite Layer (MML) from the Northern, Eastern and Western lobes of the Bushveld Complex shows significant differences in textures and in mineral chemistry. The MML in the Eastern and Western lobes is massive, with rare, small and altered pyroxene inclusions. By contrast, the MML in the Northern Lobe is more heterogeneous, and it is made of anastomosed and sometimes imbricated, thin layers of magnetitite, magnetite-rich and silicate-rich rocks, where the inclusions in Ti-magnetite are more numerous and consist of mainly altered subhedral and anhedral plagioclase. The comparison of the maximum values of the oxides shows that the MML in the Northern Lobe has the highest content of V_2O_3 (1.97 wt%), TiO_2 (22.49 wt%) and MgO (2.92 wt%), while the MML in the Eastern Lobe has the highest content of Cr_2O_3 (2.92 wt%) and Al_2O_3 (9.80 wt%), but lowest V_2O_3 (0.52 wt%). The lower TiO_2 content and higher V_2O_3 content in the MML of the Northern and Western Lobes suggest lower oxidising conditions during the crystallization of oxides. The MML in all three studied lobes consists of two layers of magnetitite, suggesting that MML was formed by two separate magma influxes, probably on a diverse and complex type of magma chamber floor. The high TiO_2 content in magnetite, together with the negative correlation between TiO_2 and V_2O_3 suggest that the maximum V content should represent a "less evolved" and less oxidized melt. In this respect, higher concentrations of V_2O_3 in magnetite can be expected in magnetitite layers with lower TiO_2. It can be inferred that the Ti-magetite in the MML from the Eastern Lobe was formed from a more evolved (TiO_2 and FeO enriched) and more oxidized (lower V_2O_3) melt, compared with the MML from the Northern and Western lobes. These findings can be used to illustrate: a) that high fO_2 can be responsible for the relatively low V content in magnetite from Fe-Ti oxide ores and b) the vanadium in magnetite decreases significantly in more evolved cumulates, due to a decreasing fO_2 with differentiation. Compositional profiles of Ti-magnetite along the stratigraphic height of the MML in the Eastern Lobe (composed of two layers, separated in the outcrop by a parting plane) depicts a cryptic variation with depth in each of the two layers, where each layer can be divided into four sublayers, labelled upwards as A, B, C (with C1, C2, C3 and C4) and D based on Cr, Mg, Ti, Al and V variation. Small scale reversals of the mentioned elements and the repetition of A, B, C and D sub-layers in each layer suggest that MML formed from two successive influxes of magma (indicated by relatively elevated values of MgO), which evolved by crystallization and cooling in a similar manner, to produce the A to D variation. Based on these observations and theoretical considerations, this study dismisses several models for the genesis of the MML: the immiscibility, the increased oxygen fugacity, the relative increase of H_2O content of the melt, pressure variation within the magma chamber, magma mixing, and crustal rock contamination. The model proposed here for MML genesis involves the crystallization of both

Ti-magnetite and ilmenite from a Fe-Ti-Ca-Al-rich melt (ferro-diorite) along its line of descent, and gravitational settling of oxides in a dynamic regime. The factor which triggered the crystallization of magnetite is a critical saturation of melt in magnetite (attaining saturation of magnetite and ilmenite in the melt after some silicates crystallized). The difference between the nature of silicate inclusions in magnetite and the nature of the magnetite floor, suggest that the Fe-rich magma was not in equilibrium with the cumulates from the present floor, but rather it was emplaced laterally on long distances, the melt being disrupted from its own cumulates. The absence of correlation between the Cr_2O_3 in magnetite and co-existing ilmenite can indicate than no in-situ fractional crystallization took place at the moment of magnetite accumulation, but rather that magnetite and ilmenite gravitationally accumulated and the grains mechanically mixed from a flowing magma. The model presented herein proposes a five stage model of MML formation: Stage 1 is represented by the intrusion of a Fe-T-Ca-Al-rich magma which expands laterally within a flat and thin magma chamber. Oxides start to crystallize within a dynamic regime of the magma. Stage 2 is given by the accumulation of oxides at the bottom of the new floor. Some plagioclase starts to crystallize (e.g. subhedral plagioclase in the MML of the Northern Lobe). Stage 3 is a short living static regime, where both plagioclase and magnetite crystallized, without fractionation, forming the thin magnetite-anorthosite layer separating the MML into two layers. Stage 4 is represented by a new influx of Fe-Ti-Ca-Al-rich magma which is emplaced above the magnetite-bearing anorthosite, flushing out the liquid which was in equilibrium with the anorthosite. The oxides started crystallizing in a dynamic regime, as in Stage 1. In stage 5, the accumulation of oxides produced the upper layer of the MML. Our interpretation is that the flow of the magma was more dynamic (probably more turbulent on long distances) in the MML of the Northern Lobe, compared to the MML in the Western and Eastern lobes, producing highly heterogeneous and imbricated thin layers of magnetitite and silicates. The presence of olivine corona around orthopyroxene suggests the incongruent melting of orthopyroxene, which points out towards a local re-heating of existing silicate layers, this being a strong argument for multiple injections in generation of MML. Massive crystallization of oxides produced the sulphur saturation of the magma and caused the precipitation of the igneous sulphides, which nucleated on the existing oxides. Later hydrothermal fluids (and/or late magmatic volatiles?) percolated the MML, producing chloritization of the included silicates, remobilization of igneous sulphides and precipitation of hydrothermal sulphides.

1. Introduction

The Bushveld Igneous Complex (BIC), the largest igneous layered intrusion on Earth (e.g. Tegner et al., 2006, Eales and Costin, 2012), and hosts incredibly rich mineral deposits, from which a few stand out as amongst the richest in the world, such as platinum and palladium (51.3% of world's production and 95.45% of world's reserves) and chromium (55.55% of world's production and 41.67% of world's reserves). The BIC holds the second place after China in the production and reserves of vanadium: 24.05% of world's production and 23.33% of world's reserves (data compiled from USGS Mineral Commodities Summary, 2016). The vanadium deposits in the BIC are hosted in Ti-magnetite rich layers present in the upper part (Upper Zone) of the BIC.

According to Cawthorn and Webb (2001) and Webb et al. (2004) the gravity data suggests that the eastern and western limbs are connected over at least 65 000 km^2 and the intrusion can be considered as a large igneous province (Coffin and Eldholm, 1994).

The present work focusses on this last type of deposit, the Fe-Ti-V oxides, trying to understand the genesis of Ti-magnetite in the Main Magnetite Layer (MML) from the Upper Zone (UZ) of the BIC. The study also compares for the first time the detailed chemistry of magnetite from the MML in the three main lobes of BIC: Western, Eastern and Northern. The aim of this study is to critically evaluate the existing models of magnetite formation and to advocate for one model which would better fit: 1) the observations (textural and micro-textural relationship between magnetite and associated mineral phases), and 2) the physical and chemical conditions of magnetite precipitation (the composition of the magma from which magnetite crystallized, mineral reactions between magnetite and other phases, variation of magnetite chemistry in between the three lobes, as well as the variation of the chemistry along vertical profiles in MML).

The Main Magnetite Layer represents an important stratigraphic marker in the Upper Zone (UZ) of the Bushveld Igneous Complex, mapped in all of its three exposed lobes (Eastern, Western and Northern) (Figure 1). It is a layer of ca. 2 m thick of magnetite (Fe_3O_4) and has been targeted by mining companies for its elevated V_2O_5 concentrations (1.8-2.2 wt%) (Maier et al., 2012). The theoretical models for magnetite genesis, and processes which were responsible for triggering magnetite crystallisation are still debated.

There have been many models proposed for magnetite formation. However, no such model has much in common with the models of chromite formation in the Lower Critical Zone (LCZ) and

Upper Critical Zone (UCZ), even though several features are strikingly similar: (1) magnetite is a spinel-type mineral, like the chromite, (2) it forms massive layers of magnetite (magnetitites), like the chromite in LCZ and UCZ; (3) it occurs as cyclic units in the UZ like the chromite in LCZ and UCZ; (4) it shows intimate relationships with plagioclase and it is spatially associated with plagioclase-rich rocks, such as leuconorites and anorthosites, like the chromite layers in the UCZ.

In addition to addressing this "un-pairing" of the models regarding the processes which lead to the formation of chromite and magnetite, the present study will attempt to take into account the variability of distinct factors existing in the three lobes (e.g. different host rocks, missing lithological terms, variations in the recognized numbers of magnetitite layers, a variation of reaction types involving magnetite and adjacent phases etc.). A comparative model should allow for distinguishing primary versus regional factors influencing the formation and composition of Ti-magnetite. Such a comparative study between magnetite from the MML in the three lobes can also account for local settings which possibly influenced the magnetite precipitation, its chemistry and possible textural relationships: (1) proximity to the footwall; (2) petrographic nature of the footwall (e.g. Malmani dolomite might have a different influence when comparing with Banded Iron Formation, or Pretoria Group quartzites or basement Archean gneisses); (3) consideration of coronitic microtextures as primary magmatic versus secondary (subsolidus reactions) features.

The implications of answering the above questions are related to a better understanding of Ti-magnetite formations (e.g. proposing a new model, or refining an existing one, or at least eliminate some models). The understanding of Ti-magnetite formation can help us better understand genetic and timing aspects related to the Bushveld Complex itself, such as: a) reflection of the present data towards the question if there is continuity between the Western and Eastern Lobes; b) implication of the emplacement of the Northern Lobe, where the timing, the spatial extent and the link to the main complex remain unclear; c) timing and conditions of observed disequilibrium textures in between oxide and silicate minerals.

In order to address these questions, I collected samples from the MML in each exposed lobe, from relatively well-characterized locations, as follows: 1) Rhovan Mine in the Western Bushveld; 2) Exploration drill core from VK5 and VL5 drills (with the permission of Bushveld Minerals) from the Northern Lobe; 3) Magnet Height classic occurrence of MML, Eastern Lobe. An extensive optical study and EPMA work were done on the selected thin sections, where quantitative analysis

and Wavelength Dispersive Spectrometry (WDS) element map distribution were carried out. Several Backscattered Electron (BSE) images were acquired to illustrate the micro-textural context of the encountered mineral phases.

The composition of oxides and silicates analysed with the electron microprobe were then grouped in mineral types, calculated based on stoichiometry and charge balance ($Fe^{3+/2+}$ estimation), and plotted in various diagrams, using MinPet2.0 software available at Rhodes University.

In order to evaluate some of the genetic models (e.g. liquid immiscibility of Fe-rich liquids from a ferro-gabbroic magma, or crystallization of magnetite from a Fe-rich magma), thermodynamic calculations for estimation of the parent magma of the UZ were performed using alphaMELTS software, version 1.4.1 (Smith and Asimow, 2005; Antoshechkina and Asimow, 2010), which employed MELTS algorithms from Ghiorso and Sack, (1995).

2. Geological Setting and introduction to the Bushveld Complex

2.1. Brief geology of the Bushveld Igneous Complex

The Bushveld Igneous Complex (BIC) represents the largest layered mafic–ultramafic intrusion known on Earth (e.g. Eales and Costin, 2012), being mapped over approximately 60,000 km^2 in sub-surface outcrop, developed in five distinct lobes: Western, Eastern, Northern, Farwestern and Southern (Bethal) (Figure 1). The ultramafic and mafic components of the BIC form the so-called Rustenburg Group. The age of BIC is ~2.056 Ga and it was intruded as a shallow but extremely large lopolith, this shape being clearly indicated by the geometry of the Western and Eastern Lobes, which gently dip towards the center (towards each other). Both Western and Eastern Lobes consist of layered plutonic rocks which show an almost identical succession of the rock layers, suggesting a continuity between the lobes (e.g. Cawthorn and Webb, 2001; Webb et al., 2004). The rock succession can be divided from bottom upwards (Eales and Cawthorn, 1996) into: 1) The Lower Zone, made of mostly harzburgites, dunites and pyroxenites, 2) the Critical Zone, distinguished by the first appearance of plagioclase layers, which is divided into two subunits: 2a) a Lower Critical Zone, made of mostly orthopyroxenites and layers of chromitite, and the Upper Critical Zone, made of mostly anorthosites, norites, orthopyroxenites and multiple layers of chromitites, some of them hosting PGE deposits. At the top of the Lower Critical Zone outcrops the well-known Merensky

Reef, typically consisting of an orthopyroxenite layer hosting discontinuous fine chromitite stringers (the lower chromitite and the upper chromitite), but also sulphides which are associated with PGMs.

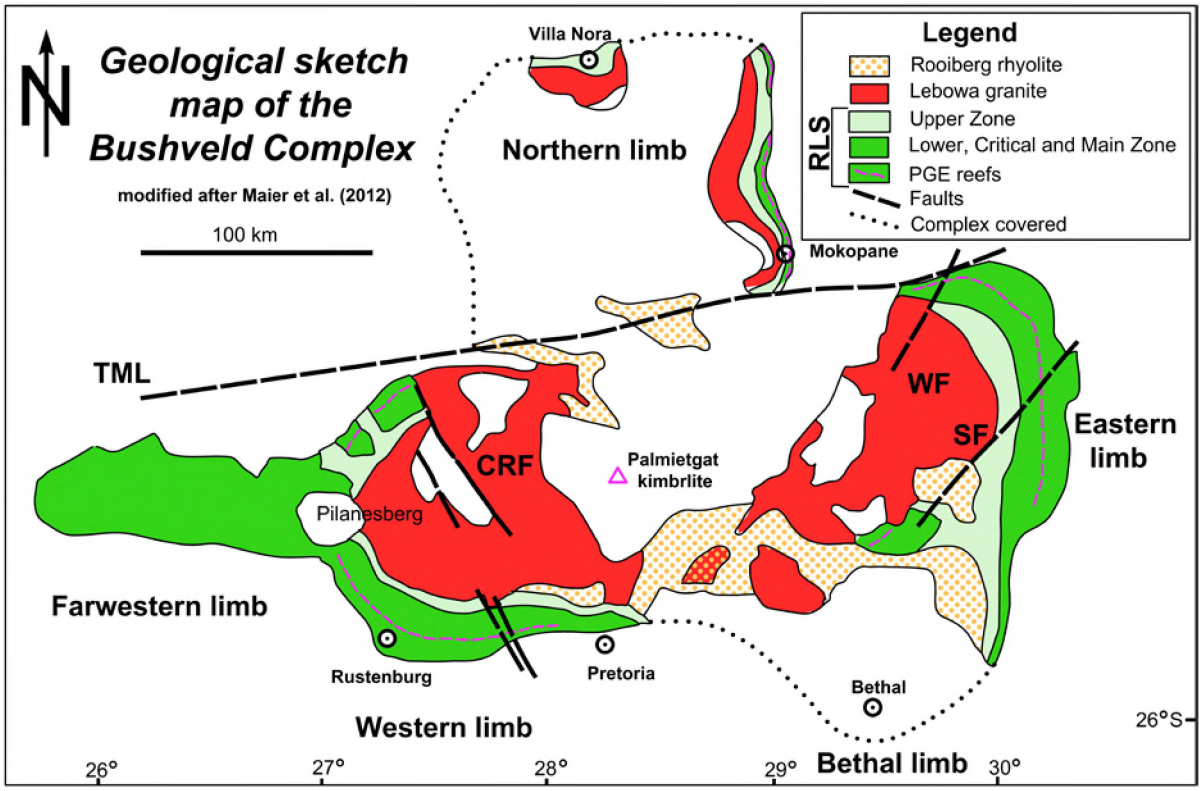

***Figure 1**: Simplified geological map of the Bushveld Complex, modified after Maier et al. (2012), showing the geological constitution of the main lobes. TML Thabazimbi–Murchison lineament, CRF Crocodile River fault, BG Brits graben, SF Steelpoort fault, WF Wonderkop fault.*

Its central part it is mostly covered by rhyolites (Rooiberg Group) which consist of the cap of the BIC, and by a very recent sedimentary cover. The central part also hosts one of the largest volumes of A-type granites (the Lebowa granites) which intruded the BIC very soon after the Rustenburg Layered Suite of the BIC was consolidated (e.g. Maier et al., 2012). The age of the granites falls within error of the BIC's age. The BIC is mostly known for hosting the world's most valuable resources in PGE (e.g. Naldrett, 2009), Cr and V, with significant Cu, Ni, Au, Sn, fluorite, Fe, (e.g., Wilson and Anhaeusser, 1998), and the biggest andalusite deposits in the world, developed in the contact metamorphic aureole of the intrusion (Oosterhuis, 1998).

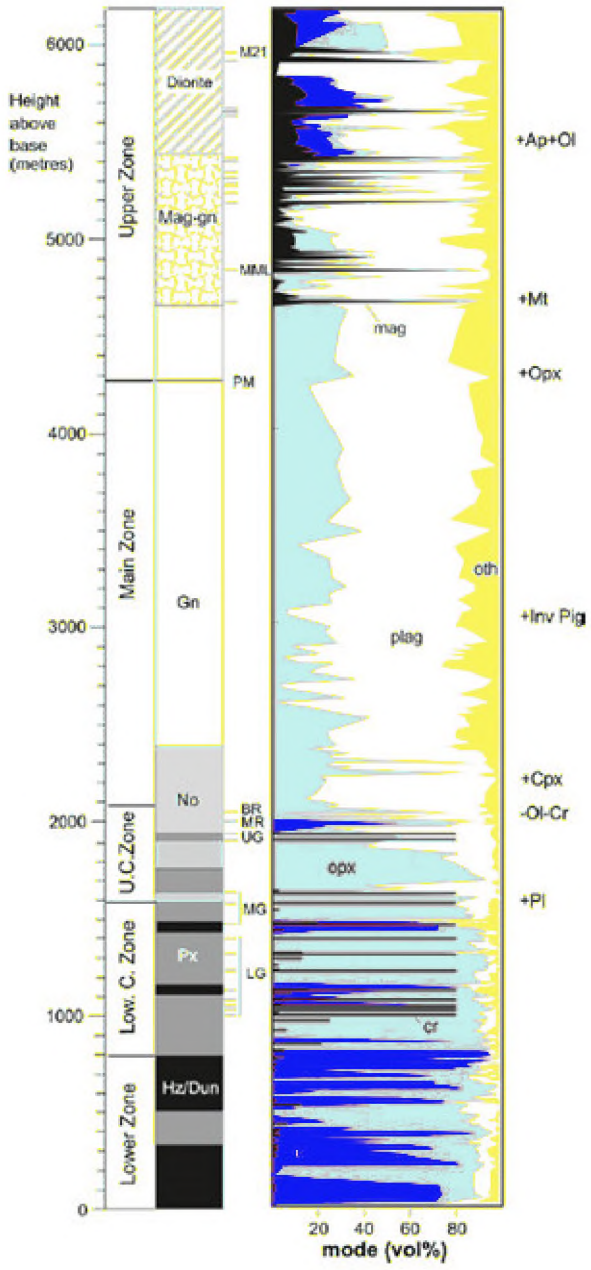

Figure 2:

Lithologic column of the Bushveld Complex, modified after Maier et al. (2012). Marker horizons: LG Lower Group chromitites, MG Middle Group chromitites, UG Upper Group chromitites, MR Merensky Reef, BR Bastard Reef, PM Pyroxenite Marker, ***MML*** *main magnetite layer, M21 magnetite layer 21. Abbreviations to the right of the column indicate first appearance (+) and disappearance (−) of cumulus phases: Pl plagioclase, Ol olivine (blue layers), Cr chromite, Cpx clinopyroxene, Inv Pig inverted pigeonite, Opx orthopyroxene, Mt or mag magnetite, Ap apatite.*

A synthetic lithologic column of the Bushveld Complex with variation of proportion of different minerals is presented in Figure 2. The Upper Zone forms the top of the Bushveld Complex, having an approximate thickness of ca. ~2100 m. It has a discordant nature (Wilson et al., 1994; Scoon, 2002) and it mostly consists of ferro-gabbronorites associated with magnetitite layers and nelsonite layers towards the top, followed by mostly ferro-diorite, without magnetitite layers. The base of the Upper Zone has a significant number of country rock xenoliths consistent with the discordant nature of the Upper Zone. According to Kent (1980), the Upper Zone starts with the first appearance in the

stratigraphic sequence of cumulus magnetite, and is overlain by the Rooiberg "floating" felsites and granophyres (Kruger, 2005). Kruger (2005) considered that the Upper Zone starts from the Pyroxenite Marker upwards. This interpretation is related to the fact that the initial $^{87}Sr/^{86}Sr$ is constant from the Pyroxenite Marker up to the Rooiberg felsites (see chapter 2.4 on "Sr isotopic composition"), and that the variation of the chemical composition from the Pyroxenite Marker upwards has a similar pattern, being intermittently well-layered and showing cyclic units. However, the content of FeO of the rocks just above the Pyroxenite Marker up to the first magnetitite layer would not support the interpretation that they formed from the same evolved liquid, rich in Fe and P. This is why most of the authors still consider the base of the Upper Zone where the first cumulus magnetite appears, as suggested by Kent (1980). The sequence of rocks between the Pyroxenite Marker and the first magnetitite layer is usually called the Main Upper Zone (MZU) (e.g., Tegner, 2006).

The lithology within the Upper Zone changes cyclically from gabbronorite and ferro-gabbronorite to ferro-diorite, with mostly leuconorite, anorthosite and magnetitite layers occuring towards the top of the intrusion in the Eastern Limb. At the top contact with the metamorphosed felsite or granophyre no chill marginal rocks were observed. Primary orthopyroxene has a variable presence in the plagioclase-dominated rocks. According to von Gruenewaldt (1973) and Molyneux (1974), the low-Ca pyroxene is pigeonite and it is more abundant near the base of the UZ, and is absent near the top. Biotite, hornblende, and, especially over the uppermost 200 m, quartz, and alkali feldspar, have been described as interstitial, late phases.

The cyclic character of the Upper Zone was first mentioned by Tegner et al. (2006), who recognized geochemical reversals of anorthite content of plagioclase and Mg# of olivine and pyroxene (Figure 3). They identified nine cycles (I to IX), with two particular cycles (V and VI) showing the most significant reversals occurring towards the very top of the Upper Zone, being also associated with the first appearance of cumulus apatite. The generalized lithologic column presented by the authors shows the distribution of the magnetitite layers, as well as the peculiar nelsonite (magnetite-ilmenite-apatite) layers towards the top of the Upper Zone (Figure 3). The authors separated the Upper Zone in three sub-zone, UZa, UZb and UZc, where the bases of subzones delineate the lowest appearance of cumulus magnetite (UZa), olivine (UZb), and apatite (UZc), respectively.

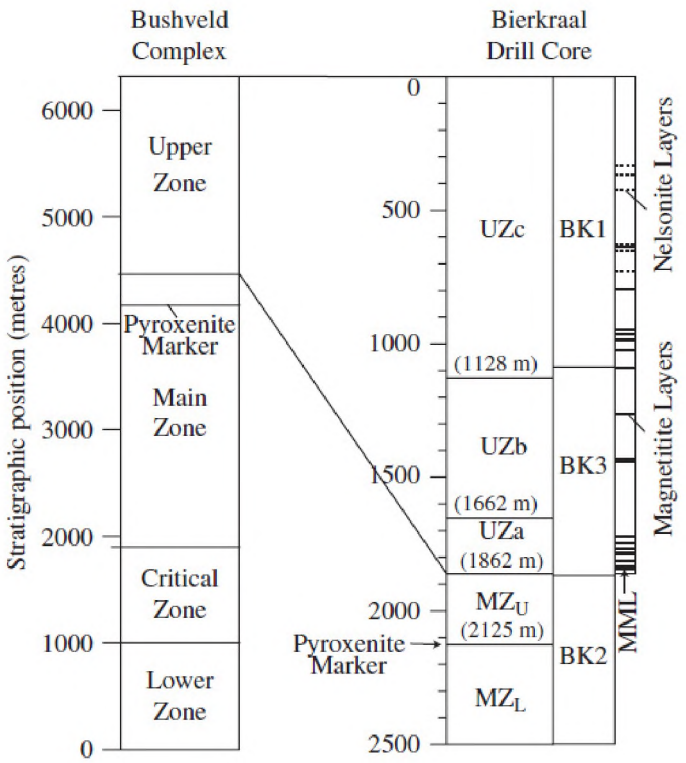

***Figure 3**: Generalized stratigraphic section of the Bushveld Complex (left) correlated with Bierkraal drill cores (right), after Tegner et al (2006). The bases of subzones in the Bierkraal cores delineate the lowest appearance of cumulus magnetite (UZa), olivine (UZb), and apatite (UZc), respectively.*

Tegner et al., (2006) showed that even starting the Upper Main Zone (MZU = the rock pile starting from the Pyroxenite Marker up to the first magnetitite layer) and continuing into the Upper Zone, the rocks pile evolves from Mg# $_{cpx}$ = 74 near the Pyroxenite Marker towards Mg# $_{cpx}$ < 5 in the nelsonite layers. This trend was interpreted by various authors (Wager and Brown, 1968; Willemse, 1969; von Gruenewaldt, 1973; Molyneux, 1974) as a result of a closed-system crystallization without magma recharge.

The re-charging of the Bushveld chamber with a new influx of magma, a hypothesis well documented for the Lower Zone and Critical Zone in explaining the formation of chromitite layers, was has also been invoked for the Upper Zone and the formation of the magnetitite layers. Merkle and von Gruenewaldt (1986) argued for magma re-charge and magma mixing based on the variations in the composition of pentlandite and olivine. The variation of the Fo content [100Mg/(Mg + Fe)] of olivine in the upper section of the UZ has been shown to be significant. The

studies of Reynolds (1985), Merkle and von Gruenewaldt (1986) and unpublished data from Grant Cawthorn (1980), show that the Fo% decreases from Fo_{44} in cycle II to Fo1 at the top of UZc. This decrease is interrupted by reversals which coincide with reversals in Mg#cpx and An%. Some of these reversal increases in Fo% are significant, for example from Fo_{34} to Fo_{52} across the boundary between cycles IV and V and from Fo_6 to Fo_{29} between cycles V and VI (Tegner et al., 2006). Within the cycle V, the olivine composition changes sharply from Fo_{54} to Fo_6, while in between cycle 6 and at the base of cycle IXA, the Fo% of olivine is relatively scattered, but generally increase. Above level IX, Fo% declines sharply to virtually pure fayalitic compositions at the top of UZc. The reversal of the Fo% in olivine, suggests that the fayalite rich olivine reacted with a more primitive magma, and thus, the magma should have been re-charged. However, no textural distinction is clearly made on the analysed olivines in the above-mentioned studies. At least some olivine grains may have become richer in Fo% by sub-solidus reaction between olivine and magnetite during cooling of the system.

Eales and Cawthorn (1996) also invoked re-charging of the magma, based on the observation that the V_2O_5 content of magnetite increases up-section, and this could not be interpreted just as a change in intensive parameters, such as fO_2, during fractional crystallization. Later, Ashwal et al. (2005) provided support for the "re-charging magma" interpretation by identifying reversals in the Mg# of pyroxene and An% of plagioclase in a drill core through the MZU and UZ in the northern limb.

The hypothesis of magma re-charging and mixing is also substantiated by Scoon and Mitchell (2012) who studied the Upper Zone rocks at Roossenekal and provided geochemical evidence of multiple episodes of magma replenishment.

2.2. Magnetitite layers

An important feature of the Upper Zone is the presence of up to 25 magnetite layers in the Eastern Lobe which cluster into four groups, each with up to 7 layers (Molyneux, 1974). Tegner et al. (2006) mentioned 30 distinct magnetite and nelsonite layers, which varies from 2 to 710 cm in thickness. In the Western Limb, the UZ is poorly-exposed in outcrop, which makes it very difficult to determine exactly the numbers of magnetitite layers. However, eight major layers have been

identified in drill-core (Cawthorn, 1996). The magnetitite layers in the Northern Lobe are more anastomosed compared with the layers from the Eastern and Western Lobes, having variable thickness, which makes the correlation of the magnetite layers across the three lobes more difficult. However, the MML, due to its relatively constant thickness and position in the stratigraphy, was recorded and mined in all three lobes.

Magnetitite layers typically show sharp bases and gradational tops. The thickest layer of magnetitite is 6 m, while the MML, close to the base of the UZ, is ca. 2 m thick. It is mined for its ~1.3% V_2O_3 content or, after other sources 1.8-2.1 V_2O_5 (Bushveld Minerals Summary report, 2013).

From the 25 layers of magnetite, two layers represent important mining targets for vanadium content of the magnetite: the Main Magnetite Layer (MML) near the base of the Upper Zone, and layer 21, towards the top of the Upper Zone (Figures 2 and 3). The Main Magnetite Layer has a relatively constant thickness of ca. 2 m and it is mined in both the Western and Eastern Bushveld, from which is extracted more than 50% of world vanadium production (Crowson, 2001). The uppermost magnetite layer (layer 21) can reach a local thickness of ca 60 m, but its regular thickness is ca. 10 m. The MML is rich in autoliths and xenoliths near its base and towards its middle level and can be traced for tens of kilometers along strike (Cawthorn and Molyneux, 1986). The layer 21 is characterized by a relatively large amount of anorthosite xenoliths and a reversal in anorthite content of the plagioclase towards more calcic values (von Gruenewaldt, 1971).

The petrogenesis of magnetitite layers of the UZ have been the focus of many studies (e.g. Bateman, 1951; Wager and Brown, 1968; Irvine, 1975; Cawthorn and McCarthy, 1980; Klemm et al., 1985; Reynolds, 1985; Vvon Gruenewaldt et al., 1985; Kruger and Smart, 1987; Von Gruenewaldt, 1993; Harney et al., 1990, 1995; Kruger, 2005). Interpretations of magnetite genesis vary and some of the genetic models are presented in chapter 2.7.

2.3. Sr isotopic composition

Tegner et al. (2006) analysed Sr isotopes in 24 samples distributed from the bottom to the top of the Upper Zone. The initial $^{87}Sr/^{86}Sr$ ratios were found to be near-constant (0.7073 ± 0.0001) which made the authors interpret that the Upper Zone formed by crystallization from a homogeneous

magma sheet, and rejecting the hypothesis of major magma recharge or assimilation. Even though small variation of initial $^{87}Sr/^{86}Sr$ ratios was identified at the base of cycle V, the combined Sr isotope datasets suggested constancy of initial $^{87}Sr/^{86}Sr$ ratios in MZU and UZ. Based on these results, Tegner et al. (2006) rejected a hypothesis in which re-charging of magma or mixing of magmas are responsible for the formation of the Upper Zone. The authors critically discuss that the initial $^{87}Sr/^{86}Sr$ ratios of the proposed re-charge magmas to the entire Bushveld Complex range from 0.7045 to 0.7090 but none has compositions close to 0.7073 (Kruger, 1994). The authors give an example of rocks in the Bethal area, located SW of the Eastern Limb, which have initial $^{87}Sr/^{86}Sr$ ratio of 0.7055 and have been explained as the products of crystallization from unadulterated Upper Zone magma (Kruger, 2005). Tegner et al. (2006) therefore concluded that recharge with magma with a Sr-isotopic composition similar to existing proposed Bushveld parental magmas can be ruled out, and that "an internal mechanism for generation of the layered MZU and UZ sequence must be sought".

2.4. The age of the Bushveld Complex

The emplacement age of the Bushveld Igneous Complex has been long known to be around 2,050 Ma (e.g. Hamilton 1977; Von Gruenewaldt et al. 1985). Scoates and Friedman (2008) published the first high-precision age determination of the Merensky Reef (2.054.4 ±1.3 Ma, U–Pb on zircons) in the Western Lobe at Rustenburg Platinum Mine, but the age was subsequently revised to 2,056.1±0.7 Ma. This new age was consistent with the age of Merensky Reef from the Eastern Limb (Driekop, 2,055.3 ±0.6 Ma -Scoates et al. 2011), and with the age of the Platreef (2,056.2 ±4.4 Ma; Yudovskaya et al. 2010), confirming that the PGE reef contemporaneously formed in the different lobes of the complex. The contemporaneity of the reef emplacement is further confirmed by Buick et al. (2001) who determined a close U–Pb age of 2,058.9± 0.8 Ma for titanite in a retrogressed xenolith in the Upper Zone. According to Scoates and Friedman (2008), this may reflect titanite crystallization during the emplacement of the early Rooiberg rhyolites (2,061±2 Ma; Walraven 1997).

Mungall et al. (2016) dated drill core samples of gabbronorite from the Main Zone and of pyroxenites from the Merensky Reef, using high precision U-Pb CA-ID-TIMS method. According to the authors, the age of the Main Zone gabbronorite is 2055.86±0.15 Ma, being 0.32 Ma older

than the 2055.54±0.27 Ma age of the underlying Merensky Reef. In a similar tone, the authors offer small differences in ages between various petrographic units (e.g. "the age of the UG1 pyroxenite is 2056.28±0.15 Ma, meaning it is 0.24 Ma older than the underlying MG4 pyroxenite (2056.04±0.15 Ma) which in turn is 0.60 Ma older than the MG2 pyroxenite below that (2055.68±0.20 Ma)"). The age data allowed Mungall et al. (2016) to support the "sill" theory, in which the chromitite-pyroxenite units were emplaced as sills into pre-existing norite or gabbronorite hosting rocks, following pre-existing structural discontinuities such as former layering. The sill emplacement, according to the authors, happened in at least three separate instances in the Upper Critical Zone. Based on this interpretation, the authors consider that anorthosites which occur along both upper and lower contacts of the ultramafic units formed during partial melting of the enclosing norites, a process which could have left plagioclase or plagioclase-chromite restites.

Despite some controversies involving different models for the Bushveld emplacement based on age results, all these age-dating studies reflected one significant interpretation: the emplacement of the Bushveld Complex was relatively short (ca. 5 Ma). Such duration of the emplacement is comparable to the emplacement period of the continental flood basalt provinces, leading the geologists to the idea that a mantle plume was involved in the origin of the Bushveld Complex (Hatton and Schweitzer, 1995; Olsson et al. 2011).

2.5. Introduction to magmatic Fe-ores

Iron ores are associated with sedimentary, igneous, metamorphic and hydrothermal rocks. The sedimentary deposits of Precambrian banded iron formation (BIF) are widespread and represent the target of the main economic exploitation of iron, where the main industrial mineral is hematite. This source type represents almost 90% of all iron ore mined (Beukes and Klein, 1992). The orthomagmatic iron ore is directly crystallized from a melt and it is represented by magnetite (rarely hematite), sometimes associated with ilmenite. The magmatic iron ores are found exclusively in association with basic and ultrabasic plutonic rocks, where many small to medium-sized magnetite deposits occur in gabbroic intrusions. However, the significant magmatic ore deposits come from large stratiform lopoliths, such as the Bushveld in South Africa or Panzhihua intrusion in China. Some of these deposits also contain Ti and V. The Ti is economically significant if granular ilmenite is present, associated with Ti-magnetite. Ulvöspinel is present as fine exsolutions in

magnetite or as an end-member in the magnetitite solid solution. If Ti is accommodated in magnetite solid solution, this represents a downgrade for the economic value of the Ti deposit. The most notorious case of orthomagmatic iron ore is represented by the magnetitite layers in the Upper Zone of the Bushveld Igneous Complex, where Ti-magnetite can contain 1.6-2.2 % V_2O_5 and can also be associated with granular ilmenite.

2.6. Existing models for Fe-Ti-V oxides with special emphasis on the magnetitite layers from the Upper Zone of the Bushveld Complex

Several possible processes responsible for the magnetite formation have been proposed and the models are still debated. These models of Fe-Ti-V oxides formation are briefly explained below.

1) *Fractional crystallization* from a long-stage evolved liquid, rich in Fe and P. This model is probably the most accepted today in the geological community working on the BIC. Detailed discussions on the differentiation of such iron-rich magma from which magnetite can crystallize and settle have been produced by McBirney and Naslund (1990) and Morse (1990) for the Skaergaard intrusion, interpretations which were considered valid for the Bushveld Complex, as well (e.g. Reynolds, 1985; Cawthorn and Molyneux, 1986). Other models relate to the same fractional crystallization model, but the attention is given to the factor which could have triggered the supra-saturation of magnetite in the melt and started the crystallization of magnetite (e.g. high oxygen fugacity, high aH_2O, pressure variation, etc). The model proposed by Reynolds (1985) implies that if significant magnetite is formed by bottom crystallization from a melt, it means that the melt should have had a much higher density than an overlying basaltic melt. Due to the density differences, the two melts cannot mix until significant magnetite is crystallized from the bottom melt, producing an evolved liquid similar in density to the overlying liquid, after which mixing takes place. The model of Reynolds is based on the direct precipitation of Ti-magnetite; however, it can also be applied to the immiscibility theory, by separation of a phosphorus-poor, Fe-Ti oxide liquid from a more complex basaltic liquid, as explained in the immiscibility models (Philpotts, 1967; Kolker, 1982). Reynolds recognized that the alternative mechanism of immiscibility could not be effectively evaluated in terms of available experimental data on Fe-Ti-V-enriched residual liquids of basaltic lineage. Another variant of fractional crystallization of magnetite is the model of Kruger and Smart (2001) in which magnetite crystallizes from a double-

diffusive convection system, also involving a stratified magma with liquid layers of different densities.

2) *Liquid immiscibility*. It is highly controversial whether liquid immiscibility is a dominant process in generating Fe–Ti oxides ore (Zhou, 2005; Pang et al., 2008, 2009; Charlier et al., 2011; Vantongeren and Mathez, 2012; Song et al., 2013; Duchesne and Liégeois, 2015; Velasco et al. 2016). The controversy is mainly due to the fact many liquid immiscible features seem to occur after substantial Fe–Ti oxides crystallization. Velasco et al. (2016) found Fe-rich melt inclusions with low-Ti magnetite, pyroxene, apatite, and minor anhydrite as inclusions in plagioclase and pyroxene phenocrysts in andesite at Laco Volcano (Chile). The authors considered that immiscible globules and the Ti-poor magnetite daughter crystals in the melt inclusions in pyroxene phenocrysts represent the parental iron oxide melt, which after their coalescence led to the formation of magnetite melts, from which the magnetite that formed the El Laco iron oxide deposits crystallized. Conversely, authors such as Jakobsen et al. (2005) reported Si-rich- and Fe-rich melt inclusions among the aggregated apatite in the upper part (above the Fe–Ti oxides layer) of the Skaergaard intrusion (Hunter and Sparks, 1987, 1990; Toplis and Carroll, 1995), a fact which suggests that massive crystallization of magnetite happened before the melt to achieve the immiscibility conditions. Similarly, in the lower part of the Panzhihua intrusion (Sichuan, SW China), as in the MML of the Bushveld Complex, there is no apatite in the Fe–Ti oxide ore layer. This contrasts with the occurrence of significant apatite bearing rocks and nelsonites in the upper part of the above mentioned intrusions (Song et al., 2013), where Si-rich and Fe-rich melt inclusions were found in the apatite (e.g. Wang et al., 2013). However, all these studies indirectly assume that the lower part of the intrusions which bear magnetite and the apatite – oxide layers in the upper part of the intrusions derive from the same parental melt. This assumption can be misleading if different parent melts are considered for the lower and upper parts of the intrusions. A detailed trace element study of the oxides from the lower and upper part of the intrusions is needed in order to elucidate if they derived or not from the same parental magma (e.g. He et al. 2016).

Magnetite formation through immiscible oxide melts at the top of the Bushveld Complex was proposed by van Tongeren and Mathez (2012). This interpretation was based on the high concentration of REE in apatite, which is three times higher in the apatite in the upper section

with magnetite, then in the immediately underlying section. The adversaries of this hypothesis (e.g. Cawthorn, 2013) suggest that the high concentration of REE in apatite is a trapped liquid shift effect, and not a primary magmatic compositional characteristic. The immiscibility in the system felsic silicate – oxide was experimentally proved a long time ago (Philpotts, 1967; Naslund, 1976). It was shown that it is possible to create two immiscible liquids, one quenching to form a mixture of magnetite and apatite in proportions about 2:1, and the other one forming a diorite (Philpotts, 1967). Naslund (1976) showed that under high fO_2 conditions, a FeO-rich melt will separate from a felsic magma. It is notorious that there is a large immiscibility field in the system $KAlSi_3O_8$-SiO_2-FeO at P=1 atm, but the field greatly diminishes in size (in temperature-composition space) in a more reducing environment. Naslund (1983) also showed that the existence of immiscibility is enhanced by high concentrations of P, Ti, and Fe, but the field diminishes with increasing Ca and Mg. All of the above conditions for the existence of immiscibility are met in the Upper Zone, but in spite of the immiscibility model of van Tongeren and Mathez (2012), the geological community is reluctant to accept this model because the textures do not suggest immiscibility. However, it is to be noted that in slowly cooled plutonic rocks, significant resorption reactions can lead to re-homogenization of the segregated liquids (Robb, 2009), or total separation of the liquids, promoting a slow crystallization of massive magnetitite and felsic igneous rock (leuconorite or anorthosite), where the immiscibility textures will not be preserved, as is evident in some volcanic rocks (Velasco et al., 2016). Panzhihua-type Fe-Ti-V ore deposits in China, often showing several similarities with the Upper Zone of the BIC, represent another occurrence where the immiscibility model was invoked (Zhou et al., 2013). However, there are authors that reject the model of magnetite formation due to immiscibility. Toplis and Carroll (1995, 1996) and Tollari et al. (2006, 2008) showed that the composition used in experiments are far away from natural magma compositions. Furthermore, they showed that using compositions close to natural basalts and diorites, magnetite (or ilmenite) crystallizes before the magmas become saturated with Fe oxide liquid. It was concluded that experimental evidence does not support the immiscibility model. More recent experimental studies (Veksler et al., 2007) on liquid immiscibility using model liquid compositions of the Middle Zone of the Skaergaard intrusion at super-liquidus temperatures of 1110 -1120 ^{0}C, showed that static experiments cannot produce liquid immiscibility due to kinetic barriers. However, the centrifugation experiment produced a thin, silicic layer (64.5 wt% SiO_2 and 7.4 wt% FeO) at the top of the main Fe-rich

glass (46 wt% SiO_2 and 21 wt% FeO). The authors mentioned that the two divergent compositions were shown in a series of static runs to produce very similar crystal assemblages of plagioclase, pyroxene, olivine, and Fe-Ti oxides. It was concluded that unmixing of complex aluminosilicate liquids may be seriously kinetically hampered probably by a nucleation barrier, and thus conventional static experiments may not correctly reproduce liquid immiscibility.

Jakobsen et al. (2005) and Charlier et al. (2011) introduced textural evidence in support of immiscibility, citing a number of researchers reporting the presence of Fe-rich and Fe-poor melt inclusions in apatites from layered intrusion. However, London (2008) argued that melt inclusions are not reliable indicators of overall melt composition, due to boundary layer effects. Eales and Cawthorn (1996) rejected the liquid immiscibility model for the Bushveld magnetite layers based on the fact that the Fe oxide liquid would not have formed sharp planar contacts with the underlying cumulates, but instead the dense liquid would have percolated into the interstitial spaces in the cumulate.

Charlier and Grove (2012) conducted crystallization experiments on compositions along tholeiitic liquid lines of descent in order to identify compositional fields of liquid immiscibility. The authors found that immiscibility develops below 1,000–1,020 C^{o} at P=1 atm and under dry conditions, without needing extreme iron enrichment. More than that, the immiscibility also develops during iron depletion and silica enrichment. The experiments showed that elevated values of $Na_2O + K_2O + P_2O_5 + TiO_2$ promotes the development of two immiscible liquids. It was also noted that higher values of CaO and Al_2O_3 in the melt stabilizes a single liquid field. The authors suggested that their data show that anhydrous, low-pressure fractional crystallization is the most favorable condition for unmixing during differentiation. With increasing pressure immiscibility is inhibited because the stability field of high-Ca clinopyroxene expands. The crystallization of Ca-clinopyroxene reduces the proportion of plagioclase to crystallize, thus enhances early iron depletion. Charlier and Grove (2012) also suggested that mixing between primitive basalt melt and Fe–Ti–P-rich ferrobasalts promote unmixing. It was also noted that water might decrease the temperature and size of the two-liquid field, potentially shifting the solvus below the liquidus, leading the system to evolve as a single-melt phase.

3) *Magma mixing.* Harney and von Gruenewaldt (1995) suggested that the magnetitite layers throughout the Upper Zone were formed in response to magma mixing, probably resulting from

the breakdown of densely stratified liquid layers or by an influx of a small volume of new magma into a more evolved magma. This model is practically disregarded by most of the geologists working on the Upper Zone magnetitites (e.g. see Cawthorn and Ashwal, 2009), even though it is somewhat similar with the model of magma mixing in explaining the formation of the chromitite layers (the Irvine model) in the Critical Zone (Irvine, 1975), which is generally accepted. The mixing models are based on the idea that the resident magma in the magmatic chamber can mix with replenishing magmas, which may cause suprasaturation in oxides due to the curvature of phase boundaries. The general criticism of this model is that, in order to form the laterally very extensive Bushveld layers, the proportions and compositions of the mixing end-members should have been broadly constant across the entire 400-km-wide intrusion, which seems difficult to accept (Maier et al., 2012).

4) *Pressure change* as the factor to trigger the magnetite crystallization. Cameron (1980) and Lipin (1993) proposed a model in which the pressure fluctuations in the magma chamber can trigger the precipitation of oxides. For example, if a particular composition of the magma can find itself outside but near the boundary of the spinel (chromite) stability field, an increase in pressure can enlarge this field, so that the spinel T-X boundary would move towards the composition of the magma, leaving it inside the stability field of spinel (chromite). The consequence of this mechanism is that the spinel (chromite) will be the only phase to crystallize, temporarily. This mechanism is convenient for an explanation of the massive oxide layers, as pressure changes would affect the entire magma chamber simultaneously. Cawthorn and Ashwal, (2009) suggest that significant reversal in An content in the overlying plagioclase compared with the underlying layer is consistent with a pressure-change hypothesis for triggering magnetite crystallization, rather than with a magma mixing model. However, Mondal and Mathez (2007) and Naldrett et al. (2012) argued that the shifts in chromite stability fields resulting from pressure change would be negligible and, on top of this, the mechanism would require a very particular composition of the melt, near the spinel boundary.

5) *High oxygen fugacity* was considered by Ulmer (1969) to trigger the crystallization of magnetite. The sudden high oxygen fugacity would have been achieved by contamination. Reynolds (1985) and von Gruenewaldt et al. (1985) also argued that the increase in oxygen fugacity was the factor

which triggered the precipitation of magnetite. Reynolds based this interpretation on the fact that the massive magnetite is typically characterized by the absence of ilmenite lamellar intergrowths. During the evolution of Ti-magnetite, high oxygen fugacity can further promote exsolution of ulvöspinel which, reacting with oxygen, produces ilmenite, aspects which are frequent in the MML. The higher oxygen fugacity in the melt could have been achieved by assimilation of H_2O-rich or CO_2-rich country rocks (e.g. Cameron, 1975, 1977; Ganino et al., 2013). This model is however rejected by Toplis and Corgne (2002) and Balane et al. (2006) who consider that relatively high V contents of the Bushveld magnetite (up to 2.2 % V_2O_5) require the fO_2 of the magma to be in a narrow range of the Nickel-Nickel oxide (NNO) to NNO-1 oxygen fugacity buffer, which is inconsistent with significant oxidation peaks.

Toplis and Carroll (2005) carried out equilibrium crystallization experiments at atmospheric pressure over a range of oxygen fugacity (fO_2) on a ferro-basaltic composition close to what is believed to be the parental magma of the exposed portion of the Skaergaard intrusion. The authors showed that before Fe-Ti oxide saturation, the liquid line of descent is little affected by fO_2. However, the appearance temperatures of the magnetite-ulvöspinel solid solution and the ilmenite-hematite solid solution strongly depend on fO_2. Above the fayalite-magnetite-quartz (FMQ) buffer magnetite is the first oxide to appear on the liquidus, but below the FMQ buffer ilmenite is the first oxide to crystallize. The appearance temperature of both magnetite and ilmenite is ~1100°C at FMQ, but the crystallization temperature of earliest ilmenite moves to lower temperatures at higher fO_2 where magnetite is the first oxide phase. The experiments of Toplis and Carroll (2005) indicate that the ferric iron content of magnetite-saturated melts varies linearly with inverse temperature, and that ilmenite saturation is closely related to melt TiO_2 content. Magnetite saturation in the melt produces an immediate enrichment of SiO_2 and depletion in FeO, whereas ilmenite saturation produces similar enrichment in SiO_2. The experimental liquids reach a maximum of ~18 wt% FeO, at ~48 wt% SiO_2 for ilmenite-saturated melts at low fO_2, more differentiated melts having lower iron and higher silica. Cotectic proportions of magnetite and ilmenite determined experimentally by Toplis and Carroll (2005) are in good agreement with data from natural samples and other experimental studies.

The oxygen fugacity can also have an effect of partitioning V in between Ti-magnetite, silicates and melt. Charlier et al. (2009) showed that high proportion of V^{4+} and V^{5+} appear at high fO_2, making these ions to be less partitioned in magnetite compared to V^{3+} (Toplis and Corgne, 2002).

It can be concluded from the above authors that the Ti-magnetite formed from a melt at high oxygen fugacity will accommodate less V_2O_3 than the Ti-magnetite formed at lower oxygen fugacity. The authors also showed that the vanadium content in magnetite decreases significantly in more evolved cumulates, due to a decreasing fO_2 with differentiation.

6) *Relative enrichment in H_2O of the melt* by prior crystallization of anhydrous silicates (probably facilitated by accessory contamination) was considered by Howarth and Prevec (2013) and Howarth et al. (2013) to trigger the crystallization of magnetite. The massive crystallization of anhydrous phases would relatively enrich the H_2O dissolved in the melt, to a point where, before the volatiles would separate out of the liquid, will trigger the crystallization of magnetite. The authors showed by means of thermodynamic modeling using Pele software (Boudreau, 1999) with MELTS algorithms (Ghiorso and Sack, 1995) that with increasing H_2O content of the melt (e.g. 4-5 wt%), the liquidus temperetures of silicates get depressed, leaving the magnetite as the phase to crystallize at liquidus. However, the limitations of this model are represented by the fact that at low pressure, not much H_2O can be dissolved in the basaltic magma, and that, if the model is true, more basaltic systems worldwide should show significant magnetite crystallization, which is not particularly evident.

7) *Reaction of H_2O-rich fluid with Fe-rich silicates.* The H_2O-rich fluid in the pores of gabbroic rocks was interpreted by Brandriss and Birts (1999) to migrate upwards through the overlying cumulate pile, and react with the gabbro cumulate (Fe-rich silicates) to produce magnetite. This model, however, cannot really explain the textural characteristics of the layering (i.e., sharp bottom contacts, anorthositic footwalls), nor the anorthosite xenoliths in the magnetitite layers of the Bushveld Complex.

8) *Oxide crystal slurries,* a model similar to the models invoked for explaining the formation of cumulates in Skaergaard intrusion (e.g. Irvine at al., 1998) or chromitites in the Critical Zone of the Bushveld Complex (e.g. Voodrouw et al., 2009; Eales and Costin, 2012; Maier et al., 2012). This model was proposed by Irvine et al. (1998) to explain the cumulate layers in the Skaergaard intrusion as precipitated from density currents of crystal slurries that sweep down the chamber walls. Maier et al. (2012) argued that such a model could potentially be applied to the Bushveld

oxide layers. However, the authors critically admit that while it is conceivable that the currents erode the mushy unconsolidated top layer of the previously deposited cumulate, density currents cannot easily explain the abundant, highly elongated, sub-horizontally orientated anorthosite autoliths within Bushveld chromitite and magnetitite layers. These fragments, the authors said, or at least their tails, should have been dismembered during flow and/or unmixed from the oxide slurries due to negative buoyancy.

2.7. Previous work on Upper Zone and its oxide ores: a chronological approach

The vast amount of information on the Bushveld Complex was first compiled by Wager and Brown (1968) who summarized a huge body of existing literature, mainly published in South Africa. One year later Willemse (1969) produced a comprehensive report for that time, a report which included the descriptions of the magnetitete layers of the Upper Zone and constituted a significant contribution to the understanding of the Bushveld Complex.

Probably one of the first relevant modern works on mapping the Upper Zone is that of Von Gruenewaldt (1971, 1973) who, besides mapping magnetitite layers, for the first time mapped a major unconformity along strike at the top of the Bushveld Complex. He named the uppermost rock type as fayalite diorite and considered it as a result of crystallization from a highly evolved magma.

Molyneux (1970) studied the geology of the Magnet Heights area with special reference to the Main Magnetite Layer. He gave a detailed description of the MML and its footwall and ceiling contacts, a detailed stratigraphic column. He interpreted the genesis of MML to be related to magnetite crystallization from a highly evolved Fe-rich liquid.

The compositional variations starting from the Pyroxenite Marker towards the top of the Upper Zone (Mg# in pyroxene, An in plagioclase, Fo content of olivine) was interpreted by Molyneux, (1974) as a result of a closed-system crystallization without magma recharge.

Cawthorn and McCarthy (1980) and McCarthy and Cawthorn (1983) analyzed trace elements of magnetite from four continuous borehole intersections through the Main Magnetitite Layer from the Upper Zone. The authors noticed a rapid depletion of Cr over short, vertical sequences near the base of the layer, which was interpreted to be related to bottom- crystallization, resulting in a chemical depletion of a thin layer of liquid. The sudden increases in Cr content of magnetite were attributed

to convection cells of lateral extents no greater than hundreds of meters, which feed the chamber with undepleted magma. According to these authors, the existence of convection cell can also explain the lateral growth of the Bushveld layers, as well as erosion of cumulates if the convection currents impinge upon the floor. Notably, the same authors suggest that the non-systematic manner of appearance of disseminated plagioclase in magnetite layers was attributed to fluctuations in pressure.

Von Gruenewaldt et al. (1985) investigated the exsolution textures in titanomagnetite grains of massive magnetite layers and their associated host rocks from the entire Upper Zone. The study revealed differences that can be related to changes in the oxidation state of the magma during crystallization and cooling. The authors show that the oxidation exsolution intergrowths indicate a higher fO_2 during formation of the magnetite layers than during crystallization of the disseminated titanomagnetite. They also suggested that a decrease in the fO_2 is required to precipitate successive titanomagnetite-rich layers upward in the sequence. The composite lamellar intergrowths of magnetite and ilmenite in the uppermost magnetite layers were explained through a subsolvus oxidation of ulvöspinel in ulvöspinel-rich magnetite, similar to the conclusions of Reynolds (1978) in his PhD thesis. Von Gruenewaldt et al. (1985) also suggested that subsolvus oxidation of ulvöspinel to ilmenite at higher temperatures near the top of the intrusion facilitated diffusion of ilmenite to produce the variety of different composite exsolution textures.

Analyzing the magnetitite layer I of the Upper Zone of the Bushveld Complex, Butcher and Merkle (1987) found that magnetite grains in all textural settings are compositionally heterogeneous. Touching magnetite grains show systematic compositional zonations, with the rims of grains marked by a decrease in Al and Mg towards the grain boundary, while the cores are characterized by a distinctive peak for these elements. It is suggested that these variations can be related to the positions of exsolved phases. For example, exsolutions in the cores are either pleonaste or a Fe^{3+}-bearing Al-Mg spinel, whereas those at the grain boundaries are more Al-rich and include corundum. Similar exsolution-related compositional patterns for Mg and Al were identified in magnetite grains which are in contact with ilmenite and plagioclase. The authors proposed a model in which a possible sequence of postcummulus events during the interval between accumulation of the magnetite and the cessation of subsolidus reactions is represented by a delicate interplay between a) depletion of the host magnetite by corundum, pleonaste and the Fe^{3+}-bearing Al-Mg spinel exsolutions, and b) diffusion of Al and Mg into the depleted areas from the surrounding

magnetite. The authors also mentioned that Cr in magnetite is affected by subsolidus re-equilibration between magnetite and ilmenite or magnetite and intercummulus liquid.

Butcher and Merkle (1991) studied the stratigraphically lowermost magnetitite layer of the Upper Zone in the Brits area of the Bushveld Complex. The authors suggest that the discordant relationship between thin (1 mm – 1 cm) magnetitite layers and laminae of ca. one grain thickness indicates a consistent younging direction upwards towards the contact with the overlying magnetite, and this observation points to the interpretation that these crystals are cumulus and have escaped modification by postcummulus overgrowth. Based on the compositional variation across individual plagioclase grains and the existence of magnetite crystals in the anorthosite, the authors suggest the existence of a crystal mush (plagioclase – magnetite – melt) where magnetite crystallization hindered the development of an ideal plagioclase adcumulate.

In an effort to explain the layering of the Upper Zone, as well as the genesis of magnetitite layers, Kruger and Smart (1987) proposed a model based on diffusion of elements during the bottom crystallization of double-diffusive convection systems using the extended Rayleigh distillation law to describe a) changes in trace element concentration during the fractional crystallization of a convective magma layer and b) diffusion of the trace element into the layer across its top diffusive boundary.

Harney and von Gruenewaldt (1995) suggested that the vanadium and Ti-bearing magnetite layers from the Upper Zone of the BIC formed due to magma mixing events, which could have resulted from a breakdown of densely stratified liquid layers or by an influx of a small volume of new magma. The authors also explained the existence of sulphides phases in the proximity of the magnetite layers by magma mixing, together with a depletion of the Fe^{3+} content of the crystallizing magma during the formation of the magnetite layers, which resulted in the formation of immiscible sulphides. These sulphides would have become concentrated within, or in close proximity to, the magnetite layers.

A complex study of the Bushveld Complex, targeting the way in which the magma filled in the Bushveld Complex, was done by Kruger (2005). The author recognized the lateral expansion, roof and floor interaction and several magmatic unconformities. The author suggested that the Upper Zone magma flowed into the chamber from the southern ''Bethal'' Lobe, as well as via the Thabazimbi Murchison Lineament (TML). Kruger (2005) also recognized the discordant character

of the Upper Zone, due to the gigantic influx of magma which eroded the Main Zone rocks and caused very large-scale unconformable relationships. However, contrary to most other authors, Kruger considers that the Upper Zone crystallization started with the Pyroxenite Marker, which is considered the base of this massive magma influx. According to this author, in the Northern Limb, this marker is represented by a troctolitic layer at the stratigraphic base of the Upper Zone. Kruger (2005), referring to the whole Bushveld Complex, stated that the outcrop patterns and the concordance of geochemical, isotopic and mineralogical data along strike, indicate that during crystallisation, the Bushveld Complex was a "wide and shallow, lobate, sill-like sheet, and the rock-strata and mineral deposits are quasi-continuous over the whole intrusion". The formation of the Ti-V-magnetitite layers was interpreted as being crystallized from an initially homogenous Fe-rich magma and was not the result of multiple intrusion.

Tegner et al. (2006) recognized the cyclic character of the Upper Zone, and following geochemical reversals of An content of plagioclase and Mg# of olivine and pyroxene, identified nine cycles (I to IX), with two particular cycles (V and VI) showing the most significant reversals towards the very top of the Upper Zone. These two cycles are also associated with the first appearance of cumulus apatite (nelsonite layers).

A new geological map of the Rustenburg Layered Suite south of the Ysterberg–Planknek fault of the northern/Potgietersrus limb of the Bushveld Complex was published by van der Merwe (2008). This map is still used today by the mining companies in mineral exploration of the Northern Lobe of the Bushveld Complex.

Cawthorn and Ashwal (2009) showed the existence of a significant reversal in An content in the plagioclase overlying the magnetitite layers, compared with the plagioclase underlying the magnetitites. Based on this observation, the authors challenged the hypothesis that such layers result from magma addition, but is rather consistent with a pressure change as a cause for triggering magnetite crystallization. The fact that the upper contacts of magnetitite layers grade into anorthosite it is interpreted to reflect settling and sorting. Notably, the authors mentioned that the rocks forming the uppermost 100 m of the intrusion contain the most sodic plagioclase, proving that there is no downward-crystallizing roof facies.

Tegner and Cawthorn (2010) measured (with electron microprobe) the FeO variation trends in the plagioclase from the Upper Zone of the Bushveld Complex and the Upper Zone of the Skaergaard

intrusion. Based on a revised mass balance model, the authors concluded that the differentiation trends of the liquids subsequent to magnetite saturation were fundamentally different in the two intrusions. For the Bushveld Complex, the inferred liquid composition contained about 15 wt% total FeO when magnetite started to crystallize, which is slightly less than the total FeO content of the subsequent cumulates. This trend is reversed for the Skaergaard intrusion, where the total FeO content of the liquid is higher than the FeO content in the cumulate pile. Despite the mineralogical similarities of the Skaergaard and Bushveld intrusions, the clear differences between the two liquid evolution trends shown by the two complexes made the authors recommend avoiding generalizations about the extent of iron enrichment in tholeiitic magmas.

Van Tongeren and Mathez (2012) suggested that the Bushveld magma developed a siliceous cap generated by liquid immiscibility. This interpretation is based on the differences in the REE content of apatite, which divide the Upper Zone in two zones: the bottom sequence, with magnetitite layers and rare apatite with low content of REE, and an upper sequence with nelsonite layers with apatite three times richer in REE compared to the apatites from the bottom sequence. This observation, combined with the negative Eu anomaly and the cumulus rocks containing orthoclase and quartz, made the author consider that the upper sequence resulted by liquid immiscibility.

Maier et al. (2012) proposed a totally different model, in which the main economic layers of chromite, PGE, Ti-V-magnetite formed by hydrodynamic sorting during the subsidence of the central subsidence of the intrusion. The authors consider that the central subsidence of the Bushveld complex happened when it was incompletely solidified, due to the crustal loading. This subsidence created slumping of semi-consolidated cumulate slurries towards the center of the intrusion and hydrodynamic unmixing of the slurries. According to Maier, the unmixing of slurries formed a) dense layers enriched in sulfides, oxides, olivine and pyroxene and b) less dense layers enriched in plagioclase. Maier suggests that the most economic PGE, Cr and V reefs formed in this way. Strong criticism of this model came from Scoon and Mitchell (2013) who cited several field aspects and previous work which was omitted by Maier et al. (2012). The main criticism was that the layering in the Bushveld Complex is overly complex to be explained by slurries unmixing and hydrodynamic sorting. More than that, the field distribution of the Iron-Rich-Ultramafic-Pegmatite (IRUP) bodies, as well as the massive Ti-magnetite layers, cannot be easily explained by such a model.

The crystal slurries model was also invoked by Eales and Costin (2012) for explaining the Lower Zone cumulates and chromititite layers from the Lower Critical Zone. The crystal slurry model was earlier used by Voordouw et al., (2009) to explain textures present in UG1 and UG2 chromitites in the Dwars River area. Roelofse and Ashwal (2012) also suggested a slurry model for the emplacement of the Lower Main Zone in the Northern Lobe of the Bushveld Complex.

Latypov et al. (2015) argued against the slurry model when explaining the Merensky Reef, by giving field evidence (e.g. erosion of the footwall), as well as theoretical arguments for "in situ" crystallization of the chromite.

Since 2012, several authors (e.g. Eales and Costin, 2012; Wilson, 2012; Yudovskaya et al. 2012) independently advocated for: 1) a parent magma of the Lower and Critical Zones of the Bushveld Complex which should have been more primitive (komatiite-like) compared to the widely accepted B1 (basalt- or picrite-type) magma, and 2) a staging chamber for the Bushveld magmatism, where significant contamination with crustal rocks took place.

During 2010-2016, Bushveld Minerals executed extensive exploration drilling of the Upper Zone in the Vliegekraal – Vriesland area in the Northern Lobe. However, the first detailed investigations around this area were done in the 1970s and mainly focussed on the MML, because of its high vanadium content. Small mining companies and then the Council for Geoscience (CGS) used the map of van der Merwe (2008) and performed more geologic mapping, ground geophysics, trenching and limited drilling south of the Mokopane (Pt) project. During 1979 - 1980, a South African government company called Mining Corporation Ltd ("MCL"), completed geological mapping, magnetic surveys, and drilling over an area grouping five farms to the south of the Mokopane project. A mineral resource of 419 Mt of V-Ti-magnetite-rich material containing 6.5 Mt of V_2O_5 along a 16 km strike was reported. The reported tonnages represent the total estimated amount of Ti-magnetite "concentrate" potentially extractable from the Main Magnetite Group layers (MAG 1 to MAG 4) to a vertical depth of 80 m and the Lower Magnetite Group to a vertical depth of 200 m (Bushveld Minerals report, 2013). The MML is represented by the MAG 3 and MAG 4 layers. The MAG 1 and MAG 2 layers were identified as less rich in V compared to the MAG3 and MAG4. Following the drilling along strike, it was noticed that the MAG 1 and MAG 2 layers represent important stratigraphic markers, along with the MML.

A regional aeromagnetic and radiometric survey was conducted in the 1990s by the CGS. It showed magnetic anomalies, trending towards north, which can be correlated with the MML and the P-Q Layers (the uppermost magnetitite layers of the Upper Zone). An important stratigraphic borehole BV-1 was drilled in 1991 on the Bellevue farm, which is ca. 2 km south-west of the Vliegekraal – Vriesland area. This borehole covered the entire Upper Zone stratigraphy and intersected 32 distinct layers of Ti-magnetite or Ti-magnetite-rich rock, with thickness from 7 cm to 13 m.

Results of the CGS aeromagnetic survey were interpreted and this was followed by drilling which resulted in the intersection of the PQ magnetite layer in 2010. In 2010 to 2011, Bushveld Minerals undertook the project and executed 4 drill holes totalling ~ 902 m on the MML and 10 drill holes totalling 2,584 on the P-Q Zone, at regular intervals, all along strike.

During 2012, Bushveld Minerals drilled 51 new boreholes totalling 3491m on the farms Vliegekraal, Vriesland and Malokong (13 boreholes totalling 927 m were drilled on the MML, and 5 boreholes totalling 1,525.39 m were drilled on the un-weathered P-Q zone). Other 33 boreholes were drilled into the weathered portion of the P-Q Zone, of which 13 successfully intersected the P-Q Zone.

The MML was intercepted in several drillholes and the apparent thickness is in the order of 7.9 m to 11.3 m, with an average thickness of 9.8 m (Bushveld Mineral Report, 2013). The MML consists of two layers rich in V and Ti, the upper layer (called MAG3) rich in Ti-V, and the lower layer (called MAG4), which is less rich in Ti and V.

In borehole VL 5 (Figure 4), the two layers are separated by a parting layer of leucogabbronorite, approximatively 2.3 m in thickness, and is very poor in Ti and V (Figure 4). According to Bushveld Minerals, the entire MML package (MAG3, MAG4 and the parting layer) has an average vanadium content of approximately 1.3% V_2O_5 with maximum concentrations of 1.5% to 1.7% V_2O_5 recorded within the layer MAG3, in the massive ore, which consists of more than 95% V-Ti-rich magnetite. At approximately 7 m and 14 m above the MML, two characteristic marker Ti-magnetite layers, MAG2 and MAG1 respectively, occur within anorthosite and leucogabbro. These two layers have average thicknesses of approximately 1.2 m (MAG2) and 1.5 m (MAG1), contain an estimated 65% to 80% Ti-magnetite and are useful stratigraphic and geological markers to the MML (Bushveld Minerals Report, 2013).

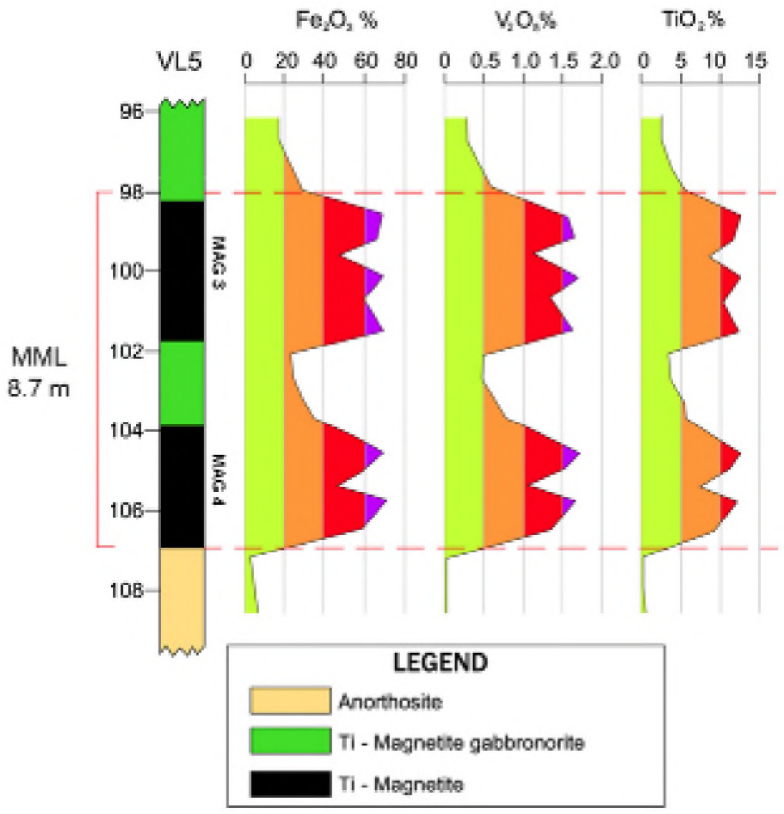

Figure 4. *The MAG3 and MAG 4 layers in borehole VL 5, constituting the MML in the Northern Limb, with values of FeO, V_2O_5 and TiO_2. The Ti-gabbronorite which is a parting layer between MAG 3 and MAG4 is rich in plagioclase, and the appropriate term based on color index of igneous plutonic rocks is leuco-gabbronorite (fom Bushveld Minerals Report, 2013)*

3. Methodology

3.1. Sampling

There are three localities where MML was sampled (Figure 5). The samples from the Northern Lobe come from the Vliegekraal – Vriesland area, where the MML was intercepted in boreholes VL 5 (samples from depth 105 m to 110 m) and VK 5 (samples from depth 128 m to 136 m) (Figure 6) and has an average thickness of ~ 9 m. The cores were accessed for this study by the kind permission of Bushveld Minerals Ltd.

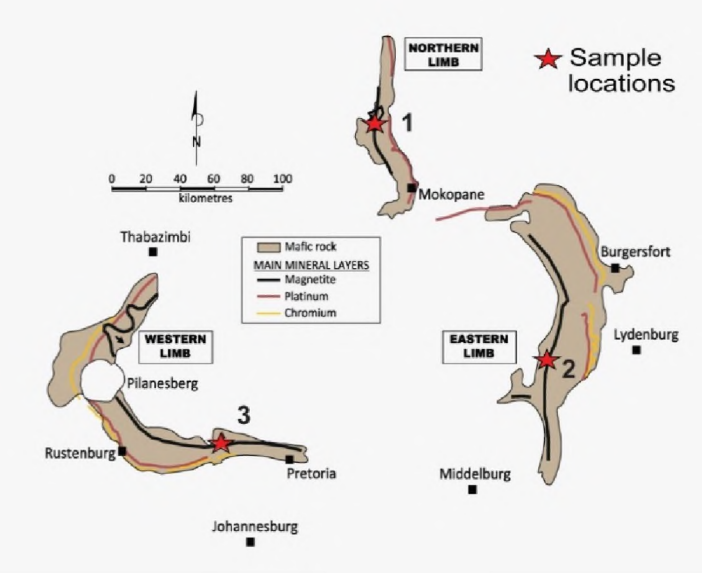

Figure 5. *Simplified sketch of the Bushveld Complex with the location of the samples: 1) Vliegekraal – Vriesland area (Northern Lobe); 2) Magnet Heights (Eastern limb); 3) Glencore's Rhovan mine (modified after Bushveld Minerals Report, 2013).*

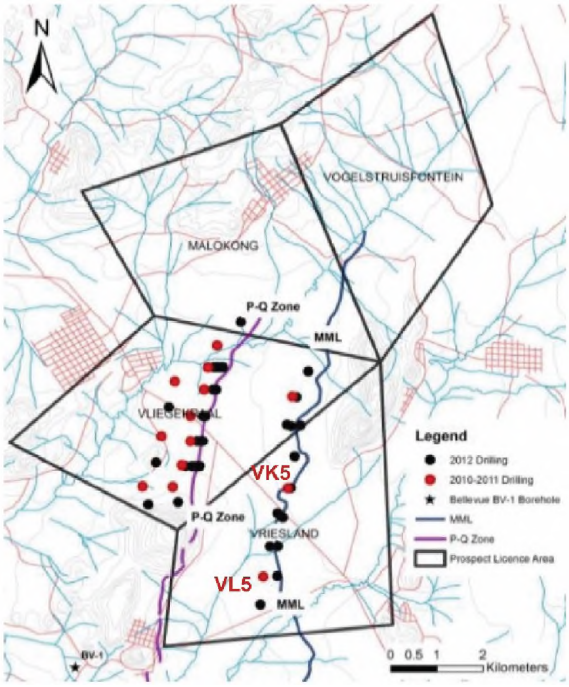

Figure 6. *Location of boreholes VL5 and VK5 in the Vliegekraal – Vriesland area (Northern Lobe). After Bushveld Minerals Report, 2013.*

The samples from the Eastern Limb were collected from the Magnet Heights occurrence (GPS coordinates for samples MML: S24^{0}52′09.5″, E29^{0}58′35.1″), an outcrop where MML is 2.05 m thick. Sampling targeted the floor and ceiling relationships, as well as the sulphide-magnetite relationships. The massive magnetite here was sampled perpendicular to the layering at 10-20 cm intervals (Figure 7). The sample labels starts with MH1 at the base of MML and ends with MH10 at the very top of the MML. A parting plane separates the MML into two sublayers. All samples represent massive Ti-magnetite. The sample MH12 (not shown in Figure 7) was collected from above the MML and it is represented by a magnetite anorthosite.

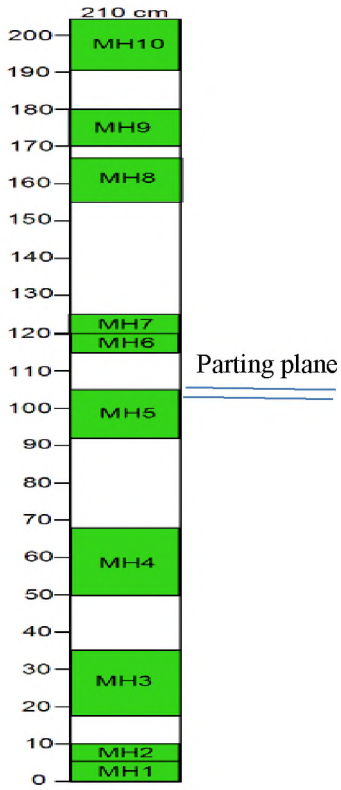

Figure 7: *Distribution of samples MH1-MH10 along the MML at the occurrence from Magnet Heights. MH1, starts at the bottom of MML.*

The samples from the Western Lobe are represented by a sequence of hand specimens taken across a single vertical section, using a similar sampling strategy to that described above for the Eastern Lobe, and come from Glencore's Rhovan mine, near Brits. The samples were collected from one outcrop (Figure 8) where the MML is massive with a variable thickness at the outcrop scale. The floor of MML is an altered anorthosite (to leuco-norite), showing large curved, non-planar surfaces at the contact with overlying MML.

***Figure 8**: Main magnetite Layer (MML) at Glencore's Rhovan mine. Notice the variable thickness of MML at the the outcrop scale, as well as the limonitized non-planar anorthosite floor of the MML*

All available MML samples from all analysed lobes were carefully logged, photographed, and marked for thin section preparation. The strategy of sample cut for thin sections and EPMA analysis, targeted the base and the top of the magnetite layer, as well as the visible inclusions in the magnetite layer. All thin sections were checked at the optical microscope and from all thin sections available, were selected the most relevant ones in terms of lack of alteration, top and floor relationships with magnetite, and visible silicate and sulphide inclusions in magnetite. These thin sections were polished in order to be analyzed at the electron microprobe and get compositional data for magnetite from the MML in the three sampled lobes.

3.2. Analytical conditions

EPMA analyses were performed at Rhodes University (Geology Department) on a Jeol JXA8230 with 4 WD spectrometers. The analytical conditions employed included an accelerating voltage of 15 kV, beam current of 20 nA, beam size of 1 micron. The ZAF correction matrix was used for quantification. For WDS element mapping, a dwell time of 20 ms was used, under stage mode. For trace element analysis the following analytical conditions were employed: accelerating voltage 25 kV, beam current 500 nA, counting times of 100 sec per peak and 50 sec per each lower and upper background, respectively. The average detection limits for Pt, Pd, Rh and Te were 32, 26, 38 and 47 ppm, respectively.

4. Results

4.1. Petrography

4.1.1. Northern Lobe

Two drill cores from MML were donated by Bushveld Minerals for this study (Figures 9 and 10): a) VL5 from depth interval 105 – 110.74 m (only showed 105-105.26 interval in Figure 10), and b) VK5 (depth interval 124-136.53 m).

In VL5, the interval 105-105.26 m represents a part of a magnetitite layer which can be attributed to MAG3 layer. No bottom or upper contacts were accessible from the core. The magnetitite layer is made of massive magnetite with has small inclusions of altered plagioclase crystals and crystal aggregates, as well as with rare veins filled with chlorite (top of VL5, Figure 10). A thin anorthosite layer of ca. 0.5 cm thickness occurs at depth 105.14 m, while below it, aggregates of plagioclase crystals become abundant at depth 105.18 m. Starting with depth 109.20 m down to the depth 110 m (Figure 9), the core is made of anorthosite with abundant crystals of magnetite, and rare rounded aggregates of magnetites which include altered plagioclase. In between the depth 110.00 m and 110.56 m, two layers of magnetitites with small and abundant crystals of plagioclase are separated by a thin layer of anorthosite. These two magnetitites layers together make the MAG 4 layer of MML.

Along strike, towards the north, the layers MAG3 and MAG4 were encountered in borehole VK5, where their thickness significantly expands (Figures 9 and 10). Here, the MAG3 layer starts at

127.28 m and ends at 129.97 m. The structure of magnetitite layer is heterogenous. In the upper part (at 127.30 m), a thin layer of clinopyroxene-magnetite bearing anorthosites develops sharp floor contact and "erosional" type upper contact. Above the erosional contact vary rare and small plagioclase crystals are embedded in magnetitite. Below the anorthosite layer, the plagioclase inclusions in magnetitite are bigger and in higher proportion. At depth 129.80 m a thin layer of clinopyroxene and magnetite-bearing anorthosite to almost ferro-gabbro in modal composition separates a top magnetitite with significant plagioclase inclusions and a bottom magnetitite poorer in plagioclase, which seems also to be more altered. This magnetitite marks the bottom of MAG 3 layer. Here, at depths 129.83 and 129.97, two peculiar heterogeneous layers occur. They contain a fine greenish mineral (olivine) and small and altered orthopyroxene and plagioclase.

Between depths of 129.97 m and 133.50 m, a heterogeneous ferro-gabbro develops. Larger crystals of orthopyroxene and plagioclase seem to be interlocked with magnetite. At the bottom of this layer, at depth ~133.70, the rock contains lesser pyroxene but more significant plagioclase. At depth 133.78 a new layer of magnetitite occurs, marking the top of MAG4 layer. Here, the oxides and sulphides are spatially related. The upper part of MAG 4 contains a heterogeneous magnetitite with significantly altered plagioclase inclusions and a thin anorthosite layer at depth 133.80 m. The frequency of the plagioclase crystals diminishes towards the bottom of MAG 4, where two anorthosite layers occur at depths 135.10 m and 135.38 m. The MAG 4 layer ends at depth 135.44. Below this depth, down to ~136 m, a coarse grain anorthosite develops, with interstitial small clinopyroxene. A ferro-gabbro layer occurs below 136 m, down to the end of our core (136.53 m).

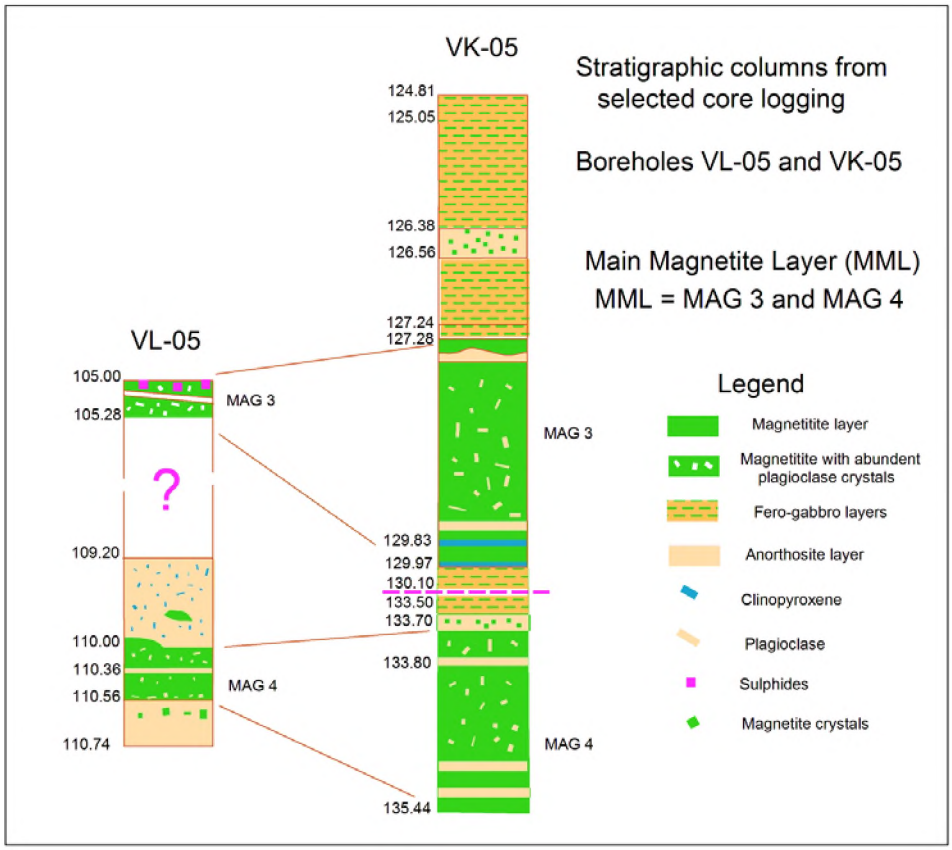

Figure 9: *Core logs for VL5 and VK5*

***Figure 10**: Collated photographs for cores VL5 and VK5 (Northern Lobe) with the location of the thin sections analyzed at the electron microprobe*

Borehole VL 5

At depth 105.05 m, the texture of magnetite ore is massive, with up to 1-2 cm sized inclusions of plagioclase and pyroxene. The plagioclase is deformed and altered to chlorite (Figure 11A). The pyroxene is rarely preserved. It is commonly totally transformed to chlorite, calcite and epidote (Figure 11B). Rare deformed biotite is included in magnetite. The biotite is chloritized and it is associated with secondary calcite and sulphides (Figure 11C). The exsolutions in magnetite are present but extremely patchy and heterogeneous. In the areas where plagioclase is totally chloritized, small and rounded inclusions occur as a heterogeneous fine mixture (called herein mixture "X") (Figure 11D, E and F).

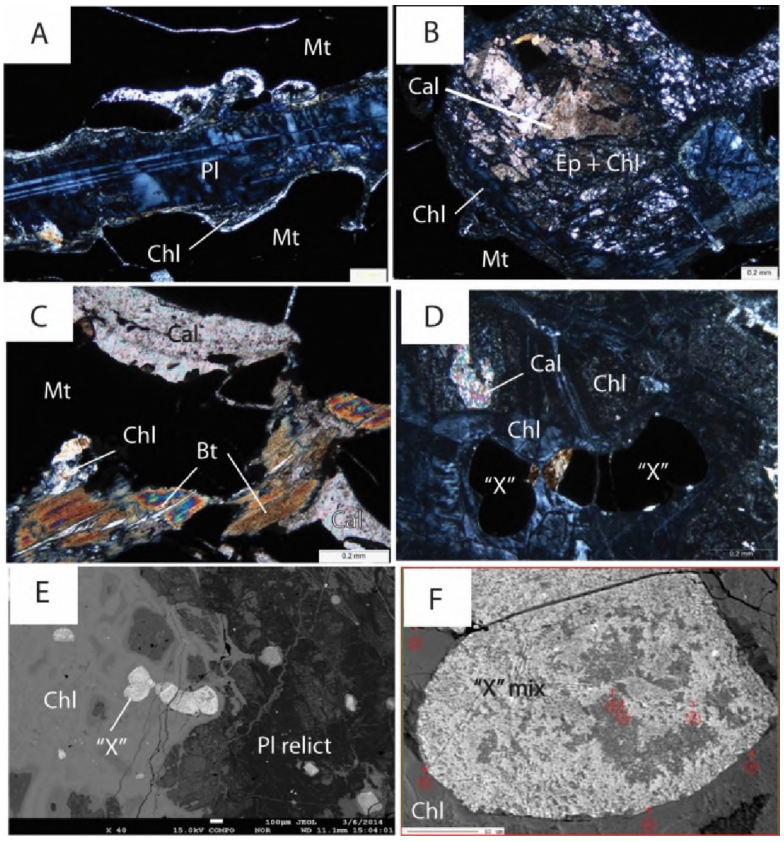

***Figure 11**: Sample from depth 105.05 m. A) Twinned plagioclase included in magnetite. The plagioclase is marginally altered to chlorite (transmitted light, crossed polars); B) rare opx shaped-aggregate included in magnetite; the opx was totally transformed into epidote + calcite + chlorite (transmitted light, crossed polars). C) Biotite in magnetite, together with secondary chlorite and calcite (transmitted light, crossed polars); D) Opaque minerals included in chloritized plagioclase. The opaque phases proved to be a mixture of phases, rich in Ti, V, Si. E) High Ti-V-oxide-silicate mixture phase ("X") included in chloritized plagioclase (BSE image). F) Detail on the "X" mixture (see text for details).*

The qualitative analysis (Figure 12) identified in the mixture the following elements: Si, Al, Fe, Ti, V, Cu, S, and less Ca and Mg. The peculiar grains of fine "X" mixture were also mapped. The WDS element distribution maps (Figure 13) show discrete distribution correlation of a) Si, Al and b) Ca, Ti, Fe, V (Cu and S were not mapped). It is possible that the mixture is made of a chlorite matrix containing submicron grains of high V Ti-magnetite, as well as discrete chalcopyrite.

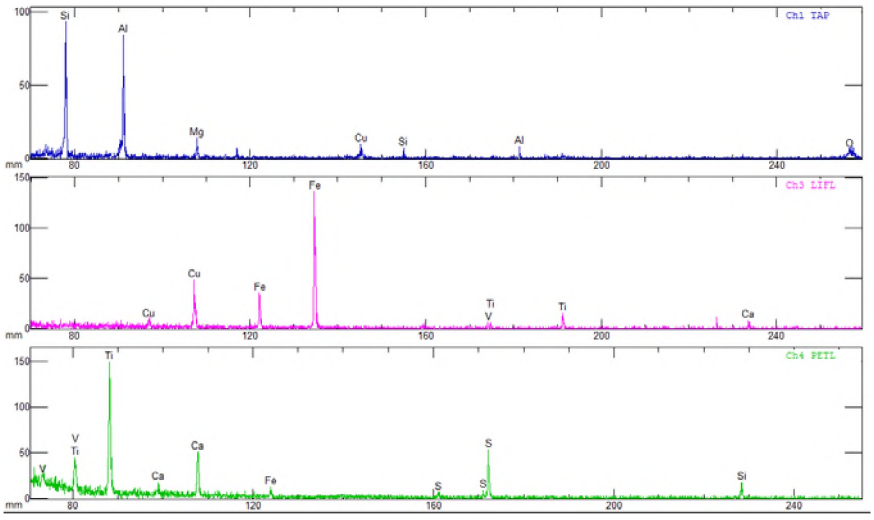

***Figure 12**: Qualitative analysis (WDS scan) of mixture "X", showing detectable elements.*

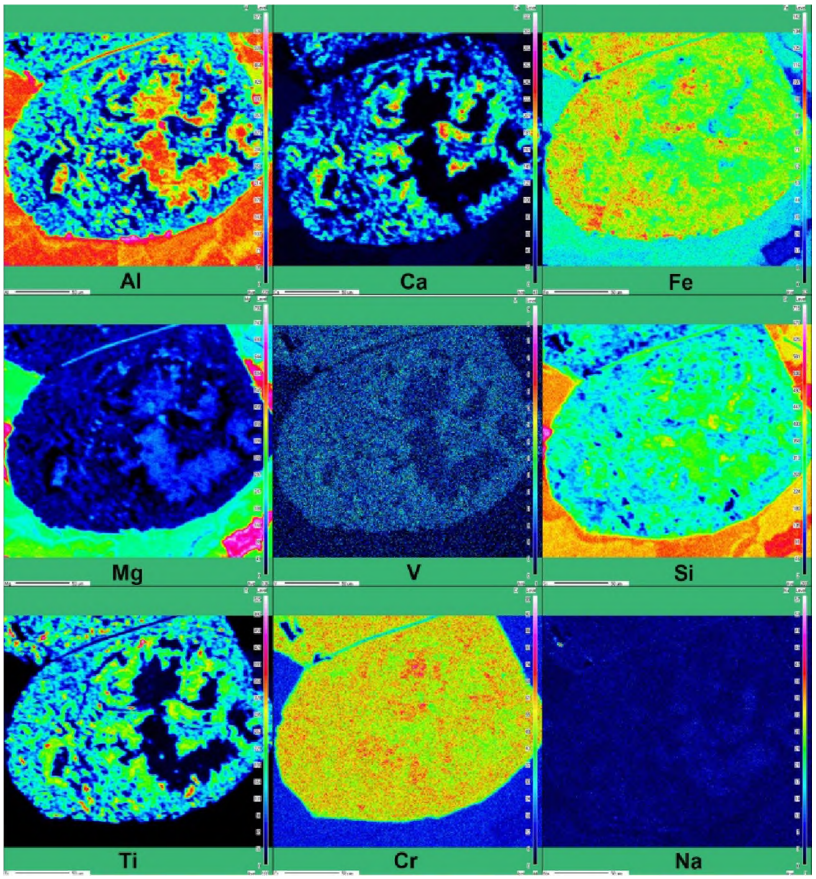

***Figure 13:** Wavelength Dispersive Spectroscopy (WDS) element map distribution for "X" mixture (Cu and S not shown). Notice heterogeneous and discrete distribution of Al, Fe, Si, vs. Ca, Ti, V.*

The sample from depth 105.05 m, like most of the samples from the MML of the Northern limb analyzed herein, shows significant alteration of the igneous silicates, as well as late/secondary phases. Peculiar pseudomorphic textures are represented by a) rutile and calcite aggregates (Figure 14A, B, C), and b) chlorite (Figure 14D). The Ti-magnetite presents fine exsolutions of spinel, as black droplets (Figure 14B) and ulvöspinel, as gray exsolution lamellae (Figure 14D).

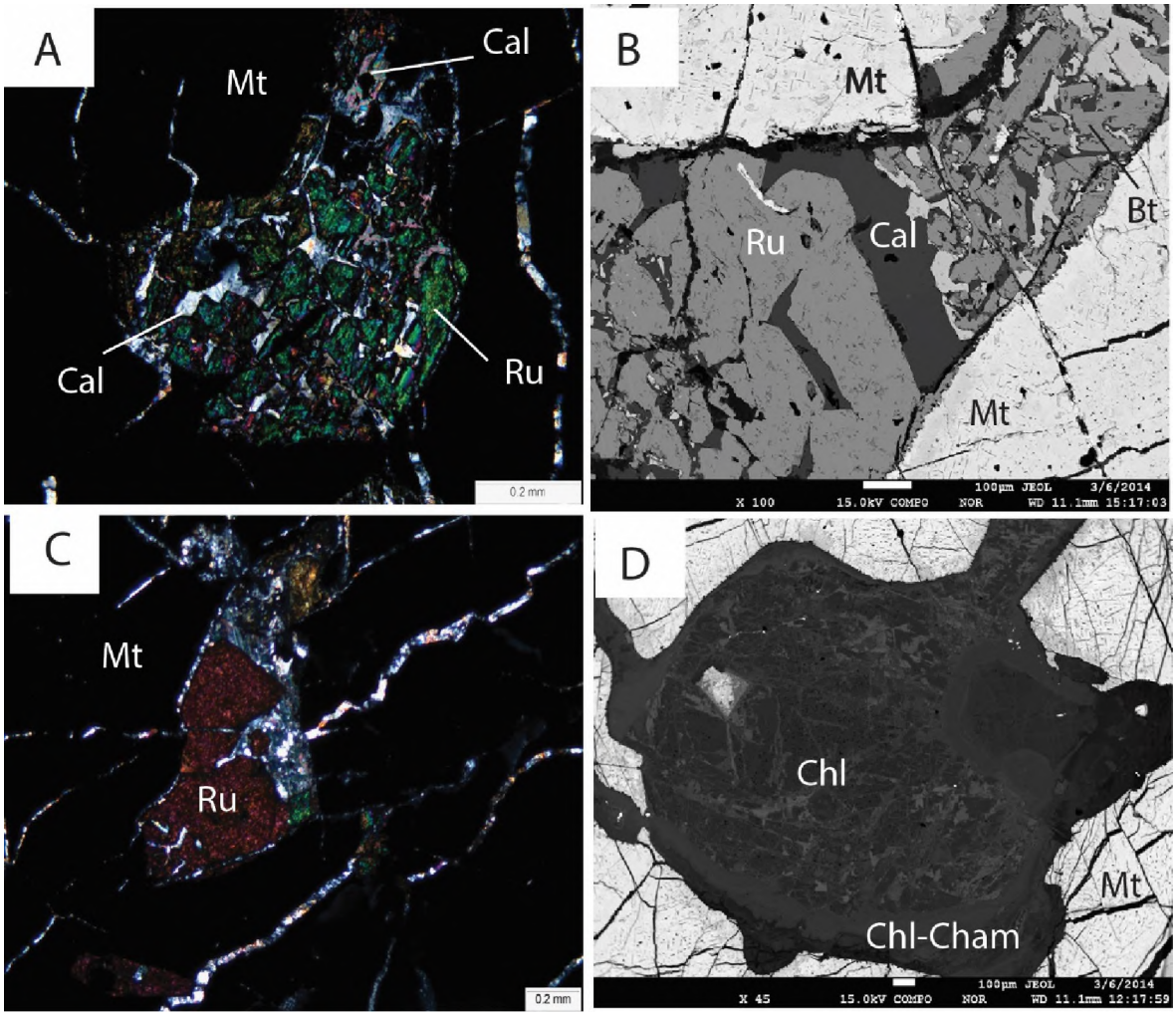

Figure 14: *Depth 105.05: A) Pseudomorph of rutile and calcite included in Ti-magnetite (transmitted light, crossed polars); B) Rutile with calcite near chloritized biotite in pseudomorph-like inclusion in Ti-magnetite (BSE image); C)Rutile and chlorite in Ti-magnetite (transmitted light, crossed polars); D) Chlorite (Chamosite) replacing a mafic mineral, probably a pyroxene; notice the fine exsolutions in host Ti-magnetite. See List of abbreviations.*

The WDS element maps (Figure 15) show the intergrowth of rutile and calcite, a rare type of intergrowth probably developed as a pseudomorphic transformation on an igneous Ti-rich mineral, such as titanite.

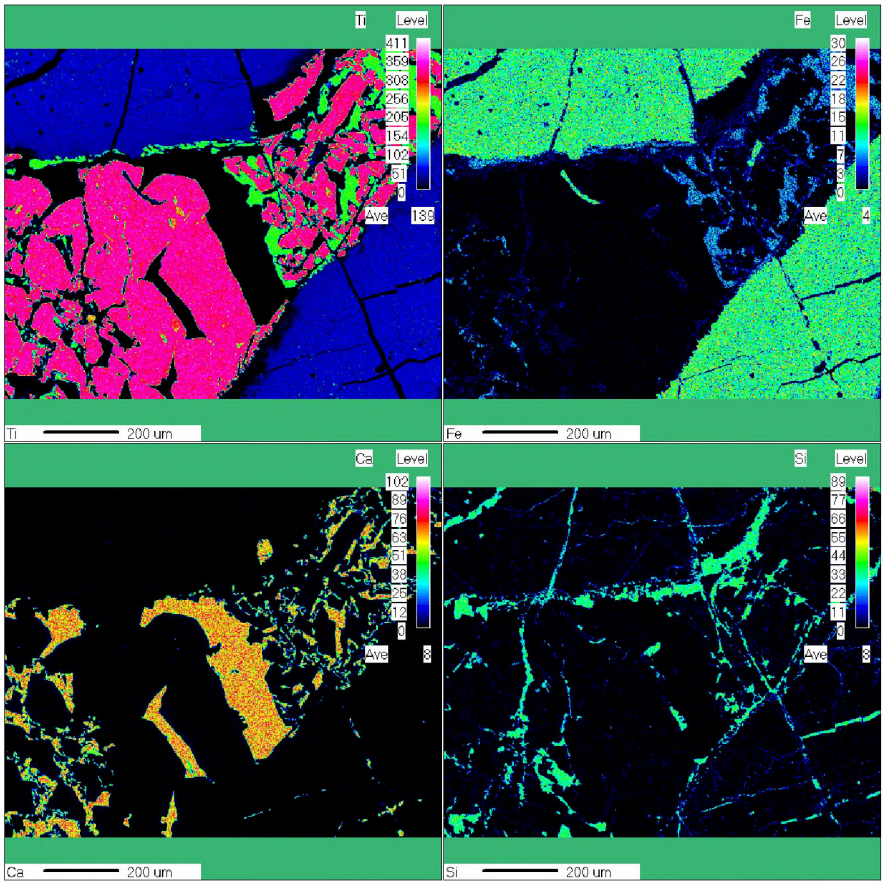

Figure 15: *WDS element map distribution for rutile and calcite in Ti-magnetite (corresponding BSE image in Figure 13B).*

At depth 125.08 m a thin anorthosite layer shows oxides (Ti-magnetite and ilmenite) interstitial to coarse subhedral plagioclase. At the contact between plagioclase and Ti-magnetite a thin amphibole corona develops (Figure 16A, C and D). The amphibole is not observed in between plagioclase and igneous, interstitial clinopyroxene. Late chlorite can grow on amphibole but can also grow on cracks which cross-cut all mineral assemblage (Figure 16 D). The coarse plagioclase crystals are often bent or show deformation twins (Figure 16 A, B).

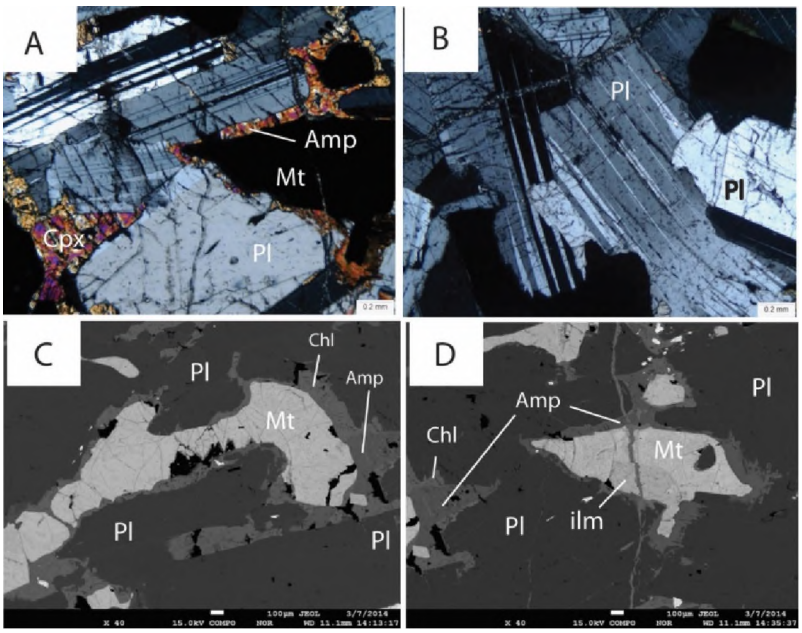

***Figure 16**: Depth 125.08 m. Thin anorthosite layer. A) Coarse grained plagioclase with an interstitial clinopyroxene and amphibole reaction corona in between magnetite and plagioclase (transmitted light, crossed polars); B) Coarse grained plagioclase with deformation twins. The opaque mineral (Ti-magnetite) seems to engulf the plagioclase (transmitted light, crossed polars); C) (Chloritized) amphibole reaction corona developed in between magnetite and plagioclase (BSE image). D) The amphibole reaction corona also developed in between ilmenite and plagioclase (BSE image)*

Just below the anorthosite layer, at depth 127.28 m, the modal proportion of oxides increases. Here, nests of kinked biotite are surrounded by fine symplectites of clinopyroxene-plagioclase, which seems to be overgrowth by long biotite flakes (Figure 17 A and B). Rare pyrite grains are present inside the symplectite.

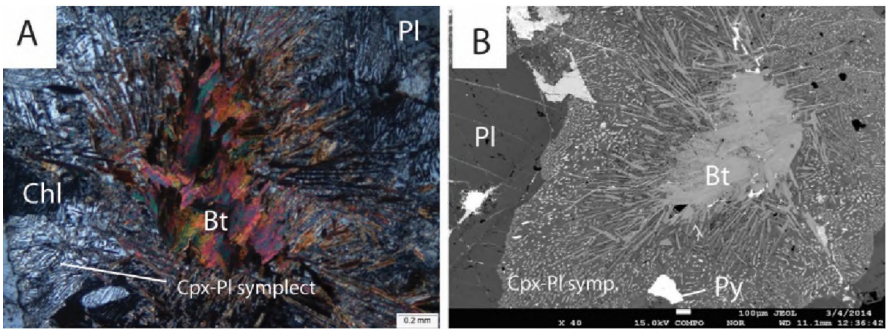

***Figure 17.** Depth 127.28 m. A) Kinked biotite aggregate within a clinopyroxene-plagioclase symplectite (transmitted light, crossed polars). B) Biotite aggregate in clinopyroxene – plagioclase symplectite. The plagioclase grain to the left is almost completely chloritized (BSE image).*

A peculiar micro-texture develops at depth 129.83 m and 129.97 m. Here, olivine corona develop between igneous orthopyroxene and Ti-magnetite (Figure 18 A-D). The olivine does not develop in between plagioclase and Ti-magnetite.

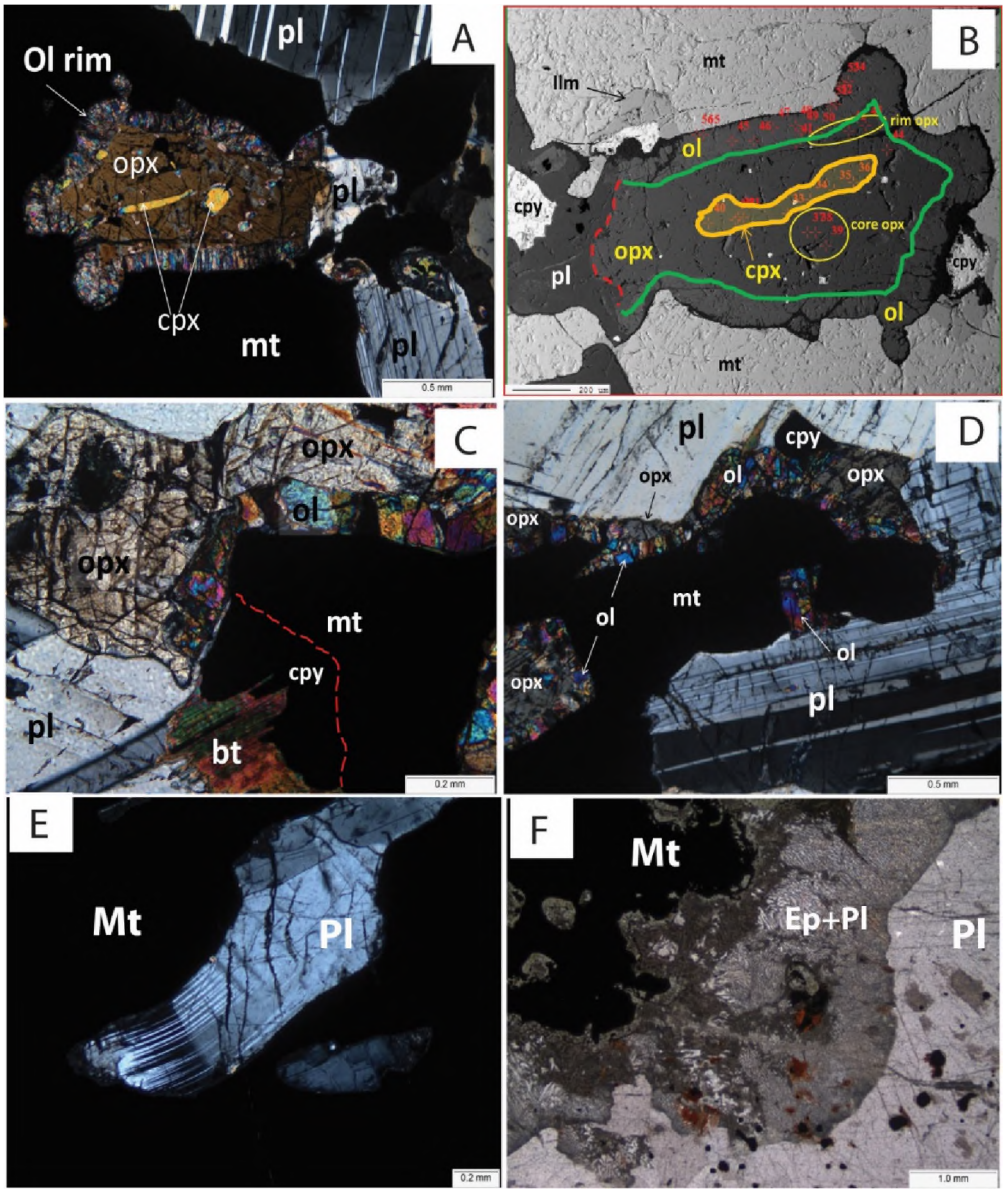

Figure 18. *Depth 129.83 m. A) Olivine reaction corona between magnetite and orthopyroxene. Notice the clinopyroxene inclusions in orthopyroxene (transmitted light, crossed polars); B) Olivine reaction corona between magnetite and orthopyroxene (BSE image). C) and D) Olivine corona does not develop in between magnetite and plagioclase (transmitted light, crossed polars); E) Kinked plagioclase with deformation twins included in magnetite (transmitted light, crossed polars); F) Fine cpx-pl symplectite growing towards plagioclase and originating in the fine mineral aggregate with olivine near the magnetite (transmitted light, crossed polars).*

The orthopyroxene contains rounded inclusions of clinopyroxene (Figure 18 A, B), suggesting a complex igneous history. Small aggregates of olivine included in Ti-magnetite represent pseudomorphs of total replacement of orthopyroxene by olivine (Figure 18 D). Chalcopyrite is intimately related to Ti-magnetite. The plagioclase included in Ti-magnetite is often deformed, showing kink bands and deformation twins (Figure 18 E).

The WDS element map (Figure 19) illustrates the bulk chemical differences in between olivine and orthopyroxene, where noticeable is the fact that olivine is significantly richer in MgO than orthopyroxene.

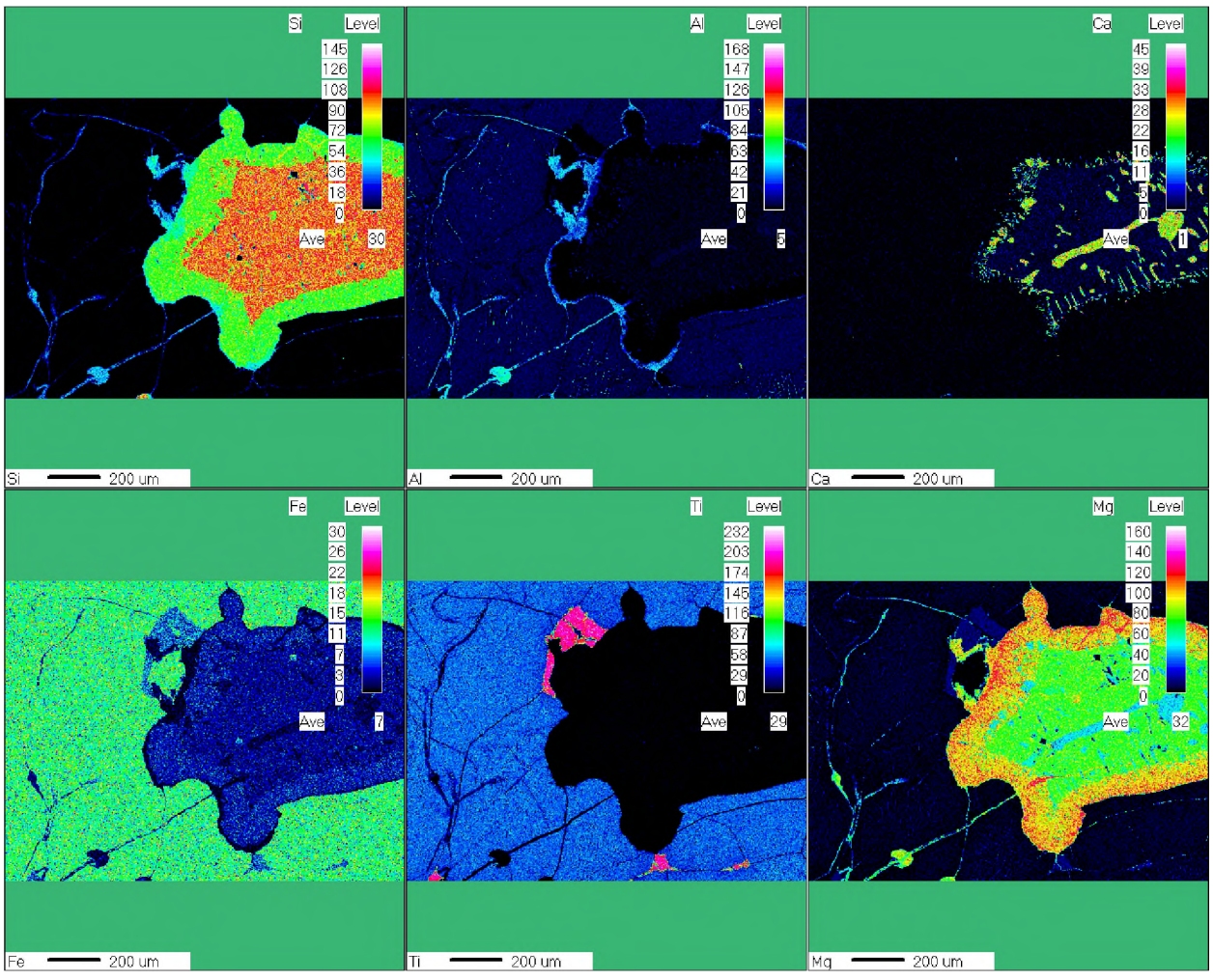

Figure 19. *Depth 129.97m. WDS element map distribution in olivine reaction corona developed in between magnetite and orthopyroxene. The corresponding BSE image is in Figure 18B.*

The development of olivine can also be noticed just above the depth 129.87 m, where it surrounds Ti-magnetite, no matter of the mineral neighbor. When the neighbor is plagioclase, a fine symplectite of clinopyroxene-plagioclase develops, radiating from the olivine towards the igneous, coarse plagioclase (Figure 20).

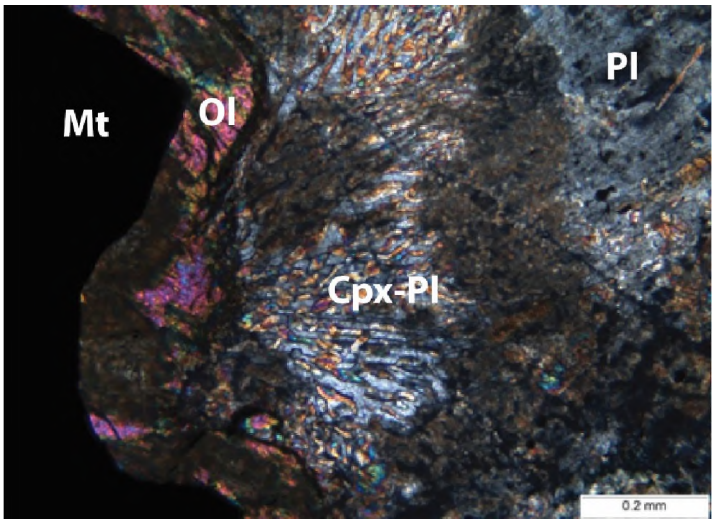

***Figure 20**: Symplectite of clinopyroxene and plagioclase developed from the olivine formed near the Ti-magnetite towards the igneous plagioclase.*

In the same area where the symplectite develops, the Ti-magnetite shows re-mobilization of the exsolution lamellae into patches made of very fine exsolution blebs (Figure 21 A and B).

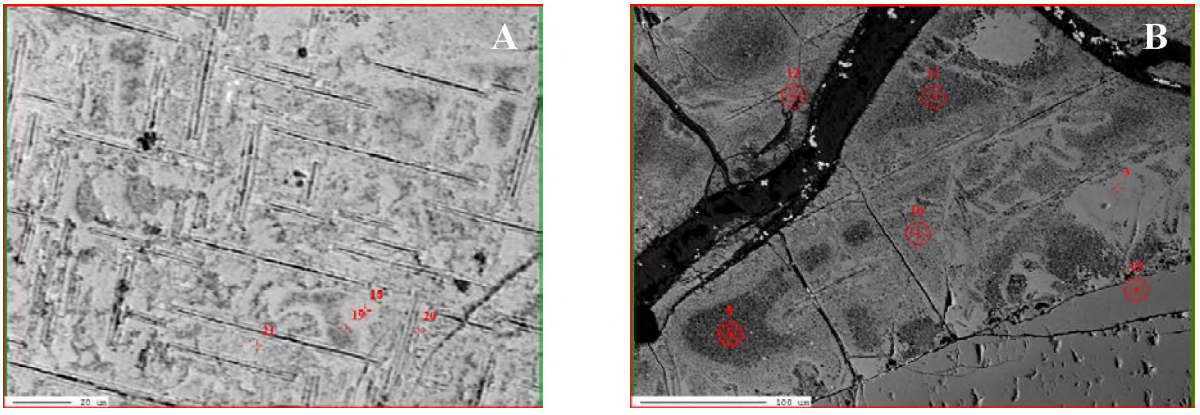

***Figure 21:** A) Small patches with no exsolution lamellae in between patches with high density of ülvospinel exsolutions in Ti-magnetite; the straight black lines are Al-spinel lamellae (BSE image); B) "Patchy" healing of exsolution lamellae in Ti-magnetite, where the exsolved phase accumulated is finer, heterogeneous darker patches. Red points and numbers represent the location of microprobe analysis.*

At depth 133.78 m, the proportion of oxides and sulphides increases. The olivine reaction between orthopyroxene and Ti-magnetite is no longer present, but orthopyroxene, as well as all other igneous phases, show chloritized margins (Figure 22 A, B, D, F). Here, chalcopyrite shows an intimate spatial relationship with Ti-magnetite (Figure 22 C), with chlorite developing around aggregates of grains made of Ti-magnetite and chalcopyrite. Rare brown amphibole can develop on the margins of Ti-magnetite, towards the plagioclase (Figure 22 E).

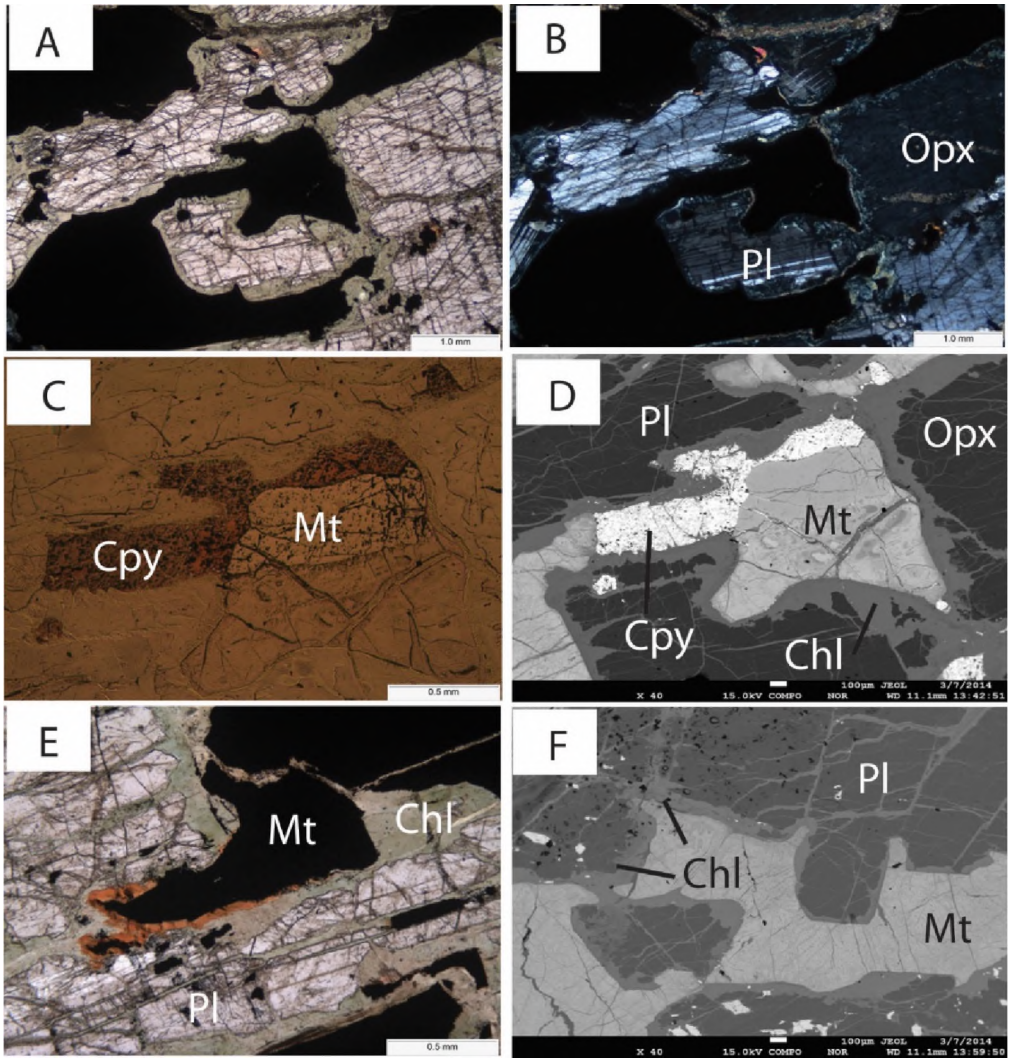

***Figure 22**. Depth 133.78 m. A) Secondary chlorite and small sulphides developed on the grain boundaries of igneous oxides and silicates (transmitted light, parallel polars); B) Same as A), in cross polars. C) Same as A and B, showing the opaque phases are magnetite and associated chalcopyrite (reflected light, crossed polars); D) Same as A, B, and C in BSE image. E) Rare biotite as part of the secondary phase developed on the grain boundaries (transmitted light, parallel polars); F) Magnetite including and "cementing" plagioclase grains (BSE image).*

At depth 135.44 m a coarse grained anorthosite develops. It is made of coarse plagioclase grains and interstitial clinopyroxene and magnetite (Figure 23 A-D). Characteristically, the clinopyroxene shows exsolution lamellae (Figure 23 B and D). Rare pyrite grains are included in plagioclase.

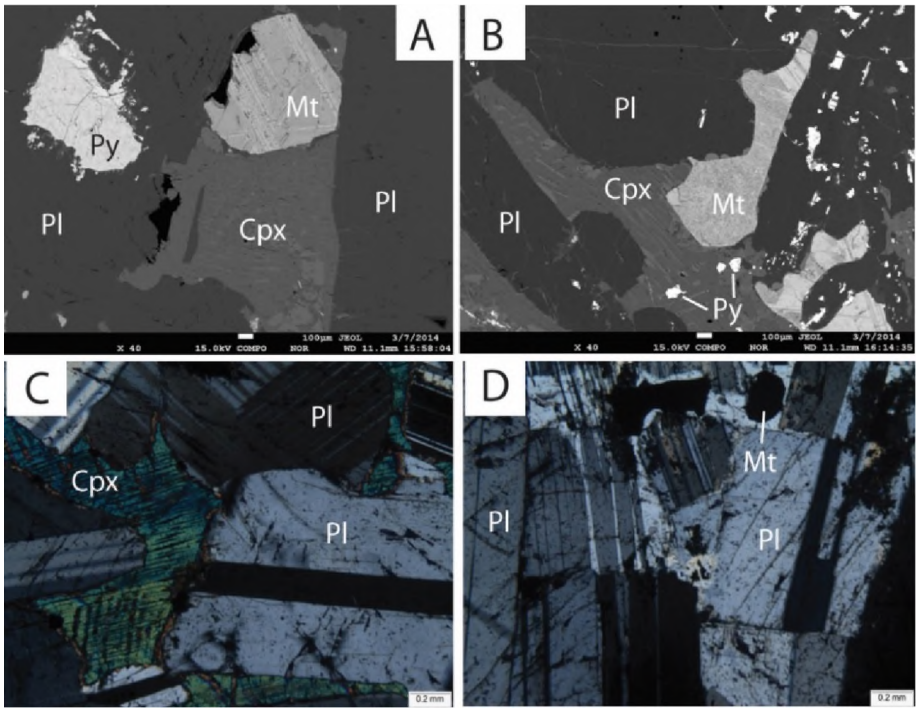

Figure 23. *Depth 135.44 m. Thin anorthosite inside the MML. A) Interstitial clinopyroxene with exsolution lamellae, magnetite and pyrite included in plagioclase (BSE image); B) Interstitial clinopyroxene with exsolution lamellae, magnetite, pyrite and coarse grains of plagioclase (BSE image); Depth 136. Anorthosite. C) Coarse grains of plagioclase and interstitial clinopyroxene with exsolution lamellae of orthopyroxene (transmitted light, parallel polars); D) Small rounded magnetite grain in plagioclase (transmitted light, parallel polars);*

Just below the anorthosite, the modal proportion of opaque minerals increases. The ilmenite is present here in the interstices as coarser grains, separated by Ti-magnetite, and it is partially included in silicate minerals (clinopyroxene). The high Cr_2O_3 and almost absent MgO in the ilmenite are distinctive (see the WDS element distribution map in Figure 24).

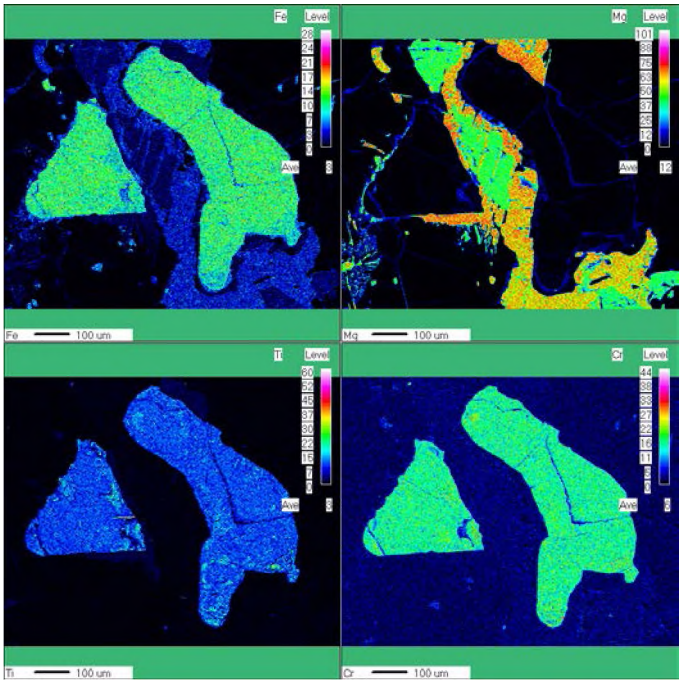

Figure 24. *Depth 135.44. WDS element distribution map of ilmenite.*

The sulphides encountered in the MML in VK5 are spatially related to Ti-magnetite and consist of pyrrhotite, chalcopyrite, and pyrite. Rare millerite (NiS) associated with pyrite was found in little vugs. No PGM were identified in the analyzed samples. However, PGE were analyzed as trace elements in the sulphides and oxides by EPMA method. The results are presented in the "Mineral Chemistry" chapter.

4.1.2. Eastern Lobe

The samples from the MML occurrence at Magnet Heights (see Figure 7) were labelled from MH1 at the base of the MML layer to MH10 at the very top. All samples consist of massive Ti-magnetite (Figure 25).

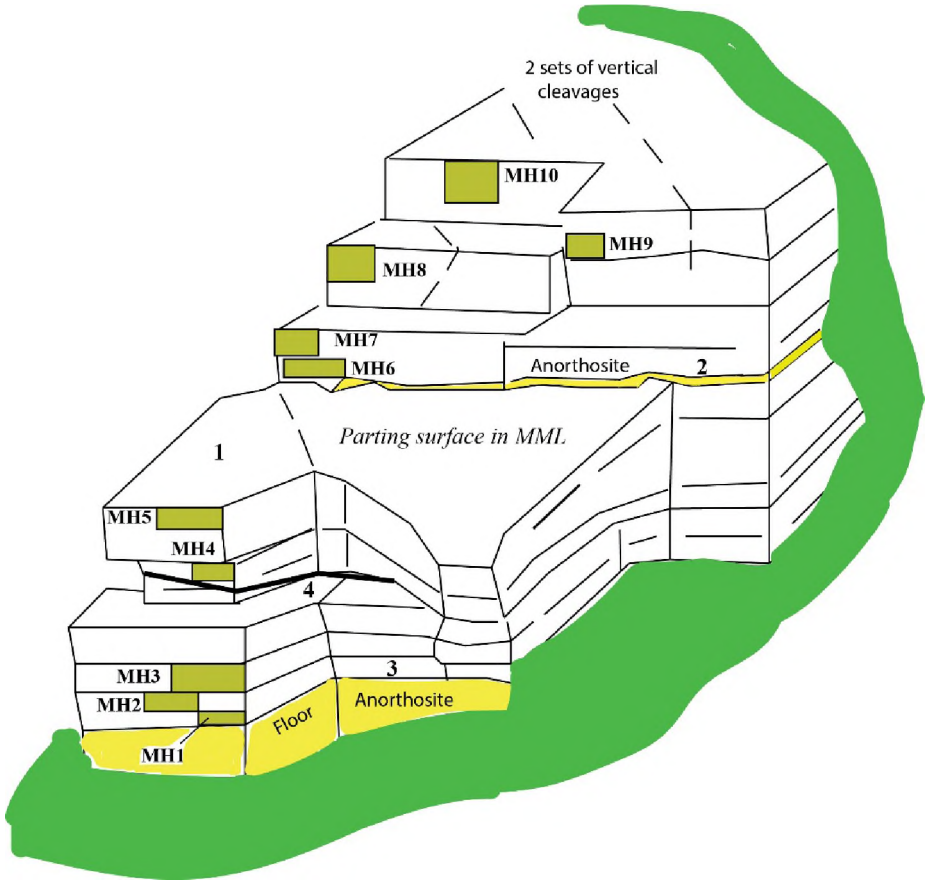

***Figure 25**: Outcrop sketch at Magnet Heights. 1. Magnetitite; 2. Thin anorthosite to separate two main layers of magnetitite; 3. White mica, limonite and disseminated pyrite at the floor contact; 4. A plane with limonite and disseminated sulphides (pyrite). MH1-MH10: sample location in the outcrop.*

The base of the MML has a relatively sharp contact between magnetitite and magnetite-bearing anorthosite, which constitutes the floor. Right at the contact, thin altered shiny surfaces show white mica with limonite and scarce disseminated pyrite. Rare and thin azurite and malachite patches on the limonite plane indicate the presence of former chalcopyrite. The MML here consists of massive Ti-magnetite (Figure 26 A, B, C and D) which includes abundant aggregates of epidote and chlorite, secondary phases probably developed on small igneous (clino)pyroxene crystals (Figure 26 A and C).

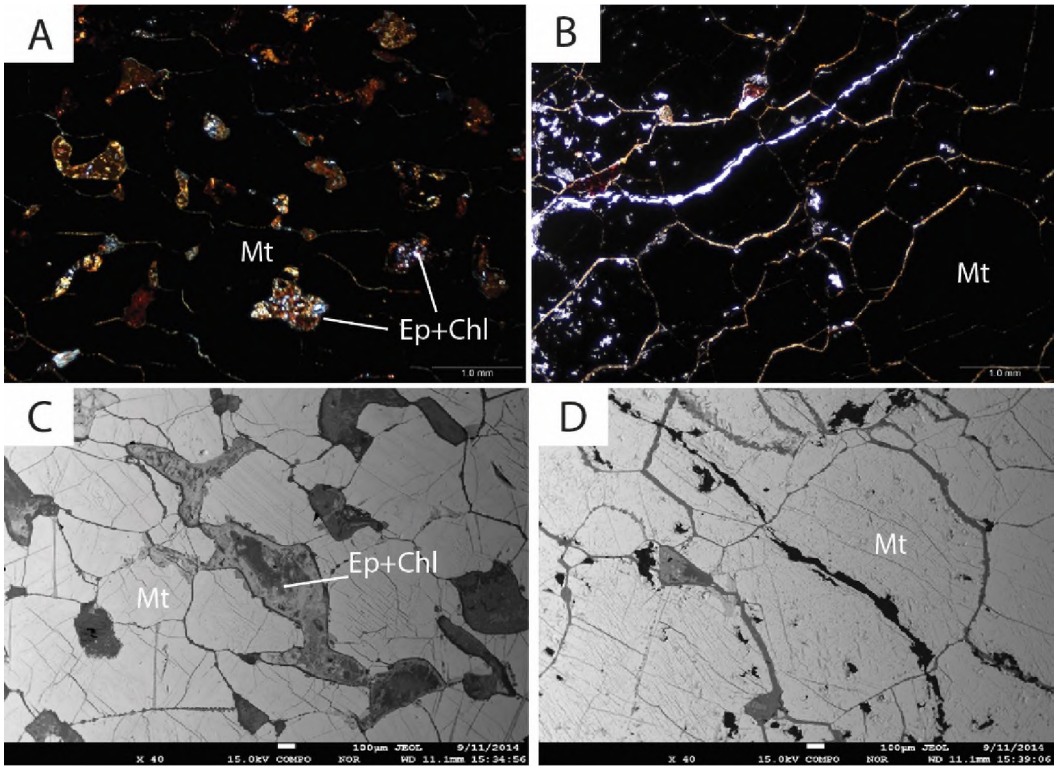

Figure 26: *Sample MH1B (base of MML). A) Massive magnetite with frequent mafic inclusions transformed into epidote and chlorite (transmitted light, crossed polars); B)Massive magnetite showing polygranular texture of magnetite, with chlorite developed along grain boundaries (transmitted light, crossed nicols); C) and D) Ti-magnetite grains with exsolution lamellae and interstitial mafic minerals altered to epidote and chlorite (BSE image).*

Just above the base of MML, the silicates are totally chloritized (Figure 27A). The Ti-magnetite presents fine exsolution lamellae of ulvöspinel (Figure 27 B, C), as well as very small "droplets" of exsolved spinel (black dots in Figure 27 D). The massive Ti-magnetite shows a polygranular pattern, where the individual grains are delimited by fine chlorite rims (Figure 27 B and D).

Upwards in the sequence, 100-700 micron-sized ilmenite grains appear as nests in the massive Ti-magnetite. The ilmenite grains can contain fine inclusions of sulphides (Figure 27 C) and totally chloritized mafic minerals (Figure 27 D).

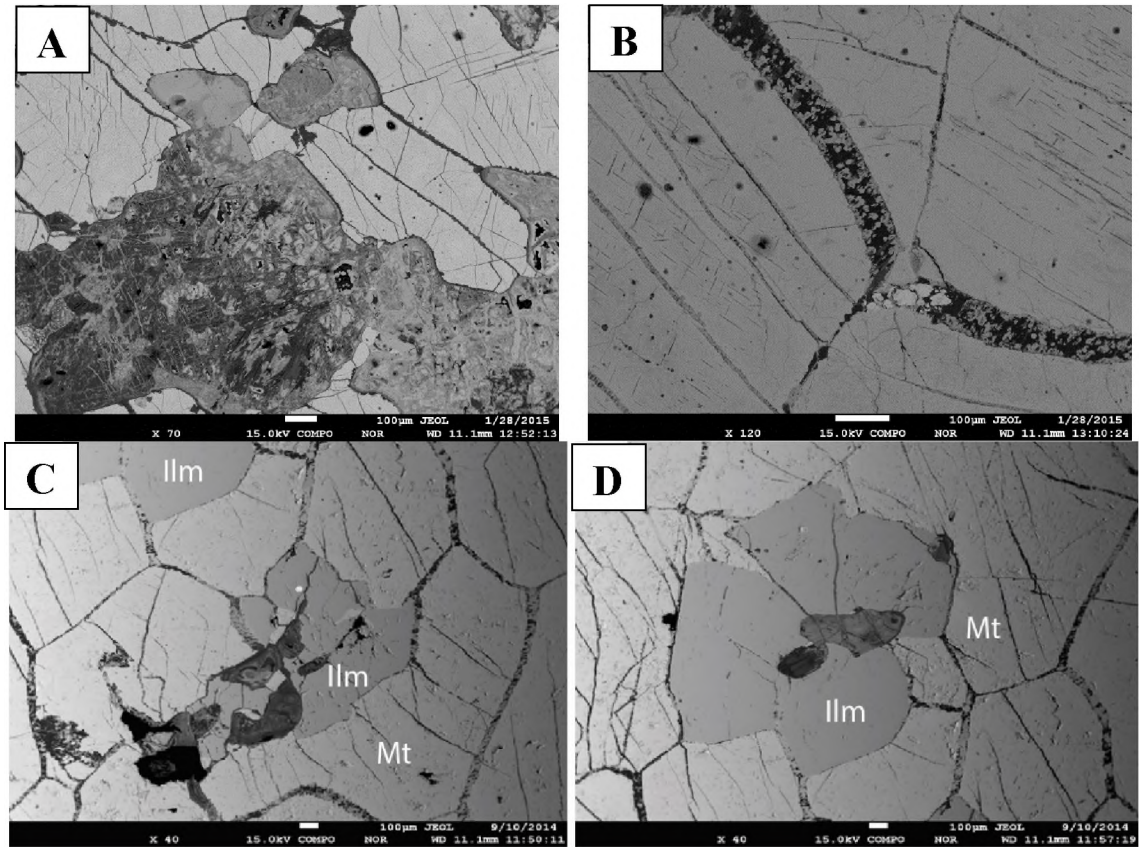

***Figure 27**: A) Sample MH2: Completely chloritized silicates associated with Ti-magnetite and ilmenite; B) Sample MH3: vein with chlorite and epidote in Ti-magnetite: C) Sample MH4. Ilmenite grains with fine sulphide and altered mafic minerals inclusions, surrounded by Ti-magnetite (BSE image); D) Sample MH4: Ilmenite grain nest with inclusions of chloritized mafic minerals; notice the very fine exsolution "droplets" of spinel as very fine black spots. The silicate inclusions are small and completely transformed into chlorite ± epidote. (BSE images).*

In sample MH5, just below the parting plane, the Ti-magnetite present patches of zones with spinel exsolutions, and patches with zones devoid of any exsolution lamellae (Figure 28A). The zones without exsolution lamellae seem to develop around larger chloritized mafic minerals which are included in Ti-magnetite and around cracks or intergranular spaces, which are also filled with chlorite (Figure 28 B). The chloritized inclusions in massive Ti-magnetite are linked one to another through a network of fine veins of chlorite developed on the intergranular spaces. In between the patches with exsolution lamellae and the patches devoid of any kind of exsolution, larger blebs of spinel are evident (Figure 28 A and B), suggesting that the exsolution lamellae around the mafic inclusions or around cracks filled with chlorite migrated, producing patches with no exsolution and with, instead, larger blebs of spinel accumulated in between the two patchy zones. A secondary

process relating the formation of chlorite and the patchy zones devoid of exsolution lamellae can be envisaged. Such a process will be discussed in the next chapters.

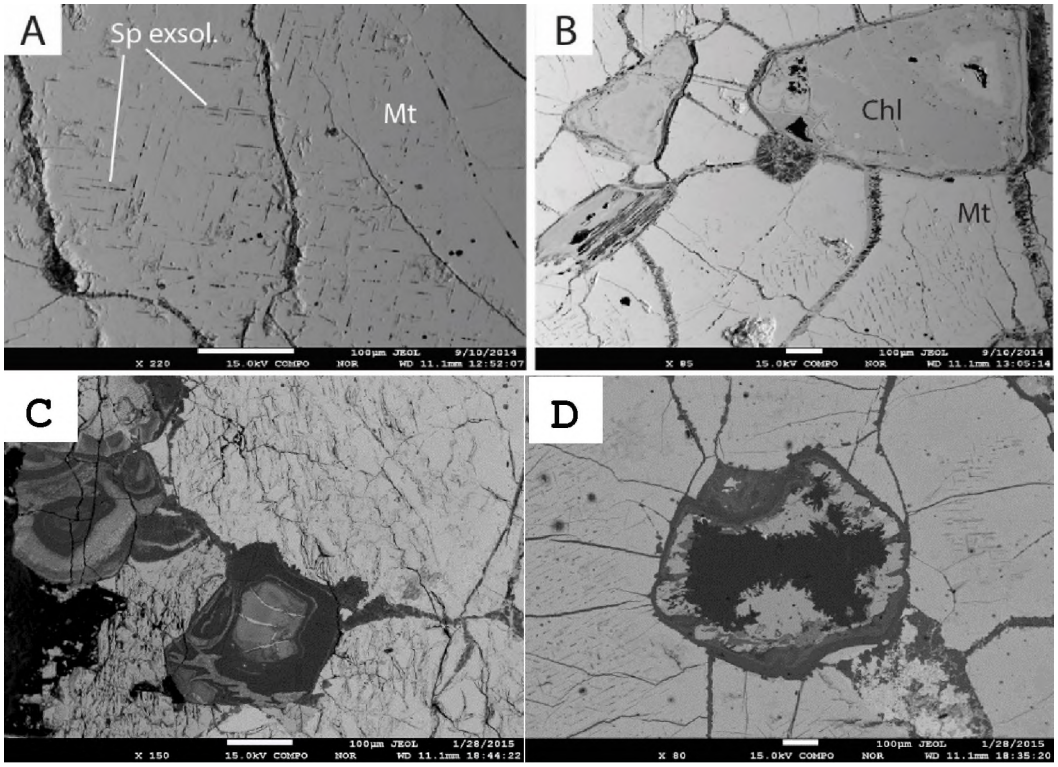

***Figure 28**: A) Sample MH5: Spinel exsolution lamellae in Ti-magnetite (BSE image); B) Sample MH5: Chloritized mafic inclusion in Ti-magnetite; notice the Ti-magnetite surrounding the inclusion showing patches depleted in spinel exsolution lamellae; C) Sample MH9: igneous silicates totally transformed to chlorite in MML; D) Sample MH10, top of MML: fine spinel exsolutions in Ti-magnetite and ignous primary silicate totally transformed to chlorite (dark gray) and epidote (light gray). BSE images.*

Above the MML and in between the third and fourth layer of magnetite, a magnetite-anorthosite was sampled (sample MH12A, Figure 29). Millimeter size grains of magnetite and ilmenite grew in between subhedral coarse grains of plagioclase. Orthopyroxene constitutes less than 15 vol%. Relationships of reciprocal inclusion of magnetite and plagioclase are obvious (Figure 29 B). The magnetite here seems to be poor in exsolution lamellae.

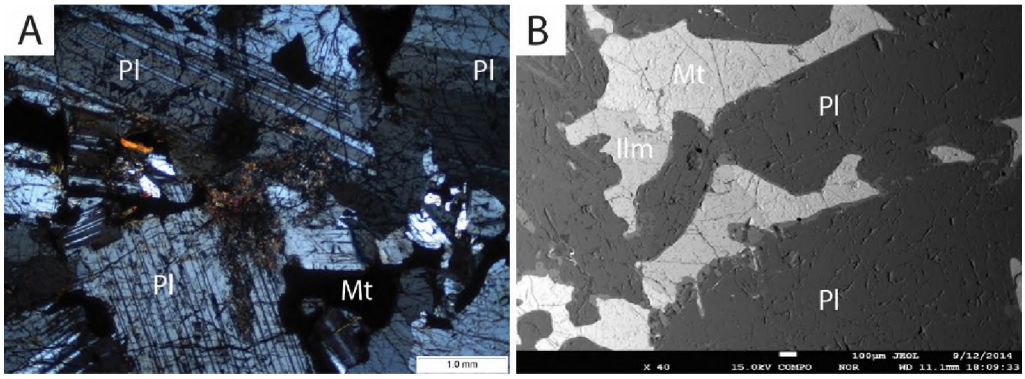

Figure 29: *Sample MH12A: magnetite-anorthosite, above MML and four other magnetite layers. A) Interstitial magnetite and coarse grained plagioclase (Transmitted light, crossed polars); B) Ti-magnetite and ilmenite inter-locked with subhedral grains of plagioclase (BSE image).*

Igneous sulphides seem to be less abundant in the MML from Magnet Heights compared to the MML from the Northern Lobe. Pyrrhotite, pyrite, and chalcopyrite are present as fine inclusions in Ti-magnetite. However, secondary pyrite, occasionally transformed to limonite, can be noticed on some fissures/planes.

4.1.3. Western Lobe

The MML at Rhovan mine has a variable thickness at the outcrop scale and an altered anorthosite floor. The contact between magnetite and anorthosite floor is sharp. However, the floor surface is not a flat plane, but rather constitutes large curved surfaces (Figure 30).

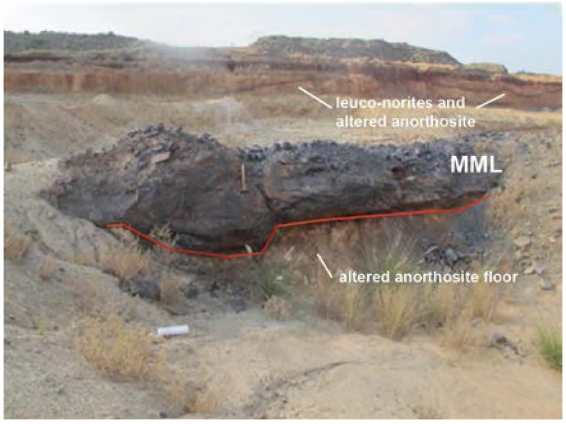

Figure 30: *The sampled outcrop of MML at Rhovan mone. Notice the non-planar anorthosite floor (in red) and the variable thickness at the outcrop scale.*

The oxide minerals in sample 10-30 show very fine exsolution lamellae in Ti-magnetite. The ilmenite occurs as anhedral grains developed along the grain boundaries of magnetite (Figure 31 A, B, D) but also as subhedral grains included in Ti-magnetite (Figure 31 C). Fine "droplets" of spinel exsolutions (black dots in Figure 31 A, B C, D) are scattered in the magnetite. Totally chloritized silicate inclusions are present in Ti-magnetite, sometimes showing a close spatial relationship with the ilmenite (Figure 31 D). Around the ilmenite and silicate inclusions, the exsolution lamellae and the exsolved spinel are less frequent (Figure 31 C, D). Some of the silicate inclusions show a preferred orientation (Figure 31 A).

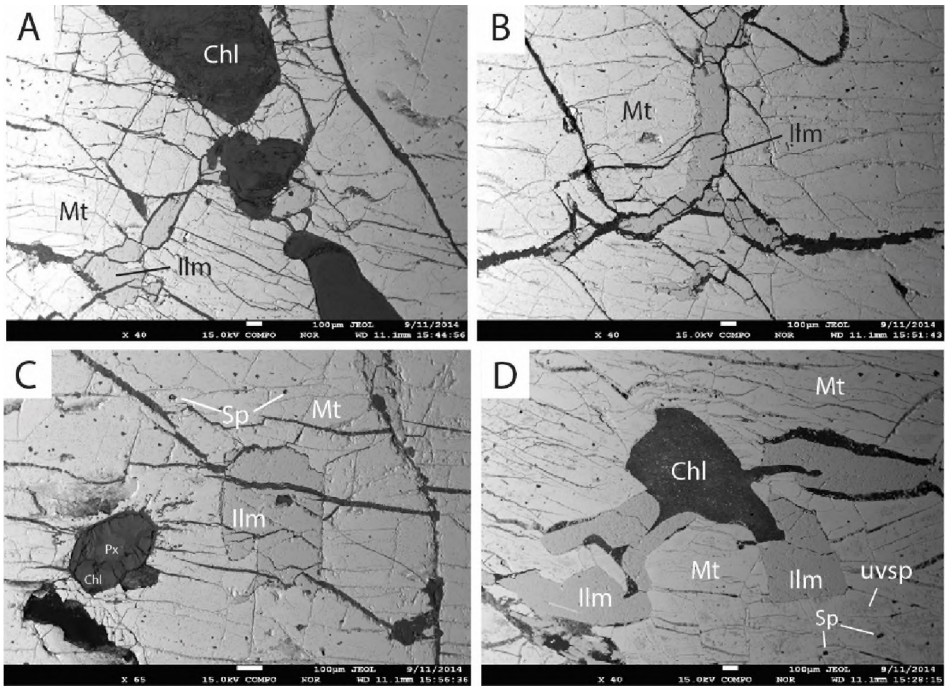

Figure 31: *Sample 10-30: A) Chloritized mafic minerals as oriented inclusions in Ti-magnetite. Notice the spinel exsolutions in Ti-magnetite (black droplets) (BSE image); B) Ilmenite developed on the grain boundaries (BSE); Sample 50-60B: C) Chloritized orthopyroxene and ilmenite included in Ti-magnetite. Notice areas of Ti-magnetite rich in spinel exsolution "droplets" (BSE image); D) Chloritized pyroxene and ilmenite grains in Ti-magnetite (BSE image).*

Sample 70-80 shows similar textural aspects as sample 10-30. The only difference is that large igneous plagioclase laths which are totally chloritized are more frequent than in sample 10-30, where the most frequent igneous silicate was pyroxene. Also notable, chlorite develops on fine cracks in magnetite (Figure 32 A) as well as on big fractures, cross-cutting both Ti-magnetite and

ilmenite grains (Figure 32 B). No PGM was identified in these samples, but rare and limonitized sulphides seem to be spatially associated with chlorite. No fresh sulphide was identified in the petrographic samples.

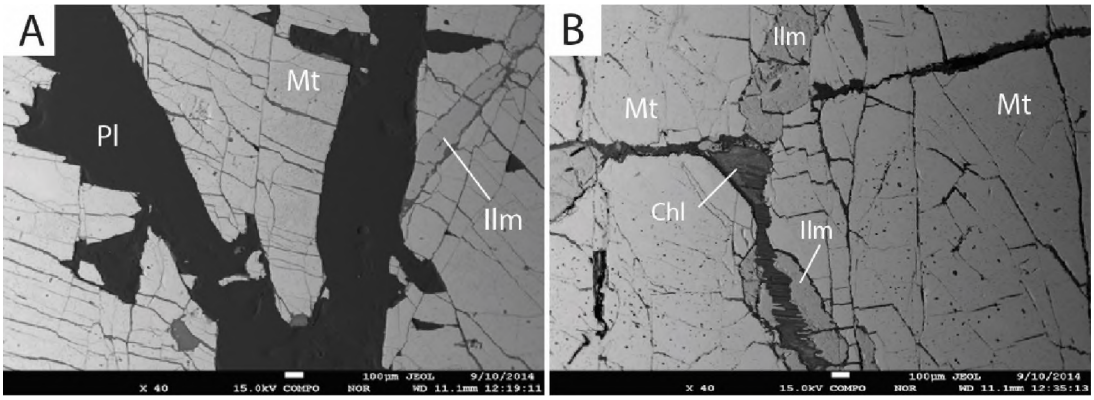

***Figure 32**: Sample 70-80: A) Laths of plagioclase included in massive Ti-magnetite; elongated ilmenite developed along magnetite grain boundary (BSE image); B) Ilmenite along Ti-magnetite grain boundary, cross-cut by chlorite deposited on a fracture and at the intersection of fractures (BSE image).*

4.2. Mineral Chemistry

4.2.1. Northern Lobe

4.2.1.1. Oxides

The chemical composition of oxides in the MML of the Northern Lobe is presented in Table 1 (averages of samples from the same depth) and the Table A1 in Appendix 1 (all EPMA data). It was noted that in borehole VK5, the Ti-magnetite shows a variability of average TiO_2 values from 8.67 % (at depth 135.44 m) to 21.26% (at depth 127.28 m). In borehole VL5 the TiO_2 values are more constant, ranging from 9-12 %. It is to be noted that Cr_2O_3 values in both VK5 and VL5 show a relatively homogenous variation around 0.3-0.8 % but with the exception of sample 135.44 where the Cr_2O_3 goes up to 2.80 %.

Table 1: Table 1: Average composition of Ti-magnetite per sample (wt.%) - Northern Lobe. The FeO and Fe_2O_3 are calculated values. The EPMA analyses of Ti-magnetite were normalized to 4 Oxygen atoms (not shown in Table 1). The total FeO wt.% measured by the microprobe was split up into $FeO_{calculated}$ and $Fe_2O_{3\ calculated}$, (both in wt.%) as follows: the $FeO_{calculated}$ was reiteratively changed until two conditions were fulfilled: a) the total cations to sum to 3.00 and b) $Fe_2O_{3calculated} = (FeO_{measured} - FeO_{calculated})*1.1$.

Sample	Borehole	Depth [m]	Average/St Dev	SiO2	Al2O3	TiO2	Cr2O3	MnO	FeO	Fe2O3	MgO	CaO	V2O3	ZnO	Total
105.05	N- Lobe Borehole VL 5	105.05	Average 105.05	0.07	1.73	11.72	0.67	0.24	22.03	61.99	0.57	0.06	1.62	0.14	100.82
			St Dev	0.05	1.17	1.75	0.12	0.06	3.77	5.59	0.44	0.09	0.09	0.16	1.00
105.12		105.12	Average 105.12	0.26	1.50	12.49	0.64	0.27	24.30	59.06	0.32	0.03	1.56	0.07	100.50
			St Dev	0.29	1.58	3.25	0.12	0.07	5.15	7.84	0.21	0.01	0.09	0.11	0.79
105.24		105.24	Average 105.24	0.05	0.81	9.46	0.63	0.16	18.41	68.84	0.05	0.04	1.67	0.08	100.19
			St Dev	0.04	0.86	1.55	0.08	0.03	3.01	5.04	0.03	0.01	0.12	0.09	0.64
125.05	N-lobe Borehole VK 5	125.05	Average 125.05	0.09	2.06	10.02	0.44	0.23	20.18	65.38	0.02	0.02	1.55	0.12	100.11
			St Dev	0.05	1.07	1.86	0.11	0.05	3.23	5.74	0.02	0.01	0.23	0.15	0.97
125.50		125.5	Average 125.5	0.09	2.06	10.02	0.44	0.23	20.18	65.38	0.02	0.02	1.55	0.12	100.11
			St Dev	0.05	1.07	1.86	0.11	0.05	3.23	5.74	0.02	0.01	0.23	0.15	0.97
126.50		126.5	Average 126.5	0.06	3.64	13.16	0.47	0.29	25.33	54.21	0.80	0.02	1.43	0.14	99.54
			St Dev	0.03	0.86	2.60	0.05	0.08	4.92	9.09	0.34	0.02	0.16	0.17	0.94
127.28		127.28	Average 127.28	0.05	0.87	21.26	0.71	0.25	37.47	38.12	0.01	0.02	1.82	0.06	100.64
			St Dev	0.02	0.43	1.15	0.02	0.03	2.58	3.58	0.02	0.01	0.20	0.06	0.32
129.83		129.83	Average 129.83	0.13	3.66	11.86	0.37	0.26	22.64	58.89	1.22	0.01	1.50	0.00	100.53
			St Dev	0.17	0.38	1.02	0.05	0.03	1.40	3.04	0.28	0.01	0.08	0.00	1.31
129.88		129.88	Average 129.88	0.07	3.58	11.90	0.35	0.27	22.02	58.39	1.45	0.01	1.52	0.11	99.68
			St Dev	0.11	0.93	1.42	0.06	0.05	2.45	4.98	0.49	0.01	0.10	0.17	1.04
133.78		133.78	Average 133.78	0.70	2.81	11.64	0.82	0.22	25.18	56.33	0.19	0.04	1.72	0.00	99.65
			St Dev	1.14	1.78	1.13	0.05	0.04	0.90	3.01	0.30	0.01	0.08	0.00	0.46
133.86		133.86	Average 133.86	0.82	2.52	13.05	0.77	0.24	26.76	53.20	0.53	0.04	1.45	0.10	99.48
			St Dev	1.49	1.71	3.23	0.12	0.07	6.90	12.36	0.85	0.09	0.15	0.18	0.93
135.44		135.44	Average 135.44	0.19	1.71	8.67	2.80	0.34	18.83	66.42	0.02	0.03	1.59	0.06	100.66
			St Dev	0.17	1.06	3.44	2.05	0.23	6.55	10.33	0.02	0.02	0.16	0.10	1.15

A negative trend can be observed in between TiO_2 and $FeO + Fe_2O_3$ (Figure 33 A), while V_2O_3 does not show any correlation trend with TiO_2 (Figure 33 B). The concentration of V_2O_3 ranges from 1.56-1.62 % in VL5, and 1.55 to 1.82 % in VK5. Al_2O_3 seems to negatively correlate with TiO_2 (not shown in Figure 33). Both ($FeO + Fe_2O_3$) and Al_2O_3 negative correlations suggest a crystallographic control of Ti replacement in octahedral sight by Fe^{3+} and Al. Two important correlations can be noted: a strong positive correlation between TiO_2 and MnO (Figure 33 C), and a negative trend in

between Cr_2O_3 + MgO vs. FeO + Fe_2O_3 + TiO_2. Both trends clearly suggest a genetic significance, which will be further discussed under the "Discussion" section.

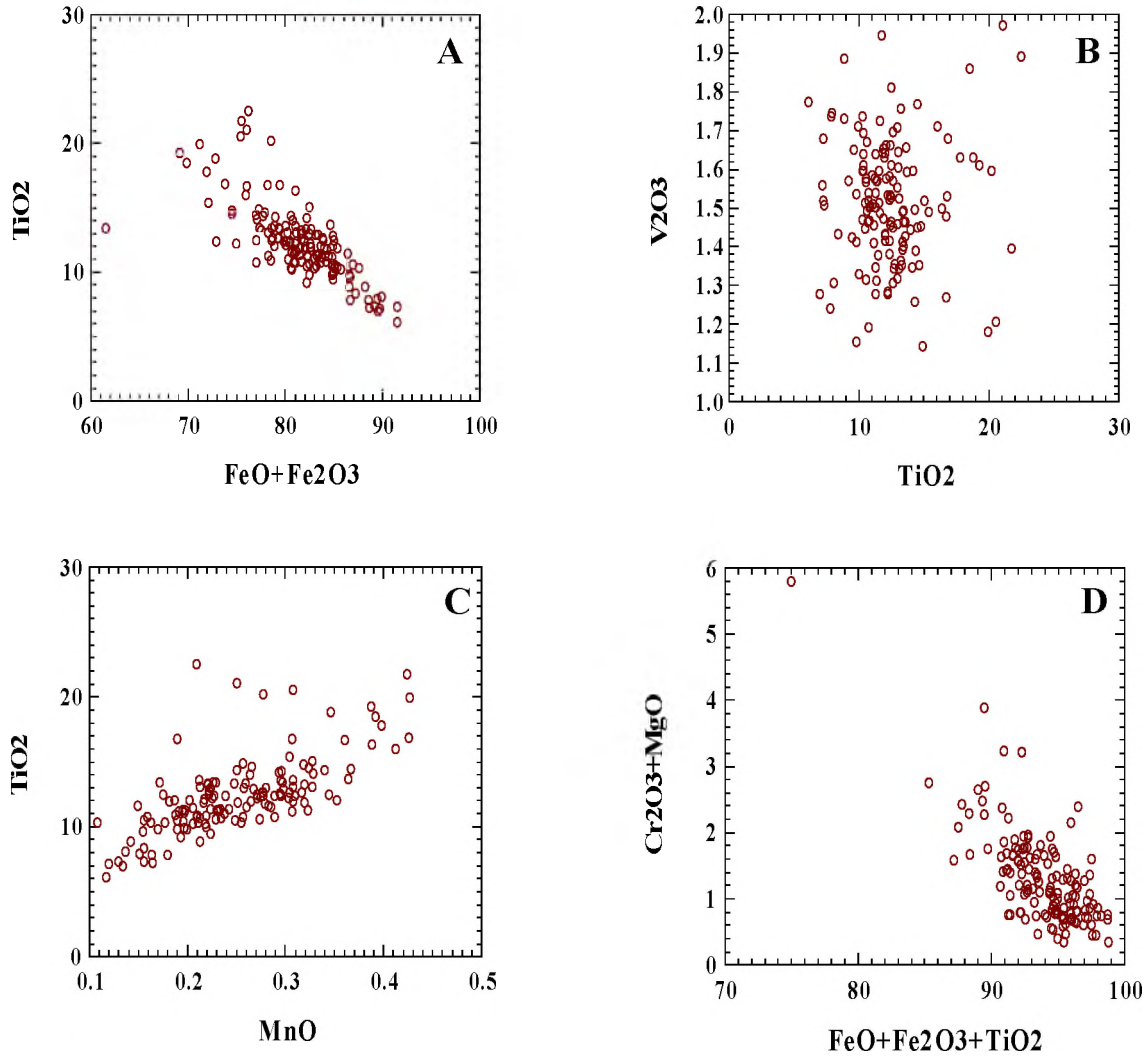

***Figure 33**: Chemical variation in Ti-magnetite in MML (Northern limb). A) Negative correlations between TiO_2 and $FeO+Fe_2O_3$; B) No correlations between V_2O_3 and TiO_2; Notice V_2O_3 variation from 1.2 to 2 wt % for a range of TiO_2 of 10-15 wt%; C) Positive correlation between MnO and TiO_2; D) Negative correlation between Cr_2O_3+MgO and $FeO+Fe_2O_3+TiO_2$ (see text for explanations). All data are plotted in wt.%.*

The logging of the cores and the petrography show that MML in the Northern Lobe is finely layered. Figure 34 illustrate the variation of certain elements in Ti-magnetite with depth in borehole VK5. It is to be noted that TiO_2, Cr_2O_3, MgO and Fe_2O_3 show significant reversals. The lowest MgO

correlates with highest TiO_2, Cr_2O_3, and V_2O_3, while the highest MgO content correlates with minimum values of the same elements.

The pattern of MgO showing two important reversals, together with the variation of the other elements with depth suggests a complex igneous evolution of the MML, which will be discussed in the following chapters.

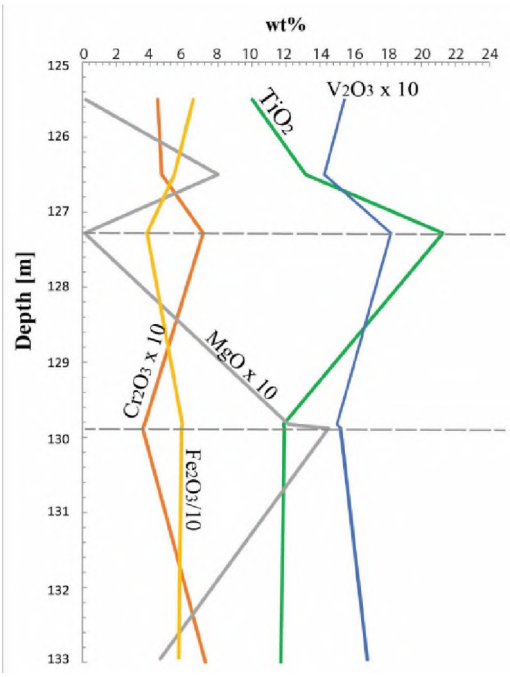

Figure 34: *Variation of Cr_2O_3, Fe_2O_3, MgO, TiO_2 and V_2O_3 with stratigraphic height (MML, borehole VK5)*

4.2.1.2. Silicates

Plagioclase

The most common silicate occurring as inclusions in Ti-magnetite is plagioclase. Even though commonly chloritized, the igneous plagioclase seems to be more frequent in the bottom part of MML in borehole VK5 where it shows coarser laths grains and has a composition of An_{55-58}. The average composition of plagioclase is presented in Table 2, while detailed EPMA data per sample is presented in Appendix 1 (Tables A2-1 to A2-11). The plagioclase here is andesine-labrodorite in

composition (Figure 35) and its chemical variation with depth suggest the existence of compositional reversals.

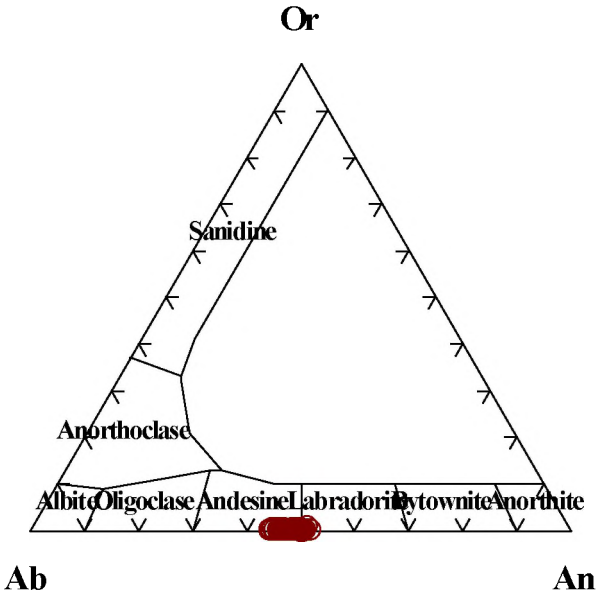

***Figure 35**: Composition of plagioclase in MML, borehole VK5.*

Table 2: Variation of plagioclase composition with depth. Borehole VK-05, Northern Lobe. Oxide data presented as wt.%. Total Fe as FeO.

Depth	Ave/StDev	SiO2	TiO2	Al2O3	FeO	MnO	MgO	CaO	Na2O	K2O	Total	Si	Ti	Al	Fe	Mn	Mg	Ca	Na	K	Total	An
125.1	Average	53.26	0.05	29.24	0.30	0.01	0.02	11.50	4.69	0.29	99.37	2.426	0.002	1.570	0.011	0.000	0.001	0.561	0.414	0.017	5.003	56.5
	StDev	0.72	0.05	0.50	0.09	0.01	0.01	0.44	0.26	0.05	0.52	0.027	0.002	0.027	0.003	0.000	0.001	0.023	0.022	0.003	0.008	2.3
125.5	Average	54.39	0.04	28.27	0.32	0.01	0.04	12.01	4.75	0.26	100.09	2.461	0.001	1.508	0.012	0.000	0.003	0.583	0.416	0.015	5.000	57.5
	StDev	1.86	0.02	1.05	0.11	0.01	0.02	1.25	0.77	0.08	0.61	0.066	0.000	0.067	0.004	0.000	0.001	0.065	0.065	0.005	0.008	6.7
127.3	Average	52.86	0.05	29.09	0.29	0.01	0.02	11.41	4.70	0.37	98.79	2.423	0.002	1.572	0.011	0.000	0.002	0.560	0.417	0.022	5.009	56.1
	StDev	0.80	0.03	0.45	0.08	0.01	0.01	0.53	0.31	0.05	0.43	0.028	0.001	0.028	0.003	0.001	0.001	0.027	0.027	0.003	0.009	2.8
129.8	Average	53.58	0.05	29.73	0.29	0.01	0.07	11.84	4.57	0.19	100.33	2.416	0.002	1.580	0.011	0.000	0.005	0.572	0.400	0.011	4.997	58.3
	St Dev	0.96	0.03	0.64	0.09	0.02	0.12	0.70	0.42	0.10	0.69	0.034	0.001	0.035	0.003	0.001	0.008	0.035	0.036	0.006	0.010	3.7
129.9	Average	53.84	0.05	29.40	0.32	0.01	0.04	10.76	5.12	0.25	99.80	2.437	0.002	1.569	0.012	0.001	0.003	0.522	0.449	0.014	5.009	53.0
	StDev	0.75	0.02	0.44	0.10	0.01	0.04	0.43	0.34	0.06	0.40	0.026	0.001	0.027	0.004	0.001	0.003	0.022	0.029	0.004	0.008	2.6
130	Average	52.40	0.05	29.72	0.31	0.01	0.04	11.96	4.41	0.16	99.05	2.396	0.002	1.602	0.012	0.000	0.002	0.586	0.391	0.009	5.001	59.5
	St Dev	1.47	0.02	0.96	0.10	0.01	0.01	1.10	0.65	0.08	0.37	0.058	0.001	0.058	0.004	0.000	0.001	0.056	0.056	0.004	0.006	5.9
133.8	Average	54.43	0.04	29.14	0.43	0.01	0.05	11.47	4.81	0.30	100.68	2.446	0.001	1.543	0.016	0.000	0.003	0.552	0.419	0.017	4.999	55.9
	St Dev	0.69	0.02	0.40	0.12	0.01	0.03	0.28	0.22	0.07	0.60	0.020	0.001	0.024	0.005	0.001	0.002	0.014	0.018	0.004	0.009	1.6
133.9	Average	54.97	0.04	27.95	0.77	0.01	0.09	11.37	4.98	0.20	100.39	2.480	0.001	1.486	0.029	0.000	0.006	0.550	0.436	0.011	5.000	55.2
	St Dev	0.97	0.02	0.48	0.73	0.01	0.12	0.55	0.38	0.05	0.46	0.031	0.001	0.029	0.028	0.001	0.008	0.027	0.032	0.003	0.015	2.9
135.4	Average	54.17	0.04	28.90	0.45	0.01	0.03	11.33	4.65	0.37	99.95	2.451	0.001	1.541	0.017	0.000	0.002	0.549	0.408	0.021	4.992	56.2
	St Dev	0.53	0.03	0.30	0.47	0.01	0.07	0.35	0.23	0.09	0.47	0.016	0.001	0.018	0.018	0.001	0.005	0.017	0.021	0.005	0.009	1.6
136.4	Average	52.89	0.04	29.33	0.46	0.01	0.02	11.74	4.37	0.33	99.20	2.416	0.001	1.579	0.018	0.000	0.002	0.575	0.387	0.019	4.996	58.6
	St Dev	1.17	0.02	0.73	0.32	0.01	0.02	0.81	0.46	0.07	0.42	0.047	0.001	0.044	0.012	0.000	0.001	0.041	0.040	0.004	0.011	4.3

Across the bottom part of the MML, the composition of plagioclase is not significantly variable, ranging from $An_{53\pm2.6}$ to $An_{58.6\pm4.3}$, however, showing few reversals. The higher variation within the sample is noted in samples from depths 125.5 (6.7%) and 130.0 (5.9%), showing the highest degree of zonation on plagioclase. These two samples also coincide with the samples where the two main reversals in plagioclase are encountered (Figure 36).

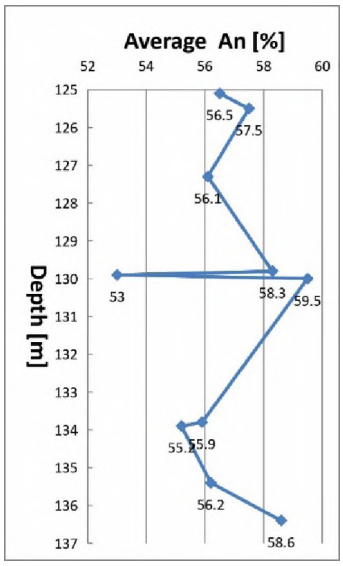

***Figure 36**: Reversals of An in plagioclase in MML from borehole VK5.*

Orthopyroxene

The orthopyroxene inclusions in Ti-magnetite are very chloritized and seem to be more abundant in VL5 samples and towards the top of MML of the VK5 samples. Less chloritized orthopyroxene grains appear at depth 129.83 m, where it includes clinopyroxene and also gives a corona reaction against the magnetite, where the corona consists of olivine. This orthopyroxene is a primary magmatic phase and has a Mg# of 70.3-72.4 (Table 3 and Appendix 1, Table A3). It contains 0.97-1.16 Al_2O_3. Few grains show relatively high CaO (3-5 wt%), pointing to pigeonite composition (Figure 37). However, the majority of the analyzed grains have low CaO, being orthopyroxene with composition En_{70-72}. The pigeonite grains have higher CaO in the core comparing to rims (Figure 37). Core to rim variation of orthopyroxene which has olivine corona shows little variation,

however, this variation is consistent from core to rim. The Mg# ($Mg/(Mg+Fe^{2+}$ in moles %) increases from 0.705 in the core to 0.725 at the rim towards the olivine (Figure 38).

Table 3: Composition of orthopyroxene- Sample 129.83 - borehole VK-05, Northern Lobe. Oxide data presented as wt.%. Total Fe as FeO.

Analysis	opx-37	opx-38	opx-39	opx-40	opx-41	opx-42	opx-43	opx-44	opx-50
Comment	core	core	core	core	rim	rim	rim	rim	core
SiO2	53.44	53.19	53.45	53.98	53.66	53.77	53.96	53.50	53.09
TiO2	0.25	0.29	0.25	0.26	0.23	0.20	0.13	0.22	0.23
Al2O3	1.09	1.02	1.01	1.09	1.16	1.10	0.97	1.10	0.98
Cr2O3	bd	bd	0.02	bd	0.04	bd	bd	bd	bd
FeO	18.66	18.39	18.50	17.08	16.24	17.04	17.05	17.56	18.26
MnO	0.39	0.37	0.33	0.32	0.33	0.35	0.36	0.33	0.35
NiO	bd	bd	bd	bd	bd	bd	0.04	bd	bd
MgO	24.82	24.80	25.02	24.09	23.60	25.19	24.89	24.95	26.06
CaO	1.15	1.18	0.86	3.09	5.06	0.71	0.97	0.93	1.06
Na2O	0.01	0.01	0.03	0.01	0.05	0.01	0.00	0.00	0.01
K2O	bd	bd	bd	bd	bd	bd	bd	bd	bd
Total	99.81	99.28	99.52	99.94	100.36	98.40	98.37	98.61	100.07
Cations normalized to 6 Oxygen atoms									
Si	1.963	1.963	1.966	1.974	1.960	1.983	1.991	1.976	1.944
Ti	0.007	0.008	0.007	0.007	0.006	0.006	0.004	0.006	0.006
Al	0.047	0.045	0.044	0.047	0.050	0.048	0.042	0.048	0.042
Fe2+	0.573	0.568	0.569	0.522	0.496	0.526	0.526	0.542	0.559
Mn	0.012	0.011	0.010	0.010	0.010	0.011	0.011	0.010	0.011
Mg	1.359	1.364	1.372	1.313	1.285	1.385	1.370	1.374	1.423
Ca	0.045	0.047	0.034	0.121	0.198	0.028	0.038	0.037	0.042
Na	0.001	0.000	0.002	0.000	0.003	0.001	0.000	0.000	0.001
Total	4.007	4.006	4.004	3.995	4.009	3.988	3.983	3.994	4.028
Mg#	70.344	70.623	70.674	71.542	72.149	72.490	72.245	71.695	71.779

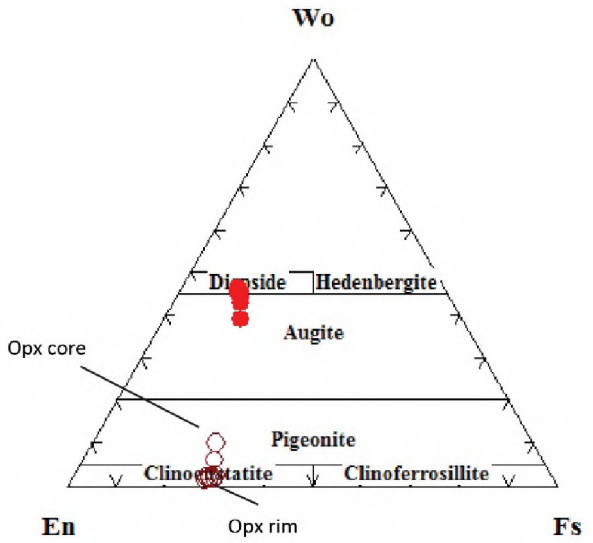

***Figure 37**: Composition of orthopyroxene and clinopyroxene from MML, Northern limb; Notice the pigeonite-rich core of some orthopyroxene and the diopside-augite range of the clinopyroxene.*

Table 4: Composition of clinopyroxene- Sample 129.83 - borehole VK-05, Northern Lobe. All oxide data presented as wt.%. Total Fe as FeO.

Sample	33cpx1	34cpx2	35cpx3	36cpx4	30cpx_1	31cpx_2	32cpx_3
Mineral	augite	augite	augite	augite	augite	augite	augite
SiO2	51.64	51.29	51.98	51.28	51.96	51.11	52.29
TiO2	0.45	0.49	0.48	0.49	0.49	0.56	0.49
Al2O3	1.96	1.99	2.01	2.06	1.98	2.12	2.02
Cr2O3	0.03	0.00	0.03	0.00	0.04	0.00	0.01
FeO	7.12	7.33	7.66	7.25	9.85	8.24	8.61
NiO	0.04	0.02	0.01	0.03	0.03	0.01	0.01
MnO	0.22	0.16	0.16	0.21	0.25	0.19	0.19
MgO	14.80	14.72	14.61	14.66	15.95	14.90	15.08
CaO	22.67	22.52	22.17	21.96	19.14	21.53	21.01
Na2O	0.27	0.25	0.28	0.29	0.21	0.28	0.23
K2O	bd	bd	bd	bd	bd	bd	bd
Total	99.20	98.77	99.40	98.22	99.89	98.93	99.96
Cation normalized to 6 Oxygen atoms							
Si	1.933	1.930	1.942	1.937	1.934	1.924	1.943
Ti	0.013	0.014	0.013	0.014	0.014	0.016	0.014
Al	0.086	0.088	0.088	0.092	0.087	0.094	0.089
Cr	0.001	0.000	0.001	0.000	0.001	0.000	0.000
Fe	0.223	0.231	0.239	0.229	0.307	0.259	0.268
Ni	0.001	0.001	0.000	0.001	0.001	0.000	0.000
Mn	0.007	0.005	0.005	0.007	0.008	0.006	0.006
Mg	0.826	0.826	0.813	0.826	0.885	0.836	0.835
Ca	0.909	0.908	0.887	0.889	0.764	0.869	0.836
Na	0.020	0.019	0.020	0.021	0.015	0.020	0.017
K	0.001	0.000	0.000	0.000	0.000	0.000	0.000
Total	4.021	4.021	4.011	4.014	4.016	4.024	4.008
Mg#	78.8	78.2	77.3	78.3	74.3	76.3	75.7

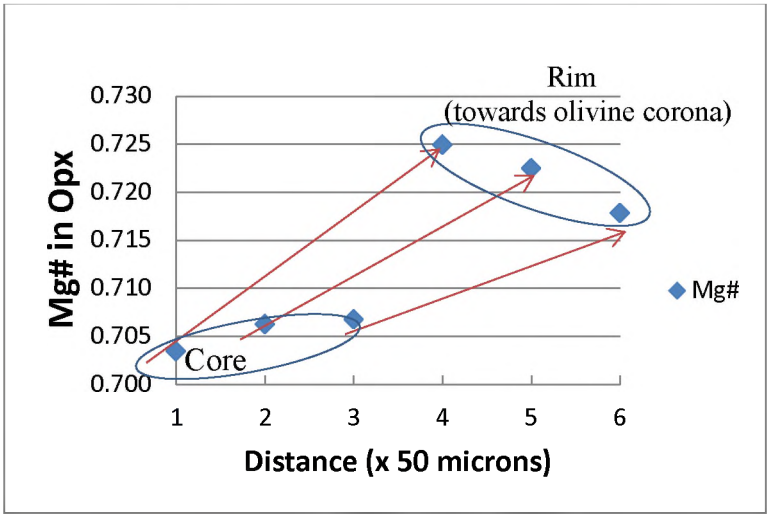

***Figure 38**: Core to rim variation of Mg# in orthopyroxene included in Ti-magnetite, towards olivine corona. Notice the Mg# increase of Opx towards the olivine.*

Clinopyroxene

The clinopyroxene was identified just as very fine-grained, rounded inclusions in orthopyroxene (e.g. Figure 18 A, B). Possibly the preservation of igneous orthopyroxene and its clinopyroxene

inclusions (against replacement by secondary hydrous minerals) was due to the protective role of the olivine corona reaction on orthopyroxene. However, in most of the analyzed MML samples, the pyroxenes included in Ti-magnetite and those outside the magnetite grains were intensely and often totally chloritized. The composition of clinopyroxene is mostly augite (Table 4 and Appendix 1, Table A4). A few grains are zoned, from augite in the core towards diopside in the rim, near the orthopyroxene host (Figure 37).

Olivine

Olivine was identified in two different contexts:

1) As a reaction corona on orthopyroxene in samples 129.83 and 129.97. It develops as a continuous reaction around orthopyroxene when it is included in Ti-magnetite (Figure 18 A and B), or as a discontinuous reaction, following the contact orthopyroxene – Ti-magnetite, only (Figure 18 C and D).
2) As polygranular aggregate around Ti-magnetite near plagioclase, which is transformed to a fine symplectite made of clinopyroxene and an acid plagioclase (Figure 20).

In the case of the reaction corona, it can be noted that a) olivine develops in the space of orthopyroxene only, without consuming the mineral volume of Ti-magnetite (e.g. Figure 39) and b) the olivine corona develops even in between ilmenite and orthopyroxene (see WDS element map in Figure 19).

The composition of olivine is presented in Table 5 and Appendix 1 (Table A5). Reaction corona olivine has a composition of Fo_{69} in the middle of the band and Fo_{72} at the rim, near magnetite. This observation of increasing MgO content in magnetite towards the Fe-rich phase (Ti-magnetite) is important is estimating the genesis of this reaction microstructure.

The olivine in Figure 18A-D and 39 develops on an igneous orthopyroxene with composition En_{70} which has a pigeonite-rich core.

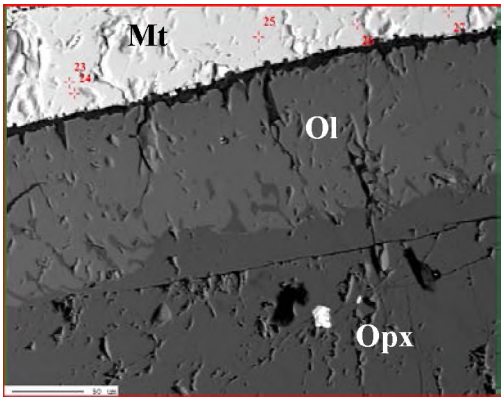

***Figure 39**: Olivine develops towards the orthopyroxene, on the orthopyroxene's space, only. Numbers represent electron microprobe analyses in Ti-magnetite. (BSE image).*

Table 5: Composition of reaction olivine - sample 129.83 (borehole VK-05, Northern Lobe). Oxide data are in wt.%; Fe total as FeO.

Analysis	ol-55	ol-56	ol-51	ol-52	ol-53	ol-45	ol-46	ol-47	ol-48	ol-49
SiO2	38.87	38.11	38.28	38.12	38.33	37.59	37.66	37.56	37.93	37.90
TiO2	0.10	0.10	0.00	0.05	0.08	0.05	0.02	0.00	0.05	0.01
Al2O3	0.00	0.01	0.00	0.01	0.00	0.01	0.01	0.01	0.00	0.00
FeO	25.33	24.99	24.25	25.44	22.98	27.47	27.52	27.24	26.51	27.60
MnO	0.31	0.27	0.26	0.27	0.26	0.34	0.28	0.35	0.32	0.30
NiO	0.06	0.05	0.04	0.05	0.02	0.05	0.06	0.03	0.06	0.06
MgO	36.14	37.13	36.07	36.32	37.19	34.96	34.83	35.50	35.98	34.93
CaO	0.03	0.00	0.02	0.02	0.02	0.04	0.06	0.04	0.00	0.04
Total	100.83	100.67	98.92	100.27	98.86	100.51	100.43	100.73	100.86	100.83
Cations normalized to 4 Oxygen atoms										
Si	0.998	1.000	0.994	0.998	1.002	1.015	1.003	1.010	1.014	0.997
Ti	0.001	0.000	0.000	0.001	0.000	0.000	0.001	0.002	0.002	0.002
Al	0.000	0.000	0.000	0.000	0.000	0.000	0.000	0.000	0.000	0.000
Fe	0.610	0.611	0.603	0.583	0.610	0.538	0.560	0.507	0.553	0.547
Mn	0.008	0.006	0.008	0.007	0.007	0.006	0.006	0.006	0.007	0.006
Ni	0.001	0.001	0.001	0.001	0.001	0.001	0.001	0.000	0.001	0.001
Mg	1.383	1.379	1.400	1.411	1.376	1.425	1.424	1.461	1.406	1.448
Ca	0.001	0.002	0.001	0.000	0.001	0.001	0.000	0.000	0.001	0.000
Total	3.001	3.000	3.006	3.001	2.997	2.985	2.995	2.987	2.984	3.001
Fo	69.1	69.0	69.6	70.5	69.0	72.3	71.5	74.0	71.5	72.3

The olivine rim developed as a band around orthopyroxene, which shows a chemical zonation given by the Mg-Fe^{2+} exchange. The center of the band is poorer in Mg and richer in Fe2+, while towards the magnetite contact, the Mg increases and Fe2+ decreases (Figure 40).

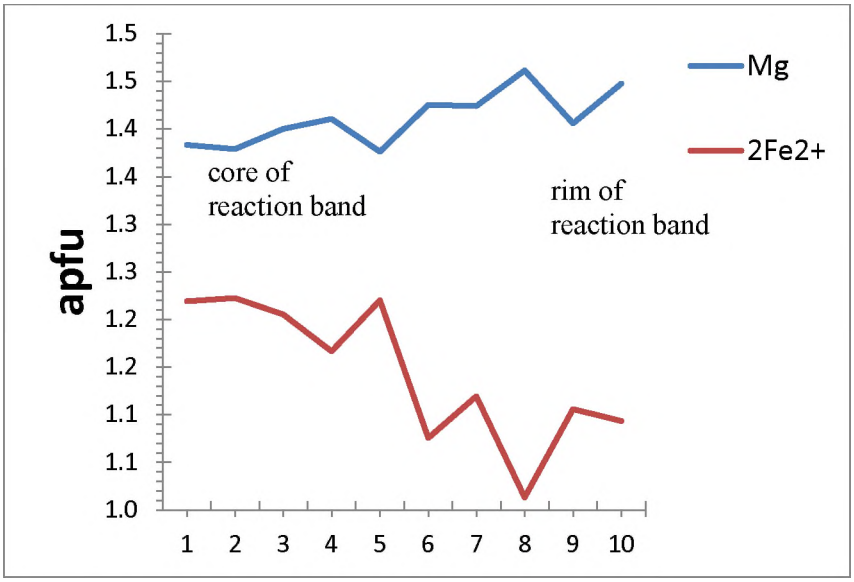

***Figure 40**: Mg vs $2Fe^{2+}$ (apfu) in olivine reaction band from core to rim towards the magnetite*

Biotite

Rare biotite grains are included in Ti-magnetite, when they are chloritized (e.g. Fig 11 C). When not included in magnetite, but it is present near the plagioclase, it can be kinked and strongly altered or recrystallized (e.g. Figure 17A, B). Their composition is phlogopite with MgO=18-19% and FeO~10% (Appendix 1, Table A6). Na_2O can reach 0.4%, while F and Cl can be as high as 0.4% and 0.25 %, respectively. All analyzed biotite grains are Ti-rich, where TiO_2 ranges from 0.9% to 4.1 %, with an average near 3.4%. The secondary biotite is texturally very different. It developed around other phases and it is spatially associated with the secondary type of sulphides. It has a stronger pleochroism under the microscope, and it is probably richer in FeO then the igneous biotite (it was not analyzed).

Amphibole

In extremely rare situations, amphibole can occur in the MML, developed as a thin brown corona on Ti-magnetite, in between Ti-magnetite and plagioclase. This amphibole has a pargasite-rich composition (composition not shown on tables). Together with biotite, the amphibole rarely survived, due to the intense chloritization.

Chlorite

Most of the chlorite which replaces igneous phases and precipitated on thin cracks inside Ti-magnetite is clinochlore (see Appendix 1, Table A7). However, in VL5 samples, the chlorite spatially related to mixture "X" shows a chamosite composition.

Sulphides

The igneous sulphides identified in the MML of the Northern Lobe in borehole VK5 are chalcopyrite ($CuFeS_2$), pentlandite $(Ni,Fe)_9S_8$, pyrrhotite (Fe_7S_8), pyrite (FeS_2), Co-bearing pyrite, millerite (NiS) and siegenite ($CoNi_2S_4$). The composition of the sulphides is presented in Appendix 1, Table A8. Millerite, siegenite and strongly limonitized pyrite were identified associated with chlorite veins, showing a secondary character (note: siegenite is mentioned in Table A8 as Ni-Co sulphide). The siegenite composition, recalculated in atoms per formula unit (apfu), is $(Co_{0.682}Fe_{0.339})_{\sum=1.021}Ni_{1.812}S_{4.108}$.

4.2.1.3. PGE trace element analysis of oxides and sulphides

No PGM's were identified in the MML of the Northern Lobe. In an attempt to identify trace elements of PGE in minerals, qualitative analyses (WDS scans on EPMA) were run on oxides and sulphides from MML samples from VL5 and VK5. Three PGEs (Pt, Pd and Rh) and Te were found to have measurable concentrations. After careful calibrations using pure metals, the above elements were quantitatively analyzed (Table 6 and Appendix 1, Table A9). The elements Pt and Rh have standard deviation higher than the measured values, showing that in fact, these elements are present below or just above the detection limits (~25 ppm). The elements Pd and Te are present in all analyzed samples, with higher concentrations, almost three times higher in sulphides than in oxides.

Table 6: Trace three PGE and Te in oxides and associated sulphides from MML (Northern Lobe, samples from borehole VK5).

Element	Ti-magnetite		Ilmenite		Chalcopyrite		Pyrite		Pyrrhotite	
	Average	St Dev	Average	St Dev	Average	St Dev	Average	St Dev	Average	St Dev
Pt	120	253	150	220	143	203	130	114	157	274
Pd	847	433	642	460	1803	494	1540	512	1428	526
Rh	71	89	110	119	70	99	110	99	28	69
Te	43	108	77	123	40	28	490	1120	67	136

Values in ppm, measured on EPMA (see analytical conditions for trace element analysis); Average and Standard deviation 1 σ for magnetite (in brackets, the number of analyses): Ti-magnetite (25), ilmenite (5) chalcopyrite (13), pyrite (3), pyrrhotite (15).

4.2.2. Eastern Lobe

4.2.2.1. Oxides

The Ti-magnetite in the MML from Magnet Heights are briefly presented as the average per sample in Table 7 and detailed EPMA data in Appendix 1, Table B1, where detailed EPMA analyses of Ti-magnetite along stratigraphic column at Magnet Heights are presented. Various diagrams related to composition variation of Ti-magnetite are showed in Figure 41A-D.

Table 7: Average composition of Ti-magnetite per sample – Magnet Height - Eastern Lobe. Oxide data as wt.%. The FeO and Fe_2O_3 are calculated values. The EPMA analyses of Ti-magnetite were normalized to 4 Oxygen atoms (not shown in Table 1). The total FeO wt.% measured by the microprobe was split up into $FeO_{calculated}$ and $Fe_2O_{3\ calculated}$, (both in wt.%) as follows: the $FeO_{calculated}$ was reiteratively changed until two conditions were fulfilled: a) the total cations to sum to 3.00 and b) $Fe_2O_{3calculated} = (FeO_{measured} - FeO_{calculated})*1.1$.

Sample	Borehole	Depth [m]	Average/St Dev	SiO2	Al2O3	TiO2	Cr2O3	MnO	FeO	Fe2O3	MgO	CaO	V2O3	ZnO	Total
MH12-A	E-lobe Magnet Heights	0.10	Average MH12-A	0.12	2.51	10.01	0.31	0.26	20.17	65.24	0.28	0.02	1.30	0.08	100.29
			St Dev	0.17	0.49	1.74	0.05	0.08	3.08	5.62	0.27	0.02	0.15	0.06	0.99
MH4		1.20	Average MH4	0.14	0.26	13.05	0.83	0.18	24.75	57.43	0.13	0.01	1.43	0.03	98.24
			St Dev	0.09	0.12	2.08	0.21	0.10	3.89	6.84	0.06	0.00	0.16	0.05	0.09
MH1-B		2.05	Average MH1-B	0.03	5.43	12.05	2.49	0.24	25.00	51.57	2.05	0.00	1.26	0.08	100.21
			St Dev	0.03	0.67	0.26	0.04	0.02	0.00	0.52	0.64	0.00	0.05	0.04	1.40

Compared to Ti-magnetite in MML in Northern Lobe, the MML in Eastern lobe at Magnet Heights shows no correlation between TiO_2 and MnO (Figure 41 A), and different Cr_2O_3 values in each analyzed sample (Figure 41 B).

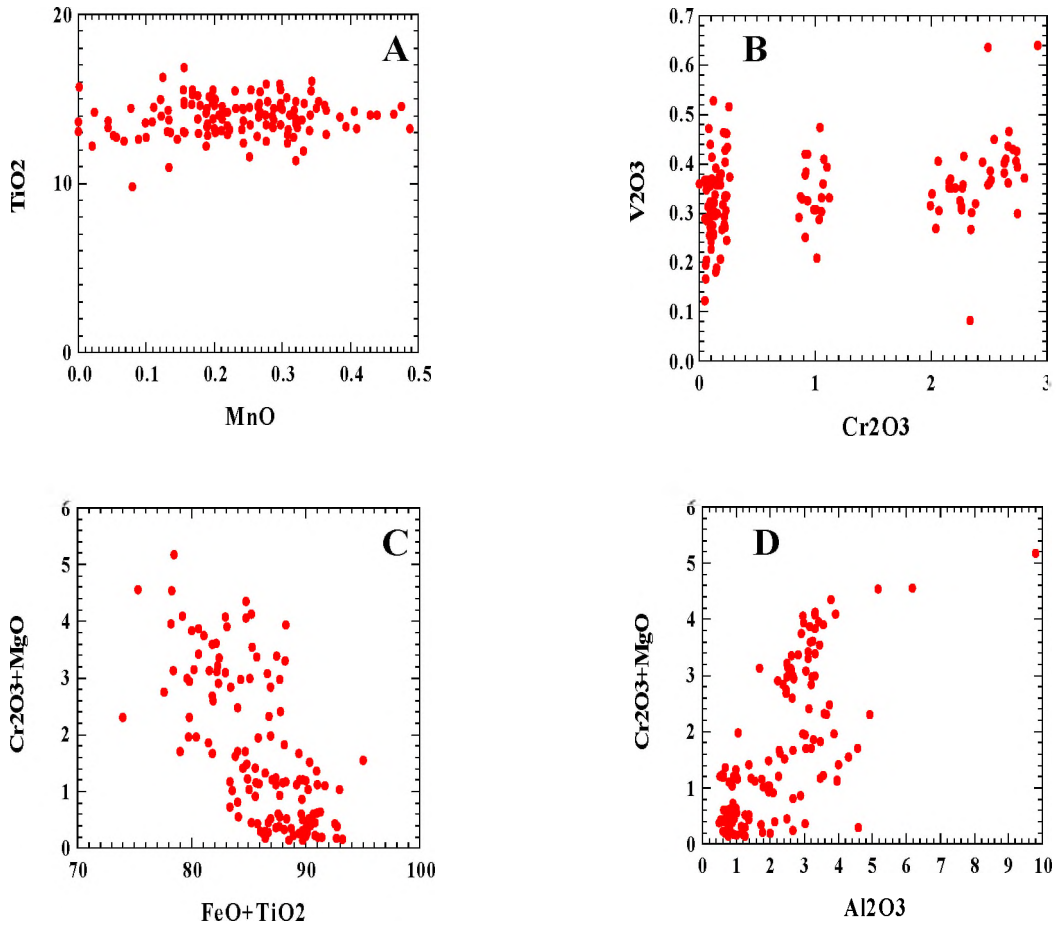

***Figure 41**: Compositional variation in Ti-magnetite from the MML of the Eastern lobe at Magnet Heights. A) MnO vs. TiO_2; B) Distinct Cr_2O_3 and V_2O_3 in three samples; C) Negative trend Cr_2O_3+MgO vs. FeO+ TiO_2; d) distinct groupings of Cr_2O_3+MgO vs Al_2O_3. See text for explanations. All data as wt.% oxide.*

A negative trend can be noticed between Cr_2O_3 + MgO and FeO + TiO_2 and a weak positive trend exists between Cr_2O_3 + MgO and Al_2O_3. Both these trends will be evaluated in discussing the genesis of Ti-magnetite in chapter "Discussions".

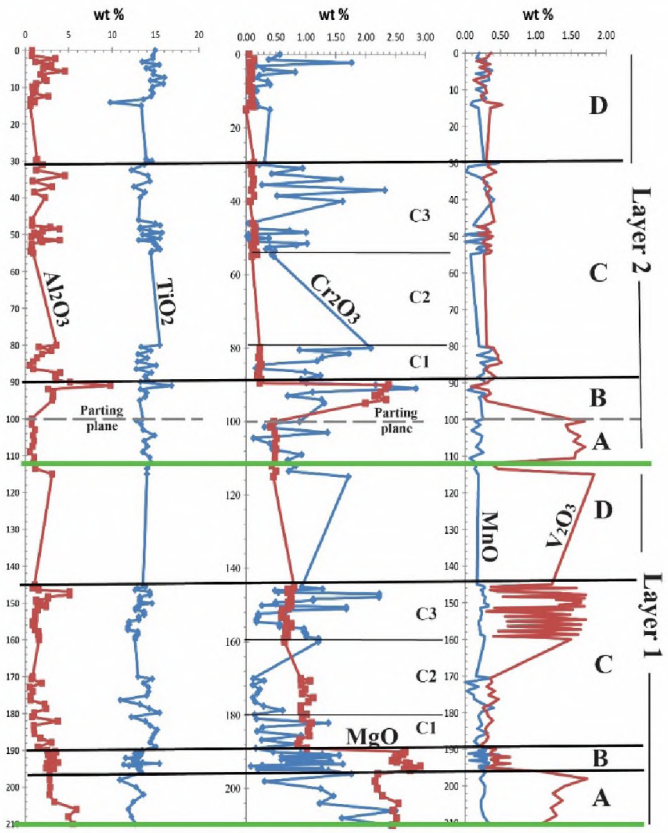

***Figure 42**: Compositional profiles in magnetite (for Cr, Mg, Ti, V) with depth (in centimeters) for MML at Magnet Heights.*

Analyzing the variation of Ti-magnetite composition with depth (Figure 42), few reversals of Cr_2O_3, MgO, Al_2O_3, V_2O_3, and TiO_2 are evident. Based on chemical variation, the MML at Magnet Heights can be separated into two layers, 1 and 2, each having four sublayers (A, B, C and D) (Figure 42). The two layers 1 and 2 can be seen as equivalents of layers MAG 3 and MAG 4, respectively, from the MML in the Northern Lobe. The layer 1 at the base of the MML, shows from bottom to top: sublayer A, defined by a peak of V_2O_3 at the base, immediately followed by sublayer B, recognized by positive peaks of Cr_2O_3 and MgO, overlain by sublayer C with peaks of Cr_2O_3 and Al_2O_3, where V_2O_3 also manifests a positive variation, followed by sublayer D, defined by constant or small positive variation of Cr_2O_3 which ends with a positive spike of Cr_2O_3. Exactly the same succession of sublayers ABCD can be observed in layer 2, above. It is to be noted that the parting plane does not separate the two layers, but it is included in layer 2. Here, in layer 2, it can be noted that just below the parting plane there is a spike in V_2O_3 (sublayer A), followed by a peak correlation of Cr_2O_3 and MgO (sublayer B; here Al_2O_3 also seems to correlate), then to the middle of the layer 2,

the peaks of Cr_2O_3 and Al_2O_3 (sublayer C), and above a zone of almost constant Cr_2O_3, an top with a positive Cr_2O_3 peak (sublayer D). The significance of the reversals and the sub-layers ABCD will be discussed in the "Discussion"chapter.

Ilmenite. The composition of ilmenite from MML at Magnet Heights is presented in Table 8 and Appendix 1, Table B2. The MgO content is 0.97-1.81 % at the base of MML and increases quickly to 4-8-5.2 % in the middle of MML (sample MH7), then stays constant at ~ 4.7-4.9 % up to the top of MML. Basically, there are few reversals which can be noticed in Figure 41. The MnO content also varies across the sampled stratigraphic column from 0.15 to 0.61 (Table 8), showing few reversals.

Table 8: Composition of ilmenite in MML at Magnet Heights, Northern Lobe. Oxide data as wt.%. Total Fe as FeO.

	Oxides (wt%)								Cations normalized to 3 Oxygen atoms							
Analysis	SiO2	TiO2	Al2O3	Cr2O3	FeO	MnO	MgO	Total	Si	Ti	Al	Cr	Fe2+	Mn	Mg	Total
MH2_ilm2	0.10	53.72	0.02	0.08	44.97	0.44	0.97	100.31	0.002	1.005	0.001	0.002	0.936	0.009	0.036	1.991
MH2_ilm4	0.34	52.94	0.23	0.04	43.09	0.49	1.81	98.95	0.009	0.996	0.007	0.001	0.901	0.010	0.068	1.992
MH7_ilm1	0.07	53.15	0.17	0.02	41.50	0.41	4.94	100.26	0.002	0.976	0.005	0.000	0.848	0.008	0.180	2.019
MH7_ilm2	0.00	53.93	0.06	0.00	40.78	0.32	4.88	99.98	0.000	0.990	0.002	0.000	0.832	0.007	0.178	2.009
MH7_ilm4	0.03	54.45	0.03	0.03	39.50	0.46	5.05	99.54	0.001	0.999	0.001	0.001	0.806	0.009	0.183	2.000
MH7_ilm5	0.02	54.88	0.03	0.00	40.22	0.43	5.01	100.59	0.000	0.998	0.001	0.000	0.813	0.009	0.181	2.001
MH7_ilm6	0.01	54.53	0.03	0.00	41.27	0.38	5.12	101.34	0.000	0.988	0.001	0.000	0.831	0.008	0.184	2.012
MH8 _ilm1_1	0.03	54.00	0.04	0.04	40.15	0.61	4.97	99.84	0.001	0.991	0.001	0.001	0.819	0.013	0.181	2.007
MH8 _ilm1_2	0.00	53.64	0.05	0.00	41.22	0.41	4.87	100.19	0.000	0.985	0.001	0.000	0.842	0.008	0.177	2.014
MH8 _ilm1_3	0.04	54.15	0.02	0.01	40.66	0.56	5.09	100.53	0.001	0.988	0.001	0.000	0.825	0.012	0.184	2.010
MH8 _ilm2_1	0.13	54.36	0.08	0.01	40.42	0.38	4.42	99.78	0.003	0.998	0.002	0.000	0.825	0.008	0.161	1.998
MH8 _ilm2_2	0.02	53.81	0.06	0.03	41.61	0.32	5.06	100.90	0.000	0.981	0.002	0.001	0.844	0.007	0.183	2.017
MH8 _ilm2_3	0.00	54.76	0.02	0.04	39.52	0.22	5.23	99.79	0.000	1.001	0.001	0.001	0.803	0.004	0.189	1.999
MH10 _ilm1	0.00	54.75	0.02	0.00	39.42	0.50	4.79	99.47	0.000	1.005	0.001	0.000	0.805	0.010	0.174	1.995
MH10 _ilm1	0.02	54.25	0.03	0.02	39.25	0.28	4.97	98.81	0.000	1.002	0.001	0.000	0.806	0.006	0.182	1.997
MH10 _ilm1	0.00	54.29	0.04	0.02	39.68	0.15	4.84	99.01	0.000	1.002	0.001	0.000	0.814	0.003	0.177	1.997
MH10 _ilm1	0.04	54.58	0.04	0.01	39.66	0.36	4.77	99.46	0.001	1.002	0.001	0.000	0.810	0.007	0.174	1.996
MH10 _ilm1	0.00	54.45	0.02	0.00	40.40	0.32	4.77	99.96	0.000	0.998	0.000	0.000	0.823	0.007	0.173	2.002

4.2.2.2. Silicates

The silicates within the MML at Magnet Heights (Samples MH1-MH10) are rare, small and completely chlortitized, as was shown in the petrography chapter. Based on optical observation and chemical analyses, the chlorite is clinochlore and rare chamosite (Appendix 1, Table B3), similar to the chlorite observed in the MML of the Northern Lobe.

At Magnet Heights, above the MML and in between the third and the fourth layer of magnetite, a magnetite-anorthosite was sampled. The plagioclase here has a composition of An_{57-58} but some grains preserve cores with An_{75} (Appendix 1, Table B4). The orthopyroxene is En_{57-58} (Appendix 1, Table B5)

4.2.2.3. Sulphides

Rare sulphides in MML at Magnet Heights proved to be galena and bornite (WDS qualitative analyses in sample MH4, not shown here). However, secondary pyrite appears to have grown on parting planes, now, most of it being almost totally limonitized.

4.2.3. Western Lobe

4.2.3.1. Oxides

Ti-magnetite. The composition of Ti-magnetite in the samples of MML from Rhovan mine are presented in Table 9 (average values), and in Appendix 1, Tables C1, C2, and C3. The TiO_2 decreases from averages of 14.77 ± 4.07 wt% to 11.86 ± 3.12% while Cr_2O_3 and MgO very variable but generally decreasing downwards. Cr_2O_3, Al_2O_3, and MnO have the tendency to decrease downwards, while Fe_2O_3 increases upwards. The V_2O_3 remains constant over the three analyzed samples.

Table 9: Composition of Ti-magnetite in MML of the W lobe at Rhovan mine. Oxide data as wt.%; The FeO and Fe_2O_3 are calculated values. The EPMA analyses of Ti-magnetite were normalized to 4 Oxygen atoms (not shown in Table 1). The total FeO wt.% measured by the microprobe was split up into $FeO_{calculated}$ and $Fe_2O_{3\ calculated}$, (both in wt.%) as follows: the $FeO_{calculated}$ was reiteratively changed until two conditions were fulfilled: a) the total cations to sum to 3.00 and b) $Fe_2O_{3calculated} = (FeO_{measured} - FeO_{calculated})*1.1$.

Sample (Depth)	0-10		50-60B		70-80	
Oxides	Average	*StDev*	Average	*StDev*	Average	*StDev*
SiO_2	0.49	*0.53*	0.53	*0.37*	0.56	*0.35*
Al_2O_3	1.66	*0.96*	1.05	*0.89*	0.68	*0.23*
TiO_2	14.77	*4.07*	13.51	*2.83*	11.86	*3.12*
Cr_2O_3	0.70	*0.02*	0.40	*0.19*	0.32	*0.06*
MnO	0.19	*0.11*	0.13	*0.08*	0.09	*0.08*
FeO	46.24	*4.00*	45.27	*2.52*	41.44	*10.93*
Fe_2O_3	33.75	*8.43*	37.20	*6.09*	37.43	*9.97*
MgO	0.24	*0.26*	0.07	*0.06*	0.11	*0.13*
CaO	0.02	*0.01*	0.02	*0.02*	0.01	*0.01*
V_2O_3	1.22	*0.28*	1.27	*0.22*	1.22	*0.33*
ZnO	0.03	*0.03*	0.05	*0.05*	0.04	*0.04*
Total	99.31	*1.36*	99.49	*1.17*	92.95	*25.41*

The Cr_2O_3 values show discrete values in two different samples (Figure 43A), suggesting processes related to the history of magma crystallization. In the same way, the negative correlation between TiO_2 and ($FeO+ Fe_2O_3$) (Figure 43 B) must have a genetic link. Even the MnO is relatively high, it

does not show any correlation with TiO_2, a fact which contrasts with the MML from the Northern Lobe (Figure 43 C). A strong negative correlation exists between V_2O_3 + TiO_2 and FeO + Fe_2O_3 (Figure 43 D). The V_2O_3 values are small compared to TiO_2, therefore the TiO_2 controls this correlation, which might have a crystallographic and genetic significance which will be discussed in the next chapter.

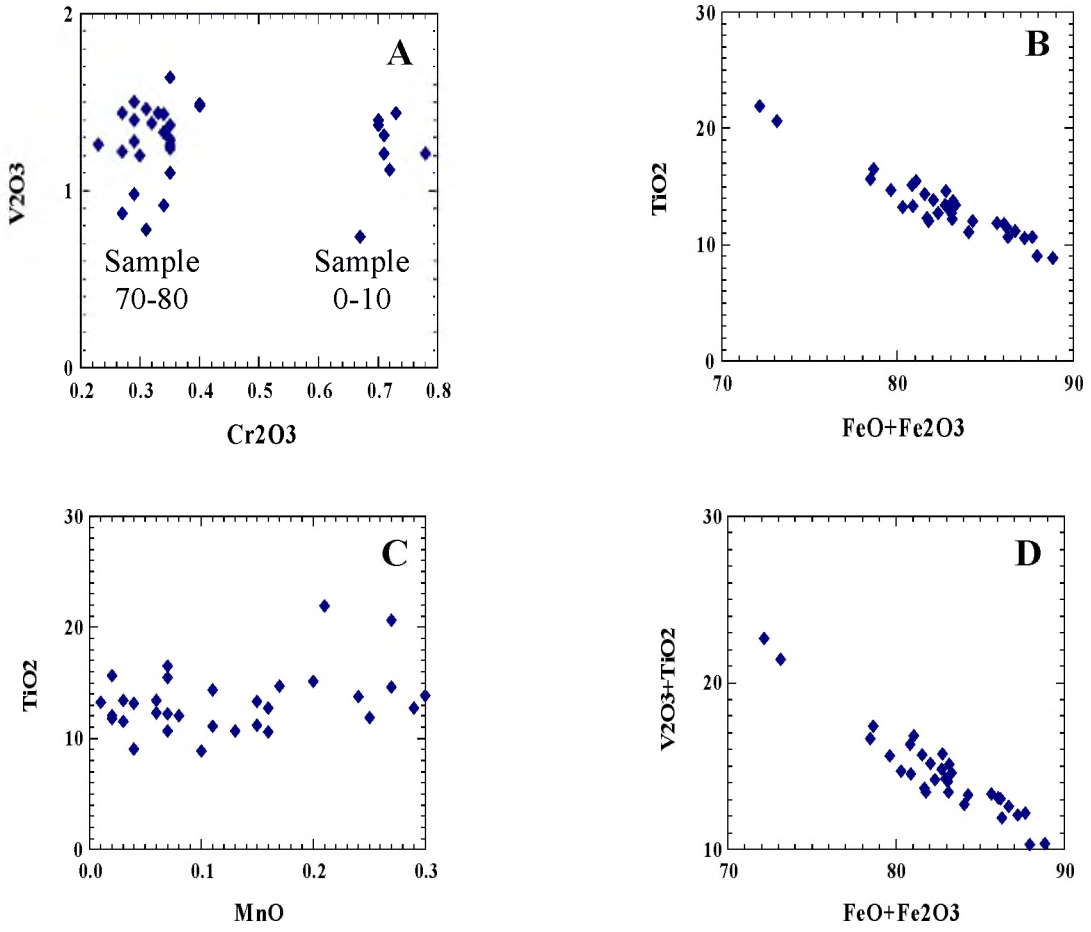

***Figure 43**: Compositional variation in Ti-magnetite of MML, Western Lobe. A) Discrete Cr_2O_3 wt.% in two different samples; B) Negative correlation between TiO_2 vs. FeO+ Fe_2O_3; C) No correlation between TiO2 vs. MnO; D) Strong negative correlation between V_2O_3+TiO2 and FeO+ Fe_2O_3 (see text for details). All oxides plotted as wt.%.*

Ilmenite. The composition of ilmenite in Rhovan mine samples are shown in Appendix 1, Table C4. The MgO content of ilmenite is 3.9 to 4.5 wt.%, while MnO can be as high as 0.60 wt%.

4.2.3.2. Silicates

The igneous silicates associated with Ti-magnetite in the MML are totally chloritized. The chlorite analyses are showed in Table 10, mostly showing clinochlore compositions (low FeO values and SiO_2 around or above 30%) and rare chamosite (high FeO and SiO_2 between 20-30%).

Table 10: Composition of chlorite formed on igneous silicates, MML, Western Lobe - Rhovan mine

Comment	SiO_2	TiO_2	Al_2O_3	Cr_2O_3	FeO	MnO	MgO	CaO	Na_2O	K_2O	Total
50-60B_1	31.03	0.04	37.25	0.26	19.62	0.04	0.82	0.09	0.04	0.02	89.21
50-60B_2	30.87	0.04	34.49	0.28	11.11	0.00	1.40	0.08	0.00	0.02	78.34
50-60B_3	21.68	0.02	32.70	0.21	26.79	0.01	0.96	0.08	0.02	0.00	82.48
0-10_1	42.13	0.00	30.12	0.06	2.33	0.00	1.56	0.42	0.07	0.03	76.94
0-10_2	38.73	0.04	27.52	0.00	2.21	0.01	1.42	0.39	0.02	0.03	70.47
0-10_3	19.73	0.03	10.90	0.01	2.80	0.00	4.26	0.38	0.03	0.01	38.56
0-10_4	29.13	0.04	25.96	0.03	5.30	0.01	10.57	0.23	0.03	0.00	71.50
0-10_5	29.33	0.00	27.93	0.02	7.45	0.00	16.70	0.29	0.02	0.02	81.82
0-10_6	25.77	0.32	18.03	0.01	5.86	0.01	5.83	0.25	0.04	0.01	56.32
0-10_7	29.09	0.02	24.87	0.03	7.24	0.02	11.03	0.37	0.04	0.04	72.94
0-10_8	33.28	0.00	25.89	0.02	6.77	0.02	8.67	0.29	0.01	0.00	75.03

4.2.3.3. Sulphides

No fresh sulphide was encountered in the three analysed samples from Rhovan mine.

4.3. Parental magma to magnetite-anorthosite layers: thermodynamic modelling using MELTS algorithms

In an attempt to understand the possible magma composition for the Upper Zone, as well as the rocks which can be derived from it by fractional crystallization, a simple MELTS exercise was performed. The starting magma composition was chosen to be the parent magma proposed by Tegner et al. (2006), page 2268, Table 4, column 6, as "calculated composition of melt at Pyroxenite Marker" (anhydrous):

SiO_2	TiO_2	Al_2O_3	Fe_2O_3*	FeO	MnO	MgO	CaO	Na_2O	K_2O	P_2O_5
51.43	1.00	16.61	8.32	4.23	0.10	4.60	9.71	2.90	0.70	0.40

**Fe_2O_3 was calculated using the alphaMELTS run at FMQ oxygen buffer at super-liquidus condition.*

The alphaMELTS calculation were done in isobaric conditions, at P=2 kbar and at oxygen buffer conditions of Hematite-Magnetite (Figure 44 and Electronic Appendix E1), Fayalite-Magnetite-Quartz FMQ (Electronic appendix E1) and FMQ + 2 (Figure 44 and electronic appendix E1).

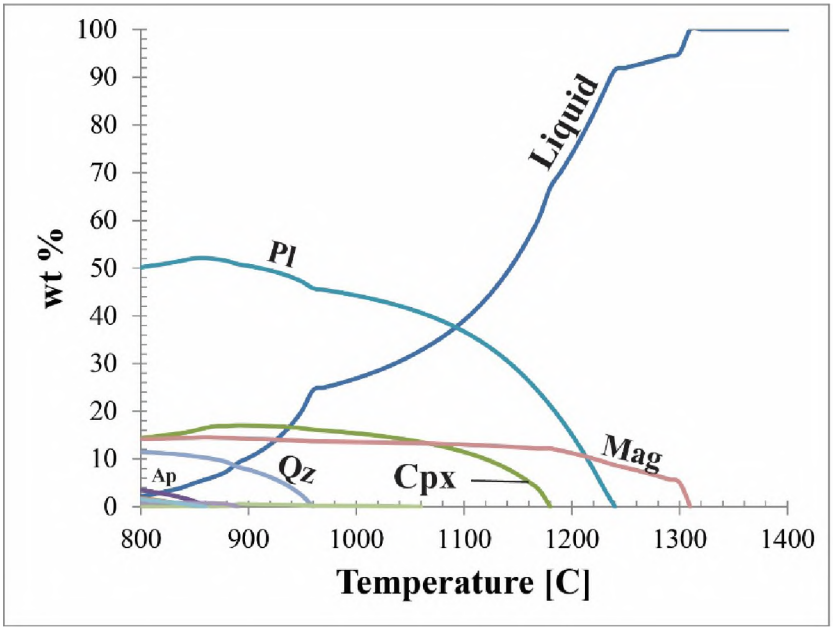

***Figure 44**: Phase proportions during isobaric crystallization at P=2 kbar calculated parental magma of the Upper Zone from Tegner et al. (2006). Oxygen buffer Hematite-Magnetite (**HM**).*

Calculated magnetite is richer in MgO (10-16%) than the measured one (Appendix 1, Table D1), suggesting that the parent magma should be significantly poorer in Mg than the melt proposed by Tegner et al. (2006). The calculations show that the first plagioclase (An_{75}) forms at T=1280 C. Its composition continuously changes with decreasing temperature (e.g. An_{48} at T=1000 C). The calculated clinopyroxene is extremely rich in Fe_2O_3 (6-10%) compared to the measured clinopyroxene (0.1-1.5%). This observation points out that the oxygen fugacity during the formation

of magnetite and clinopyroxene might not have been as high as the Hematite-Magnetite buffer. However, the HM oxygen buffer can produce magnetite on the liquidus in the interval 1300-1240 °C for the considered initial composition, and such, magnetitite layers can form without involving fractional crystallization.

At Fayalite-Magnetite-Quartz plus two log units (FMQ+2) oxygen buffer conditions, magnetite appears at T~ 1125 °C, well after (below) plagioclase and clinopyroxene (Figure 45). It is to be noted that for different temperature intervals, various rocks can form, wherein magnetitite layers would form at lower temperatures than anorthosites or leucogabbros. In these conditions, fractional crystallization is needed to account for almost monomineralic magnetitite layers.

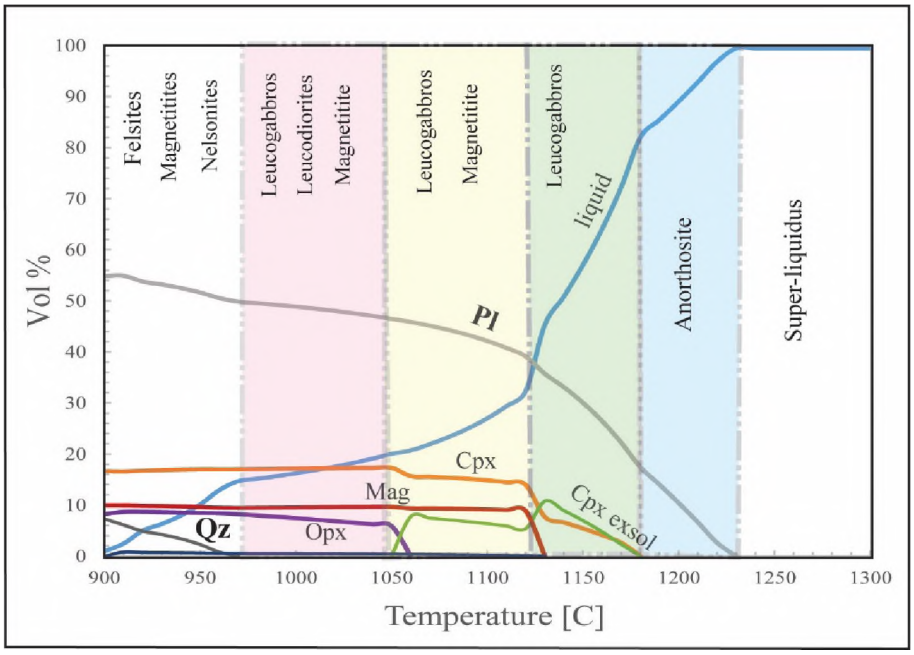

***Figure 45**: Phase proportions during isobaric crystallization at P=2 kbar calculated parental magma of the Upper Zone from Tegner et al. (2006). Oxygen buffer Fayalite-Magnetite-Quartz plus 2 log units (**FMQ+2**).*

5. Discussion

5.1. Textural differences and typology of inclusions of the MML in the three lobes

The MML in the Eastern and Western Lobes is massive, with fewer silicate inclusions than the MML in the Northern Lobe (see Table 11 for synoptic comparison of the MML in the N, E and W lobes). The MML in the Eastern and Western Lobes include mostly small, chloritized, anhedral pyroxenes, while the MML in the Northern Lobe includes mostly bigger, altered and fresh, subhedral plagioclase. The inclusions often show higher frequencies of abundance within discrete horizons, a feature which is more obvious in the MML of the Northern Lobe and can suggest some sort of flow differentiation of the magma. All silicates present inside the MML in all three studied lobes are highly affected by secondary, post-crystallization low-temperature hydrous transformations (chlorite + epidote + pyrite).

Table 11: Synoptic comparative table on the MML from the Norther, Eastern, and Western Lobes.

Lobe	**Northern**	**Eastern**	**Western**
Number of magnetite layers	2 layers (MAG3 and MAG4)	2 layers, each with sublayers A,B,$C_{1,2,3}$,D	2 layers
Structure	Anastomosed thin and heterogeneous sub-layers	massive	massive
Floor/top of the MML layers and sublayers	Undulose floors and tops	Planar floor and top	Planar to slightly undulose floor and top
Modal abundance of silicate inclusions	high	poor	poor
Dominant silicate inclusion	plagioclase	pyroxene	pyroxene
Relative size of silicate inclusions	big	small	small
Shape of silicate inclusion	subhedral	anhedral	anhedral
Magnetite included in silicates	rare	none	none
Sulphides associated with Ti-Mag	common	rare	rare
Frequency of ilmenite grains	high	high	high
Relative size of ilmenite grains	small	big	big
Exsolution in Ti-magnetite	Common (patchy, heterogeneous)	common	common
Presence of Olivine reaction corona (Fo72) at distinct depths inside the MML	Yes	No	No

The MML in the Western and Eastern Lobes is made of two distinct layers, being separated by a parting plane, or a thin magnetite bearing anorthosite layer, or being distinctive based on cryptic chemical reversals. Each layer of the MML in the Eastern Lobe at Magnet Heights is made of cycles containing various chemical reversals (sublayers A, B, C_1, C_2, C_3, D). The MML in the Northern Lobe is also formed by two main layers (identified herein as being equivalent to MAG3 and MAG4; see public Bushveld Minerals Report, 2013). However, here the magnetite-rich layers are more heterogeneous and made of imbricated (or not) thin and massive layers of magnetitite and plagioclase-rich layers. The MAG 3 and MAG 4 layers are separated by a 3-4 m thick magnetite bearing ferro-gabbro (note: the difference between a magnetite-bearing anorthosite and a ferro-gabbro is that the latter contains more modal clinopyroxene).

The MML in the Northern Lobe is not massive but is rather made of thicker, alternating and anastomosed thin (centimeter scale) magnetite-rich and silicate (plagioclase or plagioclase + clinopyroxene + magnetite)-rich layers. Peculiar to the MML of the Northern Lobe are the small (1 mm in size or smaller) inclusions of magnetite in plagioclase, inclusions which are transformed into a fine (sub-micron sized intergrowths) aggregate of oxides, chlorite (chamosite) and sulphides. This feature was not encountered in the MML of the Eastern and Western Lobes.

It is to be noted that the MML in the Eastern and Western Lobes contains coarser (mm size) ilmenite crystals, compared to the fine ilmenite grains in the MML of the Northern Lobe.

The ulvöspinel ($TiFe_2O_4$) and (Al)-spinel exsolutions (lamellae of ulvöspinel and Al-spinel and droplets of Al-spinel) in magnetite are common in the MML of all three lobes. However, it is to be noted that the exsolutions in the MML of the Northern Lobe have a patchy character and seems denser and thinner compared to the exsolution lamellae in Ti-magnetite from the MML of the Western and Eastern Lobes. In the Eastern and Western Lobe, the silicate inclusions in magnetite show a small area around them where the Ti-magnetite is depleted in exsolutions. No clear ilmenite exsolution was measured in the MML, and no connection between an ilmenite exsolution in magnetite and a discrete ilmenite grain was found. This is an important difference when comparing the MML in the Bushveld Complex with Ti-magnetite layers from other basic layered intrusions (such as the Panzhihua mafic layered intrusion in China; Howarth and Prevec, 2013; Howarth et al.,

2013). However, this feature can be present in other magnetite layers higher up in the sequence of the Upper Zone of the Bushveld Complex (e.g. Von Gruenewaldt et al., 1985).

The presence of olivine (Fo_{72}) inside the MML is restricted to the MML of the Northern Lobe, at distinct depths (129.83 and 129.97 m, borehole VK5). It appears as a reaction corona around orthopyroxene which is included in magnetite, but not around the plagioclase. It is not to be confused with cumulus (fayalitic) olivine which appears higher up in the sequence of the Upper Zone.

Sulphides grains seem to be bigger in size and more abundant in the MML of the Northern Lobe, compared to the sulphides in the MML of the Eastern and Western Lobes.

5.2. Crystallisation history

Textural observations of the MML in all three lobes show that the massive magnetitite layers always contain various proportions of igneous silicates and sulphides (even altered), with discrete intervals where the abundances of inclusions varies stratigraphically.

The silicate inclusions in Ti-magnetite are usually anhedral (E and W lobes) or subhedral (N-lobe) and don't have a corona or reaction rim towards the Ti-magnetitite host, with few notable exceptions. The massive magnetitite in the MML from the Western Lobe seems to contain less silicate (and sulphide) inclusions, in contrast to the MML from the Northern Lobe. No magnetite inclusions were noticed in the silicates included in Ti-magnetitite host rocks. This simple observation clearly suggests that magnetite was not the first mineral to crystallize and it was not an early liquidus phase. More than that, in several instances, the magnetite seems to "digest" the included silicate phases. In adjacent Ti-magnetite-rich layers, the Ti-magnetite and ilmenite are to be found in the interstitial spaces between igneous silicates. These textural observations are compatible with the interpretation that the oxides formed after the igneous silicates. From the igneous silicates included or spatially associated with the oxides, the plagioclase is more frequent than orthopyroxene or clinopyroxene. Secondary minerals (oxides, silicates, and carbonates) are somewhat different in the three lobes, suggesting differences in cooling history but also in sub-solidus transformations which affected MML.

5.2.1. Northern Lobe

The oxides (Ti-magnetite and ilmenite grains) together with included plagioclase and pyroxenes are primary, igneous phases. The exsolution lamellae of spinel and ulvöspinel that occur in Ti-magnetite are to be considered secondary phases, produced during cooling of Ti-magnetite. Rare rutile found in Ti-magnetite is also a secondary mineral, developed on former Ti-rich silicate, and associated with calcite. Secondary minerals can be divided into two categories: a) high-temperature secondary minerals and b) low-temperature secondary minerals. The high-temperature secondary minerals consist of olivine reaction coronas on orthopyroxene, rare amphibole coronas on plagioclase, and clinopyroxene (or zoisite) and plagioclase symplectites developed on igneous plagioclase. Rare olivine grains which occur within Ti-magnetite show usually a polygranular texture and represent a total (pseudomorphic) replacement of orthopyroxene by olivine. The spatial relationship between the coronitic olivine and the radiating symplectites developed on igneous plagioclase points towards a reaction where a fluid phase may have been involved. The incongruent melting of orthopyroxene to produce olivine and the SiO_2-rich melt is probably the easiest way to explain the olivine corona. The simple textbook reaction for Mg-endmembers is 2 Enstatite → Forsterite + SiO_2 (liquid):

$$2MgSiO_3 \rightarrow Mg_2SiO_4 + (SiO_2)_{liquid}$$

Chemically, the reaction involving orthopyroxene solid solution should be more complex since it requires: a) to conserve the Mg# (molar $Mg/(Mg+Fe^{2+})$) of mafic phases and b) to have other chemical components from orthopyroxene (Al_2O_3, CaO, etc) transferred into the melt. Besides these components, the liquid resulted by melting of orthopyroxene should be richer in SiO_2 based on the above mentioned reaction. The CaO in orthopyroxene is ~1.15 wt.% in the core, then it reaches 3 to 5 wt.% near the rim, and turns to 0.7-0.9 wt.% at the very rim. The CaO in olivine is 0.03 wt.%, only. These values clearly suggest that Ca (as well as Al) from the orthopyroxene was moved into a fluid phase (melt). From the EPMA measurement, the Mg# of olivine is 69 in the core of the reaction band and 72 at the rim, near magnetite, while the orthopyroxene has a Mg# of 70. It can be observed that: 1) the Mg# does not really change from the reactant (orthopyroxene) to the reaction product (olivine) and 2) near the contact with magnetite, the olivine becomes slightly richer in Mg. This is an as strong argument for a genesis of olivine based on the breakdown of orthopyroxene. At a first glance, the higher Mg and lower Fe of olivine at the contact with magnetite contact can be regarded as odd. However, the explanation is given by the subsolidus Mg-Fe exchange in between

olivine and Ti-magnetite during cooling. It is known that during cooling the Fe^{2+} partitions into the spinel mineral and the Mg into the neighbouring olivine, this being part of the fundamental basis for olivine-spinel (and orthopyroxene-spinel) thermometry in basic and ultrabasic rocks (e.g. Engi, 1983; Fabries, 1979; Liermann and Ganguli, 2002). The resulting melt should be rich(er) in SiO_2, and should also carry Al_2O_3, CaO, and MnO derived from orthopyroxene. The problem with this interpretation is that olivine occurs only at the contact between orthopyroxene and Ti-magnetite, and does not affect all the orthopyroxene (e.g. the orthopyroxene in contact with plagioclase). More than that, there is no evident chemical variation in the rim of Ti-magnetite which is in contact with the olivine reaction band. It is thus possible that this reaction of incongruent melting of orthopyroxene should be somehow controlled by the presence of an orthopyroxene-Ti-magnetite boundary. The discontinuous development of the olivine corona might raise doubts as to the existence of a fluid phase. However, the development of radiating Cpx-Pl symplectites in igneous plagioclase starting from the proximity of olivine towards the interior of the plagioclase grain is also an indicator of a reaction involving a high temperature fluid phase, a reaction which possible had the tendency to chemically balance a dense fluid phase (melt derived from breakdown of orthopyroxene?) and the solid igneous plagioclase. The development of symplectites shows that the diffusion rate was significantly higher that the growth rate, which is a typical situation for the existence of a fluid phase enhancing diffusion. The orientation of symplectites inside the igneous plagioclase shows the direction and sense of the thermal flux and mass transport (e.g. Putnis and Austrheim, 2010).

Another secondary coronitic texture is represented by rare pargasitic amphibole developed at a different level in MML from the Northern Lobe. It develops only between Ti-magnetite host and plagioclase. It suggests a late coronitic reaction involving a metamorphic or a late magmatic fluid or a reaction with a wet melt, from which amphibole crystallized. These coronas are usually thin and continuously developed around plagioclase included in Ti-magnetite. However, these textures are restricted to thin and discontinuous layers in MML, suggesting a local subsolidus reaction or a reaction between Ti-magnetite and an H_2O-rich residual fluid, rather than a larger scale reaction of the Ti-magnetite with a melt. The presence of secondary sulphides spatially related to these textures can also support the interpretation of a fluid-assisted reaction between Ti-magnetite and plagioclase.

A peculiar texture is present at depth 105 m in borehole VL5. Small opaque minerals totally included in chloritized plagioclase show (at high magnification in BSE images, only; Figure 11F) a

very fine and porous mixture between an oxide and a silicate. Micron-scale sulphides are also present within these grains. The average EPMA analyses show a mixture between Ti-magnetite, ilmenite, chamosite and Fe- and Fe-Cu sulphides. Interestingly, the V_2O_3 content in these textures is slightly higher (~ 1.8-1.9 wt %) than in the neighboring fresh Ti-magnetite. It is very probable that the lower temperature fluid responsible for the chloritization of plagioclase was also responsible for the alteration of the small Ti-magnetite (and ilmenite) inclusions in plagioclase. The presence of small Fe-Cu-bearing sulphides (probably chalcopyrite) is an evidence of this link between the texture and late- or post-magmatic processes.

The sulphides show a close relationship with Ti-magnetite. In most of the cases, the sulphides (pyrrhotite and chalcopyrite, and less frequently pyrite) appear to grow near magnetite, and very rare fine-grained sulphides (pyrrhotite and chalcopyrite) are included in magnetite. This observation can suggest that while a small amount of sulphide could have crystallized before magnetite and ilmenite, the majority of the igneous sulphides grew after the magnetite, probably using the oxide crystals as sites for nucleation. Significant pyrite and rare characteristic hydrothermal sulphides such as millerite and siegenite have developed around or near (at the exterior) of the igneous sulphides, suggesting that they have crystallized from a later fluid.

5.2.2. Eastern lobe

The MML in the Eastern Lobe (at Magnet Heights) is a massive 2 m thick layer, compared to the MML in the Northern Lobe which seems more anastomosed and heterogeneous. At Magnet Heights the Ti-magnetite and associated ilmenite include small crystals of totally chloritized igneous silicates. The habit of the altered silicates suggests that pyroxene rather than plagioclase was more abundant as inclusions in magnetite. However, the igneous silicates are present as rarer, smaller and more anhedral crystals compared to the silicate inclusions in MML of the Northern Lobe. The fact that the Ti-magnetite grains are evidently annealed makes it difficult to establish which phases crystallized first, the silicates or the oxides. If the silicates had been the first to crystallize, one would expect euhedral to subhedral habits of the grains, rather than anhedral. However, the anhedral habit of the silicates could be used to infer that 1) they were anhedral prior to their incorporation by crystallizing magnetite (pre-existing silicates in the magma chamber), or 2) they were in disequilibrium with the magma from which magnetite crystallized, and consequently were partially

digested or 3) the grains have all experienced subsolidus recrystallization, destroying any primary provenance information. The secondary minerals replacing igneous silicates are represented by chlorite, epidote, and rare calcite. Chlorite also develops along small but penetrative fractures within the massive magnetite, supporting the interpretation that it could have precipitated from a late deuteric fluid which circulated the rock during cooling and contraction of the MML.

The exsolution in Ti-magnetite seem to be less abundant in the MML of the Eastern lobe, compared to the MML in Northern and Western lobes. The fact that the area around silicate inclusions in magnetite is depleted in exsolution lamellae can suggest that later processes affected the Ti-magnetite, removing or healing the exsolutions. Such a process can be represented by local heating of MML. Late, secondary, low temperature processes also affected the MML, where the effects are represented by extensive chloritization of the silicate inclusions in magnetite (but not of the silicates outside the MML), as well as the development of secondary sulphides (mostly pyrite) on limonitized parting planes in MML, or even on fractures which cross-cut the layering, being visible especially in cross section where the sulphides were transformed to limonite by weathering.

5.2.3. Western Lobe

The MML in the Western lobe shows significantly larger individual grains of Ti-magnetite and ilmenite compared to the MML in either the Northern or Eastern Lobes. The silicates in the MML are totally chloritized and anhedral. They can be found as inclusions in Ti-magnetite and in between individual grains of Ti-magnetite. These observations suggest that some silicates crystallized before the massive crystallization of oxides and that they were partially digested by the melt to be included in Ti-magnetite as anhedral grains. The observations are not compatible with the idea that both Ti-magnetite and these silicates (plagioclase or pyroxene) crystallized together as cotectic phases in equilibrium with one another. If this had been the case, the textures would have been similar to those in the magnetite anorthosite layers or ferro-gabbros below or above the MML, where Ti-magnetite and plagioclase are intercalated and partially include one another, showing that they crystallized together. The plagioclase is these latter cases is subhedral and has escaped chloritization, features which are not common in the MML. The observations rather suggest an accumulation of magnetite crystals, with rare silicates arrested as inclusions or in between oxide grains.

Compared to the MML in the other lobes, the sulphides are less abundant in the MML of the Western Lobe.

5.3. Comparison between the mineral chemistry of MML in Northern, Eastern, and Western Lobes

The compositional ranges of minerals in the Main Magnetite Layer (MML) from the Northern, Western and Eastern lobes of the Bushveld Complex show no clear correlations between Cr_2O_3 and TiO_2 (Figure 46 A) or with V_2O_3 (Figure 46 C). However, it is evident that Cr_2O_3 in the MML of the Eastern and Western lobes has different values in individual samples (all taken from different depths) from MML of the same lobe (Figure 46 A and C), suggesting the existence of Cr_2O_3 variation with depth. In the Eastern Lobe, one sees relatively restricted compositional ranges of TiO_2 (~10-15 wt%) and V_2O_3 (<0.5 wt%), but larger variations in the Western and Northern Lobes, from ca.7-23 wt.% TiO_2 and 0.75 to 2 wt.% V_2O_3 (Figure 46 B); a notable difference is the fact that V_2O_3 is much lower in the E lobe compared to N and W lobes (Figure 46 B). The upper part of the MML in the W and N lobes contains the highest TiO_2 (~20 wt%) where V_2O_3 (0.7-2.0). A negative trend can be noticed in between V_2O_3 and TiO_2 in the W- and E limbs, only. In the E-limb, some samples of the MML contain significantly higher Cr. A clear positive correlation between TiO_2 and MnO was observed in the Northern lobe, only. Here, the Mg, Mn, and Zn have higher values than in the E and W lobes. TiO_2 variation is large in N and W limb from 8 to 20 wt% but restricted in E limb to ~12-15 wt% (Figure 46 A). The V_2O_3 variation is large in W and N-lobe (0.7-2 wt%) compared to a smaller variation in E lobe (0.2-0.6 wt%). The EPMA data on the MML from the N-lobe give oxide totals varying from 88 to 95%, where lower totals correspond to lower TiO_2 (and higher Fe_2O_3) and higher totals to higher TiO_2 (and lower Fe_2O_3). The lower totals (88-90%), can suggest the presence of γ-Fe_2O_3 (maghemite).

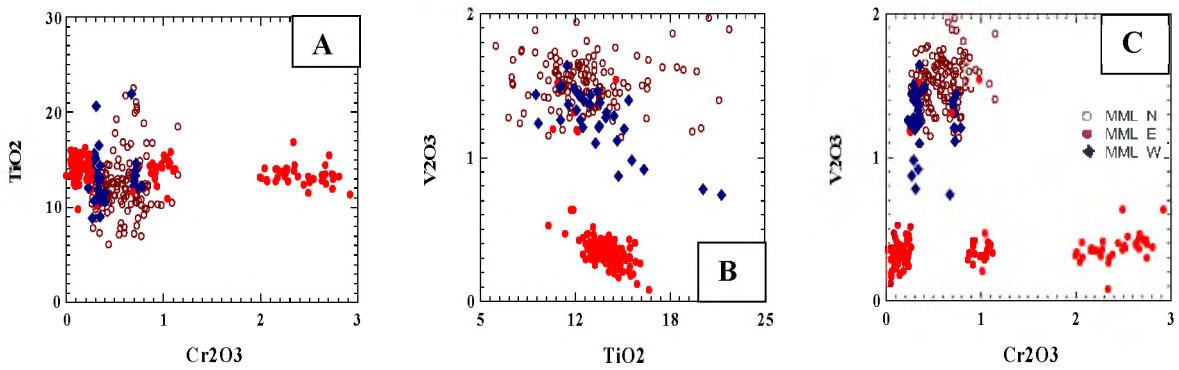

***Figure 46**: **A)** No correlation between Cr_2O_3 and TiO_2 in the three lobes. Cr_2O_3 varies across MML samples in the same lobe (e.g. E and W lobes) but it is homogenously distributed in the N limb; **B)** The highest V_2O_3 occurs in the Northern Lobe MML; V_2O_3 vs. TiO_2 are negatively correlated in Eastern and Western Lobes, but not in the Northern Lobe; **C)** No correlation is observed between V_2O_3 and Cr_2O_3 in MML of the three lobes, but at least four separate compositional clusters can be observed.*

Table 12 shows the maximum values of V_2O_3, TiO_2, Cr_2O_3, MgO, Al_2O_3 and MnO encountered in the MML analyzed samples from Northern, Eastern and Western Lobes. It is evident that the highest V_2O_3 values are found in MML of the Northern Lobe, (1.97 wt.%), while the MML in Eastern lobe at Magnet Heights doesn't exceed 0.52 wt.%. Cr_2O_3 is the highest in the MML samples of the Eastern Lobe (2.92 wt.%) and the lowest in the MML samples of the Western Lobe.

Note that other studies express the vanadium content in V_2O_5 (molecular weight = 181.88 g/mol) and not in V_2O_3 (molecular weight 149.8812 g/mol). It is considered herein that it is most useful to report the vanadium content in magnetite as V_2O_3 since vanadium is accommodated in the spinel structure mostly as V^{3+} and V^{4+} (e.g. Balane et al., 2006; Charlier et al., 2009; Toplis and Corgne, 2002), and almost none as V^{5+}. However, the mining companies, as well as other geological studies, typically report economic values expressed as V_2O_5. The conversion factor from V_2O_3 to V_2O_5 and vice-versa are given below:

V_2O_5 (wt%) = V_2O_3 (wt%) x 181.88/149.88

V_2O_3 (wt%) = V_2O_5 (wt%) x 149.88/181.88

E.g. V_2O_3 = 1.97 wt% is equivalent to 1.97 x 1.213496 = 2.3905 wt5 V_2O_5.

Table 12: Maximum values of oxides in magnetite of the MML in the N, E and W lobes

Lobe	*Highest V_2O_3*	*Highest TiO_2*	*Highest Cr_2O_3*	*Highest MgO*	*Highest Al_2O_3*	*Highest MnO*
Northern	1.97	22.49	1.09	2.92	6.13	0.43
Eastern	0.52	16.85	2.92	2.84	9.80	0.49
Western	1.64	21.95	0.78	0.69	3.85	0.69

The comparison of the maximum values of the oxides from Table 11, shows that the MML in the Northern Lobe has the highest V_2O_3 (1.97 wt.%), TiO_2 (22.49 wt.%) and MgO (2.92 wt.%), while the MML in the Eastern lobe has the highest Cr_2O_3 (2.92 wt.%) and Al_2O_3 (9.80 wt.%), but lowest V_2O_3 (0.52 wt.%). The MML in the Western Lobe is the poorest in MgO (maximum 0.69 wt%). The high TiO_2 content in magnetite is comparable in the MML of the Northern and Western lobes (22.49 and 21.95 wt%, respectively), while the MML in the Eastern Lobe has a maximum of only 16.85 wt%. The MnO is highest in the MML of the Western Lobe (0.69 wt%), while the lowest maximum value is present in the MML of the Northern Lobe (0.43 wt.%).

The highest proportions and grain size of ilmenite were found in the MML of the Eastern Lobe, where Fe^{3+}/Fe^{2+} ratios seem to be much higher than in the MML of the Western Lobe. The highest Ti content in the MML was found in the Western Lobe, while the lowest (average) TiO_2 is found in the MML of the Northern Lobe. This observation correlates with the fact that the highest proportion of ilmenite (as coarser grains but also as a higher modal proportion at thin section scale) was found in MML of the Western Lobe. However, the higher TiO_2 in Ti-magnetite also corresponds to higher proportions of ulvöspinel lamellae and lesser ilmenite exsolutions in the Ti-magnetite. These compositional and textural characteristics strongly suggest that the ilmenite crystallized from the melt and did not form by migration of exsolved ilmenite, as otherwise the Ti-magnetite would be expected to have been depleted in TiO_2. There is no another observation to suggest that the ilmenite grains in all studied MML would derive from ilmenite lamellae exsolved from Ti-magnetite. However, this scenario remains theoretically possible at least for the Northern Lobe, where TiO_2 in magnetite is lower compared to W and E lobes, and where maghemite was mentioned in the literature (e.g. Wagner, 1927) and it is also possibly indicated by our own analysis ("magnetite" analyses with totals of 88-90% and very low TiO_2). The scenario can suggest that a primitive magnetite containing ulvöspinel and Al-spinel end members in solid solution at low fO_2 exsolved ulvöspinel during cooling, which reacted with O_2, giving ilmenite lamellae (and possible maghemite) which migrated by diffusion and accumulated towards the intergranular boundaries to form individual ilmenite grains. The reaction can be:

$$2TiFe_2O_4 + 1/2O_2 \rightarrow 2FeTiO_3 + \gamma Fe_2O_3$$

Ulvöspinel Ilmenite Maghemite

A similar model was proposed by Reynolds (1978).

The composition of MML in the Northern Lobe showing a positive correlation between Cr_2O_3 + MgO vs. Al_2O_3 and a negative correlation between Cr_2O_3 + MgO vs. FeO + TiO_2, suggest a crystallization trend, where the melt becomes more evolved (richer in FeO and TiO_2) as the oxide crystallized. It also shows a crystallographic control, where Mg from the tetrahedral site of spinel-type mineral (Ti-magnetite) and Cr from the octahedral site, were substituted by Fe^{2+} and Ti, respectively, in the new magnetite formed from a more evolved melt.

Unique for the MML in the Northern Lobe is a clear positive correlation between TiO_2 and MnO (Figure 33 C). The explanation has to be related to the magma composition. If TiO_2 content of magnetite is to be correlated with a more evolved magma, then the increase of MnO is to be correlated with the assimilation of dolomite from the country rocks by the Upper Zone melts, from which Ti-magnetite derived.

The Ti-magnetite compositional variation, as well as the variation with depth of the anorthite (An) content in plagioclase (in borehole VK5), clearly suggest the existence of two discrete Ti-magnetite layers (as opposed to one interrupted one), each one marked by a decreasing and then by an increasing of An content upwards. The two layers can be probably correlated with MAG3 and MAG 4 layers, as so labelled by Bushveld Minerals Report (2013). This observation is consistent with the interpretation that MML was formed by two separate magma influxes, probably onto a diverse and complex type of floor. It has been already mentioned that the samples from the MML of the Northern Lobe are more heterogeneous and formed by thin layers of Ti-magnetite and silicates, seldom anastomosed. On the bottom of the first layer (depth 125 m), the plagioclase is fresh, subhedral and can include small crystals of magnetite, as the magnetite can include (partially or totally) the crystals of plagioclase. This clearly suggests that plagioclase and magnetite crystallized together, probably along a cotectic. This is totally different from the observations of plagioclase and magnetite from the bottom of MML in the Eastern and Western Lobes. Therefore, one possible interpretation is that on the floor of each of the two layers, the plagioclase started to crystallize together with the Ti-magnetite, and the An content in plagioclase decreased. During this process, the melt composition changed due to a small degree of assimilation of country rocks (dolomite). Thereafter, more Ca-rich silicates (plagioclase and clinopyroxene) together with the Ti-magnetite formed at the top of each layer. Within this layer, the olivine coronas on orthopyroxene are also

observed. Very probably, the assimilation of country rocks increased not only Ca and Mg (and Mn) in the melt but CO_2 and H_2O as well. The new composition of the system could have dropped the melting temperature of orthopyroxene, and the olivine formed, locally, on the expense of orthopyroxene. This process should have also produced more SiO_2 (and Al_2O_3 would be relatively depleted) in the melt, from which, at the top of the layer, a more acid plagioclase formed.

However, the depression of solidus temperature would not necessarily be significant by slightly modifying the composition of the melt, as is suggested by the lack of obvious variation in $^{87}Sr/^{86}Sr$ (e.g., Kruger, 1994; Tegner et al., 2006) which might be expected to accompany volumetrically significant carbonate assimilation. A later heating of MML as the process responsible for incongruent melting of orthopyroxene is therefore preferred.

The composition of the MML in the Eastern Lobe at Magnet Heights shows distinct clustering of C_2O_3 values for each analyzed sample, strongly suggesting the existence of Cr_2O_3 variations (reversals?) along the stratigraphic height of the MML. It is also to be noted that the samples with higher Cr_2O_3 (up to ~ 3 wt% Cr_2O_3) were found in the MML of the Eastern Lobe. Cr_2O_3 variations in MML were also reported by Cawthorn and McCarthy (1980) and McCarthy and Cawthorn (1983).

Detailed electron microprobe data along the stratigraphic height of the MML in the Eastern Lobe (composed of two layers, separated in the outcrop by a parting plane) depicts a cryptic variation with depth in each of the two layers (of ca 1 m thick). The two layers are separated by a ~5-10 cm thick magnetite + plagioclase layer (magnetite-bearing anorthosite). The electron microprobe analyses showed that each layer can be divided into four sublayers (labelled herein upwards as A, B, C and D) based on Cr, Mg, Ti, Al and V variations. Small scale reversals of the mentioned elements and the repetition of A, B, C and D sub-layers in each layer clearly suggest that the MML at Magnet Heights formed from two successive influxes of magma (indicated by elevated values of MgO), which evolved by crystallization and cooling in a similar manner, to produce the A to D variation. The influx of magma started in each layer with a high V_2O_3, relatively high MgO, but also significant Al_2O_3 (~5 wt%) and low Cr_2O_3. This observation shows that the influx of magma to form the sub-layer A was not at all a primitive magma, but an evolved one. Very probably, as shown by the numerous small silicate anhedral inclusions in Ti-magnetite, significant silicates had been already crystallized at the time of crystallizing the Ti-magnetite in sublayer A. These silicates

(e.g. pyroxenes), could have been sequestering small amounts of Cr_2O_3, resulting in a melt depleted in Cr_2O_3, but relatively rich in V_2O_3, from which Ti-magnetite and ilmenite crystallized. After crystallization of sub-layer A, the melt became gradually enriched in MgO and Cr_2O_3, being depleted in MnO, V_2O_3 or Al_2O_3, producing the sub-layer B. During the crystallization of sub-layer C, the V_2O_3 becomes relatively enriched in the melt, producing a high V_2O_3 content in magnetite at the top of it. The Cr_2O_3 and Al_2O_3 also show a positive spike at this level, suggesting that early pyroxenes and plagioclase included within Ti-magnetite reacted with the Fe-Ti-rich melt, and were partially digested, becoming highly anhedral, while Cr_2O_3, Al_2O_3 (and possibly some FeO) from the digested phases enriched the melt in these components. During these reactions at this level, the olivine coronas on pyroxene could have formed. Some late Mg-Fe ionic exchange during cooling between the Ti-magnetite and silicates is also plausible in order to explain the decreasing of MgO content in the oxide and slight MgO increase on the thin rims of silicates. The sublayer C can, in fact, be divided into three parts. The lower part (C1, Figure 42) is characterized by a significant Cr_2O_3 reversal. It starts with a positive slope showing an increase of Cr_2O_3 (or just showing variable Cr_2O_3), followed by the middle part (C2 – Figure 42) which has low Cr_2O_3 and correlates with decreasing of Al_2O_3, and the upper part (C3 – Figure 42), where the Cr_2O_3 and Al_2O_3 increase again to their maximum values, then decrease back to almost zero wt.% at the very top of the C3. This C1,2,3 succession can correlate with sublayers of different frequency of pyroxene inclusions. The C1 and C3 are relatively rich in silicate (pyroxene) inclusions, where C2 is a level where the partially digested silicate inclusions are rare. Where more digested igneous pyroxene inclusions, the Cr_2O_3 (and to a lesser extent, Al_2O_3) was partitioned into the melt from which Ti-magnetite crystallized, whereas in layers that have fewer pyroxene inclusions, the melt was not enriched in Cr_2O_3 and Al_2O_3 and hence the Ti-magnetite crystallizing out of the melt was poor in these elements.

The succession continues with low MgO and highly variable V_2O_3 in the top of sub-layer C and ends with high Cr_2O_3 in layer D.

The observed compositional patterns are compatible with the interpretation of two main Fe-Ti-rich magma influxes, containing small pre-existing crystallized silicate crystals which reacted with the melt during crystallization of Ti-magnetite and ilmenite. The relatively high MgO content of ilmenite, together with the described compositional patterns and the mineralogical observations in the MML from Magnet Heights strongly suggest that the main mineral to react with the magma was

pyroxene, rather than plagioclase. This feature contrasts with the MML in the Northern and Western Lobes.

In the Western Lobe, the MML shows discrete values of Cr_2O_3 in each analyzed sample, suggesting the existence of Cr_2O_3 reversals along the stratigraphic height of the MML. It is to be noted that V_2O_3 (and TiO_2) content is more variable compared to the MML in the Northern and Eastern Lobes, ranging from 0.7% to 1.5%. The negative correlation between V_2O_3 and TiO_2 (also present in the MML of the Eastern Lobe, but at significantly lower V_2O_3 values) strongly suggest two things: a) a crystallographic control, where Ti can be replaced by V (and vice-versa) in the octahedral site of Ti-magnetite and b) that the V_2O_3 increases with decreasing TiO_2, due to the evolution of the melt. This observation can be explained as follows: the high TiO_2 in magnetite suggests that most of Ti are incorporated in the ulvöspinel molecule of Ti-magnetite, which in turn highlights (once more) that the ilmenite grains found in these samples are not related to the exsolution of Ti from Ti-magnetite. If the increase in TiO_2 in Ti-magnetite is related to a more evolved liquid (richer in Fe and Ti), it means that the negative correlation with V suggests that the maximum V content should represent a more primitive melt, rather than a more evolved melt. In this respect, higher concentrations of V_2O_3 in magnetite can be expected in magnetitite layers with low TiO_2.

The V_2O_3 concentrations in the MML of the Western and Northern Lobes are significantly higher than in the MML of the Eastern lobe. Following the logic of the statements above, it can be inferred that the Ti-magnetite in the MML from the Eastern Lobe was formed from a more evolved (TiO_2 and FeO enriched) liquid, compared with the MML from the Northern and Western Lobes. The conclusions from Charlier et al. (2009) also support this interpretation. These authors studied the Suwalki anorthosite in Poland and found a high proportion of V^{4+} and V^{5+} ions at high fO_2, which are less partitioned into magnetite compared to V^{3+} (Toplis and Corgne, 2002). These findings can explain: a) that high fO_2 can be responsible for the relatively low V content in magnetite from Fe-Ti oxide ores and b) the vanadium in magnetite decreases significantly in more evolved cumulates, due to a decreasing fO_2 with differentiation. It is thus possible that the MLL with lower V_2O_3 contents have experienced higher oxygen fugacity and have been formed from a more evolved melt.

5.4. Genetic model of the MML

The genetic model needs to address the key question in terms of the crystallization of magnetite in the Bushveld Complex: what triggered the magnetite crystallization? Was the Fe-rich melt a product

of differentiation or a product of liquid immiscibility? Was a sudden rise of oxygen fugacity the factor triggering the magnetite crystallization? What model would accommodate our observations?

The thermodynamic calculation using MELTS algorithms suggests that for a parent magma compositions similar to that from Tegner et al., (2006), the crystallization in high oxidation conditions (HM buffer) can produce magnetite as a liquidus phase, whereas in less oxidizing conditions (FMQ+2 buffer), the silicates would crystallize before magnetite. The experimental study of Toplis and Carroll (1995) showed that at FMQ conditions, the magnetite crystallizes after silicates and before ilmenite. The thermodynamic modeling failed to reproduce the separation of two (immiscible silicate) liquids. However, keeping in mind the limitation of the thermodynamic databases which did not implement the new experiments on liquid immiscibility, it is possible this can be another reason for which no immiscibility of two liquids was observed during calculations. Recent experiments (Charlier and Grove, 2012) strongly suggest that, indeed, two liquids can separate from a basaltic (tholeiitic) liquid, but the same authors show that a melt-rich in CaO and Al_2O_3 stabilizes a single liquid and inhibits immiscibility. The high number of inclusions of plagioclase (of high anorthite content) in Ti-magnetite from the MML, together with the presence of anorthosite layers (e.g. imbrications between anorthosites and magnetite layers in the MML of the Northern Lobe) can be used to indirectly suggest that the melt from which the magnetite in MML crystallized was rich in CaO and Al_2O_3 and thus, no immiscibility can be invoked to be responsible for separation of a Fe-rich melt.

Other facts, experimentally proven, should be taken into consideration when discussing the immiscibility process as the main factor in generating the MML of the Bushveld Complex. These facts are: a) that an immiscible Fe-P rich melt should occur after significant oxides have been already crystallized (e.g. Jakobsen et al., 2005; Hunter and Sparks, 1987, 1990; Toplis and Carroll, 1995); no apatite was identified in the MML, but only in the upper part of the Upper Zone layers, therefore the existence of an immiscible Fe-P liquid cannot be accepted for MML (but can be potentially accepted for explaining the apatite bearing magnetite and nelsonite layers from the top part of the Upper Zone; b) magnetite and ilmenite have similar crystallization temperatures at fO_2 conditions around FMQ buffer and both magnetite and ilmenite have been experimentally proven to crystallize together along a cotectic (Toplis and Carroll, 1995). The textural relationship between magnetite and ilmenite grains in the MML do not support an interpretation in which the ilmenite exsolutions migrated towards the exterior of the magnetite grains to form individual coarser grains

of ilmenite. It is noteworthy that Ti-magnetite in MML is different compared to magnetite from other layered intrusions, such as the Damiao anorthosite complex (NE China, He et al., 2016) or the Panzhihua intrusion (Howarth and Prevec, 2013), in the sense that magnetite in the MML does not have ilmenite exsolutions (or the ilmenite exsolutions are extremely limited), but rather the magnetite and ilmenite grains texturally seem to have been growing together, probably along a magnetite-ilmenite cotectic (e.g. Buchanan, 1976). Texturally, there is no evidence for immiscible liquids (e.g. spheroidal inclusions of magnetite in silicates or vice-versa). Oxide layers formed from immiscible magnetite-saturated melt can be expected to display lensoid shapes (e.g. Velasco et al., 2016), should have a relatively homogenous composition, and should not show upwards variation in Cr_2O_3, MgO, etc.). Eventually, they can show a single vertical trend of the chemical change due to diffusion processes during cooling along with a thermal gradient. This is not the case for the Ti-magnetite in the MML, where complex chemical variations and reversals were encountered.

Bearing in mind all these arguments, the immiscibility genesis of Ti-magnetite within the MML of the Bushveld Complex may be rejected. However, this process might be appropriate for consideration for the genesis of the Ti-magnetite and nelsonite layers which occur on the upper part of the Upper Zone of the Bushveld Complex.

Regarding the role of the oxygen fugacity as a dominant process in triggering the crystallization of oxides, the content of TiO_2 in magnetite and the magnetite-ilmenite relationship must be discussed. It is known that in reduced melts, the magnetite structure incorporates Ti while in oxidized melts Ti is incompatible (Buddington and Lindsley, 1964; Frost and Lindsley, 1991). The elevated content of TiO_2 in Ti-magnetite points towards a more reduced melt (probably close to the FMQ buffer). The thermodynamic calculations in this study show that only for high oxygen fugacity (HM buffer) the magnetite becomes the sole liquidus phase at high temperatures, a fact which is not consistent with the high TiO_2 content of magnetite. More than that, high oxygen fugacity would influence the partitioning of vanadium in between Ti-magnetite, silicates and melt. Based on high-energy resolution fluorescence-detected X-ray absorption spectroscopy (HERFD-XAS), Bordage et al. (2011) argued that the preferred oxidation state of vanadium in spinels is V^{3+} with up to 9.5 to 16.3% V^{4+}. Toplis and Corgne (2002) experimentally demonstrated that a high proportion of V^{4+} and V^{5+} appear at high fO_2, making these ions to be significantly less strongly partitioned into magnetite compared to V^{3+} (while V^{4+} and V^{5+} will rather partition to melt). It can be inferred from this that the Ti-magnetite formed from a melt at high oxygen fugacity will accommodate less V_2O_3

than the Ti-magnetite formed at lower oxygen fugacity and that the vanadium content in magnetite decreases significantly in more evolved cumulates, due to a decrease of fO_2 with differentiation. The high V_2O_3 content in MML as a mining target for vanadium, points out towards a low oxygen fugacity of the melt from which the Ti-magnetite formed. This observation is consistent with the preceding argument of low oxygen fugacity required for accommodating Ti in magnetite. The high TiO_2 and relatively high V_2O_3 content of magnetite also point towards a less evolved melt as parent magma, melt which should be very different from a very evolved Fe-P rich melt responsible for the formation of the upper layers of magnetite in the Upper Zone. Having in mind all of the above arguments, the increased oxygen fugacity as a trigger for the Ti-magnetite crystallization can be rejected. A massive crystallization of magnetite from a relatively reduced melt (probably around FMQ oxygen buffer), would relatively increase the Sulphur concentration in the melt, that would in fact trigger the crystallization of sulphides, when the sulfur saturation was achieved. Indeed, there is textural evidence that the igneous, coarse-grained sulphides are spatially associated with the oxides, being formed near (nucleated on) oxides. Very rare situations where small sulphides are included in magnetite prove that the sulphur saturation could have been achieved even before crystallization of oxides. However, the rarity of sulphide textures rather suggests that they are exceptions.

The lack of igneous hydrated phases included in or associated with magnetite, together with the secondary character of the biotite and amphibole encountered in some reaction textures, indicate that the melt from which magnetite crystallized was mostly dry (i.e., no saturation of a hydrated phase was achieved). If magnetite had been triggered by the relative increase in H_2O during prior crystallization of anhydrous silicates (e.g. Howarth and Prevec, 2013; Howarth et al., 2013), it might be expected to observe some significant euhedral or subhedral anhydrous silicates included in magnetite and possibly some inclusions of hydrated phases. These features in MML of the Bushveld Complex were not observed. A few rare exceptions exist, wherein fine-grained igneous biotite inclusions in magnetite were identified at depth 126-133 m in borehole VK05. These inclusions can be considered igneous as they seem relict, they are deformed and partially transformed to chlorite and have high MgO (~19 wt.%) and TiO2 (~ 3-4 wt%) content. However, these inclusions are rather a rarity. Furthermore, this model cannot account for the high quantity of magnetite (the total FeO in the basaltic melt) relative to the residual liquid, or the heterogeneity of a magma chamber, nor can it explain the chemical heterogeneities in MML. We, therefore, have to reject this model for explaining the MML of the Bushveld Complex.

The pressure change as a trigger of the magnetite formation (e.g. Cameron, 1980; Lipin, 1993) cannot explain the quantity of magnetite (which should account for the total FeO dissolved in the melt), nor for the chemical variations inside the MML, unless small fluctuations of pressure can change the composition of magnetite, periodically. However, as Mathez (2007) and Naldrett et al. (2012) argued, the pressure variations would be insignificant and the model would require an absolutely particular composition of the melt, very close (but outside) the boundary of spinel stability field. More than that, this model was designed to account for the occurrence of chromite, where the stability is discussed on the Mg-spinel stability field. No data is available for the stability of a Ti-magnetite of a complex composition with pressure variation. From simple thermodynamic reasons, it is intuitive that the magnetite with such high TiO_2, Cr_2O_3, V_2O_3, etc., would have a much lower equilibrium temperature in a basaltic system compared with a pure Mg-spinel, and hence, Ti-magnetite would not be a liquidus phase in the system discussed by Cameron (1980) and Lipin (1993), a fact that negates their model. Our thermodynamic modeling using MELTS algorithms also shows that magnetite is not a liquidus phase in a basaltic system at FMQ+2, whereas experiments show that it is not a liquidus phase not even at more reduced conditions (FMQ, or lower). Therefore, even though the idea of this model is elegant, the scenario implied by the model is probably less likely and it should be rejected as unrealistic.

The magma mixing model (e.g. Harney and Gruenewaldt, 1995) can also be rejected, mostly based on the arguments of Cawthorn and Ashwal (2009) and Maier et al. (2012). Another argument in rejecting this model is that the mixing of a relatively Fe-poor basaltic melt with a more evolved melt (richer in FeO) would produce a melt with intermediate FeO, from which magnetite cannot crystallize, or at least not as a liquidus phase. The similitude of this model with Irvine (1975) model can be disregarded, as it is known that the system plagioclase - magnetite or pyroxene - magnetite should be very different from the system forsterite-chromite imagined by Irvine (1975) (e.g. in the Forsterite-Anorthite- SiO_2 ternary system the cotectic lines between spinel field and anorthite and forsterite fields, respectively, are not curved).

A scenario in which the magnetite crystallization is triggered by contamination of the basaltic melt with SiO_2-rich country rocks cannot be realistic since this would decrease the FeO content of the basaltic magma and would inhibit the crystallization of magnetite. Even considering the contamination of the magma by Banded Iron Formation (BIF) country rocks, the magnetite and hematite from BIF cannot melt at reasonable igneous temperatures, not even in a mixture with

silicates. Bowen and Schairer (1947) and Darken (1949) found that magnetite melts at T= 1597°C, while a mixture of magnetite and silica starts to melt at 1455 to 1500°C, producing very little melt. The hematite melts at T = 1575°C (Bowels et al., 2011). Even the melting of the oxides is practically improbable, the FeO might increase substantially in the liquid by reaction of the melt (undersaturated in FeO) with BIF rocks. However, no such reactions were described in BIF adjacent to the Bushveld Complex, nor BIF-reacted fragments were reported in the Upper Zone. Even the contamination of the Upper Zone melt by country rocks cannot be excluded, it cannot be advocated as a process for triggering the oxide crystallization from the magma.

Another question to be answered relates to the nature of the parental magma, specifically, whether it was "primitive" vs. "evolved" Fe-rich melt, as the TiO_2 and V_2O_3 content in Ti-magnetite suggest that the melt from which oxides crystallized was not an evolved (by fractional crystallization or other process of differentiation) melt. Probably, the answer should depict something intermediate between a "less evolved" and a "more evolved" Fe-rich melt, where a less evolved Fe-rich melt would be responsible for the formation of MML and a more evolved (P)-Fe-rich melt would be responsible for the formation of magnetite associated with apatite-bearing rocks and nelsonites at the upper part of the Upper Zone of the Bushveld Complex. It is likely that the oxides in the MML crystallized from a "less evolved melt" (probably towards basaltic andesite composition) in relatively reduced conditions (probably around FMQ oxygen buffer), as proven by high TiO_2 and relatively high V_2O_3, Cr_2O_3 and MgO content of Ti-magnetite. However, the crystallization of oxides should have been triggered by a sudden change in physicochemical parameters of the melt, followed by gravitational segregation of the oxides. If this is the case, it would be necessary that fractional crystallization be the process responsible for the separation of magnetite from the silicates, as suggested by Reynolds (1985), Cawthorn and Molyneux (1986) or Kruger (2005). However, the model of Reynolds (1985) invokes a dense Fe-rich magma at the bottom of the chamber (bottom crystallization of magnetite) and a less dense overlying Fe-poor magma on top of it. This model is not far from having two immiscible liquids, a model that has already been rejected in this study. Even if the two liquids were not derived through immiscibility, but they would represent two different liquids derived from different parental magmas, it can be considered that, in the case of such scenario, the overlying magma would lose heat extremely fast. Consequently, the two melts would start to mix due to the heat convection, enhancing the double convection mechanism triggered by the hotter magma underneath. This process of double diffusive convection

would start during the crystallization of the two magmas (e.g. Huppert and Sparks, 1984; Lowell, 1985). The model of Kruger (2005) accepts the Upper Zone (and Upper Main Zone) as a closed system, without the addition of new magma. This model comes into conflict with our observations, where the MML is consistently formed by two main layers, within which complex chemical variations and reversals are observed. Our observations point out towards accepting multiple magma fluxes, from which magnetite layers, but also Fe-rich silicate layers, anorthosites, and nelsonite layers can form. The chemical variation within the magnetite layers together with the anorthite content in plagioclase and the appearance of igneous olivine at different levels of the Upper Zone can support such interpretation of multiple magma fluxes (e.g. Scoon and Mitchell, 2012).

The fact that the MML is made of two distinct layers (with sublayers showing chemical reversals in the MML of the Eastern lobe) suggests two main injections of Fe-rich magma which probably evolved during crystallization and cooled down towards the tops, forming the sublayers A,B,$C_{1,2,3}$,D in areas where Ti-magnetite accumulated as massive ore. The existence of multiple hybrid and anastomosed layers in the MML of the Northern Lobe, totally different from the massive MML in the Eastern and Western Lobes, points out towards a more dynamic and turbulent regime of the magma intrusion in the Northern Lobe. This interpretation is also supported by the more numerous and larger inclusions of silicates (mostly plagioclase) in magnetite, compared to the rare and small inclusions (mostly pyroxene) in the magnetite of the MML in the Eastern and Western Lobes.

Based on the above arguments, several existing models for magnetite crystallization in MML of the Bushveld Complex can be rejected: the immiscibility, the increased oxygen fugacity, the relative increase of H_2O content of the melt, pressure variation within the magma chamber, magma mixing, and crustal rock contamination. The model for triggering the crystallization of Ti-magnetite in the MML of the Bushveld Complex that remains involves the crystallization of both Ti-magnetite and ilmenite from a Fe-Al-Ca-rich melt (ferro-diorite) along its line of descent, and gravitational settling of oxides. The principal factor that probably triggered the crystallization of magnetite during this process is a critical saturation of melt in magnetite (attaining saturation of magnetite and ilmenite in the melt after some silicates crystallized). This model will be discussed in more detail, below.

The MML of the Eastern and Western Lobes shows similar textures and similarities in mineral chemistry (massive magnetite, mineral chemistry of Ti-magnetite, discrete Cr_2O_3 values for samples

from different depths) and therefore it can be advocated for a common genetic scenario to explain the MML in these two lobes. Textural and chemical differences between the MML of the Eastern and Western Lobes on one hand and the MML of the Northern Lobe, on the other hand, advocates for a somewhat different genetic scenario of the MML in the Northern Lobe.

5.5. Model of oxide crystallization in the MML by fractional crystallization within a dynamic regime from a less evolved Fe-Ca-Al-rich (ferro-diorite) magma

The fact that the silicate inclusions within coarser grains of Ti-magnetite in MML at Magnet Heights (Eastern Lobe) consist mainly of pyroxene might suggest that these silicates existed as crystals in the melt from which Ti-magnetite crystallized. The anhedral shape of these inclusions suggests that the silicates were in disequilibrium with the melt from which the oxides crystallized. The textural observations don't directly support the model in which magnetite formed at liquidus temperatures, since the silicate inclusions might indicate that the silicates crystallized first, followed by magnetite. The scenario in which the magnetite and their silicate inclusions crystallized together would assume that Ti-magnetite and silicates (both pyroxene and plagioclase!) should have been at least in partial equilibrium with the melt from which Ti-magnetite formed. However, the textural observations suggest that the anhedral inclusions of pyroxene in magnetite were partially digested or reacted with the Fe-rich melt. A possible way to explain this is to consider that the Fe-rich melt thermally and/or mechanically eroded the floor, which was rich in pyroxene (i.e., an orthopyroxenite floor similar to the Pyroxenite Marker?) from which the silicates were derived. These fragments, in clear disequilibrium with the melt, were partially digested, resulting in rounded, anhedral shapes, and could have been laterally transported along with the Fe-rich melt until some of them were included within growing magnetite. One main argument against this interpretation might be that the floor of the magnetite layers in the Western and Eastern lobes is relatively planar and sharp, and doesn't show obvious erosional features. However, it is to be considered that the Fe-rich melt extensively expanded laterally in order to achieve a relatively continuous development along ca. 300 km and a relatively constant thickness in Eastern and Western Lobes. The magma emplacement could have eroded the magma chamber floor close to the magma feeder, and then extended laterally as slow, quasi-laminar flow, without eroding the floor of the magma chamber, carrying rare fragments of pyroxene and crystallizing magnetite and ilmenite. Once formed, the

oxides and their pyroxene inclusions gravitationally settled from the flowing magma at the bottom of the floor, while the magma continued to flow and crystallized more magnetite and ilmenite, which would have gravitationally settled above the already-crystallized and accumulated oxides. Indeed, there are sub-layers with different densities of silicate inclusions, which justifies the acceptance of such settling of oxide crystals into sub-layers, within a hydrodynamic regime (hydrodynamic sorting). In this way, more magnetite and ilmenite sub-layers can form, producing the sub-layers identified in the MML of the Eastern lobe. Reaction between the settled oxides and small volume of the interstitial liquid could have change the chemistry of the cumulus magnetite, as well as thin double convection cells could have also generate chemical variation with depth, as recorded by our observations. The generation of heterogeneities within the MML chamber was also considered by Cawthorn and McCarthy (1980) in order to explain the variation of Cr_2O_3 in magnetite with depth. Sub-solidus re-equilibration should have not played a significant role, since the silicate inclusions are very scarce in the massive magnetite. However, during cooling and preserving of a vertical thermal gradient within the oxide pile, some elements could have easily diffused, partially obliterating the chemical variations among the sub-layers.

As was shown earlier, the magnetite was not a liquidus phase, but some silicates (plagioclase and clinopyroxene, according to our MELTS calculations) should have crystallized before it, probably in oxygen fugacity conditions close to FMQ+2 or even FMQ, as suggested by experiments (e.g. Toplis and Corgne, 2002). Very possibly, some orthopyroxenites and leucogabbros (modal plagioclase > modal clinopyroxene) should have crystallized before magnetite and ilmenite. The floor of the MML at Magnet Heights is anorthosite. The silicate inclusions in MML at Magnet Heights are mostly pyroxene and extremely rare plagioclase. This observation can be used to suggest that the floor of the present MML is not genetically related to the MML and therefore doe not represent a cumulate derived from the same parent magma which crystallized magnetite (i.e., these observations cannot support *in situ* fractional crystallization). Rather, the MML formed from a magma intruded laterally (horizontally), carrying with it fragments of silicates from a different floor situated elsewhere. During the lateral emplacement, hydrodynamic sorting of crystals can take place (e.g. Maier et al., 2012), so that different levels within one of the MML layers can host different amounts of silicate fragments (in effect, different populations of xenocrysts in terms of mineral assemblage, grain sizes, and volumes). During the transport, magnetite and ilmenite crystallize and settle within a dynamic regime of the magma. The question arising is the fate of the resident magma

in the chamber when the Fe-rich melt was being emplaced laterally? Very probably, the new Fe-rich magma, much denser, pushed away the resident magma laterally or/and upwards. In this situation, the two magmas could not mix (the contact between the two magmas is far more limited compared to a vertical pile of two magmas exposed to thermal convection). The anastomosed layers of magnetite and silicate rocks in the Northern Lobe could represent the result of such scenario, in a more competent flow regime compared to the Eastern and Western Lobes.

The lateral transport of the magma on very long distances has to be accepted in order to explain the continuity of the MML along ca. 300 km strike along the Eastern to the Western and Northern Lobes and with remarkable similar thickness. This lateral transport of the emplaced magma is probably the main reason for which it might be very difficult to identify the cumulate rocks (e.g. leucogabbros) that formed from the melt which crystallized magnetite of the MML. It is thus possible that some orthopyroxenites and leucogabbros somewhere below in the stratigraphic sequence and situated far away from the present MML at Magnet Heights represent such a link between the MML and its possible silicate cumulates. During the formation of these cumulate rocks, and probably during magma emplacement within a hydrodynamic regime, the FeO content of the melt increased up to the point of magnetite saturation, at which it started to crystallize magnetite (and ilmenite).

Fractional crystallization can occur in a stagnant magma chamber or in a chamber where the melt flows within a hydrodynamic regime (e.g. expand laterally on long distances due to a large volume of melt). The problem of static fractional crystallization of Ti-magnetite and silicates followed by gravitational segregation of oxides within a silicate-rich melt is controlled, among other factors, by the viscosity of the melt. The Fe-Al-Ca-rich melt from which the oxides should have crystallized should have had a high viscosity (and density). The polymerization type of the magma should have been mostly a framework type (due to the high plagioclase component of the melt), polymerization broken by cubic and trigonal types of polymers reflecting the high magnetite and ilmenite components in the liquid. A high viscosity and density of the melt can make the gravitational settling of the oxides crystals difficult, especially for small crystals. More than the gravitational settling difficulty, another problem can inhibit the settling of oxides. A stagnant crystallization of oxides in a big magma chamber could have generated slow cooling and magnetite and plagioclase could have relatively easy crystallized along a silicate-magnetite cotectic. Examining the magnetite-bearing anorthosite layers which are found in between magnetite layers (e.g. sample MH12, above

MML at Magnet Heights), it is to be noticed that both plagioclase and oxides occur as large, subhedral crystals, which partially include each other. Effective fractionation of the magnetite from the silicates would not have been possible in this case, where textures indicate interlocking between oxides and plagioclase. Very probably these textures can suggest a cotectic crystallization of magnetite and plagioclase, or a recrystallization. However, triple junctions, characteristic for recrystallized grains, as well as interlocking between oxide and plagioclase grains were not observed within the MML itself.

However, within a dynamic melt regime, small crystals of oxides could easily be transported and sorted (hydrodynamic sorting), and then settled when the competence of the melt flow decreased (e.g. Maier et al., 2012). The presence of small ilmenite grains mostly in the interstitial spaces between magnetite grains or along grain boundaries suggests that such accumulation of crystals was a mechanical process, where very small grains (e.g. ilmenite) occupied the spaces between larger grains (magnetite). The result was a cumulate with the very little effective volume of the interstitial spaces so that the interstitial melt volume was minimal. Later clustering and annealing of the oxide crystals after their gravitational settling would have even more reduced the interstitial volume of the cumulate, producing massive magnetite.

Authors such as He et al. (2016) suggest that a negative correlation between the Cr_2O_3 values in magnetite and co-existing ilmenite, respectively, can advocate for Fe-Ti oxide fractionation, whereas a constant Cr_2O_3 in magnetite for variable Cr_2O_3 in ilmenite can suggest gravity settling. The data in this study do not show any clear correlation between Cr_2O_3 in magnetite and ilmenite. Most of the Cr_2O_3 values in MML ilmenite are zero or close to zero, a fact which is attributable to the partitioning of Cr between oxides and basaltic melt. The partitioning coefficient of Cr between magnetite and the basaltic melt is ~150 but can be up to 600 (Irving, 1978; Klemme et al., 2006), whereas the partition coefficient of Cr between ilmenite and the basaltic melt is 11 to 40 (Klemme et al., 2006). Based on these differences, and considering that both magnetite and ilmenite crystallize together from the same melt, chromium will mostly partition in between magnetite and melt, and ilmenite will accommodate much less or close to zero Cr_2O_3, fact recorded by the microprobe analyses. The missing correlation between the Cr_2O_3 in magnetite and co-existing ilmenite can indicate than no in-situ fractional crystallization took place at the moment of magnetite accumulation, but rather the magnetite and ilmenite gravitationally accumulated and the grains mechanically mixed from a flowing magma. However, the cyclic sub-layers in the layers of MML,

together with the missing correlations trends between the Cr_2O_3 in magnetite and ilmenite, respectively, suggest that the chemical variations in MML could have been produced by a combination of factors, such as a) differentiation in the presence of melt (e.g. flow differentiation, reaction between oxides and residual melt, existence of convective cells in each layer/sub-layer and b) possible subsolidus chemical change during cooling.

The MML being made of two layers (each with sub-layers A,B, $C_{1,2,3}$,D), requires that two relatively similar magma influxes are admitted, where the second magma influx was emplaced within a dynamic regime after a very short period of stagnation. During this stagnation period, the plagioclase and magnetite crystallized together. The plagioclase-rich rock found in between the MML layers is similar to the magnetite-anorthosite layers found in between other magnetitite layers above the MML. The thin magnetite-bearing anorthosite could have formed from the same Fe-Ca-Al rich magma as MML, but in stagnant conditions, where plagioclase and magnetite crystallized together, without gravitational separation of the crystals.

This model is shown in Figure 47, where five stages of evolution are suggested:

- Stage 1 is represented by the intrusion of a Fe-Ti-Ca-Al-rich magma which expanded laterally, within a flat and short magma chamber, flushing out the resident magma. The cumulates corresponding to this magma are not known and they would probably have been left behind at depth, where the Bushveld magma was fed from. However, some plagioclase and pyroxene should have been crystallized and settled in the magma chamber prior to any crystallization of oxide. The dynamic regime of the magma creates conditions for floor erosion, where pyroxene crystals and fragments were disaggregated and carried away with the magma from a pyroxenitic floor. This erosion of the floor was possible close to the feeder, where turbulent flow could have been more prominent. Far away from the feeder, where the magma current lost its transport capacity and magma would have rather moved relatively slowly, within a quasi-laminar flow regime, floor erosion would have been less likely. Within this less dynamic regime the oxides (Ti-magnetite and ilmenite) crystallized and settled on a "foreign" anorthosite-type of floor.
- Stage 2, where the bottom layer at the MML is formed by the gravitational segregation/accumulation of the oxide crystals in a dynamic regime. Plagioclase started to crystallize (e.g. subhedral plagioclase in MML of the Northern Lobe).

- Stage 3 is a short-lived static regime, where both plagioclase and oxide crystallized together, forming a thin layer of magnetite-bearing anorthosite found in between the two layers of MML. A similar process can be imagined for the magnetite-anorthosites found in between the magnetitite layers above the MML (e.g. sample MH12A).
- Stage 4, in which a new influx of Fe-Ti-Ca-Al-rich magma flushed out completely the residual magma left after the crystallization of plagioclase and magnetite, and started to crystallize Ti-magnetite and ilmenite, and to include some of the existing silicate fragments. The oxides crystallized in a dynamic regime, as in Stage 1.
- Stage 5, the second magnetitite layer of the MML is formed, by gravitational accumulation of oxides. Some of the silicates existing in the melt could have been included by growing crystals of magnetite.

The massive crystallization of magnetite in each layer triggered two processes: a) Sulphur saturation of the magma producing sulphide precipitation and b) nucleation of the new sulphides on the oxide grains. The quantity of oxygen was locally and fast depleted near the new formed oxide, fact which probably controlled nucleation of the sulphides on the existing oxides.

Later fluids (such as late magmatic or deuteric volatiles) percolated through the MML, producing chloritization of the included silicates, remobilization of igneous sulphides and precipitation of lower-temperature sulphides.

The flow of the magma is interpreted to have been more dynamic (probably turbulent over longer distances) in the MML of the Northern Lobe, compared to the MML in the Western and Eastern Lobes, producing highly heterogeneous and imbricated thin layers of magnetitite and silicates.

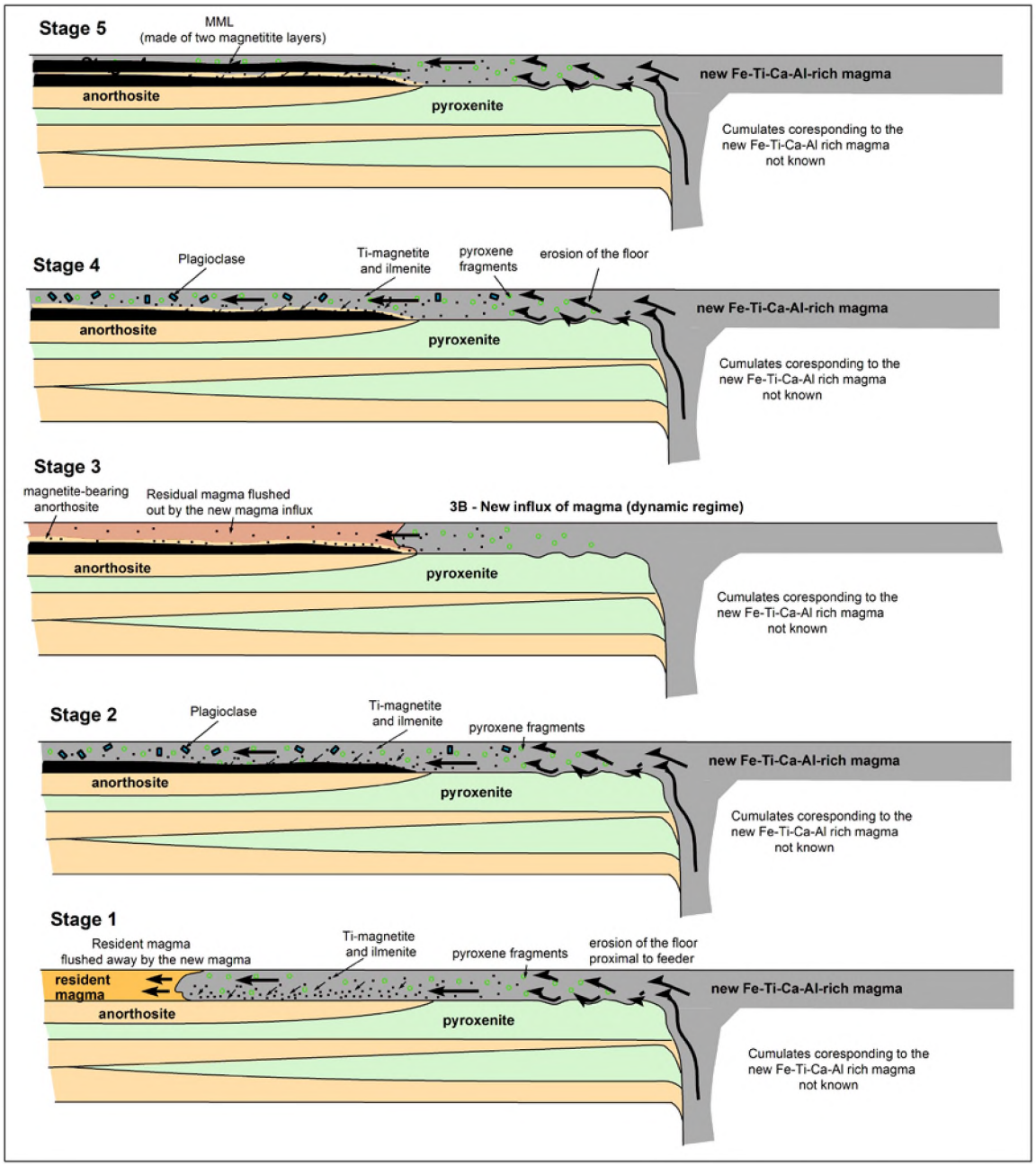

***Figure 47**: Model of oxides crystallization in the MML (Upper Zone, Bushveld Complex). The horizontal scale is exaggerated, in order to accommodate processes happening near but also far away from the magma feeder. See text for explanations.*

5.6. The significance of coronitic olivine

This study identified coronitic olivine in the MML in the Northern Lobe, at restricted depths (129-130 m), but also in the PQ layers (upper magnetitite layers of the Upper Zone). The latter is not described herein. However, no coronitic olivine was recorded by this study (or other studies) in the

MML of the Eastern and Western Lobes, a fact which clearly shows a difference in the evolution of magma crystallization in MML in the Northern Lobe compared with the MML in the Eastern and Western lobes.

The appearance of the coronitic olivine is texturally controlled by the presence of orthopyroxene inclusions in Ti-magnetite and probably represents a local chemical system, where orthopyroxene melted incongruently to form olivine and SiO_2-rich fluid/melt. The presence of these textures supports the interpretation that the orthopyroxene pre-dated the Ti-magnetite. However, the fact that the olivine corona is not developed everywhere around the orthopyroxene but only localized to orthopyroxene – Ti-magnetite interfaces strongly suggest that it is not a reaction between the orthopyroxene and a Fe-rich melt (or else all orthopyroxene crystals included in MML would have developed these olivine corona). An interpretation is favoured wherein the incongruent melting of orthopyroxene happened locally, while the Ti-magnetite was a solid phase neighboring and including orthopyroxene and plagioclase crystals. A rise in temperature would be needed for this melting to happen. Therefore, these textures represent evidence of a re-heating event, such as would result from the proximal injection of a hotter magma which could have triggered local thermal reactions and local incongruent melting of orthopyroxene. Very possibly the patchy character of the exsolution in Ti-magnetite and the widespread clinopyroxene-plagioclase symplectites which developed on igneous plagioclase near the olivine coronas, could have been produced by re-heating, causing local partial melting and high-temperature reactions (in presence of fluid/melt) between the existing phases. Therefore, the presence of coronitic olivine offers indirect evidence of multiple injections of melt, which in the MML of the Northern Lobe intruded within a more competent regime of the melt flow, and new thin bands of melt intercalated between already crystallized layers. The presence of heterogeneous and anastomosed layers of magnetite-rich and magnetite poor rocks is, therefore, evidence for lateral intrusion of magma and its crystallization within a dynamic flow regime. This anastomosed lateral intrusion of the Fe-Ca-Al-rich magma can provide the source of the heat to affect previously-crystallized layers. In addition to the coronitic olivine, other observations can support the heating of former layers, including: 1) recrystallization of olivine grains; 2) sintering (or ripening) of magnetite grains (individual grains tending to unite to produce massive magnetite; 3) patchy "healing" of exsolution in magnetite; 4) fine spinel intergrowths formed by breakdown of mafic silicates.

It must be emphasized that the olivine described here is not crystallized from magma, and hence cannot be compared or equivocated to other cumulus olivine layers/levels in the Upper Zone, where olivine (much higher in fayalite; e.g. Tegner et al., 2006) crystallized from a melt.

The model developed here requires that the resident magma existing in the magmatic chamber must have been displaced laterally or upwards by the incoming Fe-Ca-Al-rich magma. This can be possible only if the active magma chamber is relatively thin so that no substantial vertical pile of magma can form. Where the magma chamber is tall, mixing (rather than displacement) of the Fe-Ca-Al rich magma and resident magma could occur, and no massive magnetite would form, but mostly magnetite-bearing silicate rocks. This model is therefore consistent with the models of sill emplacement of Scoon and Mitchel (2012), Costin and Scoon (2013), and Mungall et al. (2016), where the authors explain the presence of anorthosites (associated with Ti-magnetite layers) as a consequence of disequilibrium partial melting of pre-existing silicate cumulates (norites) due to heat associated with new pulses of magmas. Regarding the way in which the model invokes lateral intrusion of the magma within a thin magma chamber and the process of segregation and accumulation of oxide crystals within a dynamic regime, this is also consistent with the hydrodynamic sorting model of Maier et al. (2012), as well as with the sills and slurries model of Eales and Costin (2012).

5.7. Late fluids affecting MML

The secondary transformations of silicates encountered in the MML strongly suggest that the magnetite layers were percolated by aqueous fluids. Evidence for aqueous transformations include: 1) presence of late biotite, spatially related with sulphides; 2) intense cloritization of plagioclase (to form clinochlore or /and chamosite); 3) transformation of small magnetite crystals included in plagioclase into a fine aggregate of oxide, chlorite, and sulphides; 4) remobilization of sulphides and presence of sulphides characteristic of more hydrothermal genesis (e.g. millerite, siegenite). Interestingly, these hydrometamorphic effects observed within the MML are not evident within the silicate layers below or above the MML, but rather on discrete planes usually following the layering or on some cross-cutting limonitized cleavages of the rocks.

6. Conclusions

The oxides (Ti-magnetite and ilmenite) in the Main Magnetite Layer (MML) from the Northern, Eastern and Western Lobes of the Bushveld Complex show significant differences in texture and in mineral chemistry. The MML in the Eastern and Western lobes is massive, with rare and small silicate inclusions, which are mostly altered, anhedral pyroxenes. By contrast, the MML in the Northern Lobe is more heterogeneous, and comprises anastomosed and sometimes imbricated, thin layers of magnetitite, magnetite-rich and silicate-rich rocks. Here, the inclusions in Ti-magnetite are more numerous and consist of mainly altered subhedral and anhedral plagioclase. In the MML (in all three lobes studied), there are discrete intervals where the frequency of silicate inclusions varies, suggesting some sort of variation in the mechanism of oxide precipitation and/or transport and/or deposition.

Compared to other magnetite-bearing layered intrusions (such as the Damiao anorthosite complex in northeastern China, or the Panzhihua intrusion in southwestern China) and to magnetitite and nelsonite layers higher in the stratigraphy of the Bushveld Complex, the Ti-magnetite grains in MML contain no ilmenite exsolutions (but do contain ulvöspinel and Al-spinel). The textures suggest that ilmenite grains (together with Ti-magnetite) crystallized from the melt and ilmenite grains did not form by migration of exsolved ilmenite, but rather crystallized from the magma.

The comparison of the maximum values of the oxides shows that the MML in the Northern Lobe has the highest content of V_2O_3 (1.97 wt.%), TiO_2 (22.49 wt.%) and MgO (2.92 wt.%), while the MML in the Eastern Lobe has the highest content of Cr_2O_3 (2.92 wt.%) and Al_2O_3 (9.80 wt.%), but lowest V_2O_3 (0.52 wt.%). The composition of the MML in the Western and Eastern lobes is similar, except that V_2O_3 is higher in the Western Lobe, and Cr_2O_3 is lower.

The highest proportion and grain size of ilmenite were found in the MML of the Eastern Lobe, suggesting that fO_2 correlates with Ti content of magnetite and the presence of ilmenite. According to Buddington and Lindsley (1964) and Frost and Lindsley (1991), lower amount of Ti is accommodated in magnetite in reduced melts, thus, the lower TiO_2 (and higher V_2O_3) content in the MML of the Northern and Western Lobes suggest lower oxidizing conditions during the crystallization of oxides. The high TiO_2 content in magnetite, together with the negative correlation between TiO_2 and V_2O_3 suggest that the maximum V content should represent a more primitive and less oxidized melt, rather than a more evolved and oxidized melt. In this respect, higher

concentrations of V_2O_3 in magnetite can be expected in magnetitite layers with low TiO_2. It can be inferred that the Ti-magnetite in the MML from the Eastern Lobe was formed from a more evolved (TiO_2 and FeO enriched) and more oxidized (lower V_2O_3) melt, compared with the MML from the Northern and Western Lobes. It can be inferred that high fO_2 can be responsible for the relatively low V content in magnetite and that the V in magnetite decreases significantly in more evolved cumulates, due to a decreasing of fO_2 with differentiation.

Unique for the MML in the Northern Lobe is a clear positive correlation between TiO_2 and MnO, which can be explained by assimilation of Mn-bearing dolomite from the country rocks (e.g. Malmani dolomite) by a Ti-enriched magma.

Compositional profiles of Ti-magnetite along the stratigraphic height of the MML in the Eastern Lobe at Magnet Heights (composed of two layers, separated in the outcrop by a parting plane) depicts a cryptic variation with depth in each of the two layers (of ca 1 m thick), which are separated by a ~5-10 cm thick magnetite + plagioclase layer (magnetite-bearing anorthosite). Mineral compositional analyses allowed for the discrimination of each layer into four sublayers, labelled upwards as A, B, C (with C1, C2, C3, and C4) and D. The separation can be done based on Cr, Mg, Ti, Al and V variation. Small-scale reversals of the listed elements and the repetition of A, B, C and D sub-layers in each layer suggest that MML formed from two successive influxes of magma (indicated by relatively elevated values of MgO), which evolved by crystallization and cooling in a similar manner, to produce the A to D variation.

The spatial association between oxides and igneous sulphides is explained by the fact that massive crystallization of magnetite increased the concentration of sulphur relative to other components in the melt. This increase reached the sulphur saturation and consequently, triggered the crystallization of sulphides, which nucleated on the existing magnetite crystals.

Based on our observations and theoretical considerations, our study dismisses several models for the genesis of the MML: the immiscibility, the increased oxygen fugacity, the relative increase of H_2O content of the melt, pressure variation within the magma chamber, magma mixing, and crustal rock contamination.

Our thermodynamic calculation using MELTS algorithms suggests that for a starting composition similar to that of the parent magma at the level of Pyroxenite Marker (Tegner et al., 2006), the crystallization in oxidation conditions of the FMQ+2 oxygen buffer, the silicates would crystallize

before magnetite, a fact also supported by experimental studies (e.g. Toplis and Carroll, 1995). These arguments dismiss the possibility of crystallization of Ti-magnetite as a liquidus phase at oxygen fugacity conditions lower than that of the Hematite-Magnetite buffer.

The fact that the MML is made of two distinct layers (with sublayers showing chemical reversals in the MML of the Eastern lobe) indicates two main injections of Fe-Ti-rich magma which probably evolved during crystallization, forming the sublayers A,B,$C_{1,2,3}$,D in areas where Ti-magnetite accumulated as massive ore. The existence of multiple hybrid and anastomosed layers in the MML of the Northern Lobe points towards a more dynamic and turbulent regime of magma intrusion. This interpretation is also supported by the more numerous and larger inclusions of silicates (mostly plagioclase) in magnetite, compared to the rare and small inclusions (mostly pyroxene) in the magnetite of the MML in the Eastern and Western Lobes.

The preferred model for MML genesis involves the crystallization of both Ti-magnetite and ilmenite from a Fe-Al-Ca-rich melt (ferrodiorite) along its line of descent, and gravitational settling of oxides in a dynamic regime. The factor which triggered the crystallization of magnetite is a critical saturation of melt in magnetite (attaining saturation of magnetite and ilmenite in the melt after some silicates crystallized).

The difference between the nature of silicate inclusions in magnetite and the nature of the magnetite floor suggest that the Fe-rich magma was not in equilibrium with the cumulates from the present floor, but rather it was emplaced laterally over long distances, the melt having been displaced from its own cumulates. During the lateral emplacement, hydrodynamic sorting of crystals took place (e.g. Maier et al., 2012), so that different levels within one of the MML layer host a different populations of silicate fragments. During the transport, magnetite and ilmenite crystallized and settled within a dynamic regime of the magma. During lateral emplacement, the denser Fe-Ti-Ca-Al-rich magma displaced the resident, more buoyant magma. The anastomosed layers of magnetite and silicate rocks in the Northern Lobe can be seen as a result of such a scenario, in a more competent flow regime than that evident in the Eastern and Western Lobes.

Within a dynamic melt regime, small crystals of oxides can be relatively easily transported and hydrodynamically sorted, and then settled when the capacity of the melt flow decreased. The presence of small ilmenite grains mostly in the interstitial spaces between magnetite grains or along grain boundaries suggests that such accumulation of crystals was a mechanical process, such that

very small grains (e.g. ilmenite) occupied the spaces between larger grains (magnetite). Later clustering and annealing of the oxide crystals after their gravitational settling would have re-adjusted the grain boundaries and reduced the interstitial volume of the cumulate, producing massive oxide ore. The cyclic sub-layers in the layers of MML, together with the missing correlations trends between the Cr_2O_3 in magnetite and ilmenite, respectively, suggest that the chemical variations in MML could have been produced by a combination of factors, such differentiation in the presence of melt (e.g. flow differentiation, reaction between oxides and residual melt, existence of convective cells in each layer/sub-layer) and possible subsolidus chemical change during cooling.

Given that the MML consists of two layers (each with sub-layers A,B, $C_{1,2,3}$,D), this requires two relatively similar magma influxes, where the second magma influx was emplaced within a dynamic regime after a very short period of stagnation. During this stagnation period, the plagioclase and magnetite crystallized together, without magnetite gravitational segregation, forming the plagioclase-rich rock found in between the MML layers.

This study identified coronitic olivine in the MML in the Northern Lobe, at restricted depths (129-130 m), but no such olivine was recorded by this study (or in other studies known) in the MML of the Eastern and Western lobes. The olivine described here is not crystallized from magma, and hence is not equivalent to cumulus olivine layers or levels in the Upper Zone, where much more fayalitic olivine (e.g. Tegner et al., 2006) crystallized from a melt. The presence of the coronitic olivine is texturally controlled by the presence of orthopyroxene inclusions in (or in contact with) Ti-magnetite and probably represents a local chemical system, where orthopyroxene melted incongruently to form olivine and SiO_2-rich fluid/melt. The presence of these textures supports the interpretation that the orthopyroxene pre-dated the Ti-magnetite. It is favored herein the interpretation that the incongruent melting of orthopyroxene happened locally, while the Ti-magnetite was a solid phase neighboring and including orthopyroxene and plagioclase crystals, during heating of the system. These textures represent a strong support for the acceptance of a re-heating event, probably produced by the injection of a hotter magma which could have triggered local thermal reactions and local incongruent melting of orthopyroxene. Very possibly, the patchy character of the exsolution in Ti-magnetite, the widespread clinopyroxene-plagioclase symplectites developed on igneous plagioclase near the olivine coronas, could have been produced by re-heating, causing local partial melting and high-Temperature reactions (in presence of fluid/melt) between the

existing phases. Therefore, the presence of coronitic olivine is an indirect evidence of multiple injections of melt, which in the MML of the Northern Lobe intruded within a more competent regime, where new thin bands of melt intercalated between already crystallized layers. The presence of heterogeneous and anastomosed layers of magnetite-rich and magnetite poor rocks is an evidence for magma lateral intrusion and crystallization within a dynamic flow regime. This anastomosed lateral intrusion of the Fe-Ti-Ca-Al-rich magma can be the source of the heat to former crystallized thin layers. Other observations can also support the heating of former crystallized layers: 1) recrystallization of olivine grains; 2) syntherizing magnetite grains (individual grains tend to unite to produce massive magnetite; 3) patchy "healing" of exsolution in magnetite.

The model for MML formation proposed by this work comprises of five stages. Stage 1 is represented by the intrusion of a Fe-T-Ca-Al-rich magma which expands laterally within a flat and thin magma chamber, leaving behind its plagioclase – pyroxene cumulates and eroding the floor closer to the feeder. Oxides start to crystallize within a dynamic regime of the magma, which cooled slowly as it moved away from the feeder and flushed laterally the resident magma existing in the chamber. Stage 2 is given by accumulation of oxides at the bottom of the new floor. Some plagioclase starts to crystallize (e.g. subhedral plagioclase in the MML of the Northern Lobe). The stage 3 is represented by a short living static regime, where both plagioclase and magnetite crystallized, without fractionation, forming a magnetite bearing anorthosite. The thin magnetite-anorthosite layer separating the MML into two layers formed in this way. Stage 4 is represented by a new influx of Fe-Ti-Ca-Al-rich magma which is emplaced above the magnetite bearing anorthosite, flushing out the liquid which was in equilibrium with the anorthosite. During this stage, the oxides started crystallizing in a dynamic regime, as in Stage 1. In stage 5, the accumulation of oxides produced the upper layer of the MML. Massive crystallization of oxides triggered the sulphur saturation of the magma and caused the precipitation of the igneous sulphides, which nucleated on the existing oxides.

The secondary transformations of silicates encountered in the MML strongly suggest that the magnetite layers were percolated by deuteric/late magmatic fluids, producing late biotite, spatially related with sulphides, intense cloritization of plagioclase and pyroxene (to form clinochlore or /and chamosite), transformation of small magnetite crystals included in plagioclase into a fine aggregate of oxide with elevated V_2O_3 content, chlorite and sulphides, remobilization of sulphides and precipitation of characteristic low temperature shulphides (e.g. millerite, siegenite).

References

Antoshechkina, P. M. and Asimow, P. D. (2010). alphaMELTS 3.0 and the MAGMA website: educational and research tools for studying the petrology and geochemistry of plate margins, *Abstract ED41B-0644 presented at 2010 Fall Meeting, AGU, San Francisco, Calif., 13-17 Dec.*

Arndt, N. T. and Nisbet, E. G. (2012). Processes on the Young Earth and the Habitats of Early Life. *Annual Review of Earth and Planetary Sciences* **40**, 521–549.

Ashwal, L. D., Webb, S. J. and Knoper, M. W. (2005). Magmatic stratigraphy in the Bushveld Northern Lobe: continuous geophysical and mineralogical data from the 2950 m Bellevue drillcore. *South African Journal of Geology* **108**, 199–232.

Balane, E., De Villiers, J.P.R., Eeckhout, S.G, Glatzel, P., Toplis, M.J., Allard, T., Fritsche, Galoisy, L., Calas, G. (2006). The oxidation state of vanadium in titanomagnetite from layered basic intrusions. *Am Mineral* **91**: 953–956.

Bateman, A. M. (1951). The formation of late magmatic oxide ores. *Economic Geology* **46**, 404–426.

Beukes, N.J. and Klein, C. (1992). Model for iron-formation deposition. The Proterozoic Biosphere (eds. J.W. Schopf and C. Klein), p.147-151. Cambridge, UK, Cambridge University Press.

Bordage, A., Balan, E., de Villiers, J. P. R., Cromarty, R., Juhin, A., Carvallo, C., Calas, G., Raju, P. V. S. and Glatzel, P. (2011). V oxidation state in Fe-Ti oxides by high-energy resolution fluorescence-detected X-ray absorption spectroscopy. *Physics and Chemistry of Minerals* **38**, 449–458.

Boudreau, A. E. (1999). PELE-a version of the MELTS software program for the PC platform. *Computers and Geosciences* **25**, 201–203.

Bowels, J.F.W., Howie, R.A., Vaughan, D.J.,and J. Zussman (2011). Rock-forming minerals. 5a**.** Non-silicates: oxides, hydroxides, and sulphides (2nd edition). The Geological Society, London, 920 pages.

Bowen and Schrairer (1947). The system FeO-SiO2. *Am. Jour. Sci.* 5, **24**, 177-213.

Brandriss, M. E. and Bird, D. K. (1999). Effects of H_2O on Phase Relations during Crystallization of Gabbros in the Kap Edvard Holm Complex, East Greenland. *J. Petrol.*, **40**, 1037–1064.

Buchanan, D.L. (1976). The sulphide and oxide assemblages in the Bushveld Complex rocks of the Bethal area, Geol. Soc. S. Afr., Trans. **79**, 76-80.

Buddington, A., Lindsley, D. (1964). Iron-titanium oxide minerals and synthetic equiva- lents. J. Petrol. **5**, 310–357

Buick, I.S., Maas, R., and Gibson, R. (2001). Precise U–Pb titanite age con- straints on the emplacement of the Bushveld Complex, *South Africa. J Geol Soc Lond* **158**, 3–6

Bushveld Minerals report (2013), http://www.bushveldminerals.com/upload/Reports/document/BMN_inititation_130416.pdf

Butcher, A. R. and Merkle, R. K. W. (1987). Postcumulus modification of magnetite grains in the Upper Zone of the Bushveld Complex, South Africa. *Lithos* **20**, 247–260.

Butcher, A. R. and Merkle, R. K. W. (1991). Unusual textures and structures associated with magnetitite layer in the Bushveld Complex: a contribution to the adcumulus debate. *Min. Mag.* **55**, 380-465.

Cameron, E. N. (1975). Postcumulus and subsolidus equilibration of chromite and coexisting silicates in the Eastern Bushveld Complex. *Geochimica et Cosmoohimics Acta*, **39**, 1021-1033.

Cameron, E. N. (1977). Chromite in the central sector of the eastern Bushveld Complex, South Africa. *American Mineralogist*, **62**, 1082-1096.

Cameron, E.N. (1980) Evolution of the lower critical zone, central sector, Eastern Bushveld Complex. *Economic Geology* **75**: 845–871

Cawthorn, R.G. (1996). Layered intrusions. Elsevier, Science, 530p.

Cawthorn, R. G. (2013). Rare earth element abundances in apatite in the Bushveld Complex--A consequence of the trapped liquid shift effect. *Geology* **41**, 603–606.

Cawthorn, R. G. and Ashwal, L. D. (2009). Origin of anorthosite and magnetitite layers in the Bushveld Complex, constrained by major element compositions of plagioclase. *J. Petrol* **50**, 1607–1637.

Cawthorn, R. G. and McCarthy, T. S. (1980). Variations in Cr content of magnetite from the Upper Zone of the Bushveld Complex—evidence for heterogeneity and convection currents in magma chambers. *Earth and Planetary Science Letters* **46**, 335–343.

Cawthorn, R.G. and Molyneux, T. (1986). Vanadiferous magnetite deposits of the Bushveld Complex. In: Anhaeusser, CR Maske, S (eds) Mineral deposits of Southern Africa. Geol Soc S Afr Johannesburg: 1251–1266.

Cawthorn, R. G. and Webb, S. J. (2001). Connectivity between the Western and Eastern limbs of the Bushveld Complex. *Tectonophysics,* **330**, 195-209.

Charlier, B., Namur, O., Toplis, M.J., Schiano, P., Cluzel, N., Higgins, M.D., Vander Auwera, J. (2011) Large-scale silicate liquid immiscibility during differentiation of tholeiitic basalt to granite and the origin of the Daly gap. *Geology* **39**: 907–910.

Charlier, B. and Grove, T. L. (2012). Experiments on liquid immiscibility along tholeiitic liquid lines of descent. *Contr Min Pet* **164**, 27–44.

Charlier, B., Namur, O., Duchesne, J. C., Wiszniewska, J., Parecki, A. and Auwera, J. Vander (2009). Cumulate origin and polybaric crystallization of Fe-Ti oxide ores in the Suwalki Anorthosite, Northeastern Poland. *Economic Geology* **104**, 205–221.

Charlier, B., Namur, O., Toplis, M.J., Schiano, P., Cluzel, N., Higgins, M.D., Auwera, J.V. (2011). Large-scale silicate liquid immiscibility during differentiation of tholeiitic basalt to granite and the origin of the Daly gap. Geology 39, 907–910.

Coffin, M. F. and Eldholm, O. (1994). Large igneous provinces: crustal structure, dimensions, and external consequences. *Reviews of Geophysics* **32**, 1–36.

Costin, G. and Scoon, R.N. (2013). Mineralogy and reaction textures of chromitite stringer, Upper Critical Zone, Winnaarshoek. Abstract, 6th IMSG Meeting, University of Free State, Bloemfontain, January 21-23, 2013.

Crowson P (2001). Mineral handbook 2000–2001. Mining Journal Books, Edenbridge, p 486.

Darken, L.S. (1949). Melting Point of Magnetite-Silica Mixtures in Air. *J. Am. Chem. Soc.*, **71** (3), 1114–1114

Duchesne, J.C., Liégeois, J.P., 2015. The origin of nelsonite and high-Zr ferrodiorite associ- ated with Proterozoic anorthosite. *Ore Geol. Rev.* **71**, 40–56.

Eales, H. V. and Costin, G. (2012). Crustally contaminated komatiite: Primary source of the chromitites and marginal, Lower, and Critical zone magmas in a staging chamber beneath the Bushveld Complex. *Economic Geology* **107**, 645–665.

Eales, H. V. and Cawthorn, R. G. (1996). The Bushveld Complex. In: Cawthorn, R. G. (ed.) Layered Intrusions. Amsterdam: Elsevier, pp. 181–230.

Engi, M. (1983). Equilibria involving Al–Cr spinel: Mg–Fe exchange with olivine. Experimental thermodynamic analysis, and consequences for geothermometry. *Am J Sci* **238-A**, 29–71

Fabries, J. (1979). Spinel–olivine geothermometer in peridotites from ultramafic complexes. *Contrib Mineral Petrol* **69**, 329–336

Frost, B., Lindsley, D. (1991). Chapter 12. Occurrence of iron-titanium oxides in igneous rocks. In: Linsley, D.H. (Ed.), Oxide Minerals: Petrologic and magnetic significance Reviews in Mineralogy (Mineralogical Society of America). **25**, pp. 433–468.

Ganino, C., Harris, C., Arndt, N. T., Prevec, S. A. and Howarth, G. H. (2013). Assimilation of carbonate country rock by the parent magma of the Panzhihua Fe-Ti-V deposit (SW China): Evidence from stable isotopes. *Geoscience Frontiers*. Elsevier Ltd **4**, 547–554.

Ghiorso, M. S., and Sack, R. O. (1995). Chemical mass transfer in magmatic processes IV. A revised and internally consistent thermodynamic model for the interpolation and extrapolation of liquid-solid equilibria in magmatic systems at elevated temperatures and pressures. *Contr Min Pet*, **119**(2-3), 197-212.

Hamilton, P.J. (1977). Sr isotope and trace element studies of the Great Dyke and Bushveld mafic phase and their relation to early Proterozoic magma genesis in southern Africa. *J Petrol* **18**, 24–52.

Harney, D. M. W., Von Gruenewaldt, G. (1995). Ore-forming processes in the upper part of the Bushveld complex, South Africa. *Journal of African Earth Sciences* **20**, 77–89.

Harney, D. M. W., Merkle, R. K. W. and von Gruenewaldt, G. (1990). Platinum-group element behavior in the lower part of the Upper Zone, Eastern Bushveld Complex—implications for the formation of the main magnetite layer. *Economic Geology* **85**, 1777–1789.

Hatton, C. J. and Schweitzer, J. K. (1995). Evidence for synchronous extrusive and intrusive Bushveld magmatism. *Journal of African Earth Sciences* **21**, 579–594.

He, H. L., Yu, S. Y., Song, X. Y., Du, Z. S., Dai, Z. H., Zhou, T. and Xie, W. (2016). Origin of nelsonite and Fe-Ti oxides ore of the Damiao anorthosite complex, NE China: Evidence from trace element geochemistry of apatite, plagioclase, magnetite and ilmenite. *Ore Geology Reviews*. Elsevier B.V. **79**, 367–381.

Huppert, H.E. and Sparks, R.S.J. (1984). Double-diffusive convection due to crystallization in magmas. *Annu. Rev. Earth Planet. Sci.*, **12,** 11-37.

Howarth, G. H. and Prevec, S. A. (2013). Hydration vs. oxidation: Modelling implications for Fe-Ti oxide crystallisation in mafic intrusions, with specific reference to the Panzhihua intrusion, SW China. *Geoscience Frontiers*. Elsevier Ltd **4**, 555–569.

Howarth, G. H., Prevec, S. A. and Zhou, M. F. (2013). Timing of Ti-magnetite crystallisation and silicate disequilibrium in the Panzhihua mafic layered intrusion: Implications for ore-forming processes. *Lithos*. Elsevier B.V. **170-171**, 73–89.

Hunter, R.H., Sparks, R.S.J. (1987). The differentiation of the Skaergaard intrusion. *Contrib. Mineral. Petrol.* **95**, 451–461.

Hunter, R.H., Sparks, R.S.J. (1990). The differentiation of the Skaergaard intrusion. A reply. *Contrib. Mineral. Petrol.* **104**, 248–254.

Irvine, T. N. (1975). Crystallization sequences in the Muskox intrusion and other layered intrusions. 2. Origin of chromitite layers and similar deposits of other magmatic ores. *Geochimica et Cosmochimica Acta* **39**, 991–1008.

Irvine, T.N., Andersen, J.C.O., Brooks, C.K. (1998). Included blocks (and blocks within blocks) in the Skaergaard intrusion: geological relations and the origins of rhythmic modally graded layers. *Geol Soc Amer Bull* **110**: 1398–1447.

Irving, A.J. (1978). A review of experimental studies of crystal/ liquid trace element partitioning, *Geochim. Cosmochim. Acta* **42**, 743-770.

Jakobsen, J.K., Veksler, I.V., Tegner, C., Brooks, C.K. (2005). Immiscible iron- and silica-rich melts in basalt petrogenesis documented in the Skaergaard intrusion. *Geology* **33**, 885–888.

Kent, L.E. (1980). Stratigraphy of South Africa, Part 1. Lithostratigraphy of the Republic of South Africa, South West Africa/Namibia and the Republics of Bophuthatswana, Transkei and Venda. South African Committee for Stratigraphy, Geological Survey South Africa, Handbook 8, 690 p.

Klemm, D. D., Henckel, J., Dehm, R. and von Gruenewaldt, G. (1985). The geochemistry of titanomagnetite in magnetite layers and their host rocks of the Eastern Bushveld Complex. *Economic Geology* **80**, 1075–1088.

Klemme, S., Gunther, D., Hametner, K., Prowatke, S. and Zack, T. (2006). The partitioning of trace elements between ilmenite, ulvöspinel, armalcolite and silicate melts with implications for the early differentiation of the moon. *Chemical Geology* **234**: 251-263.

Kolker, A. (1982). Mineralogy and geochemistry of Fe-Ti oxide and apatite (nelsonite) deposits and evaluation of the liquid immiscibility hypothesis: *Economic Geology*, **77**, 1146-1158.

Kruger, F. J. (1994). The Sr-isotopic stratigraphy of the western Bushveld Complex. South *African Journal of Geology* **97**, 393–398.

Kruger, F. J. (2005). Filling the Bushveld Complex magma chamber: lateral expansion, roof and floor interaction, magmatic unconformities, and the formation of giant chromitite, PGE and Ti-V-magnetitite deposits, *Mineralium Deposita* **40**, 451–472.

Kruger, F. J. and Smart, R. (1987). Diffusion of trace elements during bottom crystallization of double-diffusive convection systems: The magnetitite layers of the Bushveld Complex. *Journal of Volcanology and Geothermal Research* **34**, 133–142.

Latypov, R., Chistyakova, S., Page, A. and Hornsey, R. (2015). Field evidence for the In Situ crystallization of the merensky reef. *J Petrol* **56**, 2341–2372.

Liermann, H.P, and Ganguly, J. (2002). Diffusion coefficients of Fe2+ and Mg in aluminous spinel: experimental determination and applications to terrestrial and planetary problems. *Geochim Cosmochim Acta* **66**, 2903–2913

Lipin, B.R. (1993). Pressure increases, the formation of chromite seams, and the development of the ultramafic series in the Stillwater Complex, Montana. *J Petrol* **34**: 955–976.

London, D. (2008). Pegmatites. *Can Min Spec Pub* 10, 374p.

Lowell, R.P. (1985). Double-diffusive convection in partially molten silicate systems: Its role during magma production and in magma chambers. *J. of Volcanology and Geothermal Research*, 26, 1-2, 1-24.

Maier, W. D., Barnes, S.-J. and Groves, D. I. (2012). The Bushveld Complex, South Africa: formation of platinum–palladium, chrome- and vanadium-rich layers via hydrodynamic sorting of a mobilized cumulate slurry in a large, relatively slowly cooling, subsiding magma chamber. *Mineralium Deposita* **48**, 1–56.

McBirney, A.R. and Naslund, H.R. (1990). The differentiation of the Skaergaard Intrusion: a discussion of Hunter and Sparks. *Contr Min Pet*, **104**, 235-240.

McCarthy, T. S. and Cawthorn, R. G. (1983). The geochemistry of vanadiferous magnetite in the bushveld complex: Implications for crystallization mechanisms in layered complexes. *Mineralium Deposita* **18**, 505–518.

Merkle, R. K. W. and von Gruenewaldt, G. (1986). Compositional variation of Co-rich pentlandite: relation to the evolution of the Upper Zone of the western Bushveld Complex, South Africa. *Canadian Mineralogist* **24**, 529–546.

Molyneux, T.G. (1970). The geology of the area in the vicinity of Magnet Heights, Eastern Transvaal, with special reference to the magnetic iron ore. Special Publication of the Geological Society of South Africa, **1**, 228-241.

Molyneux, T.G. (1974) A geological investigation of the Bushveld Complex in Sekhuhuneland and part of the Steelpoort valley. *Trans Geol Soc S Afr* **77**:329–338.

Mondal, S.K. and Mathez, E.A. (2007). Origin of the UG2 chromitite layer, Bushveld Complex. *J Petrol* **48**, 495–510.

Morse, S.A. (1990). The differentiation of the Skaergaard Intrusion: a discussion of Hunter and Sparks. *Contr Min Pet*, **104**, 240-244.

Mungall, (J.E.), Kamo, S.L. and McQuade, S. (2016). U–Pb geochronology documents out-of-sequence emplacement of ultramafic layers in the Bushveld Igneous Complex of South Africa. *Nature Communications* **7**, 1-13, doi:10.1038/ncomms13385

Naldrett AJ (2009). Fundamentals of magmatic sulfide deposits. In: Li C, Ripley EM (eds) New developments in magmatic Ni–Cu and PGE deposits. Geol Publ House, 1–26.

Naldrett, A.J., Wilson, A., Kinnaird, J., Yudovskaya, M., and Chunnett, G. (2012). The origin of chromitites and related PGE mineralization in the Bushveld Complex: new mineralogical and petrological constraints. *Min Deposita* **47**, 209–232.

Naslund, H.R. (1976) Liquid immiscibilityin the system $KAlSi_3O_8$-$NaAlSi_3O_8$-FeO-Fe_2O_3- SiO_2 and its application to natural magmas. *Year Book*, Carnegie Institution of Washington, **75**, 592-597.

Naslund H.R. (1983). The effect of oxygen fugacity on liquid immiscibility in iron bearing silicate melts. *American Journal of Science*, **283**, 1034-1059.

Olsson, J. R., Söderlund, U., Hamilton, M. a., Klausen, M. B. and Helffrich, G. R. (2011). A late Archaean radiating dyke swarm as possible clue to the origin of the Bushveld Complex. *Nature Geoscience*. Nature Publishing Group **4**, 865–869.

Oosterhuis WR (1998). Andalusite, sillimanite and kyanite, 53–58. In: Wilson MGC, Anhaeusser CR (eds). The mineral resources of South Africa, handbook. Council for Geoscience, 740p.

Pang, K.N., Zhou,M.F., Lindsley, D., Zhao, D.,Malpas, J., 2008. Origin of Fe–Ti oxide ores in mafic intrusions: evidence from the Panzhihua Intrusion, SW China. *J. Petrol.* **49**, 295–313.

Pang, K.N., Li, C., Zhou,M.F., Ripley, E.M., 2009.Mineral compositional constraints on pet- rogenesis and oxide ore genesis of the late Permian Panzhihua layered gabbroic in- trusion, SW China. *Lithos* **110**, 199–214

Philpotts, A.R. (1967). Origin of certain iron-titanium oxide and apatite rocks. *Economic Geology*, **62**, 303-315.

Putnis, A. and Austrheim, H. (2010). Fluid-induced processes: metasomatism and metamorphism. *Geofluids*, **10**, 254–269.

Reynolds, I.M. (1978). A mineralogical investigation of co-existing iron-titanium oxides from various igneous rocks with special reference to some South African titaniferous iron ores. PhD thesis, Rhodes University, Grahamstown, South Africa.

Reynolds, I. M. (1985). The nature and origin of titaniferous magnetite-rich layers in the upper zone of the Bushveld complex: a review and synthesis. *Economic Geology* **80**, 1089–1108.

Robb, L. (2009) Introduction to ore-forming processes. Blackwell Science Ltd., 373 p.

Roelofse, F. and Ashwal, L. D. (2012). The Lower Main Zone in the Northern Limb of the Bushveld Complex - a 1.3 km thick sequence of intruded and variably contaminated crystal mushes. *J Petrol* **53**, 1449–1476.

Scoates, J.S., Friedman, R.M. (2008). Precise age of the platiniferous Merensky Reef, Bushveld Complex, South Africa, by the U–Pb zircon chemical abrasion ID-TIMS technique. *Economic Geology* **103**, 465–471.

Scoates, J.S., Wall, C.J., Friedman, R.M., Chamberlain, K.R. (2011). Revisiting the age of the Merensky Reef, Bushveld Complex. Abstr, Goldschmidt Conference 2011.

Scoon, R.N. (2002). A new occurrence of Merensky Reef on the flanks of the Zaaikloof dome, northeastern Bushveld Complex: Relationship between diapirism and magma replenishment. *Economic Geology*, **97**, 1037-1049.

Scoon, R. N. and Mitchell, A. A. (2012). The Upper Zone of the Bushveld Complex at Roossenekal: Geochemical Stratigraphy and Evidence of Multiple Episodes of Magma Replenishment: *South African Journal of Geology*, **114**, 515-534.

Scoon, R. N. and Mitchell, A. A. (2013). Discussion of "The Bushveld Complex, South Africa: formation of platinum–palladium, chrome- and vanadium-rich layers via hydrodynamic sorting of a mobilized cumulate slurry in a large, relatively slowly cooling, subsiding magma chamber" by Maier et al. (2013). *Mineralium Deposita* **49**, 399–404.

Smith, P.M. and Asimow, P.D. (2005). Adiabat_1ph: A new public front-end to the MELTS, pMELTS, and pHMELTS models. *Geochemistry Geophysics Geosystems,* **6**: doi: 10.1029/2004GC000816. issn: 1525-2027.

Song, X.Y., Qi, H.W., Hu, R.Z., Chen, L.M., Yu, S.Y., Zhang, J.F. (2013). Formation of thick stratiform Fe–Ti oxide layers in layered intrusion and frequent replenishment of fraction- ated mafic magma: Evidence from the Panzhihua intrusion, SW China. Geochem. Geophys.

Tegner, C. and Cawthorn, R. G. (2010). Iron in plagioclase in the Bushveld and Skaergaard intrusions: Implications for iron contents in evolving basic magmas. *Contr Min Pet* **159**, 719–730.

Tegner, C., Cawthorn, R.G., and Kruger, F.J. (2006). Cyclicity in the main and upper zones of the Bushveld Complex, South Africa: Crystallization from a zoned magma sheet: *J Petrol*, **47**, 2257–2279, doi:10.1093/petrology/egl043

Tollari, N., Toplis, M.J., Barnes, S.-J. (2006). Predicting phosphate saturation in silicate magmas: an experimental study of the effects of melt composition and temperature. *Geochim Cosmochim Acta* **70**: 1518–1536.

Tollari, N., Baker, D., Barnes, S.-J. (2008). Experimental effects of pressure and fluorine on apatite saturation in mafic magmas, with reference to layered intrusions and massif anorthosites. *Contrib Mineral Petrol* **156**: 161–175.

Toplis, M.J., Carroll,M.R. (1995). An experimental study of the influence of oxygen fugacity on Fe–Ti oxide stability, Phase relations, andmineral–melt equilibria in ferro-basaltic systems. *J. Petrol.* **36**, 1137–1171.

Toplis, M.J., Corgne, A. (2002). An experimental study of element partitioning between magnetite, clinopyroxene and iron-bearing silicate liquids with particular emphasis on vanadium. *Contr Min Petrol* **144**: 22–37.

Toplis, M.J., Carroll, M.R. (1995). An experimental-study of the influence of oxygen fugacity on Fe–Ti oxide stability, phase relations, and mineral–melt equilibria in ferro-basaltic systems. *J Petrol* **36**: 1137–1170.

Toplis, M.J., Carroll, M.R. (1996). Differentiation of ferro-basaltic magmas under conditions open and closed to oxygen: implications for the Skaergaard intrusion and other natural systems. *J Petrol* **37**: 837–858.

Ulmer, G.C. (1969). Experimental investigation of chromite spinels. *Econ Geol Monogr* **4**,114–131.

USGS, Mineral Commodities Summary (2016), http://minerals.usgs.gov/minerals/pubs/mcs/2016/mcs2016.pdf

VanTongeren, J. A (2011). The Ins and Outs of the Bushveld Complex Upper Zone. PhD thesis, School of Arts and Sciences, Columbia University, USA.

Van Tongeren, J. A. and Mathez, E. A. (2012). Large-scale liquid immiscibility at the top of the Bushveld Complex, South Africa. *Geology* **40**, 491–494.

Veksler, I.V., Dorfman, A.M., Borisov, A.A., Wirth, R., and Dingwell, D.B. (2007). Liquid immiscibility and the evolution of basaltic magmas. *J Petrol*, **48**, 2187-2210.

Velasco, F., Tornos, F. and Hanchar, J. M. (2016). Immiscible iron- and silica-rich melts and magnetite geochemistry at the El Laco volcano (northern Chile): Evidence for a magmatic origin for the magnetite deposits. *Ore Geology Reviews*. Elsevier B.V. **79**, 346–366.

van der Merwe, M. J. (2008). The geology and structure of the Rustenburg Layered Suite in the Potgietersrus/Mokopane area of the Bushveld Complex, South Africa. *Mineralium Deposita* **43**, 405–419.

Von Gruenewaldt G (1971). A petrographical and mineralogical investigation of the rocks of the Bushveld igneous complex in the Tauteshoogte–Roossenekal area of the eastern Transvaal. Ph.D. thesis, University of Pretoria, 228pp.

Von Gruenewaldt, G. (1973). The Main and Upper Zones of the Bushveld Complex in the Roossenekal area, eastern Transvaal. *Transactions Geological Society South Africa* **76**, 207-227.

Von Gruenewaldt, G. (1993). Ilmenite–apatite enrichments in the Upper Zone of the Bushveld Complex: a major titanium-rock phosphate resource. *International Geology Review* **35**, 987–1000.

Von Gruenewaldt, G., Klemm, D.D., Henckel, J., Dehm, R.M. (1985). Exsolution features in titanomagnetites from massive magnetitite layers and their host rocks of the upper zone, eastern Bushveld Complex. *Economic Geology*, **80**, 1049–1061.

Voordouw, R., Gutzmer, J., Beukes, N.J. (2009). Intrusive origin for Upper Group (UG1, UG2) stratiform chromitite seams in the Dwars River area, Bushveld Complex, South Africa. *Mineral Petrology* **97,** 75–94.

Wager, L. R. and Brown, G. M. (1968). Layered Igneous Rocks. London: Oliver and Boyd, p. 572.

Wagner P A (1927). Changes in the oxidation of iron in magnetite, *Economic Geology* **22**, 845-846

Walraven, F. (1997). Geochronology of the Rooiberg Group, Transvaal Supergroup, South Africa. University of Witwatersrand, Economic Geology Res Unit Info Circular 316, p. 21

Webb, S. J., Cawthorn, R. G., Nguuri, T. and James, D. (2004). Gravity modeling of Bushveld Complex connectivity supported by Southern African seismic experiment results. *South African Journal of Geology* **107**, 207-218.

Willemse, J. (1969). The geology of the Bushveld Igneous Complex, the largest repository of magmatic ore deposits in the world. *Economic Geology Monograph* **4**, 1–22.

Wilson, A. H. (2012). A chill sequence to the bushveld complex: Insight into the first stage of emplacement and implications for the parental magmas. *J Petrol* **53**, 1123–1168.

Wilson MGC, Anhaeusser CR (1998) The mineral resources of South Africa. Council for Geoscience, Handbook 16, 740pp

Wilson, J.R., Cawthorn, R.G., Kruger, F.J., and Grundvig, S. (1994). Intrusive origin for the unconformable Upper Zone contact in the Northern Gap, western Bushveld Complex. *South African Journal of Geology*, **97**, 462-472.

Yudovskaya, M., Kinnaird, J.A. (2010) Chromite in the Platreef (Bushveld Complex, South Africa): occurrence and evolution of its chemical composition. *Mineral Deposita* **45,** 369–391.

Yudovskaya, M., Kinnaird, J., Naldrett, A. J., Rodionov, N., Antonov, A., Simakin, S. and Kuzmin, D. (2013). Trace-element study and age dating of zircon from chromitites of the Bushveld Complex (South Africa). *Mineralogy and Petrology* **107**, 915–942.

Zhou, M.F., 2005. Geochemistry, petrogenesis and metallogenesis of the Panzhihua gabbroic layered intrusion and associated Fe–Ti–V oxide deposits, Sichuan Province, SW China. *J. Petrol.* **46**, 2253–2280

Zhou, M. F., Chen, W. T., Wang, C. Y., Prevec, S. A., Liu, P. P. and Howarth, G. H. (2013). Two stages of immiscible liquid separation in the formation of Panzhihua-type Fe-Ti-V oxide deposits, SW China. *Geoscience Frontiers*. Elsevier Ltd **4**, 481–502.

List of Tables in Appendix 1

Appendix 1

Table A1-1: Composition of Ti-magnetite (in wt%) in MML, borehole VK-05, Northern Lobe

Depth	*SiO2*	*Al2O3*	*TiO2*	*Cr2O3*	*MnO*	*FeO*	*Fe2O3**	*MgO*	*CaO*	*V2O3*	*ZnO*	*Total*
125.05	0.09	1.47	7.31	0.34	0.16	15.00	75.47	0.00	0.04	1.51	0.00	101.38
125.05	0.07	2.58	7.87	0.56	0.18	17.00	69.65	0.00	0.01	1.74	0.00	99.66
125.05	0.12	2.28	8.86	0.31	0.21	18.42	68.16	0.04	0.02	1.73	0.00	100.14
125.05	0.08	1.97	9.98	0.37	0.22	19.80	65.18	0.02	0.02	1.33	0.18	99.14
125.05	0.05	1.17	11.46	0.44	0.21	22.15	63.20	0.01	0.01	1.38	0.00	100.08
125.05	0.06	3.64	10.54	0.45	0.27	21.70	63.34	0.02	0.00	1.32	0.40	101.72
125.05	0.22	0.32	11.76	0.65	0.28	22.70	61.57	0.03	0.04	1.94	0.12	99.63
125.05	0.08	3.04	12.37	0.43	0.30	24.70	56.45	0.04	0.04	1.42	0.26	99.11
126.5	0.06	2.98	10.77	0.42	0.16	20.75	62.88	0.76	0.04	1.19	0.05	100.05
126.5	0.08	3.27	10.63	0.39	0.21	20.70	61.76	0.77	0.01	1.49	0.25	99.56
126.5	0.06	3.31	11.17	0.43	0.19	21.60	60.67	0.90	0.00	1.41	0.00	99.75
126.5	0.04	3.13	11.29	0.49	0.20	22.00	60.27	0.77	0.00	1.54	0.00	99.72
126.5	0.05	3.54	12.59	0.49	0.29	23.45	58.19	1.03	0.03	1.31	0.47	101.43
126.5	0.05	3.47	12.23	0.52	0.30	23.30	57.76	0.87	0.00	1.28	0.20	99.98
126.5	0.10	3.61	12.34	0.42	0.31	24.30	55.87	0.65	0.05	1.38	0.01	99.05
126.5	0.05	2.83	13.08	0.46	0.33	25.50	55.59	0.26	0.05	1.34	0.10	99.58
126.5	0.04	3.58	12.47	0.49	0.30	23.50	55.15	1.19	0.00	1.53	0.01	98.26
126.5	0.15	3.58	12.68	0.47	0.28	24.20	55.13	1.11	0.00	1.34	0.00	98.94
126.5	0.06	4.47	13.45	0.41	0.30	25.40	53.18	1.33	0.00	1.46	0.25	100.31
126.5	0.03	3.76	14.31	0.38	0.30	27.90	51.11	0.37	0.00	1.26	0.34	99.75
126.5	0.05	3.65	14.33	0.52	0.34	27.75	49.99	0.68	0.05	1.50	0.00	98.85
126.5	0.06	3.72	14.47	0.44	0.37	28.30	48.67	0.32	0.03	1.45	0.41	98.23
126.5	0.11	3.02	16.01	0.49	0.41	29.45	46.53	1.08	0.04	1.71	0.31	99.15
126.5	0.07	5.59	16.82	0.59	0.43	33.80	40.03	0.61	0.03	1.68	0.00	99.65
126.5	0.04	4.81	17.82	0.51	0.40	34.00	37.93	1.24	0.01	1.63	0.00	98.38
126.5	0.06	5.69	19.27	0.52	0.39	36.50	32.64	1.16	0.02	1.61	0.45	98.30
127.28	0.07	1.37	20.21	0.73	0.28	34.50	44.04	0.03	0.02	1.60	0.10	102.94
127.28	0.03	0.60	21.07	0.72	0.25	38.70	37.30	0.00	0.02	1.97	0.00	100.66
127.28	0.05	0.63	22.49	0.69	0.21	41.20	35.01	0.01	0.04	1.89	0.09	102.31
129.83	0.02	3.95	11.15	0.33	0.31	21.60	62.12	1.01	0.01	1.46	0.00	101.95
129.83	0.09	3.73	11.38	0.44	0.24	21.95	61.48	1.20	0.00	1.57	0.00	102.07
129.83	0.07	3.79	10.51	0.40	0.25	20.95	61.22	0.81	0.01	1.57	0.00	99.58
129.83	0.06	3.01	12.41	0.40	0.23	22.80	57.10	1.36	0.00	1.53	0.00	98.89
129.83	0.47	4.02	12.38	0.30	0.29	24.35	56.18	1.31	0.03	1.52	0.00	100.85
129.83	0.09	3.45	13.32	0.33	0.25	24.20	55.26	1.61	0.01	1.35	0.00	99.86
129.88	0.02	2.12	7.80	0.28	0.16	14.80	73.73	0.75	0.00	1.24	0.00	100.90
129.88	0.01	2.94	9.77	0.30	0.20	16.05	66.43	2.92	0.00	1.41	0.41	100.45
129.88	0.06	1.63	10.45	0.26	0.20	19.30	66.04	0.76	0.00	1.45	0.00	100.15
129.88	0.02	3.60	11.06	0.36	0.20	20.65	62.27	1.30	0.00	1.51	0.12	101.08
129.88	0.05	3.70	10.82	0.31	0.22	20.60	61.08	1.24	0.00	1.50	0.00	99.51
129.88	0.01	3.76	10.73	0.43	0.26	20.00	61.01	1.46	0.03	1.52	0.00	99.20

Fe2O3 calculated by stoichiometry.

Table A1-1: Composition of Ti-magnetite (in wt%) in MML, borehole VK-05, Northern Lobe (continued)

Depth	SiO2	Al2O3	TiO2	Cr2O3	MnO	FeO	Fe2O3*	MgO	CaO	V2O3	ZnO	Total
129.88	0.02	2.36	13.60	0.41	0.31	24.25	55.84	1.39	0.00	1.66	0.00	99.83
129.88	0.04	3.93	12.61	0.32	0.28	23.40	55.83	1.46	0.01	1.57	0.08	99.54
129.88	0.02	4.46	12.48	0.35	0.34	22.65	54.34	1.93	0.03	1.61	0.05	98.25
129.88	0.50	2.54	13.57	0.37	0.30	24.95	53.93	1.58	0.03	1.43	0.16	99.35
129.88	0.05	3.22	13.22	0.37	0.32	24.10	53.42	1.26	0.00	1.76	0.49	98.21
129.88	0.04	4.32	13.43	0.26	0.23	24.00	53.34	2.11	0.00	1.49	0.00	99.22
129.88	0.04	4.38	14.80	0.26	0.32	26.00	48.53	2.21	0.02	1.45	0.19	98.20
129.88	0.04	6.12	14.50	0.42	0.32	26.55	47.95	2.23	0.04	1.77	0.61	100.55
133.78	0.05	0.90	12.47	0.82	0.18	24.15	59.78	0.00	0.03	1.81	0.00	100.18
133.78	2.02	3.12	10.35	0.87	0.26	25.60	54.95	0.54	0.04	1.69	0.00	99.45
133.78	0.03	4.42	12.11	0.77	0.22	25.80	54.25	0.03	0.03	1.66	0.00	99.33
133.78	4.31	5.10	12.23	0.79	0.23	35.05	39.90	0.80	0.06	1.29	0.06	99.80
133.86	0.60	2.07	6.96	0.77	0.13	13.35	75.16	1.62	0.03	1.28	0.00	101.98
133.86	0.07	0.42	8.06	0.73	0.14	15.45	74.46	0.13	0.02	1.31	0.00	100.78
133.86	0.07	1.57	7.25	0.70	0.17	15.15	73.50	0.00	0.00	1.52	0.01	99.93
133.86	0.06	0.94	8.37	0.57	0.16	16.15	71.03	0.05	0.01	1.43	0.39	99.16
133.86	0.05	1.70	9.78	0.82	0.17	18.75	66.81	0.55	0.04	1.54	0.00	100.20
133.86	0.09	0.47	10.80	0.77	0.21	19.05	65.14	0.32	0.59	1.47	0.51	99.42
133.86	0.04	1.60	9.93	0.80	0.20	20.00	64.89	0.02	0.01	1.71	0.00	99.21
133.86	0.07	1.47	10.51	0.73	0.19	20.90	63.91	0.02	0.02	1.58	0.07	99.46
133.86	0.09	1.48	11.36	0.73	0.23	20.55	62.66	1.04	0.00	1.31	0.00	99.44
133.86	0.04	2.24	11.29	0.71	0.23	21.55	61.72	0.60	0.02	1.35	0.00	99.74
133.86	0.02	3.26	10.45	1.09	0.16	21.75	61.42	0.02	0.01	1.51	0.46	100.14
133.86	0.16	0.68	12.79	0.71	0.22	24.20	60.67	0.20	0.04	1.36	0.00	101.02
133.86	0.08	4.09	10.33	0.94	0.11	22.75	60.15	0.01	0.00	1.61	0.00	100.06
133.86	0.06	1.69	11.99	0.80	0.27	23.65	58.92	0.04	0.03	1.64	0.00	99.08
133.86	0.04	1.99	12.94	0.62	0.27	24.40	58.73	0.44	0.01	1.32	0.22	100.97
133.86	0.06	2.51	11.99	0.76	0.18	24.10	57.94	0.00	0.02	1.43	0.13	99.12
133.86	0.05	1.74	13.37	0.71	0.22	26.15	56.53	0.01	0.01	1.49	0.00	100.27
133.86	1.12	2.15	11.61	0.83	0.15	25.50	55.65	0.31	0.01	1.73	0.00	99.05
133.86	0.04	2.78	13.22	0.69	0.22	26.40	55.26	0.10	0.00	1.36	0.00	100.07
133.86	0.07	4.80	11.87	0.72	0.23	25.00	54.51	0.12	0.00	1.47	0.53	99.31
133.86	0.53	1.35	13.59	0.68	0.21	26.75	54.29	0.22	0.07	1.47	0.24	99.40
133.86	0.03	2.77	14.00	0.73	0.26	27.75	53.04	0.06	0.04	1.44	0.05	100.17
133.86	0.05	2.45	14.40	0.75	0.25	28.40	52.16	0.03	0.00	1.39	0.02	99.90
133.86	0.05	4.76	13.08	0.71	0.21	27.60	50.62	0.06	0.01	1.53	0.16	98.78
133.86	1.34	1.94	13.38	0.70	0.17	28.70	50.59	0.41	0.03	1.39	0.02	98.68
133.86	0.08	3.48	14.62	0.65	0.27	29.00	48.94	0.04	0.04	1.35	0.57	99.04
133.86	3.36	5.29	10.74	0.75	0.21	28.85	48.17	1.67	0.03	1.47	0.00	100.54
133.86	0.06	3.49	14.90	0.76	0.26	29.90	47.38	0.03	0.00	1.14	0.00	97.92
133.86	0.08	1.44	16.74	0.89	0.19	32.10	47.30	0.02	0.05	1.48	0.00	100.29

Fe2O3 calculated by stoichiometry

Table A2-1: Composition of plagioclase (in wt%) in MML, Borehole VK-05, Northern Lobe Depth 125.05 m

Comment	SiO2	TiO2	Al2O3	FeO	MnO	MgO	CaO	Na2O	K2O	Total	Si	Ti	Al	Fe	Mn	Mg	Ca	Na	K	Total	An
125.05l1	54.2	0.03	28.6	0.13	0	0.03	11	4.95	0.36	99.4	2.463	0.001	1.534	0.005	0	0.002	0.537	0.436	0.021	4.998	54
125.05l1	54	0.03	28.9	0.29	0	0.02	11.3	4.83	0.34	99.8	2.448	0.001	1.545	0.011	0	0.001	0.549	0.424	0.02	5	55.3
125.05l1	53.3	0.03	28.8	0.26	0.02	0.02	11.3	4.78	0.31	98.7	2.441	0.001	1.553	0.01	0.001	0.001	0.553	0.425	0.018	5.003	55.5
125.05l1	52.2	0	29.4	0.36	0	0.01	11.7	4.85	0.31	98.8	2.398	0	1.594	0.014	0	0.001	0.575	0.432	0.018	5.031	56.1
125.05l1	52.7	0.07	29.4	0.29	0	0.02	11.8	4.68	0.27	99.2	2.408	0.002	1.582	0.011	0	0.001	0.579	0.415	0.016	5.014	57.3
125.05l1	53.2	0.02	29.3	0.29	0	0.03	11.2	4.81	0.27	99.1	2.429	0.001	1.574	0.011	0	0.002	0.546	0.425	0.016	5.004	55.3
125.05l1	53.6	0.05	29	0.27	0.03	0.02	11	4.99	0.3	99.3	2.442	0.002	1.556	0.01	0.001	0.001	0.538	0.441	0.017	5.008	54
125.05l1	53.4	0.08	29.3	0.27	0	0.01	11.3	4.75	0.31	99.4	2.43	0.003	1.571	0.01	0	0.001	0.548	0.419	0.018	5	55.6
125.05l1	54	0.04	28.8	0.16	0.01	0.02	11.3	4.69	0.3	99.2	2.456	0.001	1.543	0.006	0	0.001	0.548	0.414	0.017	4.987	56
125.05l1	53	0.02	29	0.2	0	0.01	11.5	4.6	0.3	98.6	2.432	0.001	1.566	0.008	0	0.001	0.564	0.409	0.018	4.998	56.9
125.05l1	53.7	0.04	29.3	0.32	0.03	0.01	11.3	4.87	0.31	100	2.432	0.001	1.564	0.012	0.001	0.001	0.55	0.427	0.018	5.007	55.3
125.05l1	53.3	0.05	29.2	0.3	0.03	0.01	11.3	4.67	0.33	99.2	2.428	0.002	1.572	0.011	0.001	0.001	0.553	0.413	0.019	5	56.1
125.05l1	53.7	0.04	29.1	0.32	0.03	0.02	11.3	4.97	0.27	99.7	2.437	0.001	1.555	0.012	0.001	0.001	0.551	0.438	0.016	5.011	54.8
125.05l1	54	0.08	29.4	0.34	0.03	0.02	11.5	4.66	0.34	100	2.436	0.003	1.56	0.013	0.001	0.001	0.554	0.407	0.02	4.995	56.5
125.05l1	52.9	0.03	29.3	0.26	0	0.02	11.7	4.58	0.32	99.1	2.416	0.001	1.579	0.01	0	0.001	0.573	0.406	0.019	5.005	57.4
125.05l1	53.4	0.05	29.2	0.19	0	0.02	11.5	4.64	0.32	99.3	2.431	0.002	1.569	0.007	0	0.001	0.559	0.41	0.019	4.997	56.6
125.05l1	53.1	0.04	30.6	0.31	0.02	0.02	11.6	4.69	0.28	101	2.388	0.001	1.623	0.012	0.001	0.001	0.56	0.409	0.016	5.012	56.9
125.05l1	53.9	0.03	29.1	0.31	0	0.04	11.2	4.88	0.35	99.7	2.442	0.001	1.555	0.012	0	0.003	0.542	0.429	0.02	5.004	54.7
125.05l1	52.7	0.06	29.1	0.24	0.01	0.03	11.4	4.74	0.33	98.6	2.42	0.002	1.576	0.009	0	0.002	0.56	0.422	0.019	5.011	55.9
125.05l1	53.7	0.04	29	0.27	0	0.03	11.7	4.68	0.33	99.7	2.436	0.001	1.552	0.01	0	0.002	0.568	0.412	0.019	5.002	56.9
125.05l1	54.5	0.07	28.6	0.23	0.01	0.03	10.8	4.95	0.31	99.5	2.47	0.002	1.527	0.009	0	0.002	0.526	0.435	0.018	4.99	53.7
125.05l1	52.4	0.06	29	0.34	0	0.02	11.7	4.59	0.18	98.3	2.416	0.002	1.574	0.013	0	0.001	0.577	0.41	0.011	5.005	57.8
125.05l1	53.5	0.02	29.3	0.31	0	0.02	11.4	4.85	0.21	99.6	2.432	0.001	1.566	0.012	0	0.001	0.554	0.427	0.012	5.004	55.8
125.05l1	53	0.11	29.2	0.21	0	0.01	11.6	4.66	0.23	99	2.423	0.004	1.57	0.008	0	0.001	0.569	0.413	0.013	5.001	57.2
125.05l1	53.1	0.01	29.4	0.51	0	0.03	11.7	4.55	0.24	99.5	2.417	0	1.576	0.019	0	0.002	0.573	0.402	0.014	5.003	57.9
125.05l1	53.8	0.03	29.2	0.47	0	0.03	11.5	4.74	0.37	100	2.436	0.001	1.555	0.018	0	0.002	0.555	0.416	0.021	5.004	55.9
125.05l1	53.2	0.04	28.9	0.41	0.01	0.02	11.5	4.59	0.33	98.9	2.434	0.001	1.557	0.016	0	0.001	0.562	0.408	0.019	4.999	56.8
125.05l1	51.9	0.27	30.1	0.39	0.01	0.02	12.6	4.04	0.23	99.5	2.368	0.009	1.618	0.015	0	0.001	0.617	0.357	0.013	5	62.5
125.05l1	51.2	0.15	30.8	0.46	0	0.02	13.1	3.76	0.18	99.6	2.337	0.005	1.658	0.018	0	0.001	0.639	0.333	0.01	5.001	65.1

Table A2-2: Composition of plagioclase (in wt%) in MML, Borehole VK-05, Northern Lobe Depth 126.50 m

Comment	SiO2	TiO2	Al2O3	FeO	MnO	MgO	CaO	Na2O	K2O	Total	Si	Ti	Al	Fe	Mn	Mg	Ca	Na	K	Total	An
126-5l1 Line	55.76	0.04	27.74	0.28	0.02	0.06	11.46	5.12	0.28	100.76	2.501	0.001	1.466	0.011	0.001	0.004	0.551	0.445	0.016	4.995	54.4
126-5l1 Line	55.15	0.01	27.96	0.18	0.00	0.04	11.49	5.15	0.28	100.26	2.486	0	1.486	0.007	0	0.003	0.555	0.45	0.016	5.004	54.4
126-5l1 Line	55.54	0.04	28.07	0.25	0.02	0.04	11.74	5.12	0.27	101.09	2.486	0.001	1.481	0.009	0.001	0.003	0.563	0.444	0.015	5.003	55.1
126-5l1 Line	55.10	0.06	28.18	0.60	0.02	0.04	11.69	4.84	0.27	100.80	2.475	0.002	1.492	0.023	0.001	0.003	0.563	0.421	0.015	4.995	56.4
126-5l2 Line	55.21	0.00	28.09	0.53	0.01	0.02	11.81	4.96	0.30	100.93	2.478	0	1.486	0.02	0	0.001	0.568	0.432	0.017	5.003	55.9
126-5l2 Line	55.38	0.05	27.50	0.32	0.00	0.02	11.30	5.29	0.34	100.20	2.5	0.002	1.463	0.012	0	0.001	0.547	0.463	0.02	5.008	53.1
126-5l2 Line	55.36	0.04	27.81	0.24	0.00	0.02	11.37	5.24	0.34	100.42	2.493	0.001	1.476	0.009	0	0.001	0.549	0.458	0.02	5.006	53.5
126-5l2 Line	55.34	0.06	28.02	0.20	0.02	0.02	11.49	5.06	0.32	100.53	2.488	0.002	1.485	0.008	0.001	0.001	0.553	0.441	0.018	4.997	54.6
126-5l2 Line	55.84	0.04	27.41	0.27	0.02	0.03	11.07	5.22	0.35	100.25	2.515	0.001	1.455	0.01	0.001	0.002	0.534	0.456	0.02	4.994	52.9
126-5l2 Line	56.87	0.07	26.97	0.35	0.00	0.02	10.31	5.83	0.36	100.78	2.545	0.002	1.422	0.013	0	0.001	0.494	0.506	0.021	5.005	48.4
126-5l2 Line	55.32	0.02	27.80	0.32	0.00	0.02	11.17	5.34	0.33	100.32	2.494	0.001	1.477	0.012	0	0.001	0.539	0.467	0.019	5.01	52.6
126-5l2 Line	55.28	0.08	28.26	0.58	0.00	0.05	11.62	4.97	0.31	101.15	2.475	0.003	1.491	0.022	0	0.003	0.557	0.432	0.018	5.001	55.3
126-5l1 Line	55.99	0.04	27.96	0.23	0.00	0.04	11.82	4.77	0.22	101.07	2.5	0.001	1.472	0.009	0	0.003	0.566	0.413	0.013	4.975	57.1
126-5l1 Line	55.55	0.03	27.91	0.29	0.03	0.04	11.59	4.88	0.22	100.54	2.495	0.001	1.478	0.011	0.001	0.003	0.558	0.425	0.013	4.984	56.0
126-5l1 Line	55.48	0.02	28.01	0.30	0.00	0.03	11.74	5.07	0.20	100.85	2.487	0.001	1.48	0.011	0	0.002	0.564	0.441	0.011	4.998	55.5
126-5l1 Line	55.15	0.05	27.84	0.32	0.00	0.01	11.62	5.04	0.24	100.27	2.488	0.002	1.48	0.012	0	0.001	0.562	0.441	0.014	4.998	55.3
126-5l1 Line	56.03	0.05	27.96	0.23	0.02	0.04	11.23	5.23	0.26	101.05	2.503	0.002	1.472	0.009	0.001	0.003	0.537	0.453	0.015	4.994	53.4
126-5l1 Line	55.27	0.07	27.42	0.20	0.01	0.03	11.39	5.22	0.25	99.86	2.501	0.002	1.463	0.008	0	0.002	0.552	0.458	0.014	5.001	53.9
126-5l1 Line	54.69	0.06	27.90	0.29	0.05	0.02	11.89	5.04	0.22	100.16	2.474	0.002	1.487	0.011	0.002	0.001	0.576	0.442	0.013	5.008	55.9
126-5l1	50.94	0.01	30.36	0.34	0.03	0.04	14.42	3.18	0.09	99.41	2.335	0	1.64	0.013	0.001	0.003	0.708	0.283	0.005	4.989	71.1
126-5l4	49.34	0.02	31.35	0.29	0.02	0.04	15.58	2.61	0.06	99.31	2.272	0.001	1.702	0.011	0.001	0.003	0.769	0.233	0.004	4.995	76.4
126-5l4	49.72	0.01	31.13	0.34	0.00	0.02	15.45	2.72	0.06	99.45	2.286	0	1.687	0.013	0	0.001	0.761	0.243	0.004	4.994	75.5
126-5l4	49.49	0.07	30.97	0.31	0.01	0.05	15.26	2.82	0.07	99.05	2.284	0.002	1.685	0.012	0	0.003	0.755	0.253	0.004	4.999	74.6
126-5l5 Line	49.29	0.03	30.89	0.65	0.00	0.08	15.39	2.59	0.09	99.01	2.28	0.001	1.684	0.025	0	0.006	0.763	0.232	0.005	4.996	76.3
126-5l5 Line	54.76	0.04	27.92	0.27	0.03	0.04	11.68	5.01	0.20	99.95	2.479	0.001	1.489	0.01	0.001	0.003	0.566	0.439	0.012	5.001	55.7
126-5l5 Line	54.89	0.04	27.67	0.32	0.00	0.06	11.34	4.89	0.30	99.51	2.492	0.001	1.481	0.012	0	0.004	0.552	0.431	0.017	4.99	55.2
126-5l5 Line	54.04	0.03	28.10	0.32	0.00	0.05	11.77	4.69	0.24	99.24	2.464	0.001	1.51	0.012	0	0.003	0.575	0.415	0.014	4.994	57.3
126-5l6o1	53.08	0.04	28.70	0.36	0.00	0.02	12.54	4.52	0.19	99.45	2.423	0.001	1.544	0.014	0	0.001	0.613	0.4	0.011	5.009	59.9
126-5l6o2	53.59	0.03	28.88	0.43	0.00	0.03	12.35	4.49	0.22	100.02	2.43	0.001	1.544	0.016	0	0.002	0.6	0.395	0.013	5.001	59.5
126-5l6o3	53.55	0.03	28.63	0.19	0.02	0.05	12.45	4.60	0.29	99.81	2.434	0.001	1.534	0.007	0.001	0.003	0.606	0.406	0.017	5.009	58.9
126-5l6o4	54.03	0.02	28.00	0.35	0.00	0.05	11.77	4.67	0.26	99.15	2.466	0.001	1.506	0.013	0	0.003	0.576	0.413	0.015	4.994	57.4
126-5l1	54.44	0.00	28.27	0.30	0.03	0.05	11.70	4.70	0.28	99.77	2.468	0	1.51	0.011	0.001	0.003	0.568	0.413	0.016	4.992	57.0
126-5l1	54.19	0.01	28.32	0.31	0.00	0.05	11.93	4.80	0.32	99.93	2.457	0	1.513	0.012	0	0.003	0.58	0.422	0.019	5.006	56.8
126-5l1	54.27	0.00	28.24	0.32	0.01	0.05	12.07	4.73	0.27	99.96	2.46	0	1.509	0.012	0	0.003	0.586	0.415	0.016	5.001	57.6
126-5l2 Line	54.90	0.01	27.84	0.30	0.01	0.04	11.30	5.05	0.37	99.82	2.487	0	1.486	0.011	0	0.003	0.548	0.444	0.021	5.002	54.1
126-5l2 Line	54.88	0.03	27.93	0.38	0.01	0.03	11.39	5.18	0.30	100.13	2.481	0.001	1.488	0.014	0	0.002	0.552	0.454	0.017	5.009	54.0
126-5l2 Line	55.38	0.04	27.53	0.18	0.02	0.05	11.11	5.31	0.32	99.94	2.503	0.001	1.467	0.007	0.001	0.003	0.538	0.465	0.018	5.004	52.7
126-5l2 Line	54.92	0.01	28.02	0.29	0.03	0.06	11.48	5.18	0.26	100.25	2.479	0	1.491	0.011	0.001	0.004	0.555	0.453	0.015	5.009	54.3
126-5l2 Line	55.74	0.05	27.69	0.44	0.00	0.07	11.33	4.96	0.32	100.60	2.503	0.002	1.466	0.017	0	0.005	0.545	0.432	0.018	4.987	54.8
126-5l2 Line	55.02	0.06	27.26	0.09	0.00	0.03	11.29	5.32	0.32	99.39	2.502	0.002	1.461	0.003	0	0.002	0.55	0.469	0.019	5.009	53.0
126-5l3	55.21	0.02	27.85	0.32	0.06	0.04	11.73	5.04	0.35	100.62	2.485	0.001	1.477	0.012	0.002	0.003	0.566	0.44	0.02	5.006	55.2
126-5l3	54.78	0.06	27.35	0.32	0.01	0.06	11.41	5.02	0.38	99.39	2.494	0.002	1.468	0.012	0	0.004	0.557	0.443	0.022	5.002	54.5
126-5l3	54.16	0.04	27.95	0.28	0.01	0.06	11.75	4.84	0.32	99.41	2.467	0.001	1.501	0.011	0	0.004	0.574	0.427	0.019	5.004	56.3

Table A2-3: Composition of plagioclase (in wt%) in MML, Borehole VK-05, Northern Lobe Depth 127.28 m

Comment	SiO2	TiO2	Al2O3	FeO	MnO	MgO	CaO	Na2O	K2O	Total	Si	Ti	Al	Fe	Mn	Mg	Ca	Na	K	Total	An
127.28l1	53.1	0.02	29.4	0.18	0.03	0.02	11.3	4.76	0.29	99.14	2.421	0.001	1.583	0.007	0.001	0.001	0.554	0.421	0.017	5.006	55.8
127.28l1	54.4	0.08	28.7	0.35	0	0.03	11.4	4.53	0.32	99.80	2.462	0.003	1.528	0.013	0	0.002	0.554	0.398	0.019	4.979	57.1
127.28l1	52.8	0.04	29.5	0.23	0	0.02	11.7	4.59	0.34	99.31	2.411	0.001	1.587	0.009	0	0.001	0.572	0.406	0.02	5.007	57.3
127.28l1	52.5	0.09	28.9	0.39	0.01	0.02	11.8	4.69	0.35	98.66	2.413	0.003	1.567	0.015	0	0.001	0.58	0.418	0.02	5.019	57.0
127.28l1	52.2	0.07	29.6	0.23	0	0.03	11.5	4.45	0.28	98.34	2.403	0.003	1.605	0.009	0	0.002	0.565	0.397	0.017	5	57.7
127.28l1	52.8	0.02	29.1	0.29	0.06	0.04	11.3	4.86	0.35	98.83	2.42	0.001	1.574	0.011	0.002	0.003	0.556	0.432	0.021	5.019	55.1
127.28l1	52.2	0.06	29.6	0.43	0.02	0.02	12	4.35	0.26	98.96	2.395	0.002	1.598	0.017	0.001	0.001	0.59	0.387	0.015	5.005	59.5
127.28l1o3	52.6	0.03	29.3	0.21	0	0.03	11.4	4.59	0.4	98.58	2.415	0.001	1.585	0.008	0	0.002	0.563	0.409	0.023	5.007	56.6
127.28l1im1	52.6	0.04	29	0.21	0	0.02	11.4	4.65	0.41	98.26	2.423	0.001	1.573	0.008	0	0.001	0.563	0.416	0.024	5.009	56.1
127.28l1im5	52.1	0.06	29.2	0.27	0	0.02	11.8	4.54	0.41	98.43	2.403	0.002	1.587	0.01	0	0.002	0.582	0.406	0.024	5.017	57.5
127.28l2	53.8	0.01	28.9	0.29	0.01	0.03	10.8	5.07	0.4	99.24	2.45	0	1.549	0.011	0	0.002	0.527	0.447	0.023	5.01	52.9
127.28l2	54.6	0	28.1	0.26	0.01	0.02	10	5.51	0.46	98.96	2.491	0	1.507	0.01	0.001	0.002	0.489	0.487	0.027	5.013	48.8
127.28l2	54.2	0.03	28.1	0.28	0	0.01	10.2	5.37	0.45	98.52	2.482	0.001	1.515	0.011	0	0.001	0.499	0.477	0.026	5.011	49.8
127.28l2o1	53	0.06	29.1	0.48	0.01	0.03	11.5	4.71	0.38	99.19	2.421	0.002	1.567	0.018	0	0.002	0.563	0.418	0.022	5.013	56.1
127.28l2o3	52.5	0.02	29.6	0.28	0	0.02	11.8	4.5	0.37	99.07	2.401	0.001	1.597	0.011	0	0.001	0.578	0.399	0.022	5.01	57.9
127.28l2o4	52	0.03	29.2	0.26	0	0.01	11.8	4.57	0.37	98.25	2.403	0.001	1.589	0.01	0	0	0.583	0.41	0.022	5.018	57.4
127.28l2im1	52.3	0.07	29.2	0.26	0.02	0.02	11.6	4.53	0.39	98.37	2.408	0.003	1.586	0.01	0.001	0.001	0.574	0.404	0.023	5.01	57.3
127.28l2im2	52.3	0.07	29.4	0.26	0	0.05	11.7	4.5	0.39	98.71	2.404	0.003	1.591	0.01	0	0.003	0.576	0.401	0.023	5.01	57.6
127.28l2im3	52.3	0.05	29.1	0.26	0	0.02	11.7	4.47	0.37	98.34	2.412	0.002	1.581	0.01	0	0.001	0.579	0.399	0.022	5.006	57.9

Table A2-4: Composition of plagioclase (in wt%) in MML, Borehole VK-05, Northern Lobe Depth 129.83 m

Comment	SiO2	TiO2	Al2O3	FeO	MnO	MgO	CaO	Na2O	K2O	Total	Si	Ti	Al	Fe	Mn	Mg	Ca	Na	K	Total	An
129.83l2	53.7	0.08	28.9	0.24	0	0.06	11.2	5.03	0.32	99.55	2.442	0.003	1.548	0.009	0	0.004	0.545	0.443	0.018	5.012	54.2
129.83l2	54.2	0.07	29.2	0.15	0	0.03	11.2	4.89	0.32	100.01	2.446	0.003	1.553	0.006	0	0.002	0.543	0.428	0.018	4.998	54.9
129.83l2	54.3	0.02	29.1	0.23	0.01	0.04	11.1	5.06	0.36	100.28	2.448	0.001	1.549	0.009	0	0.003	0.537	0.442	0.021	5.009	53.7
129.83al2	52.1	0.02	30.9	0.32	0	0.04	13.3	3.86	0.14	100.68	2.352	0.001	1.644	0.012	0	0.002	0.641	0.338	0.008	4.998	64.9
129.83l1	52.8	0	30.3	0.31	0	0.06	12.5	4.07	0.18	100.26	2.386	0	1.614	0.012	0	0.004	0.608	0.357	0.011	4.991	62.3
129.83l1	54.4	0.1	29.3	0.25	0	0.04	11.5	4.83	0.26	100.66	2.441	0.003	1.55	0.009	0	0.003	0.555	0.42	0.015	4.998	56.1
129.83l1	54.3	0.07	29.6	0.31	0.05	0.05	11.6	4.95	0.13	101.04	2.431	0.002	1.56	0.012	0.002	0.003	0.558	0.43	0.007	5.005	56.1
129.83l1	55	0.04	30.1	0.39	0.02	0.05	11.8	4.42	0.1	101.9	2.434	0.001	1.571	0.014	0.001	0.004	0.561	0.379	0.006	4.971	59.3
129.83l1	53.5	0.04	29.3	0.49	0	0.46	11.5	4.63	0.1	99.97	2.42	0.001	1.563	0.019	0	0.031	0.556	0.406	0.006	5.003	57.4
129.83l2	53.7	0.01	30.1	0.34	0	0.03	12.1	4.49	0.09	100.91	2.408	0	1.593	0.013	0	0.002	0.582	0.391	0.005	4.993	59.5
129.83l2	53.8	0.06	29.3	0.31	0	0.06	11.3	4.84	0.19	99.83	2.435	0.002	1.562	0.012	0	0.004	0.548	0.425	0.011	4.999	55.7
129.83x1	53.4	0.05	29.6	0.16	0.03	0.03	11.8	4.48	0.14	99.67	2.419	0.002	1.584	0.006	0.001	0.002	0.572	0.394	0.008	4.989	58.7
129.83x1	51.5	0.05	30.7	0.28	0.05	0.02	13	3.89	0.08	99.54	2.349	0.002	1.65	0.011	0.002	0.001	0.636	0.344	0.005	4.999	64.6

Table A2-5: Composition of plagioclase (in wt%) in MML, Borehole VK-05, Northern Lobe Depth 129.88 m

Comment	SiO2	TiO2	Al2O3	FeO	MnO	MgO	CaO	Na2O	K2O	Total	Si	Ti	Al	Fe	Mn	Mg	Ca	Na	K	Total	An
129-88l1 Line 001	53.16	0.07	30.04	0.51	0.02	0.00	11.17	4.70	0.26	99.93	2.407	0.002	1.603	0.019	0.001	0	0.542	0.413	0.015	5.003	55.9
129-88l1 Line 002	53.56	0.07	29.61	0.18	0.02	0.00	11.02	4.81	0.28	99.55	2.429	0.002	1.583	0.007	0.001	0	0.536	0.423	0.016	4.996	55.0
129-88l1 Line 004	55.11	0.04	28.76	0.24	0.02	0.03	10.02	5.31	0.37	99.90	2.484	0.001	1.528	0.009	0.001	0.002	0.484	0.464	0.021	4.994	49.9
129-88l1 Line 005	55.45	0.08	29.11	0.23	0.01	0.04	10.40	5.36	0.34	101.02	2.474	0.003	1.531	0.009	0	0.003	0.497	0.464	0.019	4.999	50.7
129-88l1 Line 006	54.89	0.07	29.13	0.34	0.00	0.01	10.28	5.34	0.28	100.34	2.466	0.002	1.543	0.013	0	0.001	0.495	0.465	0.016	5	50.7
129-88l1 Line 008	53.16	0.04	29.60	0.46	0.02	0.13	10.92	4.88	0.32	99.53	2.417	0.001	1.586	0.017	0.001	0.009	0.532	0.43	0.019	5.012	54.2
129-88l2 Line 001	53.62	0.05	29.49	0.33	0.04	0.06	10.95	5.18	0.11	99.83	2.428	0.002	1.574	0.012	0.001	0.004	0.531	0.454	0.007	5.014	53.5
129-88l2 Line 002	53.45	0.06	29.47	0.47	0.00	0.04	10.91	4.98	0.21	99.59	2.427	0.002	1.577	0.018	0	0.003	0.531	0.438	0.012	5.008	54.1
129-88l2 Line 003	53.68	0.06	29.93	0.39	0.03	0.02	11.10	4.92	0.28	100.41	2.418	0.002	1.589	0.015	0.001	0.001	0.536	0.43	0.016	5.008	54.6
129-88l2 Line 004	53.35	0.06	29.86	0.32	0.00	0.03	11.15	4.86	0.27	99.90	2.415	0.002	1.593	0.012	0	0.002	0.541	0.427	0.015	5.007	55.0
129-88l2 Line 005	54.04	0.04	29.38	0.20	0.00	0.01	10.60	5.26	0.30	99.83	2.444	0.001	1.566	0.008	0	0.001	0.513	0.461	0.018	5.011	51.7
129-88l2 Line 006	53.94	0.00	29.37	0.24	0.01	0.08	10.76	4.86	0.31	99.57	2.444	0	1.569	0.009	0.001	0.005	0.522	0.427	0.018	4.994	54.0
129-88l1 Line 001	54.21	0.06	28.66	0.28	0.02	0.03	10.35	5.49	0.17	99.27	2.464	0.002	1.535	0.011	0.001	0.002	0.504	0.484	0.01	5.013	50.5
129-88l1 Line 002	54.36	0.05	29.11	0.42	0.00	0.04	10.46	5.63	0.22	100.29	2.45	0.002	1.547	0.016	0	0.002	0.505	0.492	0.013	5.027	50.0
129-88l1 Line 003	52.05	0.03	30.34	0.49	0.02	0.22	11.98	4.04	0.24	99.41	2.373	0.001	1.631	0.019	0.001	0.015	0.585	0.357	0.014	4.996	61.2
129-88l1 Line 004	53.22	0.07	29.57	0.36	0.01	0.03	11.16	4.98	0.20	99.60	2.418	0.002	1.583	0.014	0	0.002	0.543	0.439	0.012	5.014	54.6
129-88l1 Line 005	53.34	0.07	29.83	0.40	0.02	0.02	10.95	5.04	0.22	99.89	2.415	0.003	1.592	0.015	0.001	0.001	0.531	0.443	0.013	5.014	53.8
129-88l1 Line 006	53.26	0.02	29.74	0.41	0.04	0.02	11.03	4.96	0.21	99.69	2.417	0.001	1.591	0.016	0.001	0.001	0.537	0.436	0.012	5.011	54.5
129-88l1 Line 001	53.33	0.04	29.52	0.25	0.00	0.03	11.11	5.03	0.26	99.57	2.423	0.001	1.58	0.01	0	0.002	0.541	0.443	0.015	5.015	54.2
129-88l1 Line 003	54.49	0.08	28.89	0.21	0.00	0.02	10.21	5.42	0.32	99.64	2.466	0.003	1.541	0.008	0	0.001	0.495	0.475	0.019	5.008	50.1
129-88l1 Line 004	54.63	0.10	28.79	0.37	0.00	0.03	10.30	5.49	0.29	100.00	2.466	0.004	1.532	0.014	0	0.002	0.498	0.48	0.016	5.013	50.1
129-88l1 Line 005	54.52	0.07	28.68	0.20	0.00	0.04	10.22	5.53	0.27	99.53	2.47	0.003	1.532	0.008	0	0.003	0.496	0.486	0.015	5.012	49.7
129-88l1 Line 006	54.41	0.05	29.00	0.34	0.02	0.03	10.52	5.35	0.17	99.89	2.458	0.002	1.544	0.013	0.001	0.002	0.509	0.469	0.01	5.008	51.5
129-88l1 Line 001	53.48	0.08	29.41	0.17	0.03	0.04	10.89	5.14	0.13	99.37	2.431	0.003	1.575	0.006	0.001	0.003	0.53	0.453	0.007	5.009	53.5
129-88l1 Line 002	53.93	0.04	29.41	0.29	0.00	0.02	10.70	5.44	0.20	100.03	2.437	0.001	1.566	0.011	0	0.002	0.518	0.476	0.011	5.023	51.5
129-88l1 Line 006	53.12	0.02	29.76	0.25	0.02	0.06	10.66	5.13	0.19	99.21	2.419	0.001	1.597	0.01	0.001	0.004	0.52	0.453	0.011	5.014	52.8

Table A2-6: Composition of plagioclase (in wt%) in MML, Borehole VK-05, Northern Lobe, Depth 129.97 m

Comment	SiO2	TiO2	Al2O3	FeO	MnO	MgO	CaO	Na2O	K2O	Total	Si	Ti	Al	Fe	Mn	Mg	Ca	Na	K	Total	An
129.97l1	52.5	0.04	29.5	0.32	0.01	0.02	11.8	4.47	0.18	98.86	2.406	0.001	1.592	0.012	0	0.001	0.58	0.397	0.011	5	58.7
129.97l2	52.6	0.07	29.5	0.27	0	0.02	11.7	4.55	0.2	98.9	2.407	0.002	1.592	0.01	0	0.001	0.574	0.404	0.012	5.002	58
129.97l5	52.4	0.07	29.5	0.26	0	0.03	11.8	4.59	0.17	98.81	2.403	0.002	1.594	0.01	0	0.002	0.578	0.408	0.01	5.007	58
129.97l6	52.3	0.09	29.4	0.38	0.02	0.04	11.6	4.4	0.12	98.38	2.404	0.003	1.596	0.015	0.001	0.003	0.574	0.392	0.007	4.995	59
129.97l7	52.7	0.05	29.7	0.4	0.05	0.04	11.9	4.56	0.12	99.44	2.401	0.002	1.594	0.015	0.002	0.003	0.58	0.403	0.007	5.006	58.6
129.97l8	50.9	0.06	30.5	0.32	0	0.03	13	3.8	0.12	98.74	2.342	0.002	1.656	0.012	0	0.002	0.64	0.339	0.007	5.001	64.9
129.97x2	49.1	0.01	32.3	0.55	0.03	0.04	14.5	2.95	0.01	99.45	2.255	0	1.746	0.021	0.001	0.003	0.713	0.262	0.001	5.003	73.1
129.97x3	53	0.07	29.3	0.23	0	0.05	11.8	4.57	0.09	99.1	2.419	0.002	1.577	0.009	0	0.003	0.574	0.404	0.005	4.995	58.4
129.97x3	53.3	0.07	29.5	0.24	0	0.06	11.8	4.65	0.06	99.66	2.42	0.002	1.575	0.009	0	0.004	0.574	0.409	0.003	4.997	58.2
129.97x3	52.3	0.04	29.6	0.28	0	0.05	11.8	4.47	0.11	98.62	2.398	0.001	1.603	0.011	0	0.003	0.579	0.398	0.006	5.001	58.9
129.97x1	49.7	0.07	30.9	0.44	0	0.04	13.8	3.32	0.08	98.42	2.303	0.002	1.689	0.017	0	0.003	0.685	0.298	0.005	5.002	69.3
129.97x2	50.2	0.03	31.4	0.43	0	0.03	13.8	3.3	0.06	99.28	2.302	0.001	1.7	0.016	0	0.002	0.679	0.293	0.004	4.996	69.6
129.97x3	50	0.02	31	0.24	0.03	0.03	13.7	3.25	0.07	98.35	2.314	0.001	1.688	0.009	0.001	0.002	0.679	0.291	0.004	4.989	69.7
129.97x5	49	0.03	31.9	0.52	0	0.04	14.5	2.95	0.06	99.05	2.262	0.001	1.734	0.02	0	0.003	0.718	0.263	0.004	5.004	72.9
129.97l1o1	53.8	0.03	28.9	0.26	0.01	0.06	11	4.91	0.23	99.15	2.449	0.001	1.55	0.01	0	0.004	0.536	0.434	0.013	4.998	54.5
129.97l1o2	53.5	0.07	28.9	0.2	0.01	0.03	11.1	5	0.23	99.13	2.441	0.002	1.555	0.008	0	0.002	0.543	0.442	0.013	5.007	54.4
129.97l1o3	53.4	0.08	28.5	0.34	0	0.06	11.1	4.82	0.34	98.65	2.45	0.003	1.539	0.013	0	0.004	0.546	0.428	0.02	5.002	54.9
129.97l1o4	53.2	0.05	29.3	0.19	0.02	0.02	11	5.04	0.21	99	2.429	0.002	1.575	0.007	0.001	0.001	0.537	0.446	0.012	5.01	54
129.97l1o5	53.4	0.06	29.3	0.21	0	0.04	11.3	4.67	0.17	99.14	2.432	0.002	1.572	0.008	0	0.003	0.553	0.413	0.01	4.992	56.7
129.97l1i	53.3	0.05	29.7	0.31	0	0.05	11.3	4.63	0.1	99.5	2.421	0.002	1.588	0.012	0	0.003	0.551	0.407	0.006	4.99	57.2
129.97l1i	53.8	0.03	28.4	0.22	0	0.02	10.8	5.11	0.15	98.57	2.464	0.001	1.534	0.008	0	0.001	0.528	0.454	0.009	4.999	53.3
129.97l1i	53.6	0.06	29	0.26	0.01	0.03	11.2	4.85	0.22	99.26	2.442	0.002	1.557	0.01	0	0.002	0.545	0.428	0.013	4.999	55.3
129.97l1i	53.1	0.07	29.4	0.43	0	0.05	11.5	4.72	0.23	99.5	2.419	0.002	1.574	0.016	0	0.003	0.561	0.417	0.013	5.007	56.6
129.97l2o1	53.4	0.01	29.3	0.26	0.01	0.04	11.2	4.84	0.27	99.31	2.43	0	1.571	0.01	0	0.003	0.548	0.427	0.016	5.005	55.3
129.97l2o2	53.4	0.08	29.2	0.41	0	0.01	11.1	4.9	0.24	99.43	2.431	0.003	1.567	0.016	0	0.001	0.543	0.432	0.014	5.006	54.9
129.97l2o3	53.6	0.03	29	0.18	0.01	0.02	11.1	4.86	0.23	99	2.444	0.001	1.558	0.007	0	0.001	0.543	0.43	0.013	4.998	55.1
129.97l2im1	53	0.02	29.5	0.21	0	0.05	11.7	4.66	0.14	99.32	2.415	0.001	1.583	0.008	0	0.003	0.573	0.411	0.008	5.002	57.8
129.97l2im4	52.4	0.03	29.7	0.32	0	0.01	11.9	4.64	0.21	99.25	2.396	0.001	1.601	0.012	0	0.001	0.581	0.411	0.012	5.014	57.9

Table A2-7: Composition of plagioclase (in wt%) in MML, Borehole VK-05, Northern Lobe, Depth 133.86 m

Comment	SiO2	TiO2	Al2O3	FeO	MnO	MgO	CaO	Na2O	K2O	Total	Si	Ti	Al	Fe	Mn	Mg	Ca	Na	K	Total	An
133-86l2o3	55.21	0.05	28.04	0.55	0.03	0.08	11.43	4.99	0.19	100.57	2.483	0.002	1.486	0.021	0.001	0.005	0.551	0.435	0.011	4.995	55.3
133-86l2o4	55.50	0.05	26.95	2.16	0.00	0.28	10.34	5.25	0.19	100.72	2.505	0.002	1.434	0.082	0	0.019	0.5	0.459	0.011	5.011	51.5
133-86l2o5	56.33	0.02	27.51	0.38	0.00	0.06	10.86	5.21	0.20	100.57	2.524	0.001	1.453	0.014	0	0.004	0.521	0.453	0.011	4.981	52.9
133-86l2o6	55.06	0.03	27.46	0.47	0.03	0.03	10.75	6.02	0.22	100.07	2.493	0.001	1.466	0.018	0.001	0.002	0.522	0.528	0.013	5.043	49.1
133-86l2im1	55.16	0.04	28.16	0.51	0.05	0.04	11.56	5.07	0.11	100.70	2.478	0.001	1.491	0.019	0.002	0.003	0.556	0.442	0.006	4.999	55.4
133-86l2im2	56.71	0.07	27.43	0.46	0.00	0.05	10.44	5.51	0.27	100.94	2.532	0.002	1.443	0.017	0	0.003	0.499	0.477	0.015	4.99	50.4
133-86l2im5	55.07	0.10	27.90	0.41	0.01	0.04	11.49	4.94	0.15	100.11	2.486	0.003	1.484	0.015	0	0.003	0.556	0.432	0.009	4.989	55.8
133-86l2im6	56.04	0.04	27.99	0.48	0.00	0.04	11.20	5.06	0.16	101.01	2.503	0.001	1.474	0.018	0	0.003	0.536	0.438	0.009	4.982	54.5
133-86l3o1	55.44	0.05	27.49	0.41	0.00	0.04	11.33	5.35	0.17	100.28	2.5	0.002	1.461	0.015	0	0.003	0.547	0.467	0.01	5.006	53.4
133-86l3o2	55.03	0.04	27.54	1.28	0.00	0.19	10.50	5.15	0.23	99.96	2.494	0.001	1.471	0.049	0	0.013	0.51	0.452	0.013	5.002	52.3
133-86l3o3	54.88	0.06	28.19	0.32	0.01	0.05	11.77	4.85	0.17	100.30	2.474	0.002	1.498	0.012	0	0.003	0.569	0.424	0.01	4.992	56.7
133-86l3im1	55.25	0.07	28.28	0.47	0.02	0.05	11.63	5.04	0.14	100.95	2.476	0.002	1.494	0.018	0.001	0.003	0.558	0.438	0.008	4.998	55.6
133-86l3im2	52.21	0.03	28.04	3.79	0.04	0.61	11.15	4.30	0.15	100.32	2.395	0.001	1.516	0.145	0.002	0.042	0.548	0.383	0.009	5.041	58.3
133-86l1o1	54.14	0.02	28.26	0.27	0.00	0.05	12.09	4.47	0.17	99.47	2.461	0.001	1.514	0.01	0	0.003	0.589	0.394	0.01	4.983	59.3
133-86l1o2	54.46	0.03	28.40	0.55	0.03	0.02	11.84	4.55	0.19	100.07	2.463	0.001	1.514	0.021	0.001	0.001	0.574	0.399	0.011	4.985	58.3
133-86l1im1	54.09	0.03	28.49	0.50	0.00	0.05	12.17	4.71	0.18	100.22	2.447	0.001	1.519	0.019	0	0.003	0.59	0.413	0.01	5.004	58.2
133-86l1im2	54.72	0.03	28.84	0.58	0.00	0.01	12.09	4.58	0.17	101.02	2.453	0.001	1.524	0.022	0	0.001	0.581	0.398	0.01	4.988	58.7
133-86l1im4	54.12	0.01	28.75	0.63	0.00	0.05	12.02	4.59	0.16	100.33	2.445	0	1.531	0.024	0	0.003	0.582	0.402	0.009	4.995	58.6
133-86l1im6	53.06	0.03	28.22	1.18	0.00	0.17	11.81	4.54	0.18	99.19	2.433	0.001	1.525	0.045	0	0.012	0.58	0.404	0.011	5.011	58.3
133-86l1im7	54.13	0.04	28.52	0.87	0.01	0.04	12.10	4.68	0.18	100.57	2.445	0.001	1.518	0.033	0	0.003	0.585	0.409	0.01	5.005	58.3
133-86l1im8	54.61	0.06	28.42	1.04	0.00	0.03	11.91	4.62	0.18	100.87	2.457	0.002	1.507	0.039	0	0.002	0.574	0.403	0.01	4.994	58.2
133-86l2o1	55.59	0.04	27.62	0.58	0.02	0.05	11.18	5.21	0.28	100.57	2.5	0.001	1.464	0.022	0.001	0.003	0.539	0.455	0.016	5.002	53.4
133-86l2o2	55.93	0.07	27.40	0.53	0.02	0.04	11.03	5.24	0.31	100.57	2.513	0.002	1.451	0.02	0.001	0.003	0.531	0.456	0.018	4.996	52.8
133-86l2o3	55.80	0.05	27.40	0.48	0.01	0.06	10.97	5.21	0.28	100.26	2.514	0.002	1.455	0.018	0.000	0.004	0.529	0.455	0.016	4.993	52.9
133-86l2o4	55.07	0.05	27.65	0.53	0.00	0.04	11.00	5.19	0.28	99.81	2.495	0.002	1.476	0.020	0.000	0.003	0.534	0.456	0.016	5.002	53.1
133-86l2o5	55.57	0.03	27.73	0.69	0.00	0.04	11.07	5.24	0.26	100.63	2.498	0.001	1.469	0.026	0.000	0.003	0.533	0.456	0.015	5.002	53.1

Table A2-8: Composition of plagioclase (in wt%) in MML, Borehole VK-05, Northern Lobe, Depth 133.44 m

Comment	SiO2	TiO2	Al2O3	FeO	MnO	MgO	CaO	Na2O	K2O	Total	Si	Ti	Al	Fe	Mn	Mg	Ca	Na	K	Total	An
135.44l1	54.1	0.03	28.79	0.42	0.04	0.03	11.00	4.70	0.67	99.82	2.455	0.001	1.539	0.016	0.002	0.002	0.534	0.413	0.039	5.001	54.2
135.44l1	54.4	0.06	28.97	0.45	0.02	0.02	11.57	4.59	0.40	100.44	2.449	0.002	1.538	0.017	0.001	0.001	0.559	0.401	0.023	4.991	56.9
135.44l1	55.1	0.05	28.93	0.29	0.00	0.01	11.38	4.55	0.40	100.71	2.469	0.002	1.528	0.011	0.000	0.001	0.546	0.396	0.023	4.976	56.6
135.44l1	54	0.05	28.66	0.23	0.01	0.03	11.27	4.79	0.39	99.44	2.456	0.002	1.536	0.009	0.000	0.002	0.549	0.422	0.022	4.998	55.3
135.44l1	54	0.06	29.20	0.41	0.02	0.03	11.83	4.47	0.38	100.37	2.435	0.002	1.553	0.015	0.001	0.002	0.572	0.391	0.022	4.993	58.1
135.44l1	54.5	0.00	28.61	0.40	0.00	0.03	11.12	4.70	0.41	99.81	2.469	0.000	1.526	0.015	0.000	0.002	0.539	0.413	0.023	4.987	55.3
135.44	54	0.01	28.98	0.40	0.01	0.01	11.37	4.77	0.37	99.87	2.445	0.000	1.547	0.015	0.000	0.001	0.552	0.419	0.021	5.000	55.6
135.44	53.9	0.00	28.55	0.53	0.03	0.03	10.87	4.84	0.42	99.22	2.459	0.000	1.534	0.020	0.001	0.002	0.531	0.428	0.024	4.999	54.0
135.44l1	54.3	0.06	28.50	0.20	0.00	0.02	11.27	4.74	0.42	99.53	2.466	0.002	1.525	0.008	0.000	0.001	0.548	0.417	0.024	4.991	55.4
135.44l1	54.4	0.05	28.85	0.46	0.01	0.02	11.30	4.65	0.39	100.15	2.457	0.002	1.535	0.017	0.000	0.001	0.546	0.407	0.022	4.987	56.0
135.44l1	54.9	0.01	28.22	2.40	0.00	0.33	10.63	4.09	0.35	100.88	2.470	0.000	1.497	0.090	0.000	0.022	0.513	0.357	0.020	4.969	57.6
135.44l1	52.8	0.09	29.35	0.39	0.00	0.03	11.88	4.52	0.34	99.37	2.409	0.003	1.579	0.015	0.000	0.002	0.581	0.400	0.020	5.009	58.0
135.44l1	53.8	0.04	29.26	0.29	0.00	0.01	11.71	4.52	0.36	99.96	2.434	0.001	1.561	0.011	0.000	0.001	0.568	0.397	0.021	4.994	57.6
135.44l1	53.5	0.04	29.21	0.49	0.00	0.03	11.93	4.18	0.32	99.71	2.430	0.001	1.563	0.018	0.000	0.002	0.580	0.368	0.018	4.980	60.0
135.44l1	54.7	0.08	29.01	0.37	0.01	0.00	11.48	4.63	0.33	100.60	2.457	0.003	1.536	0.014	0.000	0.000	0.553	0.403	0.019	4.985	56.7
135.44l1	53.6	0.07	29.17	0.46	0.00	0.01	11.48	4.49	0.35	99.58	2.434	0.002	1.562	0.017	0.000	0.001	0.559	0.396	0.020	4.991	57.3
135.44l1	54.6	0.08	29.05	0.15	0.02	0.02	10.98	4.95	0.27	100.09	2.459	0.003	1.543	0.006	0.001	0.001	0.530	0.432	0.015	4.990	54.2
135.44l1	54.5	0.00	28.92	0.27	0.00	0.00	11.06	4.96	0.23	99.94	2.461	0.000	1.539	0.010	0.000	0.000	0.535	0.434	0.013	4.992	54.5
135.44l1	54.1	0.06	29.15	0.14	0.02	0.02	11.41	4.91	0.32	100.09	2.442	0.002	1.552	0.005	0.001	0.001	0.552	0.430	0.018	5.003	55.2
135.44l1	54.3	0.00	28.66	0.21	0.01	0.01	11.07	4.91	0.32	99.44	2.463	0.000	1.534	0.008	0.000	0.001	0.538	0.432	0.018	4.994	54.5

Table A2-9: Composition of plagioclase (in wt%) in MML, Borehole VK-05, Northern Lobe, Depth 133.78 m

Comment	SiO2	TiO2	Al2O3	FeO	MnO	MgO	CaO	Na2O	K2O	Total	Si	Ti	Al	Fe	Mn	Mg	Ca	Na	K	Total	An
133.78l2	53.55	0.04	29.82	0.45	0.00	0.06	12.03	4.59	0.09	100.63	2.41	0.001	1.582	0.017	0	0.004	0.58	0.401	0.005	5	58.8
133.78l2	56.34	0.01	28.64	0.46	0.01	0.02	11.24	5.16	0.26	102.14	2.491	0	1.492	0.017	0	0.001	0.532	0.442	0.015	4.991	53.8
133.78l2	54.96	0.03	28.97	0.69	0.00	0.14	11.12	5.03	0.27	101.21	2.457	0.001	1.527	0.026	0	0.009	0.533	0.436	0.015	5.004	54.2
133.78l1	54.12	0.03	29.41	0.61	0.00	0.05	11.70	4.60	0.34	100.86	2.431	0.001	1.557	0.023	0	0.003	0.563	0.401	0.019	4.999	57.3
133.78l1	54.08	0.05	29.28	0.41	0.00	0.06	11.63	4.79	0.36	100.66	2.434	0.002	1.553	0.015	0	0.004	0.561	0.418	0.021	5.007	56.1
133.78l1	54.65	0.05	29.19	0.44	0.00	0.05	11.35	4.66	0.36	100.75	2.452	0.002	1.543	0.017	0	0.003	0.546	0.405	0.021	4.988	56.2
133.78l1	54.25	0.00	29.22	0.41	0.00	0.03	11.69	4.74	0.33	100.67	2.44	0	1.549	0.015	0	0.002	0.563	0.413	0.019	5.002	56.6
133.78l1	54.93	0.04	28.92	0.28	0.00	0.05	11.43	4.98	0.38	101.01	2.459	0.001	1.526	0.01	0	0.003	0.548	0.432	0.022	5.003	54.7
133.78l1	53.85	0.08	29.48	0.38	0.01	0.05	11.82	4.73	0.29	100.69	2.423	0.003	1.563	0.014	0	0.003	0.57	0.413	0.017	5.007	57.0
133.78l1	54.57	0.04	29.25	0.39	0.00	0.02	11.30	4.86	0.30	100.73	2.449	0.001	1.547	0.015	0	0.001	0.543	0.423	0.017	4.996	55.2
133.78l1	54.40	0.00	29.27	0.33	0.05	0.04	11.30	4.60	0.28	100.27	2.449	0	1.553	0.012	0.002	0.003	0.545	0.402	0.016	4.983	56.6
133.78l1	53.68	0.04	29.07	0.36	0.00	0.07	11.46	4.59	0.27	99.54	2.438	0.001	1.556	0.014	0	0.005	0.558	0.404	0.016	4.992	57.1
133.78l1	54.54	0.03	28.12	0.55	0.02	0.08	11.01	5.24	0.38	99.97	2.471	0.001	1.502	0.021	0.001	0.005	0.535	0.46	0.022	5.018	52.6
133.78l1	54.13	0.06	29.35	0.29	0.00	0.02	11.53	4.72	0.25	100.35	2.438	0.002	1.558	0.011	0	0.001	0.556	0.412	0.014	4.994	56.6

Table A2-10: Composition of plagioclase (in wt%) in MML, Borehole VK-05, Northern Lobe, Depth 133.86 m

Comment	SiO2	TiO2	Al2O3	FeO	MnO	MgO	CaO	Na2O	K2O	Total	Si	Ti	Al	Fe	Mn	Mg	Ca	Na	K	Total	An
133-86l2o3	55.21	0.05	28.04	0.55	0.03	0.08	11.43	4.99	0.19	100.57	2.483	0.002	1.486	0.021	0.001	0.005	0.551	0.435	0.011	4.995	55.3
133-86l2o4	55.50	0.05	26.95	2.16	0.00	0.28	10.34	5.25	0.19	100.72	2.505	0.002	1.434	0.082	0	0.019	0.5	0.459	0.011	5.011	51.5
133-86l2o5	56.33	0.02	27.51	0.38	0.00	0.06	10.86	5.21	0.20	100.57	2.524	0.001	1.453	0.014	0	0.004	0.521	0.453	0.011	4.981	52.9
133-86l2o6	55.06	0.03	27.46	0.47	0.03	0.03	10.75	6.02	0.22	100.07	2.493	0.001	1.466	0.018	0.001	0.002	0.522	0.528	0.013	5.043	49.1
133-86l2im1	55.16	0.04	28.16	0.51	0.05	0.04	11.56	5.07	0.11	100.70	2.478	0.001	1.491	0.019	0.002	0.003	0.556	0.442	0.006	4.999	55.4
133-86l2im2	56.71	0.07	27.43	0.46	0.00	0.05	10.44	5.51	0.27	100.94	2.532	0.002	1.443	0.017	0	0.003	0.499	0.477	0.015	4.99	50.4
133-86l2im5	55.07	0.10	27.90	0.41	0.01	0.04	11.49	4.94	0.15	100.11	2.486	0.003	1.484	0.015	0	0.003	0.556	0.432	0.009	4.989	55.8
133-86l2im6	56.04	0.04	27.99	0.48	0.00	0.04	11.20	5.06	0.16	101.01	2.503	0.001	1.474	0.018	0	0.003	0.536	0.438	0.009	4.982	54.5
133-86l3o1	55.44	0.05	27.49	0.41	0.00	0.04	11.33	5.35	0.17	100.28	2.5	0.002	1.461	0.015	0	0.003	0.547	0.467	0.01	5.006	53.4
133-86l3o2	55.03	0.04	27.54	1.28	0.00	0.19	10.50	5.15	0.23	99.96	2.494	0.001	1.471	0.049	0	0.013	0.51	0.452	0.013	5.002	52.3
133-86l3o3	54.88	0.06	28.19	0.32	0.01	0.05	11.77	4.85	0.17	100.30	2.474	0.002	1.498	0.012	0	0.003	0.569	0.424	0.01	4.992	56.7
133-86l3im1	55.25	0.07	28.28	0.47	0.02	0.05	11.63	5.04	0.14	100.95	2.476	0.002	1.494	0.018	0.001	0.003	0.558	0.438	0.008	4.998	55.6
133-86l3im2	52.21	0.03	28.04	3.79	0.04	0.61	11.15	4.30	0.15	100.32	2.395	0.001	1.516	0.145	0.002	0.042	0.548	0.383	0.009	5.041	58.3
133-86l1o1	54.14	0.02	28.26	0.27	0.00	0.05	12.09	4.47	0.17	99.47	2.461	0.001	1.514	0.01	0	0.003	0.589	0.394	0.01	4.983	59.3
133-86l1o2	54.46	0.03	28.40	0.55	0.03	0.02	11.84	4.55	0.19	100.07	2.463	0.001	1.514	0.021	0.001	0.001	0.574	0.399	0.011	4.985	58.3
133-86l1im1	54.09	0.03	28.49	0.50	0.00	0.05	12.17	4.71	0.18	100.22	2.447	0.001	1.519	0.019	0	0.003	0.59	0.413	0.01	5.004	58.2
133-86l1im2	54.72	0.03	28.84	0.58	0.00	0.01	12.09	4.58	0.17	101.02	2.453	0.001	1.524	0.022	0	0.001	0.581	0.398	0.01	4.988	58.7
133-86l1im4	54.12	0.01	28.75	0.63	0.00	0.05	12.02	4.59	0.16	100.33	2.445	0	1.531	0.024	0	0.003	0.582	0.402	0.009	4.995	58.6
133-86l1im6	53.06	0.03	28.22	1.18	0.00	0.17	11.81	4.54	0.18	99.19	2.433	0.001	1.525	0.045	0	0.012	0.58	0.404	0.011	5.011	58.3
133-86l1im7	54.13	0.04	28.52	0.87	0.01	0.04	12.10	4.68	0.18	100.57	2.445	0.001	1.518	0.033	0	0.003	0.585	0.409	0.01	5.005	58.3
133-86l1im8	54.61	0.06	28.42	1.04	0.00	0.03	11.91	4.62	0.18	100.87	2.457	0.002	1.507	0.039	0	0.002	0.574	0.403	0.01	4.994	58.2
133-86l2o1	55.59	0.04	27.62	0.58	0.02	0.05	11.18	5.21	0.28	100.57	2.5	0.001	1.464	0.022	0.001	0.003	0.539	0.455	0.016	5.002	53.4
133-86l2o2	55.93	0.07	27.40	0.53	0.02	0.04	11.03	5.24	0.31	100.57	2.513	0.002	1.451	0.02	0.001	0.003	0.531	0.456	0.018	4.996	52.8
133-86l2o3	55.80	0.05	27.40	0.48	0.01	0.06	10.97	5.21	0.28	100.26	2.514	0.002	1.455	0.018	0.000	0.004	0.529	0.455	0.016	4.993	52.9
133-86l2o4	55.07	0.05	27.65	0.53	0.00	0.04	11.00	5.19	0.28	99.81	2.495	0.002	1.476	0.020	0.000	0.003	0.534	0.456	0.016	5.002	53.1
133-86l2o5	55.57	0.03	27.73	0.69	0.00	0.04	11.07	5.24	0.26	100.63	2.498	0.001	1.469	0.026	0.000	0.003	0.533	0.456	0.015	5.002	53.1

Table A2-11: Composition of plagioclase (in wt%) in MML, Borehole VK-05, Northern Lobe, Depth 136.42 m

Comment	SiO2	TiO2	Al2O3	FeO	MnO	MgO	CaO	Na2O	K2O	Total	Si	Ti	Al	Fe	Mn	Mg	Ca	Na	K	Total	An
136.42l1o1	53.18	0.06	29.15	0.44	0.00	0.03	11.67	4.55	0.40	99.48	2.423	0.002	1.566	0.017	0	0.002	0.57	0.402	0.023	5.005	57.3
136.42l1o2	52.37	0.04	29.68	0.56	0.02	0.02	12.05	4.29	0.32	99.35	2.393	0.001	1.599	0.022	0.001	0.001	0.59	0.38	0.018	5.005	59.7
136.42l1o3	52.44	0.06	29.22	0.49	0.00	0.03	11.47	4.36	0.38	98.45	2.414	0.002	1.585	0.019	0	0.002	0.565	0.389	0.022	4.997	57.9
136.42l1o4	52.99	0.02	29.34	0.42	0.01	0.02	11.82	4.43	0.36	99.41	2.416	0.001	1.577	0.016	0	0.002	0.577	0.391	0.021	5.001	58.3
136.42l1o5	53.63	0.04	29.09	0.32	0.03	0.03	11.63	4.34	0.38	99.49	2.438	0.001	1.558	0.012	0.001	0.002	0.566	0.383	0.022	4.984	58.3
136.42l1im2	52.72	0.00	29.34	0.34	0.00	0.00	11.50	4.48	0.32	98.70	2.417	0	1.586	0.013	0	0	0.565	0.398	0.019	4.998	57.5
136.42l1im3	53.14	0.08	29.37	0.36	0.01	0.02	11.50	4.45	0.35	99.28	2.422	0.003	1.578	0.014	0.001	0.001	0.562	0.393	0.02	4.993	57.6
136.42x1	53.14	0.02	29.03	0.26	0.00	0.02	11.38	4.63	0.31	98.79	2.433	0.001	1.566	0.01	0	0.001	0.558	0.411	0.018	4.998	56.5
136.42l1	53.77	0.08	29.10	0.41	0.03	0.01	11.34	4.60	0.36	99.70	2.439	0.003	1.556	0.015	0.001	0.001	0.551	0.404	0.021	4.992	56.5
136.42l1	52.72	0.04	29.25	0.22	0.00	0.00	12.00	4.27	0.32	98.82	2.416	0.001	1.58	0.008	0	0	0.589	0.38	0.019	4.992	59.6
136.42l1	52.44	0.06	29.53	1.48	0.00	0.00	11.90	4.37	0.31	100.09	2.389	0.002	1.585	0.056	0	0	0.581	0.386	0.018	5.018	59.0
136.42l1	48.86	0.00	31.97	0.96	0.01	0.08	14.66	2.75	0.11	99.40	2.251	0	1.736	0.037	0	0.005	0.724	0.246	0.006	5.007	74.2
136.42l1	53.73	0.06	28.93	0.24	0.00	0.03	11.28	4.62	0.35	99.24	2.446	0.002	1.553	0.009	0	0.002	0.55	0.407	0.02	4.989	56.3
136.42l1	53.29	0.04	29.11	0.23	0.01	0.02	11.60	4.52	0.27	99.09	2.432	0.001	1.566	0.009	0	0.001	0.567	0.4	0.015	4.992	57.7
136.42l1	52.90	0.02	29.25	0.56	0.00	0.05	11.53	4.34	0.41	99.06	2.42	0.001	1.577	0.021	0	0.003	0.565	0.385	0.024	4.995	58.0
136.42l1	53.60	0.02	28.69	0.30	0.00	0.03	11.58	4.16	0.28	98.66	2.452	0.001	1.547	0.012	0	0.002	0.568	0.369	0.017	4.966	59.5
136.42l1	54.27	0.06	28.58	0.24	0.01	0.01	10.74	5.08	0.33	99.32	2.467	0.002	1.531	0.009	0	0.001	0.523	0.447	0.019	4.999	52.9

Table A3: Composition of orthopyroxene- Depth 129.83 m - borehole VK-05, Northern limb

Analysis	opx-37	opx-38	opx-39	opx-40	opx-41	opx-42	opx-43	opx-44	opx-50
Comment	core	core	core	core	rim	rim	rim	rim	core
SiO2	53.44	53.19	53.45	53.98	53.66	53.77	53.96	53.50	53.09
TiO2	0.25	0.29	0.25	0.26	0.23	0.20	0.13	0.22	0.23
Al2O3	1.09	1.02	1.01	1.09	1.16	1.10	0.97	1.10	0.98
Cr2O3	bd	bd	0.02	bd	0.04	bd	bd	bd	bd
FeO	18.66	18.39	18.50	17.08	16.24	17.04	17.05	17.56	18.26
MnO	0.39	0.37	0.33	0.32	0.33	0.35	0.36	0.33	0.35
NiO	bd	bd	bd	bd	bd	bd	0.04	bd	bd
MgO	24.82	24.80	25.02	24.09	23.60	25.19	24.89	24.95	26.06
CaO	1.15	1.18	0.86	3.09	5.06	0.71	0.97	0.93	1.06
Na2O	0.01	0.01	0.03	0.01	0.05	0.01	0.00	0.00	0.01
K2O	bd	bd	bd	bd	bd	bd	bd	bd	bd
Total	99.81	99.28	99.52	99.94	100.36	98.40	98.37	98.61	100.07
Cations normalized to 6 Oxygen atoms									
Si	1.963	1.963	1.966	1.974	1.960	1.983	1.991	1.976	1.944
Ti	0.007	0.008	0.007	0.007	0.006	0.006	0.004	0.006	0.006
Al	0.047	0.045	0.044	0.047	0.050	0.048	0.042	0.048	0.042
Fe2+	0.573	0.568	0.569	0.522	0.496	0.526	0.526	0.542	0.559
Mn	0.012	0.011	0.010	0.010	0.010	0.011	0.011	0.010	0.011
Mg	1.359	1.364	1.372	1.313	1.285	1.385	1.370	1.374	1.423
Ca	0.045	0.047	0.034	0.121	0.198	0.028	0.038	0.037	0.042
Na	0.001	0.000	0.002	0.000	0.003	0.001	0.000	0.000	0.001
Total	4.007	4.006	4.004	3.995	4.009	3.988	3.983	3.994	4.028
Mg#	70.344	70.623	70.674	71.542	72.149	72.490	72.245	71.695	71.779

Table A4: Composition of clinopyroxene - Depth 129.83 m - borehole VK-05, Northern limb

Sample	33cpx1	34cpx2	35cpx3	36cpx4	30cpx_1	31cpx_2	32cpx_3
Mineral	augite	augite	augite	augite	augite	augite	augite
SiO2	51.64	51.29	51.98	51.28	51.96	51.11	52.29
TiO2	0.45	0.49	0.48	0.49	0.49	0.56	0.49
Al2O3	1.96	1.99	2.01	2.06	1.98	2.12	2.02
Cr2O3	0.03	0.00	0.03	0.00	0.04	0.00	0.01
FeO	7.12	7.33	7.66	7.25	9.85	8.24	8.61
NiO	0.04	0.02	0.01	0.03	0.03	0.01	0.01
MnO	0.22	0.16	0.16	0.21	0.25	0.19	0.19
MgO	14.80	14.72	14.61	14.66	15.95	14.90	15.08
CaO	22.67	22.52	22.17	21.96	19.14	21.53	21.01
Na2O	0.27	0.25	0.28	0.29	0.21	0.28	0.23
K2O	bd	bd	bd	bd	bd	bd	bd
Total	99.20	98.77	99.40	98.22	99.89	98.93	99.96
Cation normalized to 6 Oxygen atoms							
Si	1.933	1.930	1.942	1.937	1.934	1.924	1.943
Ti	0.013	0.014	0.013	0.014	0.014	0.016	0.014
Al	0.086	0.088	0.088	0.092	0.087	0.094	0.089
Cr	0.001	0.000	0.001	0.000	0.001	0.000	0.000
Fe	0.223	0.231	0.239	0.229	0.307	0.259	0.268
Ni	0.001	0.001	0.000	0.001	0.001	0.000	0.000
Mn	0.007	0.005	0.005	0.007	0.008	0.006	0.006
Mg	0.826	0.826	0.813	0.826	0.885	0.836	0.835
Ca	0.909	0.908	0.887	0.889	0.764	0.869	0.836
Na	0.020	0.019	0.020	0.021	0.015	0.020	0.017
K	0.001	0.000	0.000	0.000	0.000	0.000	0.000
Total	4.021	4.021	4.011	4.014	4.016	4.024	4.008
Mg#	78.8	78.2	77.3	78.3	74.3	76.3	75.7

Table A5: Composition of reaction olivine - Depth 129.83 m (borehole VK-05, Northern lobe)

Analysis	ol-55	ol-56	ol-51	ol-52	ol-53	ol-45	ol-46	ol-47	ol-48	ol-49
SiO2	38.87	38.11	38.28	38.12	38.33	37.59	37.66	37.56	37.93	37.90
TiO2	0.10	0.10	0.00	0.05	0.08	0.05	0.02	0.00	0.05	0.01
Al2O3	0.00	0.01	0.00	0.01	0.00	0.01	0.01	0.01	0.00	0.00
FeO	25.33	24.99	24.25	25.44	22.98	27.47	27.52	27.24	26.51	27.60
MnO	0.31	0.27	0.26	0.27	0.26	0.34	0.28	0.35	0.32	0.30
NiO	0.06	0.05	0.04	0.05	0.02	0.05	0.06	0.03	0.06	0.06
MgO	36.14	37.13	36.07	36.32	37.19	34.96	34.83	35.50	35.98	34.93
CaO	0.03	0.00	0.02	0.02	0.02	0.04	0.06	0.04	0.00	0.04
Total	100.83	100.67	98.92	100.27	98.86	100.51	100.43	100.73	100.86	100.83
Cations normalized to 4 Oxygen atoms										
Si	0.998	1.000	0.994	0.998	1.002	1.015	1.003	1.010	1.014	0.997
Ti	0.001	0.000	0.000	0.001	0.000	0.000	0.001	0.002	0.002	0.002
Al	0.000	0.000	0.000	0.000	0.000	0.000	0.000	0.000	0.000	0.000
Fe	0.610	0.611	0.603	0.583	0.610	0.538	0.560	0.507	0.553	0.547
Mn	0.008	0.006	0.008	0.007	0.007	0.006	0.006	0.006	0.007	0.006
Ni	0.001	0.001	0.001	0.001	0.001	0.001	0.001	0.000	0.001	0.001
Mg	1.383	1.379	1.400	1.411	1.376	1.425	1.424	1.461	1.406	1.448
Ca	0.001	0.002	0.001	0.000	0.001	0.001	0.000	0.000	0.001	0.000
Total	3.001	3.000	3.006	3.001	2.997	2.985	2.995	2.987	2.984	3.001
Fo	69.1	69.0	69.6	70.5	69.0	72.3	71.5	74.0	71.5	72.3

Table A6: Composition of biotite - Depths 126m to 133 m. Base of MML, borehole VK-05, Northern lobe.

Analysis	SiO2	TiO2	Al2O3	Cr2O3	MgO	FeO	MnO	BaO	CaO	Na2O	K2O	F	Cl	Total
126-5_1_bt1 Line 001	39.63	3.92	14.49	0.04	18.30	10.96	0.03	0.17	0.06	0.30	8.07	0.42	0.22	96.39
126-5_1_bt1 Line 002	40.34	3.42	14.54	0.04	19.26	9.77	0.00	0.18	0.05	0.32	8.21	0.38	0.23	96.51
126-5_1_bt1 Line 003	39.03	3.40	14.34	0.03	18.60	9.71	0.05	0.17	0.04	0.35	8.72	0.29	0.25	94.80
126-5_1_bt1 Line 004	39.44	3.76	14.30	0.00	18.44	10.22	0.08	0.24	0.04	0.37	9.13	0.29	0.22	96.35
126-5_1_bt1 Line 005	38.94	3.45	14.81	0.01	18.47	10.47	0.05	0.14	0.06	0.40	8.61	0.40	0.27	95.85
126-5_1_bt1 Line 006	39.48	3.66	14.70	0.07	18.32	10.30	0.05	0.20	0.01	0.36	8.58	0.45	0.21	96.16
126-5_1_bt2 Line 003	39.49	3.51	14.63	0.01	18.74	10.73	0.04	0.20	0.13	0.28	7.60	0.38	0.21	95.74
126-5_1_bt2 Line 005	39.73	3.62	15.22	0.02	18.46	10.64	0.06	0.16	0.19	0.30	7.95	0.53	0.23	96.85
126-5_1_bt2 Line 006	40.88	2.86	19.07	0.01	15.46	9.06	0.03	0.13	0.25	0.28	7.99	0.41	0.19	96.38
126-5_1_bt2 Line 007	39.29	3.49	15.21	0.06	18.26	10.93	0.01	0.17	0.23	0.33	7.72	0.64	0.19	96.22
126-5_1_bt2 Line 008	39.92	3.37	14.73	0.02	18.42	9.75	0.00	0.15	0.16	0.31	8.26	0.56	0.23	95.59
126-5_2_bt1 Line 002	37.69	3.40	14.88	0.06	18.38	10.95	0.01	0.15	0.13	0.35	8.09	0.15	0.24	94.37
126-5_2_bt1 Line 005	39.51	3.10	14.92	0.04	19.64	8.90	0.00	0.12	0.01	0.34	8.94	0.58	0.22	96.03
126-5_3_bt1 Line 001	38.66	4.04	14.42	0.01	17.11	11.21	0.00	0.21	0.04	0.21	9.46	0.49	0.18	95.79
126-5_3_bt1 Line 002	38.85	3.57	14.44	0.02	17.54	11.38	0.01	0.20	0.03	0.31	9.44	0.44	0.22	96.22
126-5_3_bt1 Line 006	38.49	3.49	14.08	0.05	16.57	11.41	0.03	0.19	0.09	0.29	9.24	0.49	0.26	94.43
127.28_3_bt1_3	37.93	3.71	14.87	0.00	19.03	8.77	0.02	0.28	0.02	0.24	10.04	0.88	0.30	95.64
129.97_2_bt?	38.50	2.93	15.64	0.04	20.95	6.94	0.01	0.28	0.06	0.68	9.20	0.16	0.14	95.41
133.78_1_bt1_2	36.65	3.52	16.30	0.04	18.23	11.92	0.01	0.12	0.03	0.51	7.90	0.00	0.16	95.33
133.78_1_bt1_3	38.55	3.22	15.49	0.01	20.32	8.86	0.04	0.22	0.03	0.53	9.17	0.18	0.18	96.68
133-86_3_???	36.44	1.24	17.05	0.06	20.36	12.03	0.04	0.00	0.03	0.35	7.11	0.04	0.02	94.74
133-86_3_???	38.46	1.32	17.48	0.00	21.00	7.84	0.00	0.05	0.17	0.37	8.12	0.27	0.02	94.97
133-86_3_???	39.22	2.03	16.93	0.09	21.69	6.71	0.02	0.06	0.01	0.43	8.33	0.00	0.03	95.54
133-86_3_???	39.27	2.00	17.11	0.06	20.92	7.01	0.03	0.04	0.05	0.44	8.61	0.20	0.03	95.66
133-86_3_bt2	38.56	1.93	17.63	0.04	21.22	6.89	0.05	0.05	0.04	0.28	8.81	0.05	0.04	95.54
133-86_3_bt3	38.56	0.98	18.90	0.06	21.31	6.22	0.05	0.06	0.01	0.34	8.81	0.29	0.02	95.46
133-86_3_bt4	38.33	0.92	18.33	0.06	21.02	6.66	0.01	0.03	0.01	0.37	9.12	0.20	0.03	95.01

Table A7: Composition of chlorite – depths 105 m to 133 m) from borehole VK-05, Northern lobe

Depth_Comment	Mineral	SiO2	TiO2	Al2O3	Cr2O3	FeO	MnO	MgO	CaO	Na2O	K2O	F	Cl	Total
105.12_1_inclmag_7	chl	20.30	0.05	31.40	0.14	13.34	0.00	19.65	0.09	0.00	0.00	0.16	0.14	85.18
105.12_1_inclmag_8	chl	20.47	0.08	30.88	0.09	18.00	0.04	16.91	0.08	0.03	0.02	0.08	0.15	86.80
105.12_1_inclmag_9	chl	21.12	0.04	30.98	0.12	16.05	0.04	17.61	0.13	0.00	0.02	0.00	0.12	86.20
105.12_3_bt1_1	chl	33.60	2.58	14.71	0.00	9.51	0.04	26.66	0.41	0.21	0.96	0.21	0.03	88.84
105.12_3_bt1_2	chl	31.11	2.67	14.56	0.03	10.44	0.02	26.84	0.23	0.08	0.09	0.08	0.08	86.20
105.12_3_bt1_4	clinochl	32.38	2.99	14.48	0.02	10.01	0.01	26.04	0.77	0.10	0.31	0.41	0.08	87.43
105.12_3_bt1_6	chl	29.43	11.54	16.35	0.02	7.47	0.05	26.72	0.37	0.03	0.09	0.22	0.05	92.35
105.12_3_bt2_1	clinochl	34.41	2.49	14.97	0.03	10.65	0.04	25.63	0.35	0.45	1.98	0.27	0.12	91.31
105.12_3_bt2_2	clinochl	33.62	2.78	14.59	0.00	10.13	0.00	26.13	0.50	0.16	0.73	0.53	0.08	89.02
105.12_3_bt2_3	clinochl	31.78	3.00	16.31	0.07	9.87	0.01	26.64	0.44	0.05	0.22	0.29	0.07	88.66
105.12_3_bt2_4	clinochl	31.70	2.80	15.93	0.05	9.11	0.00	26.37	0.40	0.10	0.33	0.51	0.08	87.22
105.12_3_bt2_5	clinochl	33.84	2.54	15.01	0.01	10.20	0.00	26.44	0.36	0.38	1.84	0.31	0.09	90.90
105.12_3_bt2_6	clinochl	35.15	2.81	15.18	0.03	8.83	0.00	25.20	0.30	0.51	3.10	0.44	0.06	91.51
105.12_3_bt2_7	clinochl	33.02	4.29	14.55	0.04	10.40	0.00	24.17	1.69	0.14	0.50	0.14	0.05	88.97
126-5_2_bt1 Line 001	chl	34.91	2.43	15.74	0.00	15.10	0.05	17.56	1.39	0.17	3.23	0.09	0.14	90.83
126-5_2_chl1 Line 002	chl	26.86	0.01	18.49	0.03	30.39	0.15	5.43	1.51	1.12	0.06	0.00	0.03	84.10
127.28_2_bt1_1	chl	29.22	0.03	15.21	0.03	38.15	0.27	5.13	0.43	0.04	0.17	0.12	0.00	88.77
127.28_2_bt1_2	chl	28.98	0.00	14.68	0.02	38.88	0.25	5.06	0.45	0.05	0.17	0.00	0.00	88.55
127.28_2_bt1_3	chl	30.11	0.00	13.46	0.00	38.88	0.27	5.34	0.49	0.04	0.30	0.04	0.00	88.93
127.28_3_bt1_?	chl	20.17	11.82	15.03	0.11	35.63	0.64	4.80	0.39	0.08	0.14	0.10	0.00	88.96
129.83_bt1_3	chl	32.35	0.06	14.75	0.00	5.72	0.00	29.78	0.07	0.06	0.03	0.00	0.17	82.97
133.78_3_bt1_1	chl	27.66	0.02	16.35	0.09	38.50	0.07	5.15	0.21	0.06	0.05	0.01	0.00	88.20
133.78_3_bt1_3	chl	27.82	0.04	16.08	0.03	38.20	0.09	4.76	0.17	0.04	0.03	0.00	0.00	87.28
133.78_3_bt1_4	chl	27.02	0.11	17.83	0.06	38.26	0.11	5.03	0.19	0.06	0.02	0.00	0.04	88.74
133-86_3_bt1	chl	26.05	0.09	18.39	0.05	33.84	0.04	8.49	0.10	0.02	0.01	0.00	0.00	87.08
133-86_3_bt2	chl	25.07	0.05	19.08	0.00	35.39	0.06	6.19	0.07	0.00	0.00	0.00	0.00	85.91
133-86_3_bt3	chl	27.80	0.04	16.08	0.02	32.87	0.05	9.40	0.01	0.00	0.01	0.00	0.00	86.28
133-86_3_chl1	chl	24.35	0.00	19.95	0.00	35.28	0.05	6.32	0.05	0.00	0.01	0.00	0.00	86.00
133-86_3_sc1	chl	26.67	0.02	16.41	0.01	37.16	0.04	6.28	0.07	0.00	0.00	0.00	0.01	86.69
133-86_3_sc2	chl	25.99	0.00	17.16	0.04	36.50	0.07	6.49	0.06	0.00	0.01	0.00	0.02	86.33
133-86_3_sc3	chl	26.03	0.04	16.77	0.02	36.77	0.07	5.88	0.08	0.00	0.00	0.18	0.00	85.78
133-86_3_unk1	chl	26.40	0.03	17.77	0.04	33.76	0.10	7.94	0.11	0.00	0.01	0.00	0.00	86.17
133-86_3_unk2	chl	26.30	0.00	18.94	0.02	35.56	0.09	6.45	0.15	0.01	0.01	0.00	0.00	87.52
133-86_3_unk3	chl	26.28	0.01	18.05	0.00	35.43	0.07	7.42	0.10	0.00	0.01	0.07	0.00	87.41
133-86_3_unk4	chl	26.36	0.01	17.34	0.02	35.40	0.04	7.39	0.12	0.01	0.00	0.00	0.00	86.69
133-86_4_chl_co1	chl	26.45	0.08	18.70	0.00	34.60	0.08	4.69	0.31	0.03	0.02	0.00	0.08	85.02
133-86_4_chl_co2	chl	26.47	0.03	18.74	0.03	36.81	0.10	4.96	0.27	0.03	0.03	0.00	0.05	87.50
133-86_4_chl_co3	chl	25.60	0.01	18.64	0.00	34.89	0.08	4.84	0.26	0.03	0.03	0.00	0.03	84.39
133-86_4_chl_co4	chl	27.50	0.06	18.33	0.04	34.67	0.07	4.59	0.30	0.03	0.13	0.00	0.06	85.81
133-86_4_chl_co5	chl	26.64	0.06	18.00	0.02	35.46	0.04	4.90	0.31	0.00	0.02	0.00	0.02	85.48
133-86_4_chl_co6	chl	24.82	0.04	19.40	0.00	35.64	0.13	5.17	0.15	0.00	0.02	0.00	0.00	85.41
133-86_4_chl_rim1	chl	26.15	0.04	18.96	0.00	35.15	0.14	5.05	0.26	0.02	0.02	0.02	0.10	85.89
133-86_4_chl_rim1	chl	26.05	0.05	19.22	0.02	37.48	0.13	3.03	0.39	0.04	0.03	0.19	0.04	86.59
133-86_4_chl_rim2	cham	26.75	0.08	24.01	0.03	12.09	0.00	22.32	0.06	0.01	0.01	0.00	0.01	85.36
133-86_4_chl_rim2	chl	25.94	0.09	18.91	0.00	35.90	0.07	4.77	0.24	0.01	0.03	0.00	0.19	86.10
133-86_4_chl_rim3	chl	28.61	0.03	16.32	0.01	32.06	0.12	9.19	0.21	0.00	0.03	0.00	0.02	86.58
133-86_4_chl_rim3	chl	25.55	0.13	23.54	0.02	23.03	0.08	13.92	0.17	0.00	0.01	0.00	0.01	86.47
133-86_4_chl_rim4	chl	27.66	0.12	18.01	0.00	31.37	0.05	9.73	0.20	0.00	0.02	0.00	0.01	87.21
133-86_4_chl_rim5	chl	24.74	2.86	19.70	0.07	19.24	0.05	14.93	0.04	0.21	2.77	0.04	0.07	84.70
133-86_4_chl_rim6	chl	25.46	0.11	18.90	0.04	37.72	0.15	4.29	0.31	0.05	0.06	0.11	0.07	87.19
133-86_4_chl_rim7	chl	24.86	0.15	23.75	0.05	22.85	0.03	13.22	0.14	0.04	0.08	0.02	0.00	85.18
133-86_4_chl_rim8	chl	27.51	0.19	19.38	0.05	28.02	0.07	11.12	0.21	0.00	0.02	0.02	0.02	86.61

Table A7: Composition of chlorite – depths 105 m to 133 m) from borehole VK-05, Northern lobe (continued)

Depth_Comment	Mineral	SiO2	TiO2	Al2O3	Cr2O3	FeO	MnO	MgO	CaO	Na2O	K2O	F	Cl	Total
133-86_5_chl1_co1	chl	26.35	0.04	18.51	0.00	35.47	0.11	5.23	0.21	0.02	0.02	0.00	0.04	86.01
133-86_5_chl1_co2	chl	26.33	0.03	18.37	0.02	35.57	0.10	5.00	0.21	0.00	0.01		0.01	85.66
133-86_5_chl1_co3	chl	25.55	0.05	19.97	0.00	32.22	0.06	7.69	0.12	0.02	0.01		0.00	85.74
133-86_5_chl1_co4	chl	25.01	0.03	20.93	0.03	32.21	0.05	7.13	0.13	0.00	0.01		0.00	85.63
133-86_5_chl1_rim1	chl	25.37	0.02	18.20	0.02	33.35	0.14	6.15	0.25	0.08	0.04		0.01	83.64
133-86_5_chl1_rim2	chl	23.63	0.01	21.10	0.02	33.94	0.06	6.50	0.04	0.00	0.01		0.00	85.32
133-86_5_chl1_rim3	chl	27.95	0.14	15.72	0.04	33.20	0.11	7.92	0.19	0.00	0.03		0.00	85.33
133-86_5_chl1_rim4	chl	25.81	0.03	18.94	0.00	35.70	0.11	5.02	0.31	0.03	0.01		0.03	85.99
133-86_5_chl1_rim5	chl	25.81	0.01	20.69	0.01	35.89	0.13	6.28	0.15	0.00	0.02		0.00	88.99
133-86_5_chl1_rim6	chl	25.76	0.03	18.81	0.01	36.20	0.09	5.10	0.19	0.00	0.01		0.00	86.18
133-86_5_chl2_co1	chl	25.90	0.08	18.97	0.01	35.70	0.11	5.27	0.22	0.01	0.01		0.02	86.29
133-86_5_chl2_co2	chl	25.68	0.02	19.46	0.00	34.76	0.13	5.17	0.24	0.00	0.01		0.03	85.51
133-86_5_chl2_co3	chl	25.05	0.10	26.06	0.01	12.40	0.04	18.57	0.09	0.03	0.00		0.04	82.39
133-86_5_chl2_co4	chl	25.93	0.07	19.19	0.00	35.74	0.09	5.23	0.24	0.08	0.02		0.03	86.66
133-86_5_chl2_co5	chl	25.68	0.05	18.84	0.05	35.19	0.14	4.91	0.22	0.04	0.00		0.02	85.15
133-86_5_chl2_rim2	chl	22.93	0.04	23.19	0.04	32.57	0.02	6.75	0.06	0.01	0.01		0.01	85.64
133-86_5_chl2_rim3	chl	26.47	0.00	22.90	0.03	27.22	0.07	9.59	0.12	0.00	0.02		0.00	86.42
70-80_?_1	chl	20.17	4.80	17.81	0.12	47.84	0.11	3.04	0.26	0.11	0.04	0.00	0.05	94.34
70-80_?_11	chl	32.64	0.53	28.24	0.09	23.78	0.06	5.71	0.24	0.10	0.09	0.00	0.02	91.48
70-80_?_2	chl	23.57	4.28	20.76	0.11	36.61	0.08	4.13	0.22	0.07	0.06	0.00	0.06	89.93
70-80_?_3	chl	31.25	0.90	22.48	0.06	17.97	0.07	10.42	0.60	0.06	0.05	0.00	0.03	83.88
70-80_?_4	chl	24.31	0.95	13.79	0.01	6.07	0.02	15.62	0.43	0.03	0.05	0.00	0.33	61.52
70-80_?_5	clinochl	32.84	0.92	19.12	0.03	7.35	0.08	22.69	0.48	0.09	0.07	0.25	0.01	83.82
70-80_?_5	clinochl	32.84	0.92	19.12	0.03	7.35	0.08	22.69	0.48	0.09	0.07	0.25	0.01	83.82
70-80_?_5	clinochl	32.84	0.92	19.12	0.03	7.35	0.08	22.69	0.48	0.09	0.07	0.25	0.01	83.82
70-80_?_8	chl	30.32	8.00	16.70	0.01	15.32	0.10	16.12	0.74	0.07	0.05	0.03	0.01	87.44
70-80_?_9	chl	28.38	0.26	25.71	0.10	26.80	0.07	6.81	0.22	0.11	0.05	0.00	0.06	88.55
70-80_?1	chl	32.23	0.03	27.35	0.01	12.79	0.02	6.01	0.20	0.08	0.10	0.00	0.12	78.91
70-80_?2	chl	33.85	0.09	27.99	0.08	16.72	0.00	4.32	0.19	0.11	0.09	0.06	0.10	83.54
70-80_?3	chl	30.47	0.10	26.01	0.08	20.40	0.03	4.76	0.22	0.05	0.01	0.00	0.14	82.24
70-80_bt?_1	chl	33.15	1.82	18.40	0.02	6.76	0.03	21.28	0.75	0.02	0.03	0.19	0.03	82.40
70-80_bt?_4	chl	30.27	0.26	22.46	0.00	4.16	0.00	0.88	0.22	0.03	0.02	0.00	0.41	58.61
70-80_bt?_5	chl	31.36	0.32	25.54	0.05	14.16	0.00	0.89	0.23	0.06	0.01	0.02	0.31	72.87
70-80_p3_?1_10	chl	36.73	0.09	29.00	0.07	16.89	0.02	3.81	0.23	0.09	0.06	0.00	0.07	87.05
70-80_p3_?1_12	chl	26.76	0.09	28.38	0.02	9.42	0.04	17.37	0.15	0.05	0.01	0.00	0.06	82.34
70-80_p3_?1_12	chl	26.76	0.09	28.38	0.02	9.42	0.04	17.37	0.15	0.05	0.01	0.00	0.06	82.34
70-80_p3_?1_12	chl	26.76	0.09	28.38	0.02	9.42	0.04	17.37	0.15	0.05	0.01	0.00	0.06	82.34
70-80_p3_?1_13	chl	36.01	0.09	26.54	0.06	14.59	0.03	2.11	0.23	0.07	0.02	0.00	0.16	79.87
70-80_p3_?1_8	chl	31.67	0.10	25.96	0.07	20.44	0.02	4.08	0.21	0.05	0.07	0.00	0.12	82.76
70-80_p3_?1_8	chl	31.67	0.10	25.96	0.07	20.44	0.02	4.08	0.21	0.05	0.07	0.00	0.12	82.76
70-80_p3_?1_8	chl	31.67	0.10	25.96	0.07	20.44	0.02	4.08	0.21	0.05	0.07	0.00	0.12	82.76
70-80_p3_?1_9	chl	26.59	0.09	23.97	0.10	29.42	0.08	4.23	0.25	0.07	0.06	0.06	0.33	85.14
MH4_?_10	chl	23.48	0.17	23.67	0.00	33.84	0.02	11.85	0.04	0.06	0.03	0.00	0.06	93.20
MH4_?_11	chl	24.31	0.06	28.60	0.02	7.03	0.02	25.34	0.00	0.02	0.01	0.11	0.24	85.65
MH4_?_11	chl	24.31	0.06	28.60	0.02	7.03	0.02	25.34	0.00	0.02	0.01	0.11	0.24	85.65
MH4_?_11	chl	24.31	0.06	28.60	0.02	7.03	0.02	25.34	0.00	0.02	0.01	0.11	0.24	85.65
MH4_?_13	chl	31.12	3.14	23.62	0.03	11.80	0.09	11.10	0.06	0.15	0.08	0.10	0.05	81.28
MH4_?_15	chl	30.09	3.17	22.37	0.02	11.93	0.09	12.40	0.12	0.23	0.15	0.34	0.05	80.80
chl: unclassified chlorite; clinochl: clinochlore; cham: chamosite														

Table A-8: Composition of sulphides - Depth 129.83 m (borehole VK-05, Northern lobe)

Sample-comment	Mineral	Au	S	Fe	Ni	Cu	Hg	Co	As	Ag	Pb	Total
133-86_5_s1_co2	Chalcopyrite	0.00	34.98	29.90	0.00	34.89	0.24	0.02	0.03	0.00	0.00	100.06
133-86_5_s1_rim3	Chalcopyrite	0.00	35.25	30.47	0.00	33.97	0.35	0.00	0.01	0.00	0.01	100.06
133-86_5_s1_co1	Chalcopyrite	0.01	35.13	30.30	0.02	34.63	0.31	0.03	0.00	0.00	0.04	100.46
133-86_4_s1_co1	Chalcopyrite	0.00	35.20	30.37	0.00	33.52	0.23	0.04	0.00	0.00	0.04	99.41
133-86_4_s1_co2	Chalcopyrite	0.07	35.07	30.68	0.00	33.45	0.37	0.00	0.00	0.00	0.00	99.64
133-86_4_s1_rim2	Chalcopyrite	0.05	34.83	30.14	0.05	34.42	0.16	0.04	0.00	0.00	0.07	99.76
133-86_s2	Chalcopyrite	0.01	35.36	30.13	0.04	34.42	0.31	0.07	0.00	0.00	0.07	100.41
133-86_4_s2_rim2	Chalcopyrite	0.00	34.87	29.79	0.00	34.41	0.26	0.01	0.00	0.00	0.01	99.35
133-86_4_s2_co2	Chalcopyrite	0.00	34.41	29.76	0.16	34.39	0.29	0.01	0.00	0.00	0.00	99.03
133-86_5_s3	Chalcopyrite	0.03	34.40	30.33	0.00	34.32	0.25	0.05	0.04	0.00	0.00	99.43
133-86_s3	Chalcopyrite	0.07	34.34	30.13	0.15	35.30	0.39	0.04	0.01	0.00	0.00	100.42
133-86_4_s2_rim1	Chalcopyrite	0.01	34.82	30.09	0.06	34.25	0.14	0.01	0.00	0.00	0.02	99.39
133-86_4_s2_co1	Chalcopyrite	0.05	34.89	30.06	0.00	34.24	0.34	0.01	0.00	0.00	0.00	99.60
133-86_5_s2_rim1	Chalcopyrite	0.05	35.03	29.90	0.21	34.23	0.37	0.03	0.00	0.00	0.01	99.84
133-86_s4	Chalcopyrite	0.07	34.68	29.90	0.00	34.22	0.19	0.02	0.02	0.00	0.05	99.15
133-86_s3	Chalcopyrite	0.12	34.66	30.16	0.02	34.15	0.22	0.04	0.01	0.00	0.00	99.38
133-86_s1	Chalcopyrite	0.01	34.76	30.26	0.00	34.12	0.24	0.06	0.00	0.00	0.00	99.45
133-86_3_s1	Chalcopyrite	0.00	34.41	30.51	0.09	34.11	0.30	0.01	0.02	0.00	0.06	99.50
133-86_s1	Chalcopyrite	0.06	35.61	30.45	0.06	34.11	0.14	0.02	0.00	0.00	0.07	100.51
133-86_5_s2_co1	Chalcopyrite	0.00	35.12	30.04	0.00	34.06	0.26	0.03	0.03	0.00	0.10	99.64
126-5_2_s1 Line 002	Chalcopyrite	0.10	34.53	29.82	0.04	34.99	0.33	0.03	0.00	0.00	0.04	99.87
126-5_2_s1 Line 004	Chalcopyrite	0.05	34.95	30.10	0.00	34.88	0.21	0.04	0.00	0.00	0.00	100.23
126-5_2_s1 Line 001	Chalcopyrite	0.05	34.49	29.44	0.11	34.86	0.32	0.02	0.00	0.00	0.00	99.30
133-86_s2	Chalcopyrite	0.00	35.69	30.23	0.10	34.79	0.27	0.08	0.00	0.00	0.06	101.22
133-86_5_s1_rim1	Chalcopyrite	0.10	35.32	30.63	0.00	34.74	0.28	0.03	0.00	0.00	0.10	101.19
133-86_4_s1_rim1	Chalcopyrite	0.00	34.86	30.36	0.05	34.65	0.28	0.04	0.01	0.00	0.00	100.26
133-86_s4	Chalcopyrite	0.00	34.75	30.03	0.12	34.56	0.36	0.01	0.03	0.00	0.00	99.85
126-5_2_s1 Line 003	Chalcopyrite	0.13	34.11	29.30	0.00	34.41	0.27	0.01	0.00	0.00	0.03	98.26
126-5_4_s1_2	Pyrrhotite	0.00	40.07	58.99	0.61	0.01	0.21	0.08	0.00	0.00	0.11	100.07
133-86_6_s1_co4	Pyrrhotite	0.01	39.50	59.34	0.34	0.00	0.23	0.07	0.01	0.00	0.00	99.51
133-86_6_s1_co5	Pyrrhotite	0.00	39.18	59.00	0.21	0.04	0.35	0.09	0.04	0.00	0.00	98.90
133-86_6_s1_rim3	Pyrrhotite	0.01	39.76	58.45	0.08	0.00	0.31	0.08	0.04	0.00	0.00	98.73
105-24_1_s1_1	Co-bearing Pyrite	0.02	53.97	41.85	0.12	0.00	0.41	3.69	0.00	0.00	0.03	100.09
105-24_1_s1_2	Co-bearing Pyrite	0.00	53.92	42.80	0.00	0.01	0.35	3.09	0.02	0.00	0.00	100.18
105-24_1_s1_3	Co-bearing Pyrite	0.08	53.68	42.25	0.00	0.00	0.41	2.83	0.02	0.00	0.06	99.33
105-24_1_s1_4	Co-bearing Pyrite	0.00	53.16	43.15	0.00	0.00	0.49	2.31	0.03	0.00	0.00	99.14
105-24_1_s1_6	Co-bearing Pyrite	0.00	53.50	43.03	0.00	0.05	0.42	2.26	0.03	0.00	0.00	99.28
105-24_1_s2_2	Co-bearing Pyrite	0.07	53.31	44.30	0.23	0.00	0.45	1.62	0.00	0.00	0.05	100.03
105-24_1_s1_5	Co-bearing Pyrite	0.10	53.64	43.79	0.01	0.00	0.29	1.55	0.02	0.00	0.04	99.44
105-24_2_s1 Line 005	Co-bearing Pyrite	0.03	53.29	45.17	0.12	0.01	0.37	1.06	0.00	0.00	0.00	100.04
105-24_2_s1 Line 006	Pyrite	0.01	53.76	44.83	0.69	0.01	0.46	0.80	0.02	0.00	0.00	100.57
105-24_1_s1_co2	Pyrite	0.02	53.32	45.58	0.12	0.00	0.31	0.77	0.01	0.00	0.00	100.13
105-24_2_s1 Line 001	Pyrite	0.00	53.32	44.27	0.68	0.00	0.33	0.55	0.02	0.00	0.02	99.19
105-24_1_s1_co1	Pyrite	0.00	53.93	46.06	0.28	0.00	0.40	0.27	0.00	0.00	0.00	100.94
105-24_2_s1 Line 003	Pyrite	0.08	53.46	45.12	0.33	0.00	0.39	0.05	0.00	0.00	0.03	99.46
105-24_2_s1 Line 002	Pyrite	0.02	53.26	44.55	0.52	0.53	0.27	0.05	0.03	0.00	0.00	99.22
105-24_2_s1 Line 004	Pyrite	0.00	53.59	46.37	0.06	0.00	0.38	0.03	0.01	0.00	0.00	100.44
105-24_1_s2_4	Ni-Co-sulphide	0.00	42.41	5.62	34.52	0.00	0.21	12.88	0.02	0.00	0.02	95.67
105-24_1_s2_5	Ni-Co-sulphide	0.00	42.05	5.74	34.42	0.00	0.24	12.94	0.00	0.00	0.00	95.38
105-24_1_s2_co2	Ni-Co-sulphide	0.04	42.81	5.72	34.34	0.00	0.29	12.96	0.00	0.00	0.12	96.28
105-24_1_s2_3	Ni-Co-sulphide	0.00	42.17	5.76	34.16	0.00	0.28	12.44	0.00	0.00	0.00	94.81
105-24_1_s2_co1	Ni-Co-sulphide	0.00	42.49	5.96	34.00	0.00	0.34	12.69	0.00	0.00	0.25	95.72
105-24_1_s2_7	Ni-Co-sulphide	0.07	42.94	6.71	33.66	0.00	0.43	12.46	0.01	0.00	0.03	96.31
105-24_1_s2_1	Ni-Co-sulphide	0.03	42.28	6.24	32.92	0.19	0.28	13.05	0.00	0.00	0.01	94.99
105-24_1_s2_6	Ni-Co-sulphide	0.05	42.45	6.48	32.72	0.00	0.33	12.88	0.00	0.00	0.19	95.09
126-5_4_s1_2	Pyrrhotite	0.00	40.07	58.99	0.61	0.01	0.21	0.08	0.00	0.00	0.11	100.07
133-86_6_s1_co4	Pyrrhotite	0.01	39.50	59.34	0.34	0.00	0.23	0.07	0.01	0.00	0.00	99.51
133-86_6_s1_co5	Pyrrhotite	0.00	39.18	59.00	0.21	0.04	0.35	0.09	0.04	0.00	0.00	98.90
133-86_6_s1_rim3	Pyrrhotite	0.01	39.76	58.45	0.08	0.00	0.31	0.08	0.04	0.00	0.00	98.73
133-86_6_s1_rim2	Pentlandite	0.00	35.51	28.32	30.20	0.00	0.21	6.03	0.02	0.00	0.07	100.37
133-86_6_s1_co2	Pentlandite	0.08	34.96	28.94	29.70	0.00	0.24	6.00	0.04	0.00	0.04	100.00
133-86_6_s1_rim1	Pentlandite	0.00	34.47	28.94	29.50	0.05	0.37	5.26	0.00	0.00	0.00	98.58
133-86_6_s1_co1	Pentlandite	0.03	35.27	28.90	28.15	0.00	0.26	6.05	0.02	0.00	0.00	98.67

Table A9: Trace elements in oxides and sulphides at the base of MML, borehole VK5, N-lobe (wt%)

Analysis	Comment	As	Bi	Cu	Te	Rh	Pt	Pd	Ru
1	133.78_quitar_shape_mag1	0	0	0.041	0.012	0.005	0	0.132	0
2	133.78_quitar_mag2	0	0	0.063	0.024	0.008	0	0.056	0
3	133.78_quitar_mag3	0.036	0	0.047	0	0.011	0.03	0.123	0
4	133.78_quitar_mag_mix1	0	0	0	0	0.024	0	0.041	0
5	133.78_quitar_mag_mix2	0.018	0	0	0.002	0	0.059	0.1	0
6	133.78_quitar_mag_mix3	0.012	0.091	0	0	0.008	0	0.143	0
7	133.78_quitar_mag_mix4	0.047	0.026	0.055	0	0	0	0.145	0
8	133.78_quitar_mag_mix5	0.032	0.075	0	0	0	0	0.1	0
9	133.78_quitar_mag_mix6	0.036	0.013	0	0	0.006	0	0.045	0.01
10	133.78_quitar_mag_mix7	0.014	0	0	0	0	0.041	0.097	0
11	133.78_quitar_mag_mix8	0.051	0	0	0	0	0.086	0.1	0
12	133.78_quitar_mag_mix9	0	0.075	0	0	0.025	0	0.036	0
13	133.78_quitar_ilm1_rim1	0	0.205	0.018	0	0	0	0.025	0
14	133.78_quitar_ilm1_rim2	0.009	0.072	0.039	0.034	0.015	0	0.111	0
15	133.78_quitar_ilm1_co1	0.037	0	0	0	0	0	0.112	0
16	133.78_quitar_ilm1_co2	0.031	0.078	0	0	0.007	0.055	0.104	0
17	133.78_x1_mag1	0.033	0	0	0	0.019	0	0.05	0
18	133.78_x1_mag2	0.029	0.097	0.026	0	0.002	0	0.117	0
19	133.78_x1_mag_mix1	0.042	0.107	0.067	0	0	0	0.023	0
20	133.78_x1_mag_mix2	0.029	0	0	0	0	0	0.03	0
21	133.78_x1_mag_mix3	0.029	0.077	0.054	0	0	0	0.14	0
22	133.78_x1_mag_mix4	0	0	0.076	0.04	0.019	0	0.047	0
23	133.78_x1_mag_mix5	0	0	0.069	0.049	0.011	0.013	0.154	0
24	133.78_x1_ilm1	0.009	0.054	0.126	0.002	0.009	0	0.033	0
25	133.78_x1_ilm2	0.023	0	0.02	0.01	0.035	0.035	0	0
26	133.78_cpy1	0.001	0.069	33.528	0.006	0	0.043	0.18	0
27	133.78_cpy2	0.008	0.017	32.421	0	0	0	0.241	0
28	133.78_pyrh1	0.002	0	0.267	0	0	0	0.238	0
29	133.78_pyrh2	0.015	0	0.318	0	0	0.067	0.13	0
30	133.78_sulph3	0	0	0	0.034	0	0	0.165	0
31	133.78_sulph4	0.023	0	0.017	0.006	0	0	0.12	0
32	133.78_sulph5	0	0	0	0	0	0.027	0.114	0
33	133.78_sulph6	0	0	0	0	0.017	0	0.09	0
34	133.78_x1_cpy1	0	0	33.635	0.006	0.021	0	0.12	0
35	133.78_x1_cpy2	0.032	0	33.367	0	0.014	0.054	0.096	0
36	133.78_x1_sulph_sec1	0.056	0	32.577	0	0	0.011	0.034	0
37	133.78_x1_sulph_sec2	0.042	0	31.621	0.016	0.001	0	0.092	0
38	133.78_x1_sulph_sec3	0.007	0	31.299	0	0	0	0.086	0

Table A10: Composition of Ti-magnetite in MML from borehole VL-05, Northern lobe

Comment	SiO2	CaO	TiO2	Al2O3	FeO	ZnO	MnO	NiO	V2O3	MgO	Cr2O3	Total
105.05_1_1_1	0.02	0.05	13.01	4.39	76.67	0.00	0.26	0.07	1.65	0.34	0.53	96.99
105.05_1_1_2	0.07	0.04	12.63	1.55	78.31	0.00	0.32	0.00	1.70	0.65	0.53	95.78
105.05_1_1_3	0.05	0.03	13.68	0.37	79.19	0.08	0.36	0.08	1.59	0.10	0.65	96.17
105.05_1_1_4	0.06	0.04	11.19	1.19	78.79	0.18	0.23	0.12	1.58	1.54	0.62	95.52
105.05_1_1_5	0.02	0.04	9.09	1.40	82.81	0.00	0.23	0.08	1.88	0.28	0.84	96.67
105.05_1_1_7	0.04	0.02	10.60	1.53	80.75	0.27	0.23	0.09	1.67	0.89	0.71	96.78
105.05_1_1_8	0.21	0.03	7.90	1.12	82.67	0.33	0.15	0.03	1.75	0.76	0.60	95.54
105.05_1_1_9	0.06	0.03	12.06	0.58	79.15	0.43	0.19	0.01	1.58	0.57	0.70	95.35
105.05_2_1	0.03	0.05	10.35	2.09	77.32	0.00	0.18	0.14	1.60	0.49	0.87	93.12
105.05_2_3	0.05	0.01	12.42	2.80	76.75	0.00	0.24	0.05	1.66	0.29	0.84	95.12
105.05_3_1	0.08	0.31	13.33	1.67	76.92	0.10	0.26	0.04	1.41	0.05	0.64	94.82
105.05_3_2	0.02	0.07	14.41	4.59	71.38	0.15	0.26	0.00	1.54	0.00	0.54	92.95
105.12_3_1_2	0.06	0.03	12.94	0.57	77.90	0.00	0.30	0.04	1.55	0.63	0.59	94.60
105.12_3_1_3	0.02	0.11	1.08	0.24	87.40	0.05	0.03	0.09	1.85	0.07	0.64	91.57
105.12_3_1_4	0.93	0.02	0.27	2.06	87.61	0.00	0.01	0.06	1.63	0.41	0.61	93.60
105.12_3_1_5	0.03	0.05	1.10	1.47	88.66	0.41	0.00	0.04	1.72	0.07	0.72	94.26
105.12_3_1_7	1.10	0.00	5.45	1.41	84.97	0.08	0.06	0.03	1.89	0.42	0.57	95.96
105.12_3_1_8	0.06	0.01	11.84	0.69	78.39	0.00	0.22	0.05	1.64	0.41	0.52	93.83
105.12_3_1_9	0.05	0.03	11.87	0.60	79.52	0.22	0.25	0.04	1.65	0.36	0.61	95.20
105-24_1_1 001	0.09	0.05	10.32	0.20	81.42	0.05	0.16	0.01	1.64	0.07	0.67	94.68
105-24_1_1 004	1.53	0.06	10.90	6.13	73.46	0.12	0.19	0.00	1.50	3.29	0.60	97.78
105-24_1_1 005	0.01	0.06	12.61	1.49	75.75	0.25	0.22	0.00	1.63	0.06	0.64	92.74
105-24_1_1 006	0.03	0.03	7.18	1.23	82.90	0.12	0.12	0.03	1.56	0.06	0.54	93.81
105-24_1_1 007	0.03	0.02	8.86	0.33	81.72	0.00	0.14	0.05	1.89	0.08	0.74	93.87
105-24_1_1 008	0.06	0.13	11.82	0.71	75.72	0.08	0.20	0.00	1.57	0.24	0.67	91.21
105-24_2_1 001	0.06	0.04	17.70	4.21	67.82	0.00	0.33	0.00	1.27	0.05	0.59	92.06
105-24_2_1 002	0.10	0.10	15.82	4.07	69.98	0.28	0.32	0.00	1.44	0.06	0.54	92.73
105-24_2_1 003	0.09	0.09	14.57	0.61	74.84	0.00	0.31	0.06	1.54	0.04	0.66	92.82
105-24_2_2_1	0.50	0.07	13.13	0.90	75.39	0.05	0.24	0.01	1.62	0.32	0.63	92.87
105-24_2_2_2	0.00	0.04	11.29	2.13	78.50	0.00	0.20	0.01	1.64	0.00	0.59	94.40
105-24_2_3 001	0.05	0.03	13.75	1.05	75.28	0.35	0.23	0.00	1.62	0.01	0.60	93.00
105-24_2_3 002	0.10	0.05	26.66	2.87	61.15	0.14	0.61	0.05	1.26	0.11	0.52	93.51
105-24_2_3 003	0.07	0.02	11.89	1.32	76.46	0.26	0.26	0.03	1.65	0.03	0.60	92.59
105-24_2_3 004	0.21	0.08	12.66	2.68	70.51	0.14	0.31	0.01	1.31	0.44	0.50	88.85
105-24_2_3 005	0.09	0.04	9.62	0.17	80.42	0.22	0.16	0.05	1.65	0.02	0.63	93.06
105-24_2_3 006	0.19	0.10	10.29	0.35	76.64	0.06	0.20	0.05	1.61	0.12	0.65	90.30

Table A11: Composition of ilmenite in MML borehole VL-05, at depth 105.05 m (Northern lobe)

Comment	CaO	TiO2	Al2O3	FeO	ZnO	MnO	NiO	V2O3	MgO	Cr2O3	Total
105.05_2_ilm1	0.33	53.03	0.03	43.79	0.54	0.64	0.00	0.28	2.31	0.02	100.96
105.05_2_ilm2	0.20	52.84	0.03	45.47	0.27	0.87	0.04	0.25	1.78	0.00	101.75
105.05_2_ilm3	0.12	53.44	0.03	45.41	0.01	0.81	0.00	0.32	1.91	0.03	102.10

Table A12: Composition of Ti-magnetite at depth 105.24 m, borehole VL-05, Norhern lobe

Comment	CaO	TiO2	Al2O3	FeO	ZnO	MnO	NiO	V2O3	MgO	Cr2O3	Nb2O5	Total
105-24_1_1 1	0.05	10.32	0.20	81.42	0.05	0.16	0.01	1.64	0.07	0.67	0.00	94.59
105-24_1_1 5	0.06	12.61	1.49	75.75	0.25	0.22	0.00	1.63	0.06	0.64	0.03	92.73
105-24_1_1 6	0.03	7.18	1.23	82.90	0.12	0.12	0.03	1.56	0.06	0.54	0.00	93.78
105-24_1_1 7	0.02	8.86	0.33	81.72	0.00	0.14	0.05	1.89	0.08	0.74	0.00	93.83
105-24_1_1 8	0.13	11.82	0.71	75.72	0.08	0.20	0.00	1.57	0.24	0.67	0.02	91.15
105-24_2_1 1	0.04	17.70	4.21	67.82	0.00	0.33	0.00	1.27	0.05	0.59	0.00	92.01
105-24_2_1 2	0.10	15.82	4.07	69.98	0.28	0.32	0.00	1.44	0.06	0.54	0.02	92.63
105-24_2_1 3	0.09	14.57	0.61	74.84	0.00	0.31	0.06	1.54	0.04	0.66	0.01	92.73
105-24_2_2_1	0.07	13.13	0.90	75.39	0.05	0.24	0.01	1.62	0.32	0.63	0.02	92.38
105-24_2_2_2	0.04	11.29	2.13	78.50	0.00	0.20	0.01	1.64	0.00	0.59	0.00	94.40
105-24_2_3 1	0.03	13.75	1.05	75.28	0.35	0.23	0.00	1.62	0.01	0.60	0.03	92.95
105-24_2_3 2	0.05	26.66	2.87	61.15	0.14	0.61	0.05	1.26	0.11	0.52	0.00	93.42
105-24_2_3 3	0.02	11.89	1.32	76.46	0.26	0.26	0.03	1.65	0.03	0.60	0.00	92.52
105-24_2_3 5	0.04	9.62	0.17	80.42	0.22	0.16	0.05	1.65	0.02	0.63	0.00	92.97

Table B1: Composition of Ti-magnetite along stratigraphic column - Magnet Heights, Eastern lobe. "Line" suggest that the analyses were taken along a profile line perpendicular to layering, across the available samples

No.	Depth	Comment	SiO2	Al2O3	FeO	MnO	Cr2O3	TiO2	MgO	V2O3	Total
1	2000.00	MH2 Line 001	0.02	3.32	72.26	0.20	2.75	13.01	1.37	0.30	93.22
2	1998.52	MH2 Line 002	0.04	3.11	67.15	0.25	2.74	13.44	0.68	0.39	87.80
3	1997.04	MH2 Line 003	0.04	2.37	73.78	0.34	2.65	13.15	0.20	0.41	92.93
4	1995.58	MH2 Line 004	0.01	3.32	69.71	0.20	2.81	13.22	1.26	0.37	90.90
5	1994.11	MH2 Line 005	0.00	3.22	75.79	0.33	2.74	11.94	0.24	0.43	94.68
6	1992.63	MH2 Line 006	0.12	2.67	73.77	0.32	2.92	11.34	0.08	0.64	91.85
7	1991.13	MH2 Line 007	0.10	2.50	68.86	0.34	2.71	15.45	0.27	0.43	90.66
8	1989.67	MH2 Line 008	0.04	2.90	66.62	0.24	2.67	14.43	1.08	0.36	88.34
9	1988.21	MH2 Line 009	0.01	3.79	71.23	0.19	2.73	13.54	1.62	0.41	93.50
10	1986.69	MH2 Line 010	0.02	2.81	73.20	0.07	2.67	12.49	0.70	0.47	92.43
11	1985.17	MH2 Line 011	0.06	2.98	75.37	0.31	2.52	12.88	1.42	0.37	95.91
12	1983.69	MH2 Line 012	0.00	3.30	75.02	0.31	2.44	12.41	0.94	0.40	94.82
13	1982.25	MH2 Line 013	0.10	3.04	75.10	0.25	2.49	11.56	0.59	0.64	93.75
14	1980.76	MH2 Line 014	0.06	3.24	69.17	0.14	2.54	13.01	1.07	0.45	89.68
15	1979.49	MH2 Line 015	0.04	3.16	67.40	0.49	2.49	13.24	1.38	0.36	88.56
16	1977.87	MH2 Line 016	0.12	2.63	70.15	0.05	2.51	12.84	0.59	0.39	89.27
17	1976.19	MH2 Line 017	0.03	2.95	72.18	0.15	2.50	12.61	1.56	0.36	92.34
18	1974.94	MH2 Line 018	0.02	3.57	69.67	0.29	2.63	13.44	1.27	0.38	91.26
19	1973.31	MH2 Line 019	0.06	3.45	72.46	0.19	2.63	12.84	0.91	0.40	92.94
20	1971.76	MH2 Line 020	0.09	2.55	68.74	0.30	2.66	13.47	0.45	0.44	88.71
34	1768.61	MH3 Line 001	0.04	1.43	73.25	0.20	1.02	15.03	0.16	0.21	91.33
35	1767.12	MH3 Line 002	0.01	3.05	69.70	0.13	0.86	14.35	0.85	0.29	89.25
36	1765.46	MH3 Line 003	0.09	1.74	71.02	0.18	0.89	14.60	0.26	0.33	89.11
37	1763.90	MH3 Line 004	0.06	1.80	69.99	0.10	0.88	13.60	0.14	0.33	86.90
38	1762.37	MH3 Line 005	0.05	1.07	72.09	0.32	1.06	14.85	0.92	0.30	90.65
39	1760.78	MH3 Line 006	0.06	0.99	71.93	0.18	1.03	15.21	0.18	0.29	89.85
40	1758.97	MH3 Line 007	0.02	0.98	72.05	0.24	1.05	14.37	0.28	0.33	89.32
41	1757.56	MH3 Line 008	0.06	3.73	70.19	0.21	1.10	13.84	1.37	0.39	90.90
42	1755.93	MH3 Line 009	0.03	0.78	79.47	0.19	0.94	12.21	0.17	0.33	94.10
43	1754.44	MH3 Line 010	0.44	1.03	72.51	0.23	1.01	15.47	0.14	0.31	91.14
44	1752.75	MH3 Line 011	0.04	2.42	76.07	0.41	0.91	14.26	0.61	0.25	94.97
45	1751.32	MH3 Line 012	0.01	2.24	73.87	0.24	0.91	13.21	0.29	0.38	91.15
46	1749.68	MH3 Line 013	0.10	0.61	79.07	0.13	1.04	10.94	0.15	0.47	92.51
47	1748.12	MH3 Line 014	0.02	0.60	73.39	0.12	1.12	13.97	0.11	0.33	89.68
48	1746.54	MH3 Line 015	0.03	2.28	67.96	0.28	1.08	15.86	0.55	0.41	88.44
49	1744.96	MH3 Line 016	0.04	0.88	73.19	0.02	0.94	14.20	0.18	0.42	89.88
50	1743.32	MH3 Line 017	0.03	0.52	75.29	0.19	0.98	14.18	0.23	0.31	91.73
51	1741.79	MH3 Line 018	0.35	1.93	79.28	0.00	0.92	13.64	0.11	0.38	96.61
52	1740.07	MH3 Line 019	0.03	0.66	76.33	0.36	1.07	14.62	0.30	0.36	93.73
53	1738.69	MH3 Line 020	0.18	0.87	77.21	0.16	0.91	12.98	0.12	0.42	92.85
54	874.53	MH6A Line 001	0.04	3.11	75.02	0.22	1.99	13.17	1.31	0.32	95.18
55	872.81	MH6A Line 002	0.12	2.51	67.49	0.32	2.06	12.70	1.09	0.31	86.59
56	871.02	MH6A Line 003	0.01	2.48	69.58	0.06	2.28	12.70	0.93	0.42	88.45

Table B1: Composition of Ti-magnetite along stratigraphic column - Magnet Heights, Eastern lobe. "Line" suggest that the analyses were taken along a profile line perpendicular to layering. (Continued)

No.	Depth	Comment	SiO2	Al2O3	FeO	MnO	Cr2O3	TiO2	MgO	V2O3	Total
58	867.69	MH6A Line 005	0.09	2.70	66.69	0.21	2.18	13.14	0.76	0.35	86.11
59	866.02	MH6A Line 006	0.09	2.65	67.80	0.21	2.04	14.06	0.57	0.27	87.68
60	864.36	MH6A Line 007	0.03	3.17	67.97	0.20	2.34	13.82	1.26	0.27	89.05
61	862.49	MH6A Line 008	0.02	3.20	69.42	0.29	2.16	13.98	0.69	0.36	90.12
62	860.96	MH6A Line 009	0.07	6.18	61.28	0.31	2.28	14.02	2.27	0.36	86.77
63	859.22	MH6A Line 010	0.06	2.63	69.17	0.04	2.25	13.27	1.11	0.33	88.86
64	857.51	MH6A Line 011	0.15	3.31	66.87	0.10	2.16	12.73	0.84	0.35	86.50
65	855.80	MH6A Line 012	0.06	2.61	64.35	0.34	2.17	14.04	0.97	0.37	84.90
66	854.10	MH6A Line 013	0.06	2.47	63.93	0.24	2.26	13.67	0.49	0.31	83.44
67	852.39	MH6A Line 014	0.02	3.43	63.77	0.29	2.35	14.42	1.60	0.30	86.18
68	850.74	MH6A Line 015	0.09	3.93	65.45	0.33	2.21	13.75	1.89	0.35	87.99
69	849.15	MH6A Line 016	0.14	1.69	68.65	0.37	2.06	12.91	1.07	0.41	87.29
70	847.44	MH6A Line 017	0.05	9.80	61.62	0.16	2.33	16.85	2.84	0.08	93.73
71	845.59	MH6A Line 018	0.04	3.32	66.18	0.21	2.27	13.81	1.56	0.35	87.74
72	844.07	MH6A Line 019	0.05	2.21	69.32	0.13	2.01	13.05	0.89	0.34	87.99
73	842.29	MH6A Line 020	0.01	5.17	64.95	0.29	2.38	13.29	2.16	0.32	88.57
74	716.37	MH7 Line 001	0.06	3.64	64.26	0.15	0.24	15.53	2.06	0.24	86.19
75	715.24	MH7 Line 002	0.04	3.26	66.69	0.20	0.22	14.79	1.64	0.27	87.11
76	715.23	MH7 Line 003	0.20	3.21	62.76	0.12	0.20	16.25	1.52	0.27	84.52
77	715.22	MH7 Line 004	0.29	2.95	65.99	0.23	0.19	14.43	1.76	0.38	86.23
78	715.21	MH7 Line 005	0.06	3.55	70.87	0.28	0.22	14.05	1.01	0.34	90.37
79	715.20	MH7 Line 006	0.07	3.46	69.59	0.18	0.25	13.79	0.92	0.43	88.69
80	715.19	MH7 Line 007	0.06	3.87	65.94	0.13	0.26	13.78	1.71	0.37	86.13
82	715.17	MH7 Line 009	0.09	4.02	69.94	0.26	0.18	14.53	1.24	0.37	90.62
83	715.16	MH7 Line 010	0.78	1.01	69.51	0.27	0.24	14.59	0.31	0.34	87.05
84	715.15	MH7 Line 011	0.03	0.93	76.97	0.26	0.22	12.78	0.98	0.29	92.47
85	715.14	MH7 Line 012	0.17	0.49	72.59	0.31	0.22	15.08	0.16	0.33	89.35
86	715.13	MH7 Line 013	0.65	2.66	67.60	0.27	0.20	14.20	1.46	0.32	87.36
87	715.12	MH7 Line 014	0.05	2.65	69.44	0.20	0.21	14.62	0.60	0.28	88.05
88	715.11	MH7 Line 015	0.34	0.95	73.77	0.22	0.25	12.91	0.20	0.52	89.17
89	715.10	MH7 Line 016	1.13	1.37	71.52	0.44	0.23	14.04	1.19	0.46	90.37
90	715.09	MH7 Line 017	0.21	1.94	71.85	0.18	0.21	12.98	1.27	0.46	89.09
91	715.08	MH7 Line 018	0.17	3.03	71.37	0.35	0.23	14.46	1.72	0.43	91.74
92	715.07	MH7 Line 019	0.13	1.54	77.64	0.39	0.22	13.35	0.89	0.40	94.57
93	715.06	MH7 Line 020	0.06	3.59	71.30	0.20	0.23	15.51	2.09	0.31	93.26
100	426.77	MH8 Line 001	0.11	0.93	73.28	0.08	0.10	14.45	0.46	0.27	89.67
101	425.14	MH8 Line 002	0.07	0.63	75.01	0.21	0.18	14.56	0.42	0.36	91.45
102	423.29	MH8 Line 003	0.07	0.81	75.47	0.30	0.17	15.53	0.46	0.38	93.18
103	421.68	MH8 Line 004	0.08	0.69	75.39	0.17	0.13	15.26	0.48	0.30	92.49
104	421.38	MH8 Line 005	0.07	0.67	75.65	0.19	0.11	15.14	0.33	0.30	92.47
105	418.52	MH8 Line 006	0.10	0.74	75.42	0.35	0.12	14.84	0.39	0.37	92.34
106	417.03	MH8 Line 007	0.06	1.95	72.87	0.28	0.09	14.85	0.84	0.25	91.20
107	415.54	MH8 Line 008	0.00	3.96	72.83	0.00	0.12	13.08	1.02	0.25	91.26
108	414.05	MH8 Line 009	0.06	1.74	73.21	0.17	0.16	15.52	0.18	0.30	91.34

Table B1: Composition of Ti-magnetite along stratigraphic column - Magnet Heights, Eastern lobe. "Line" suggest that the analyses were taken along a profile line perpendicular to layering. (Continued)

No.	Depth	Comment	SiO2	Al2O3	FeO	MnO	Cr2O3	TiO2	MgO	V2O3	Total
111	409.23	MH8 Line 012	0.41	1.01	77.51	0.00	0.15	15.73	0.02	0.19	95.02
112	407.38	MH8 Line 013	0.23	1.99	76.70	0.30	0.15	14.38	0.04	0.36	94.13
113	405.85	MH8 Line 014	0.05	3.96	75.99	0.31	0.13	13.20	1.00	0.32	94.95
114	404.33	MH8 Line 015	0.02	2.89	76.41	0.32	0.14	13.28	0.72	0.30	94.08
115	402.65	MH8 Line 016	0.06	0.76	72.56	0.25	0.14	15.54	0.18	0.18	89.68
116	401.09	MH8 Line 017	0.07	0.82	75.13	0.12	0.15	14.97	0.13	0.30	91.69
117	399.57	MH8 Line 018	0.05	0.77	76.71	0.15	0.11	13.06	0.04	0.41	91.30
118	397.77	MH8 Line 019	0.07	0.79	71.20	0.43	0.18	14.02	0.27	0.21	87.17
119	396.32	MH8 Line 020	0.04	0.55	72.35	0.22	0.13	13.41	0.31	0.34	87.34
126	24.57	MH10 Line 001	0.08	0.60	77.01	0.19	0.00	13.37	0.39	0.36	91.99
127	22.98	MH10 Line 002	0.10	1.14	79.94	0.08	0.12	9.80	0.19	0.53	91.90
128	20.80	MH10 Line 003	0.16	0.77	72.27	0.11	0.11	14.48	0.17	0.32	88.38
129	19.53	MH10 Line 004	0.07	0.60	75.28	0.11	0.06	13.63	0.17	0.29	90.19
130	18.03	MH10 Line 005	0.05	2.66	72.04	0.30	0.10	14.49	0.15	0.24	90.03
131	16.62	MH10 Line 006	0.06	0.91	77.98	0.27	0.10	14.73	0.08	0.23	94.34
132	14.99	MH10 Line 007	0.09	1.18	71.95	0.25	0.10	14.50	0.07	0.31	88.46
133	33.43	MH10 Line 008	0.08	0.82	76.13	0.16	0.05	14.67	0.18	0.29	92.37
134	31.83	MH10 Line 009	0.12	1.27	72.64	0.30	0.10	15.90	0.05	0.28	90.64
135	30.26	MH10 Line 010	0.17	2.48	75.84	0.19	0.06	14.41	0.40	0.20	93.74
136	28.63	MH10 Line 011	0.02	2.14	74.07	0.34	0.05	16.03	0.36	0.12	93.12
137	27.10	MH10 Line 012	0.06	1.77	75.24	0.33	0.08	14.74	0.13	0.29	92.64
138	25.37	MH10 Line 013	0.09	4.60	71.26	0.16	0.07	14.82	0.22	0.36	91.56
139	23.89	MH10 Line 014	0.02	2.09	71.66	0.39	0.10	13.93	0.82	0.32	89.32
140	22.23	MH10 Line 015	0.04	3.02	71.95	0.27	0.06	15.44	0.29	0.21	91.27
141	20.73	MH10 Line 016	0.12	1.17	75.91	0.28	0.10	13.47	0.17	0.36	91.57
142	19.13	MH10 Line 017	0.03	3.47	73.43	0.30	0.06	14.70	1.76	0.17	93.92
143	17.56	MH10 Line 018	0.04	0.74	75.03	0.17	0.13	14.69	0.37	0.30	91.47
144	15.90	MH10 Line 019	0.05	0.73	72.46	0.29	0.07	13.77	0.19	0.31	87.87
145	14.44	MH10 Line 020	0.05	0.80	72.61	0.20	0.05	14.95	0.56	0.37	89.60
174	1.74	MH9_1	0.01	1.37	78.61	0.27	0.13	13.91	0.31	0.30	94.90
180	1.80	MH9 Line 001	0.04	4.30	80.83	0.22	0.11	14.20	1.45	0.37	101.52
181	1.81	MH9 Line 002	0.02	2.27	76.20	0.41	0.06	13.23	1.61	0.35	94.15
182	1.82	MH9 Line 003	0.07	1.00	77.48	0.32	0.13	13.79	0.51	0.30	93.60
183	1.83	MH9 Line 004	0.03	3.14	75.27	0.28	0.08	12.50	2.32	0.37	93.99
184	1.84	MH9 Line 005	0.11	0.87	78.43	0.32	0.12	14.34	0.26	0.27	94.72
185	1.85	MH9 Line 006	0.19	4.57	70.61	0.21	0.12	14.11	1.59	0.26	91.66
186	1.86	MH9 Line 007	0.07	1.25	76.12	0.02	0.09	12.21	0.43	0.44	90.63
187	1.87	MH9 Line 008	0.05	1.98	71.32	0.04	0.09	13.71	0.94	0.32	88.47
188	1.88	MH9 Line 009	0.06	1.26	71.86	0.48	0.07	14.58	0.22	0.36	88.88
189	1.89	MH9 Line 010	0.05	4.93	61.37	0.09	0.09	12.58	2.22	0.47	81.79
190	1.90	MH9 Line 011	0.07	0.89	70.95	0.24	0.13	12.39	0.60	0.30	85.57

Table B2: Composition of ilmenite - Magnet Heights, Eastern lobe.

	Oxides (wt%)								Cations normalized to 3 Oxygen atoms							
Analysis	SiO2	TiO2	Al2O3	Cr2O3	FeO	MnO	MgO	Total	Si	Ti	Al	Cr	Fe2+	Mn	Mg	Total
MH2_ilm2	0.10	53.72	0.02	0.08	44.97	0.44	0.97	100.31	0.002	1.005	0.001	0.002	0.936	0.009	0.036	1.991
MH2_ilm4	0.34	52.94	0.23	0.04	43.09	0.49	1.81	98.95	0.009	0.996	0.007	0.001	0.901	0.010	0.068	1.992
MH7_ilm1	0.07	53.15	0.17	0.02	41.50	0.41	4.94	100.26	0.002	0.976	0.005	0.000	0.848	0.008	0.180	2.019
MH7_ilm2	0.00	53.93	0.06	0.00	40.78	0.32	4.88	99.98	0.000	0.990	0.002	0.000	0.832	0.007	0.178	2.009
MH7_ilm4	0.03	54.45	0.03	0.03	39.50	0.46	5.05	99.54	0.001	0.999	0.001	0.001	0.806	0.009	0.183	2.000
MH7_ilm5	0.02	54.88	0.03	0.00	40.22	0.43	5.01	100.59	0.000	0.998	0.001	0.000	0.813	0.009	0.181	2.001
MH7_ilm6	0.01	54.53	0.03	0.00	41.27	0.38	5.12	101.34	0.000	0.988	0.001	0.000	0.831	0.008	0.184	2.012
MH8 _ilm1_1	0.03	54.00	0.04	0.04	40.15	0.61	4.97	99.84	0.001	0.991	0.001	0.001	0.819	0.013	0.181	2.007
MH8 _ilm1_2	0.00	53.64	0.05	0.00	41.22	0.41	4.87	100.19	0.000	0.985	0.001	0.000	0.842	0.008	0.177	2.014
MH8 _ilm1_3	0.04	54.15	0.02	0.01	40.66	0.56	5.09	100.53	0.001	0.988	0.001	0.000	0.825	0.012	0.184	2.010
MH8 _ilm2_1	0.13	54.36	0.08	0.01	40.42	0.38	4.42	99.78	0.003	0.998	0.002	0.000	0.825	0.008	0.161	1.998
MH8 _ilm2_2	0.02	53.81	0.06	0.03	41.61	0.32	5.06	100.90	0.000	0.981	0.002	0.001	0.844	0.007	0.183	2.017
MH8 _ilm2_3	0.00	54.76	0.02	0.04	39.52	0.22	5.23	99.79	0.000	1.001	0.001	0.001	0.803	0.004	0.189	1.999
MH10 _ilm1_	0.00	54.75	0.02	0.00	39.42	0.50	4.79	99.47	0.000	1.005	0.001	0.000	0.805	0.010	0.174	1.995
MH10 _ilm1_	0.02	54.25	0.03	0.02	39.25	0.28	4.97	98.81	0.000	1.002	0.001	0.000	0.806	0.006	0.182	1.997
MH10 _ilm1_	0.00	54.29	0.04	0.02	39.68	0.15	4.84	99.01	0.000	1.002	0.001	0.000	0.814	0.003	0.177	1.997
MH10 _ilm1_	0.04	54.58	0.04	0.01	39.66	0.36	4.77	99.46	0.001	1.002	0.001	0.000	0.810	0.007	0.174	1.996
MH10 _ilm1_	0.00	54.45	0.02	0.00	40.40	0.32	4.77	99.96	0.000	0.998	0.000	0.000	0.823	0.007	0.173	2.002

Table B3: Composition of chlorite in MML at Magnet Heights, Eastern lobe.

Analysis	SiO2	Al2O3	TiO2	Cr2O3	MnO	FeO	MgO	CaO	Na2O	K2O	F	Cl	Total
MH1B_1	23.48	23.67	0.17	0.00	0.02	33.84	11.85	0.04	0.06	0.03	0.00	0.06	93.20
MH1B_2	24.31	28.60	0.06	0.02	0.02	7.03	25.34	0.00	0.02	0.01	0.11	0.24	85.65
MH1B_3	31.12	23.62	3.14	0.03	0.09	11.80	11.10	0.06	0.15	0.08	0.10	0.05	81.28
MH1B_4	30.09	22.37	3.17	0.02	0.09	11.93	12.40	0.12	0.23	0.15	0.34	0.05	80.80
MH1B_5	35.57	27.88	0.05	0.07	0.02	16.16	6.04	0.36	0.08	0.08	0.00	0.01	86.32
MH1B_6	30.96	27.07	0.08	0.11	0.02	26.07	0.04	0.12	0.05	0.02	0.03	0.00	84.55
MH1B_7	29.26	26.08	0.05	0.15	0.03	26.44	0.06	0.10	0.04	0.03	0.00	0.01	82.22
MH1B_8	27.65	21.76	0.04	0.15	0.00	31.91	2.96	0.26	0.11	0.09	0.00	0.00	84.91
MH4_10	27.64	17.11	5.03	0.09	0.03	26.07	9.12	0.27	0.07	0.06	0.00	0.00	85.49
MH4_11	27.56	17.85	0.00	0.00	0.09	32.73	8.14	0.31	0.00	0.06	0.00	0.00	86.74
MH4_13	27.48	22.56	0.00	0.05	0.31	16.09	16.61	0.16	0.04	0.04	0.00	0.00	83.33
MH4_15	27.12	23.27	0.05	0.02	0.03	8.47	24.44	0.15	0.05	0.01	0.00	0.17	83.73

Table B4: Composition of plag in mag-anorthosite between layer 3 and 4 above the MML at Magnet Heights

Comment	1	2	3	4	5	7	8	9	11	12	13	14	16	17	18	19	20	21
SiO2	53.38	53.35	48.87	54.24	53.35	53.58	53.96	54.09	53.77	54.19	53.94	54.09	53.40	53.21	53.50	53.76	54.17	54.41
TiO2	0.06	0.02	0.02	0.06	0.05	0.03	0.07	0.02	0.07	0.06	0.01	0.01	0.02	0.00	0.06	0.03	0.06	0.02
Al2O3	29.31	29.07	32.16	29.25	29.01	28.98	28.72	29.09	29.08	28.63	28.63	29.21	29.47	29.17	29.35	29.03	28.69	29.01
FeO	0.40	0.17	0.27	0.25	0.30	0.22	0.34	0.22	0.25	0.09	0.22	0.22	0.18	0.35	0.19	0.26	0.24	0.24
MnO	0.01	0.00	0.00	0.03	0.01	0.01	0.00	0.00	0.01	0.00	0.02	0.01	0.00	0.00	0.00	0.00	0.00	0.00
MgO	0.01	0.02	0.02	0.01	0.00	0.03	0.02	0.00	0.03	0.00	0.02	0.01	0.01	0.02	0.01	0.01	0.00	0.01
CaO	11.87	12.12	15.41	11.92	12.11	12.16	11.69	11.90	11.88	11.41	11.72	12.08	12.13	11.97	12.07	11.93	11.88	11.78
BaO	0.02	0.05	0.01	0.05	0.01	0.03	0.04	0.04	0.05	0.01	0.03	0.04	0.01	0.00	0.03	0.04	0.04	0.02
Na2O	4.55	4.48	2.69	4.65	4.55	4.70	4.71	4.55	4.78	4.86	4.70	4.61	4.39	4.55	4.48	4.59	4.60	4.66
K2O	0.33	0.28	0.11	0.28	0.30	0.33	0.38	0.35	0.31	0.35	0.29	0.28	0.25	0.27	0.32	0.33	0.34	0.32
Total	99.93	99.57	99.57	100.73	99.68	100.06	99.92	100.25	100.24	99.61	99.58	100.55	99.86	99.55	100.01	99.98	100.03	100.47
Cations normalized to 8 Oxygen atoms																		
Si	2.421	2.427	2.246	2.438	2.426	2.429	2.446	2.442	2.432	2.459	2.451	2.436	2.420	2.422	2.423	2.436	2.451	2.450
Ti	0.002	0.001	0.001	0.002	0.002	0.001	0.002	0.001	0.002	0.002	0.000	0.000	0.001	0.000	0.002	0.001	0.002	0.001
Al	1.567	1.559	1.742	1.549	1.555	1.548	1.534	1.548	1.550	1.531	1.534	1.550	1.574	1.565	1.567	1.550	1.530	1.539
Fe2+	0.015	0.007	0.010	0.009	0.011	0.008	0.013	0.008	0.009	0.003	0.008	0.008	0.007	0.013	0.007	0.010	0.009	0.009
Mn	0.000	0.000	0.000	0.001	0.000	0.000	0.000	0.000	0.000	0.000	0.001	0.000	0.000	0.000	0.000	0.000	0.000	0.000
Mg	0.001	0.001	0.002	0.001	0.000	0.002	0.001	0.000	0.002	0.000	0.001	0.001	0.001	0.002	0.001	0.001	0.000	0.001
Ca	0.577	0.591	0.759	0.574	0.590	0.591	0.568	0.576	0.576	0.554	0.570	0.583	0.589	0.584	0.586	0.579	0.576	0.568
Ba	0.000	0.001	0.000	0.001	0.000	0.001	0.001	0.001	0.001	0.000	0.000	0.001	0.000	0.000	0.001	0.001	0.001	0.000
Na	0.400	0.395	0.240	0.405	0.401	0.413	0.414	0.398	0.419	0.428	0.414	0.403	0.386	0.401	0.393	0.403	0.404	0.407
K	0.019	0.016	0.007	0.016	0.017	0.019	0.022	0.020	0.018	0.020	0.017	0.016	0.015	0.016	0.018	0.019	0.020	0.018
Total	5.003	4.998	5.006	4.996	5.003	5.012	5.002	4.993	5.010	4.998	4.997	4.998	4.992	5.004	4.997	4.999	4.993	4.993
An	57.9	59.0	75.5	57.7	58.5	57.8	56.6	57.9	56.8	55.3	57.0	58.2	59.5	58.3	58.7	57.8	57.6	57.2

Table B5: Composition of selected orthopyroxene in magnetite bearing anorthosite between layer 3 and 4 above the MML at Magnet Heights, Eastern lobe.

Oxide	MH12_2	MH12_3
SiO2	51.38	52.07
TiO2	0.33	0.24
Al2O3	1.92	0.75
Cr2O3	0.02	0.00
FeO	25.20	25.06
MnO	0.51	0.61
MgO	19.09	19.43
CaO	0.81	0.99
Na2O	0.02	0.00
K2O	0.06	0.00
Total	99.34	99.16

Cation	MH12_2	MH12_3
Si	1.957	1.986
Ti	0.009	0.007
Al	0.086	0.034
Cr	0.000	0.000
Fe2+	0.803	0.799
Mn	0.017	0.020
Mg	1.083	1.105
Ca	0.033	0.040
Na	0.001	0.000
K	0.003	0.000
Total	3.993	3.991
Mg#	57.4	58.0

Table C1: Composition of Ti-magnetite in sample 10-30, Rhovan mine, Western lobe

No.	Comment	SiO2	CaO	TiO2	Al2O3	FeO	ZnO	MnO	V2O3	MgO	Cr2O3	Total
1	0-10_m1 Line 001	0.23	0.02	13.84	1.37	73.88	0.05	0.30	1.31	0.22	0.71	91.93
2	0-10_m1 Line 002	1.33	0.02	12.03	1.23	73.62	0.06	0.02	1.44	0.10	0.73	90.57
3	0-10_m1 Line 003	0.18	0.00	11.41	0.68	75.00	0.05	0.21	1.10	0.10	0.82	89.56
4	0-10_m1 Line 004	0.10	0.02	14.63	0.55	74.54	0.11	0.27	1.12	0.21	0.72	92.25
5	0-10_m1_1	0.04	0.03	12.72	1.66	74.60	0.02	0.29	1.37	0.69	0.70	92.11
7	0-10_m1_3	0.68	0.00	21.95	0.76	66.15	0.00	0.21	0.74	0.04	0.67	91.20
8	0-10_m1_4	0.19	0.03	13.31	3.28	72.88	0.00	0.15	1.21	0.17	0.71	91.93
10	0-10_mag1 002	0.50	0.04	12.22	0.69	74.68	0.07	0.07	1.21	0.07	0.78	90.34
11	0-10_mag1 003	1.02	0.04	12.26	1.10	73.51	0.00	0.06	1.40	0.08	0.70	90.17
12	0-10_mag1 004	0.32	0.03	13.45	0.69	72.87	0.00	0.03	1.35	0.05	0.64	89.41

Table C2: Composition of Ti-magnetite in sample 50-60B, Rhovan mine, Western lobe

Depth	SiO2	Al2O3	TiO2	Cr2O3	MnO	FeO	Fe2O3*	MgO	CaO	V2O3	ZnO	Total
50-60B	0.10	0.55	14.63	0.72	0.27	45.53	37.24	0.21	0.02	1.12	0.11	100.48
50-60B	0.50	0.69	12.22	0.78	0.07	43.67	39.45	0.07	0.04	1.21	0.07	98.78
50-60B	1.02	1.10	12.26	0.70	0.06	44.46	37.21	0.08	0.04	1.40	0.00	98.33
50-60B	0.73	0.62	16.48	0.34	0.07	48.08	30.56	0.07	0.01	0.92	0.00	97.89
50-60B	0.43	0.99	15.44	0.29	0.07	47.34	33.70	0.02	0.01	1.40	0.00	99.69
50-60B	1.50	1.28	12.76	0.34	0.16	46.17	36.13	0.01	0.00	1.43	0.03	99.80
50-60B	0.39	0.65	11.20	0.35	0.15	43.13	43.57	0.04	0.00	1.37	0.06	100.90
50-60B	0.47	0.64	13.39	0.27	0.06	45.05	38.26	0.04	0.03	1.22	0.06	99.50
50-60B	0.59	0.73	14.39	0.35	0.11	46.06	35.48	0.09	0.00	1.29	0.12	99.21
50-60B	0.23	3.85	11.08	0.35	0.11	43.56	40.47	0.07	0.02	1.64	0.05	101.41
50-60B	0.55	0.69	8.90	0.27	0.10	41.16	47.67	0.01	0.00	1.44	0.00	100.78
50-60B	0.28	1.84	20.64	0.31	0.27	51.39	21.73	0.15	0.01	0.78	0.00	97.38
50-60B	0.48	0.44	12.02	0.23	0.08	43.40	40.87	0.04	0.05	1.26	0.11	98.97
50-60B	0.14	0.58	13.80	0.29	0.24	44.73	38.42	0.12	0.02	1.28	0.13	99.75

Fe2O3 estimated by stoichiometry

Table C3: Composition of Ti-magnetite in sample 70-80, Rhovan mine, Western lobe

Depth	SiO2	Al2O3	TiO2	Cr2O3	MnO	FeO	Fe2O3*	MgO	CaO	V2O3	ZnO	Total
70-80	0.52	0.52	10.66	0.35	0.13	42.49	43.80	0.02	0.00	1.26	0.00	99.75
70-80	0.45	0.53	11.76	0.34	0.02	43.72	42.33	0.09	0.02	1.33	0.01	100.58
70-80	0.57	0.55	9.06	0.35	0.04	40.90	47.04	0.08	0.02	1.24	0.11	99.96
70-80	1.13	1.21	13.25	0.31	0.01	44.94	35.37	0.48	0.03	1.46	0.05	98.25
70-80	0.19	0.40	10.60	0.40	0.16	42.07	45.16	0.07	0.00	1.49	0.00	100.54
70-80	1.20	0.84	15.67	0.29	0.02	47.71	30.74	0.23	0.00	0.98	0.02	97.69
70-80	0.07	0.76	11.89	0.33	0.25	42.81	42.87	0.28	0.02	1.44	0.03	100.74
70-80	0.39	0.65	15.11	0.30	0.20	46.38	34.45	0.04	0.00	1.20	0.00	98.72
70-80	0.47	0.46	13.43	0.32	0.03	44.94	37.76	0.06	0.01	1.38	0.08	98.94
70-80	0.35	0.50	11.56	0.40	0.03	43.45	42.73	0.02	0.02	1.48	0.01	100.55
70-80	0.63	0.61	13.12	0.35	0.04	44.73	38.22	0.13	0.00	1.10	0.12	99.05
70-80	0.37	0.56	10.66	0.29	0.07	42.81	44.88	0.00	0.00	1.50	0.00	101.14

Fe2O3 estimated by stoichiometry

Table C4: The composition of ilmenite from sample 10-30, Rhovan mine, Western lobe

Comment	SiO2	CaO	TiO2	Al2O3	FeO	ZnO	MnO	MgO	Cr2O3	Total
0-10_ilm_1	0.02	0.01	53.44	0.02	41.20	0.02	0.46	4.42	0.00	99.59
0-10_ilm_1 001	0.01	0.00	54.11	0.03	39.48	0.00	0.51	4.37	0.05	98.56
0-10_ilm_1 002	0.02	0.02	54.16	0.01	40.96	0.00	0.43	4.48	0.01	100.10
0-10_ilm_1 003	0.02	0.01	53.60	0.02	40.95	0.05	0.45	4.49	0.03	99.62
0-10_ilm_1 004	0.02	0.01	54.05	0.01	40.42	0.00	0.47	4.40	0.04	99.43
0-10_ilm_2	0.01	0.00	53.89	0.01	40.87	0.04	0.42	4.57	0.00	99.81
0-10_ilm_3	0.03	0.01	53.77	0.02	41.41	0.00	0.60	4.26	0.07	100.18
0-10_ilm1 001	0.03	0.03	53.87	0.05	40.40	0.00	0.52	4.44	0.02	99.36
0-10_ilm1 002	0.02	0.02	54.00	0.01	40.53	0.00	0.51	4.13	0.06	99.26
0-10_ilm1 003	0.04	0.00	53.31	0.04	41.05	0.00	0.50	3.95	0.00	98.87
0-10_ilm1 004	0.00	0.00	53.91	0.02	40.85	0.00	0.59	3.91	0.04	99.33